UNIVERSITÄT
SIEGEN

Christian Hesch

Dynamics of continua with interfaces

Herausgeber: Peter Betsch

Schriftenreihe des Lehrstuhls für Numerische Mechanik

Band VII

Dynamics of continua with interfaces

der Naturwissenschaftlich-Technischen Fakultät
der Universität Siegen
zur Erlangung der venia legendi für das Fach

Mechanik

vorgelegte Habilitationsschrift

von
Dr.-Ing. Christian Hesch

Gutachter:
Prof. Dr.-Ing. habil. Peter Betsch
Prof. Dr.-Ing. Wolfgang A. Wall

Tag der Einreichung: 06.06.2012
Vollzug des Habilitationsverfahrens: 24.05.2013

Impressum
Prof. Dr.-Ing. habil. Peter Betsch
Lehrstuhl für Numerische Mechanik
Universität Siegen
57068 Siegen
ISSN 1866-1203
URN urn:nbn:de:hbz:467-7496

Preface

This thesis is based on my work at the Chair of Computational Mechanics at the University of Siegen. It summarizes numerous articles [33, 34, 37, 12, 36, 35, 39, 38, 2, 21] which have been published by the author.

First of all I want to thank Peter Betsch for his outstanding support throughout many difficult years. His continuous inspiration and motivation in many discussions, the freedom to develop and work on my own research projects and the permanent support have been the foundation of this work. Moreover, I thank Professor Wall for acting as referee of this thesis.

I'd like to thank all co-workers inside and outside of the chair. It was a great pleasure to me to work with Nicolas Sänger, Melanie Krüger, Marlon Franke, Michael Groß, Ralf Siebert, Denis Anders, Stefan Uhlar, Kerstin Weinberg and many others. Furthermore, I'd like to thank Javier Bonet, Antonio Gil and Aurelio Arranz Carreño for a great time in Swansea and many inspiring discussions.

I've received great support from many personal friends throughout the past years and I fear, once I start with names I will forget someone. Thanks to all of you! Finally I'd like to thank my parents for the continuous support during all the years of my life.

To a very special friend: 0 errors, 0 warning, 0 badboxes

Siegen, June 2012, Christian Hesch

Introduction

Continuum mechanics is nowadays widely used to describe the material behavior of systems, which occupies a specific area in space. In contrast to atomistic and molecular models, which can be solved using molecular dynamics or Monte-Carlo simulations, we consider the system to exist as a continuum. Due to their different material behavior we distinguish between solid mechanics and fluid mechanics. The typical deformation of the former one allows us to follow the movement of each particle in space, whereas we can not do this for the latter one. This leads to different formulations, which will be presented here.

Typically, we want to achieve a solution for the balance of linear momentum for the continuum mechanical system. Additionally, we will derive a pure mass transport problem to demonstrate the capabilities of the numerical framework we have developed to solve these kind of problems. Once we have introduced the continuum mechanical framework, we can extent this to include further physical effects. Moreover, we extent the solid mechanical system to include thermal contributions and apply an additional pressure field to enforce the incompressibility of the fluids in the case of low Mach numbers.

Within the continuous setting, we can define various interfaces. Internal interfaces can be used to decompose bodies into different subsets, e.g. to define areas with different physical properties or, on a more technical level, to enable parallelization on modern cluster architectures. External interfaces on solids can be used to include contact between multiple bodies. Additionally we could establish an interface at the external boundary to transfer momentum between a solid and the surrounding fluid. To avoid technical problems in the case of large deformations of solids, embedded within a fluid, we employ continuum immersed strategies to include the effects of fluid-structure interaction. Finally, we want to use phase field models for the simulation of phase separation and coarsening in solder alloys. We obtain sharp interfaces between the phases using the well known Cahn-Hilliard model to represent the free energy of the phases as well as of the interface. Similar to the immersed strategies, we aim at the simulation of the whole domain, avoiding the explicit representation of interfaces.

To solve the arising initial boundary value problem in space, we first apply the finite element method for all problems at hand. In particular, we introduce Lagrangian as well as NURBS based shape functions for the underlying approximation of the field equations, written in weak form. Furthermore, we show how to incorporate discrete interface models in an optimal sense with regard to the consistency error at the interface using the Mortar method. The application of Mortar methods to NURBS will be shown as well. Due to the higher continuity requirement of the Cahn-Hilliard equation, the use of NURBS seems to be natural for this kind of problems.

Since we deal with initial boundary value problems, suitable time integration schemes have to be developed as well. In general, we use a common implicit integration scheme for all problems at hand, such that we could use various fields simultaneously in a consistent framework. If possible, we aim at the development of structure preserving integrators, since they provide enhanced numerical stability for large time steps. For the explicit interface representation we apply additional augmentation techniques to simplify the algebraic constraints and verify the underlying conservation properties.

The outline of this work is as follows. The fundamental equations in strong and weak form are outlined in Section 1. The spatial discretization based on finite elements will be dealt with in Section 2. The discretization in time using implicit and structure preserving schemes is presented in Section 3. Domain decomposition methods are addressed in Section 4, whereas contact problems are addressed in Section 5. In Section 6 we introduce immersed strategies for fluid-structure interaction problems and demonstrate the application of NURBS to phase field problems in Section 7. We provide representative examples at the end of Section 4, 5, 6 and 7. Eventually, conclusions are drawn in Section 8.

Contents

1 Continuum mechanical considerations

In this section we provide an outline of the fundamental equations for the underlying problems at hand. We start by considering solid mechanical problems in strong and weak form (see Hesch & Betsch [33, 34, 39]), thermomechanical problems (see Hesch & Betsch [35]), fluid problems (see Hesch et al. [38]) and in a last step unsteady transport problems (see Anders et al. [2]).

1.1 Solid mechanics

First, we consider a general non-linear mechanical system, occupying the space $\mathcal{B}_0 \subset \mathbb{R}^d$, $d \in [2, 3]$, in the reference configuration. The deformation mapping $\boldsymbol{\varphi}(\boldsymbol{X}, t) : \mathcal{B}_0 \times [0, T] \rightarrow \mathbb{R}^d$, where $[0, T]$ denotes the time interval under consideration, characterizes the current position of the material point $\boldsymbol{X} \in \mathcal{B}_0$ at time t. The linear momentum is given by $\boldsymbol{\pi} = \rho_0 \boldsymbol{v}$, where ρ_0 denotes the density in the reference configuration and $\boldsymbol{v} : \mathcal{B}_0 \times [0, T] \rightarrow \mathbb{R}^d$, $\boldsymbol{v} = \dot{\boldsymbol{\varphi}} = \partial \boldsymbol{\varphi} / \partial t$ the material velocity. The material surface $\partial \mathcal{B}_0$ is partitioned into the Dirichlet boundary $\partial \mathcal{B}_0^{\boldsymbol{u}}$ and the Neumann boundary $\partial \mathcal{B}_0^{\boldsymbol{\sigma}}$. We require that the portions $\partial \mathcal{B}_0^{\boldsymbol{u}}$ and $\partial \mathcal{B}_0^{\boldsymbol{\sigma}}$ satisfy

$$\partial \mathcal{B}_0^{\boldsymbol{u}} \cup \partial \mathcal{B}_0^{\boldsymbol{\sigma}} = \partial \mathcal{B}_0 \quad \text{and} \quad \partial \mathcal{B}_0^{\boldsymbol{u}} \cap \partial \mathcal{B}_0^{\boldsymbol{\sigma}} = \emptyset \tag{1.1}$$

Furthermore, we assume the existence of a strain energy function $\Psi(\boldsymbol{C}) : \mathcal{B}_0 \times [0, T] \rightarrow \mathbb{R}$, where $\boldsymbol{C} : \mathcal{B}_0 \times [0, T] \rightarrow \mathbb{R}^{d \times d}$ denotes the right Cauchy-Green deformation tensor, given by $\boldsymbol{C} = \boldsymbol{F}^T \boldsymbol{F}$ and $\boldsymbol{F} : \mathcal{B}_0 \times [0, T] \rightarrow \mathbb{R}^{d \times d}$, $\boldsymbol{F} = \nabla_{\boldsymbol{X}} \boldsymbol{\varphi}$ denotes the deformation gradient. The Lagrangian form of the balance of linear momentum is given by

$$\begin{aligned} \dot{\boldsymbol{\varphi}} &= \rho_0^{-1} \boldsymbol{\pi} \\ \dot{\boldsymbol{\pi}} &= \operatorname{Div}(\boldsymbol{P}) + \bar{\boldsymbol{B}} \end{aligned} \tag{1.2}$$

supplemented by the boundary conditions

$$\begin{aligned} \boldsymbol{\varphi} &= \bar{\boldsymbol{\varphi}} \quad \text{on} \quad \partial \mathcal{B}_0^{\boldsymbol{u}} \times [0, T] \\ \boldsymbol{P}\boldsymbol{N} &= \bar{\boldsymbol{T}} \quad \text{on} \quad \partial \mathcal{B}_0^{\boldsymbol{\sigma}} \times [0, T] \end{aligned} \tag{1.3}$$

where $\boldsymbol{P} = 2\boldsymbol{F} \nabla_{\boldsymbol{C}} \Psi(\boldsymbol{C})$ denotes the first Piola-Kirchhoff stress tensor, $\boldsymbol{N}$ the outward unit normal vector in the reference configuration, $\bar{\boldsymbol{B}}$ the applied body forces and $\bar{\boldsymbol{T}}$ the prescribed tractions. To complete the set of equations for the initial-boundary value problem we have to prescribe appropriate initial conditions

$$\boldsymbol{\varphi}(\cdot, 0) = \boldsymbol{X}, \quad \dot{\boldsymbol{\varphi}}(\cdot, 0) = \boldsymbol{v}_0 \tag{1.4}$$

for the position as well as for the velocity. Equation (1.2) along with (1.3) represents the strong formulation of the problem, whereas the weak form will be derived next. To this end we introduce the space of admissible test functions $\mathcal{V}^{\varphi}$ defined by

$$\mathcal{V}^{\varphi} = \{\delta\boldsymbol{\varphi} \in \mathbb{H}^1(\mathcal{B}) \mid \delta\boldsymbol{\varphi}(\boldsymbol{X}) = \boldsymbol{0} \,\forall\, \boldsymbol{X} \in \partial\mathcal{B}_0^{\boldsymbol{u}}\} \tag{1.5}$$

along with the L_2-inner product on $\mathcal{B}_0$

$$\int\limits_{\mathcal{B}_0} (\bullet) \cdot (\bullet) \,\mathrm{d}V =: \langle \bullet, \bullet \rangle_{\mathcal{B}_0} \quad \text{and} \quad \int\limits_{\partial\mathcal{B}_0} (\bullet) \cdot (\bullet) \,\mathrm{d}A =: \langle \bullet, \bullet \rangle_{\partial\mathcal{B}_0} \tag{1.6}$$

where the Sobolev functional space $\mathbb{H}^1$ contains the set of square integrable functions with square integrable gradient. Summarized, the weak form reads

$$\langle \rho_0 \ddot{\boldsymbol{\varphi}}, \delta\boldsymbol{\varphi} \rangle_{\mathcal{B}_0} + \langle \boldsymbol{P}, \nabla_{\boldsymbol{X}} (\delta\boldsymbol{\varphi}) \rangle_{\mathcal{B}_0} = \langle \rho_0 \bar{\boldsymbol{B}}, \delta\boldsymbol{\varphi} \rangle_{\mathcal{B}_0} + \langle \bar{\boldsymbol{T}}, \delta\boldsymbol{\varphi} \rangle_{\partial\mathcal{B}_0^{\sigma}} \tag{1.7}$$

This equation has to hold for all $\delta\boldsymbol{\varphi} \in \mathcal{V}^{\varphi}$.

Conservation properties. Setting $\delta\boldsymbol{\varphi} = \boldsymbol{\zeta}$, where $\boldsymbol{\zeta} \in \mathbb{R}^d$ is arbitrary and constant, it is straightforward to show that (1.7) yields the balance law for linear momentum in integral form

$$\boldsymbol{\zeta} \cdot \frac{d}{dt}\boldsymbol{L} = \langle \boldsymbol{\zeta}, \bar{\boldsymbol{T}} \rangle_{\partial\mathcal{B}_0^{\sigma}} + \langle \boldsymbol{\zeta}, \bar{\boldsymbol{B}} \rangle_{\mathcal{B}_0} \tag{1.8}$$

Here, the total linear momentum is given by $\boldsymbol{L} = \int_{\mathcal{B}_0} \boldsymbol{\pi} \,\mathrm{d}V$ and the right-hand side of (1.8) characterizes the resultant external force applied to the continuum body. Similarly, substituting $\delta\boldsymbol{\varphi} = \boldsymbol{\zeta} \times \boldsymbol{\varphi}$ into (1.7), the integral form of the balance law for angular momentum is recovered

$$\boldsymbol{\zeta} \cdot \frac{d}{dt}\boldsymbol{J} = \langle \boldsymbol{\zeta}, \boldsymbol{\varphi} \times \bar{\boldsymbol{T}} \rangle_{\partial\mathcal{B}_0^{\sigma}} + \langle \boldsymbol{\zeta}, \boldsymbol{\varphi} \times \bar{\boldsymbol{B}} \rangle_{\mathcal{B}_0} \tag{1.9}$$

In this connection, $\boldsymbol{J} = \int_{\mathcal{B}_0} \boldsymbol{\varphi} \times \boldsymbol{\pi} \,\mathrm{d}V$ is the total angular momentum of the continuum body with respect to the origin of the inertial frame of reference. The right-hand side of (1.9) equals the resultant external torque about the origin. We next consider the integral form of the balance law for energy. Substituting $\delta\boldsymbol{\varphi} = \dot{\boldsymbol{\varphi}}$ into (1.7) yields

$$\underbrace{\frac{\mathrm{d}}{\mathrm{d}t}\langle \frac{1}{2}\dot{\boldsymbol{\varphi}}, \boldsymbol{\pi} \rangle_{\mathcal{B}_0}}_{dT/dt} + \underbrace{\langle \frac{1}{2}\boldsymbol{\Sigma}, \dot{\boldsymbol{C}} \rangle_{\mathcal{B}_0}}_{W} = \underbrace{\langle \dot{\boldsymbol{\varphi}} \cdot \bar{\boldsymbol{T}} \rangle_{\partial\mathcal{B}_0^{\sigma}} + \langle \dot{\boldsymbol{\varphi}}, \bar{\boldsymbol{B}} \rangle_{\mathcal{B}_0}}_{P^{\mathrm{ext}}} \tag{1.10}$$

Here, T denotes the total kinetic energy of the continuum body, W the net working and P^{ext} the power of external forces. Furthermore, the second Piola-Kirchhoff stress tensor $\boldsymbol{\Sigma} = \boldsymbol{F}^{-1}\boldsymbol{P}$ has been introduced. For a purely mechanical system, the net working equals the change in internal energy $W = \dot{E}$ and we obtain

$$\frac{\mathrm{d}}{\mathrm{d}t}(T + E) = P^{\mathrm{ext}} \tag{1.11}$$

which is the global form of the energy balance law.

1.2 Thermomechanical systems

Next, we extent the previously developed formulation to include thermal contributions. Details on the continuum description of thermoelastic solids can be found in textbooks such as Holzapfel [40] and Gonzalez & Stuart [28].

The absolute temperature θ is assumed to be a smooth function of $(\boldsymbol{X}, t) \in \mathcal{B}_0 \times [0, T] \to \mathbb{R}$. We further assume that the material behavior is governed by the free energy function $\Psi = \hat{\Psi}(\boldsymbol{C}, \theta)$. Accordingly, the nominal (or first Piola-Kirchhoff) stress tensor $\boldsymbol{P}$, and the entropy η are defined by

$$\begin{aligned} \boldsymbol{P} &= 2\boldsymbol{F}\nabla_{\boldsymbol{C}}\, \hat{\Psi}(\boldsymbol{C}, \theta) \\ \eta &= -\nabla_{\theta}\, \hat{\Psi}(\boldsymbol{C}, \theta) \end{aligned} \tag{1.12}$$

Moreover, the nominal heat flux vector $\boldsymbol{Q}$ is defined by

$$\boldsymbol{Q} = -\widehat{\boldsymbol{K}}(\boldsymbol{C}, \theta)\, \mathrm{Grad}(\theta) \tag{1.13}$$

Here, $\widehat{\boldsymbol{K}}(\boldsymbol{C}, \theta)$ is a thermal conductivity tensor which must be positive semi-definite. Note that the constitutive laws (1.12) and (1.13) are thermodynamically consistent in the sense that they satisfy the restrictions imposed by the second law of thermodynamics (in the form of the Clausius-Duhem inequality). The Lagrangian form of the local balance of linear momentum and energy for a thermoelastic body can be written as

$$\begin{aligned} \dot{\boldsymbol{\varphi}} &= \rho_0^{-1}\boldsymbol{\pi} \\ \dot{\boldsymbol{\pi}} &= \mathrm{Div}(\boldsymbol{P}) + \bar{\boldsymbol{B}} \\ \theta\dot{\eta} &= -\,\mathrm{Div}(\boldsymbol{Q}) + \bar{R} \end{aligned} \tag{1.14}$$

where $\bar{R}(\boldsymbol{X}, t)$ denotes the material descriptions of prescribed heat supply per unit volume. The above equations have to be satisfied for all $\boldsymbol{X} \in \mathcal{B}_0$ and $t \geq 0$. To complete the initial-boundary value problem for the thermoelastic body under consideration the equations in (1.14) have to be supplemented by appropriate initial and boundary conditions. Accordingly, initial conditions in $\mathcal{B}_0$ and at time $t = 0$ are specified by

$$\boldsymbol{\varphi}(\cdot, 0) = \boldsymbol{X}\,, \quad \dot{\boldsymbol{\varphi}}(\cdot, 0) = \boldsymbol{v}_0\,, \quad \theta(\cdot, 0) = \theta_0 \quad \text{in } \mathcal{B}_0 \tag{1.15}$$

where $\boldsymbol{v}_0$ and θ_0 are prescribed fields. Moreover, boundary conditions on $\partial\mathcal{B}_0$ at times $t \geq 0$ are given by

$$\begin{aligned} \boldsymbol{\varphi} &= \bar{\boldsymbol{\varphi}} \quad \text{on } \partial\mathcal{B}_0^u \times [0, T]\,, & \theta &= \bar{\theta} \quad \text{on } \partial\mathcal{B}_0^\theta \times [0, T] \\ \boldsymbol{P}\boldsymbol{N} &= \bar{\boldsymbol{T}} \quad \text{on } \partial\mathcal{B}_0^\sigma \times [0, T]\,, & \boldsymbol{Q} \cdot \boldsymbol{N} &= -\bar{Q} \quad \text{on } \partial\mathcal{B}_0^{\mathrm{Q}} \times [0, T] \end{aligned} \tag{1.16}$$

Analogues to the mechanical field, $\partial\mathcal{B}_0^\theta$ and $\partial\mathcal{B}_0^{\mathrm{Q}}$ are subsets of $\partial\mathcal{B}_0$ with the properties $\partial\mathcal{B}_0^\theta \cup \partial\mathcal{B}_0^{\mathrm{Q}} = \partial\mathcal{B}_0$ and $\partial\mathcal{B}_0^\theta \cap \partial\mathcal{B}_0^{\mathrm{Q}} = \emptyset$. As before, $\boldsymbol{N}$ denotes the unit outward normal field on $\partial\mathcal{B}_0$, and $\bar{\boldsymbol{\varphi}}$, $\bar{\boldsymbol{T}}$, $\bar{\theta}$ and $\bar{Q}$ are prescribed fields.

The weak form can be derived by pre-multiplication of $(1.14)_2$ using the previously introduced test functions $\delta\boldsymbol{\varphi}$. Subsequent integration yields

$$\langle \delta\boldsymbol{\varphi}, \dot{\boldsymbol{\pi}} \rangle_{\mathcal{B}_0} = \langle \delta\boldsymbol{\varphi}, \mathrm{Div}(\boldsymbol{P}) + \bar{\boldsymbol{B}} \rangle_{\mathcal{B}_0} \tag{1.17}$$

Similarly, $(1.14)_3$ leads to

$$\langle \delta\theta, \theta\dot{\eta} \rangle_{\mathcal{B}_0} = \langle \delta\theta, \bar{R} - \mathrm{Div}(\boldsymbol{Q}) \rangle_{\mathcal{B}_0} \tag{1.18}$$

where the space of admissible test functions $\mathcal{V}^\theta$ of the temperature field is defined as

$$\mathcal{V}^\theta = \{\delta\theta \in \mathbb{H}^1(\mathcal{B}) \mid \delta\theta(\boldsymbol{X}) = 0 \; \forall \; \boldsymbol{X} \in \partial\mathcal{B}_0^\theta\} \tag{1.19}$$

Applying integration by parts along with the divergence theorem, (1.17) and (1.18) can be recast as follows

$$\begin{aligned} \langle \delta\boldsymbol{\varphi}, \dot{\boldsymbol{\pi}} \rangle_{\mathcal{B}_0} + \langle \boldsymbol{P}, \nabla_{\boldsymbol{X}} (\delta\boldsymbol{\varphi}) \rangle_{\mathcal{B}_0} &= \langle \delta\boldsymbol{\varphi}, \bar{\boldsymbol{T}} \rangle_{\mathcal{B}_0^\sigma} + \langle \delta\boldsymbol{\varphi}, \bar{\boldsymbol{B}} \rangle_{\mathcal{B}_0} \\ \langle \delta\theta, \theta\dot{\eta} \rangle_{\mathcal{B}_0} - \langle \boldsymbol{Q}, \nabla_{\boldsymbol{X}} (\delta\theta) \rangle_{\mathcal{B}_0} &= \langle \delta\theta, \bar{Q} \rangle_{\partial\mathcal{B}_0^Q} + \langle \delta\theta, \bar{R} \rangle_{\mathcal{B}_0} \end{aligned} \tag{1.20}$$

These equations have to hold for all $\delta\boldsymbol{\varphi} \in \mathcal{V}^\varphi$ and $\delta\theta \in \mathcal{V}^\theta$. While the balance of linear momentum and the balance of energy are stated in weak form, we retain the kinematic relationship $(1.14)_1$ in local form.

Conservation properties. Next, we summarize the fundamental balance laws in global form. The balance laws for linear and angular momentum can be derived analogues to the purely mechanical case, setting $\delta\boldsymbol{\varphi} = \boldsymbol{\zeta}$ and $\delta\boldsymbol{\varphi} = \boldsymbol{\zeta} \times \boldsymbol{\varphi}$ respectively and we obtain once again

$$\boldsymbol{\zeta} \cdot \frac{d}{dt}\boldsymbol{L} = \langle \boldsymbol{\zeta}, \bar{\boldsymbol{T}} \rangle_{\partial\mathcal{B}_0^\sigma} + \langle \boldsymbol{\zeta}, \bar{\boldsymbol{B}} \rangle_{\mathcal{B}_0} \tag{1.21}$$

and

$$\boldsymbol{\zeta} \cdot \frac{d}{dt}\boldsymbol{J} = \langle \boldsymbol{\zeta}, \boldsymbol{\varphi} \times \bar{\boldsymbol{T}} \rangle_{\partial\mathcal{B}_0^\sigma} + \langle \boldsymbol{\zeta}, \boldsymbol{\varphi} \times \bar{\boldsymbol{B}} \rangle_{\mathcal{B}_0} \tag{1.22}$$

Note, that we restrict for simplicity of exposition our attention on thermoelastic problems with pure Neumann data, i.e. $\partial\mathcal{B}_0^{\boldsymbol{u}} = \partial\mathcal{B}_0^\theta = \emptyset$. Next, we consider the integral form of the balance law for energy. Substituting $\delta\boldsymbol{\varphi} = \dot{\boldsymbol{\varphi}}$ into $(1.20)_1$ yields

$$\frac{\mathrm{d}}{\mathrm{d}t}\langle \frac{1}{2}\dot{\boldsymbol{\varphi}}, \boldsymbol{\pi} \rangle_{\mathcal{B}_0} + \langle \frac{1}{2}\boldsymbol{\Sigma}, \dot{\boldsymbol{C}} \rangle_{\mathcal{B}_0} = \langle \dot{\boldsymbol{\varphi}} \cdot \bar{\boldsymbol{T}} \rangle_{\partial\mathcal{B}_0^\sigma} + \langle \dot{\boldsymbol{\varphi}}, \bar{\boldsymbol{B}} \rangle_{\mathcal{B}_0} \tag{1.23}$$

The relationship between the free energy Ψ and the specific internal energy e is given by

$$\Psi = e - \theta\eta \tag{1.24}$$

Differentiation with respect to time yields

$$\dot{\Psi} = \dot{e} - \dot{\theta}\eta - \theta\dot{\eta} \tag{1.25}$$

On the other hand the constitutive equations (1.12) are based on the free energy function $\hat{\Psi}(\boldsymbol{C}, \theta)$ and thus imply

$$\dot{\Psi} = \underbrace{\frac{\partial \hat{\Psi}(\boldsymbol{C}, \theta)}{\partial \boldsymbol{C}}}_{\frac{1}{2}\boldsymbol{\Sigma}} : \dot{\boldsymbol{C}} + \underbrace{\frac{\partial \hat{\Psi}(\boldsymbol{C}, \theta)}{\partial \theta}}_{-\eta} \dot{\theta} \tag{1.26}$$

Accordingly, taking into account (1.25) and (1.26), the stress power can be written as

$$\frac{1}{2}\boldsymbol{\Sigma} : \dot{\boldsymbol{C}} = \dot{e} - \theta\dot{\eta} \tag{1.27}$$

Introducing the total internal energy of the continuum body $E = \int_{\mathcal{B}_0} e \, \mathrm{d}V$, the net working can now be written in the form

$$W = \dot{E} - \int\limits_{\mathcal{B}_0} \theta\dot{\eta} \, \mathrm{d}V \tag{1.28}$$

Testing $(1.20)_2$ on the constant and arbitrary $\delta\theta = \zeta$, $\zeta \in \mathbb{R}$, gives

$$\langle \zeta, \theta\dot{\eta} \rangle_{\mathcal{B}_0} = -\langle \zeta, \boldsymbol{Q} \cdot \boldsymbol{N} \rangle_{\partial\mathcal{B}_0^Q} + \langle \zeta, \bar{R} \rangle_{\mathcal{B}_0} =: \zeta Q \tag{1.29}$$

where Q is the total net heating of the continuum body. Substituting (1.29) into (1.28), we recover the first law of thermodynamics in the form $dE/dt = W + Q$. Moreover, in view of (1.10), the global form of the energy balance law can be written as

$$\frac{d}{dt}\left[T + E\right] = P^{\text{ext}} + Q \tag{1.30}$$

In the case of external forces associated with a potential energy V^{ext}, i.e. $P^{\text{ext}} = -dV^{\text{ext}}/dt$ we obtain

$$\frac{d}{dt}\left[T + E + V^{\text{ext}}\right] = Q \tag{1.31}$$

which is the global energy balance law for a thermomechanical system.

1.3 Fluid mechanics

To catch fluid mechanical properties, we write the fluid system in terms of an Eulerian description using the inverse mapping $\boldsymbol{X} = \boldsymbol{\varphi}^{-1}(\boldsymbol{x}(t), t)$. For the time differential of a physical quantity $f(\boldsymbol{x}(t), t)$, it follows immediately that

$$\dot{f} = \frac{\partial f}{\partial t} + \boldsymbol{v} \cdot \nabla_{\boldsymbol{x}} f \tag{1.32}$$

Without loss of generality we restrict ourselves to the incompressible case and obtain for the conservation of mass equation

$$\nabla_{\boldsymbol{x}} \cdot \boldsymbol{v} = \frac{\dot{J}}{J} \equiv 0 \tag{1.33}$$

where $J = \det(\boldsymbol{F})$. For a Newtonian viscous fluid the Cauchy stress tensor $\boldsymbol{\sigma} : \mathcal{B} \times [0,\, T] \to \mathbb{R}^{d \times d}$ is defined by

$$\boldsymbol{\sigma} = -p\boldsymbol{I} + \lambda(\nabla_{\boldsymbol{x}} \cdot \boldsymbol{v})\boldsymbol{I} + \mu \left(\nabla_{\boldsymbol{x}} \boldsymbol{v} + \nabla_{\boldsymbol{x}} \boldsymbol{v}^T\right) \tag{1.34}$$

where μ denotes the dynamic viscosity and λ the second coefficient of viscosity. Here, the pressure $p : \mathcal{B} \times [0, T] \to \mathbb{R}$ is a sufficiently smooth function and can be regarded as Lagrange multiplier introduced to enforce condition (1.33). Note that for the case of an incompressible fluid the second term on the right hand side vanishes. The non-conservative Eulerian form of the balance of linear momentum reads

$$\rho \dot{\boldsymbol{v}} = \nabla_{\boldsymbol{x}} \cdot \boldsymbol{\sigma} + \rho \boldsymbol{g} \tag{1.35}$$

where ρ denotes the density and $\boldsymbol{g}$ a prescribed body force per unit of mass. Finally, suitable boundary conditions need to be introduced as follows

$$\begin{aligned} \boldsymbol{v} = \boldsymbol{u}, &\quad \text{on} \quad \partial\mathcal{B}^u \times [0,\, T] \\ \boldsymbol{\sigma} \cdot \boldsymbol{n} = \boldsymbol{h}, &\quad \text{on} \quad \partial\mathcal{B}^\sigma \times [0,\, T] \end{aligned} \tag{1.36}$$

Here, $(1.36)_1$ and $(1.36)_2$ denote the Dirichlet and Neumann boundary conditions, respectively, assuming $\partial\mathcal{B}^u \cup \partial\mathcal{B}^\sigma = \partial\mathcal{B}$, $\partial\mathcal{B}^u \cap \partial\mathcal{B}^\sigma = \emptyset$ and $\boldsymbol{n}$ the outward unit normal vector on the actual configuration.

As before, we recast the above system of partial differential equations in its variational counterpart, i.e. the weak form. Hence, suitable functional spaces of test functions $\mathcal{V}^v$ and $\mathcal{V}^p$ for both, the velocity and pressure field, are defined by

$$\begin{aligned} &\mathcal{V}^v =: \{\delta\boldsymbol{v} \in \mathbb{H}^1(\mathcal{B}) \mid \delta\boldsymbol{v}(\boldsymbol{x}) = \boldsymbol{0}\; \forall\, \boldsymbol{x} \in \partial\mathcal{B}^u\} \\ &\mathcal{V}^p =: \{\delta p \in L_2(\mathcal{B})\} \end{aligned} \tag{1.37}$$

Finally, we recast the balance of linear momentum as follows

$$\langle \rho(\dot{\boldsymbol{v}} - \boldsymbol{g}), \delta\boldsymbol{v}\rangle_{\mathcal{B}} + \langle \boldsymbol{\sigma}, \nabla_{\boldsymbol{x}} (\delta\boldsymbol{v})\rangle_{\mathcal{B}} = \langle \boldsymbol{h}, \delta\boldsymbol{v}\rangle_{\partial\mathcal{B}^\sigma} \tag{1.38}$$

supplemented by the kinematic constraint

$$\langle \nabla_{\boldsymbol{x}} \cdot \boldsymbol{v}, \delta p\rangle_{\mathcal{B}} = 0 \tag{1.39}$$

Note that we perform the integration on the spatial configuration in (1.38) and (1.39). Furthermore, both equations (1.38-1.39) have to hold for all $\delta\boldsymbol{v} \in \mathcal{V}^v$ and $\delta p \in \mathcal{V}^p$ for all times $t \in [0,\, T]$.

1.4 Unsteady convective transport

To describe unsteady transport problems appropriately, we assume the existence of a sufficiently smooth time dependent scalar valued concentration field $c : \mathcal{B} \times [0, T] \to \mathbb{R}$. The local, convective form of the unsteady transport problem is then given by

$$\dot{c}(\boldsymbol{x}, t) = s(\boldsymbol{x}, t) \tag{1.40}$$

supplemented by the boundary conditions

$$\begin{aligned} c = g \quad &\text{on} \quad \partial\mathcal{B}^g \times [0,\, T] \\ \boldsymbol{J} \cdot \boldsymbol{n} = h \quad &\text{on} \quad \partial\mathcal{B}^h \times [0,\, T] \end{aligned} \tag{1.41}$$

and the initial condition

$$c(\boldsymbol{x}, 0) = c_0(\boldsymbol{x}) \tag{1.42}$$

where $s(\boldsymbol{x}, t)$ denotes a source term and $\boldsymbol{J} = \boldsymbol{v}c$ the flux of concentration. Furthermore, $\partial\mathcal{B}^g \cup \partial\mathcal{B}^h = \partial\mathcal{B}$, $\partial\mathcal{B}^g \cap \partial\mathcal{B}^h = \emptyset$ has to be valid at the boundary. Taking (1.32) into account and assuming that the source term is zero, i.e. the flux is divergence free, we can rewrite (1.40) in the so-called conservation law form (see Donea & Huerta [19])

$$\frac{\partial c}{\partial t} = -\nabla \cdot \boldsymbol{J} \tag{1.43}$$

We further assume that the material behavior is governed by the free energy function $\Psi(c, t) : \mathcal{B} \times [0, T] \to \mathbb{R}$ and define the chemical potential as follows

$$\mu = \frac{\partial \Psi(c, t)}{\partial c} \tag{1.44}$$

Note that the constitutive equation (1.44) is thermodynamical consistent. Next, we postulate that the flux of concentration is driven by the spatial gradient of the chemical potential, weighted by the mobility $\boldsymbol{M} : \mathcal{B} \times [0, T] \to \mathbb{R}^{d \times d}$. For thermodynamical reasoning the mobility is chosen to be concentration dependent in form of

$$\boldsymbol{M} = \frac{1}{\theta} c\,(1 - c)\, \boldsymbol{D} = M\,(c)\, \boldsymbol{D} \tag{1.45}$$

where $\boldsymbol{D}$ is the tensor valued tracer diffusivity of the composition and θ is a temperature dependent material specific parameter. For later use we derive next the Cahn-Hilliard equation, which rests on a specific formulation of the free energy function. Therefore, we split up this function into a configurational free energy Ψ^{con} and an interfacial/surface energy contribution $\Psi^{\text{surf}} = \frac{\kappa}{2} \|\nabla c\|^2$, which is related to the curvature of the phase islands. Here, κ denotes a material parameter, related to the surface energy density. Application of the variational derivative for functionals involving spatial derivatives

$$\delta_c\,(\bullet) = \partial_c\,(\bullet) - \nabla \cdot (\partial_{\nabla c}\,(\bullet))\,. \tag{1.46}$$

yields the Cahn-Hilliard equation

$$\frac{\partial c}{\partial t} = \nabla \cdot (\boldsymbol{M}(c) \nabla (\partial_c \Psi^{\text{con}}\,(c) - \kappa \Delta c)) \tag{1.47}$$

provided that the additional boundary condition

$$\nabla c \cdot \boldsymbol{n} = 0 \quad \text{on} \quad \partial\mathcal{B} \times [0, T] \tag{1.48}$$

is valid.

To recast the diffusion equation in weak form, we define the space of admissible test functions $\mathcal{V}^c$ according to

$$\mathcal{V}^c = \{\delta c \in \mathbb{H}^2(\mathcal{B}) \mid \delta c = 0 \; \forall \; \boldsymbol{x} \in \partial\mathcal{B}^g\} \tag{1.49}$$

Subsequent integrations yields

$$\langle \delta c, \frac{\partial c}{\partial t} \rangle_{\mathcal{B}} = \langle \delta c, \nabla \cdot (\boldsymbol{M} \nabla \mu) \rangle_{\mathcal{B}} \tag{1.50}$$

Applying integration by parts along with the divergence theorem, we obtain the weak form as follows

$$\begin{aligned} \langle \frac{\partial c}{\partial t}, \delta c \rangle_{\mathcal{B}} = &- \langle M\,(c)\,[\partial_c^2 \Psi^{\mathrm{con}}] \nabla c \boldsymbol{D}^{\mathrm{T}}, \nabla \delta c \rangle_{\mathcal{B}} - \langle \kappa \Delta c [\partial_c M] \nabla c \boldsymbol{D}^{\mathrm{T}}, \nabla \delta c \rangle_{\mathcal{B}} \\ &- \langle M\,(c)\, \kappa \Delta c \boldsymbol{D}^{\mathrm{T}}, \nabla \otimes \nabla \delta c \rangle_{\mathcal{B}} \end{aligned} \tag{1.51}$$

supplemented by the constraints

$$\int_{\partial\mathcal{B}} \nabla c \cdot \boldsymbol{n} \; \mathrm{d}A = 0 \tag{1.52}$$

Note that we have made use of the boundary conditions $(1.41)_1$, $(1.41)_2$ and (1.48), assuming that the Neumann boundary condition at $\partial\mathcal{B}^h \times [0,\, T]$ is set to zero, i.e. no material flows into the domain.

Conservation properties. To verify the fundamental mass conservation property, we substitute the test functions $\delta c = \zeta$, where $\zeta \in \mathbb{R}$ is arbitrary and constant and obtain

$$\langle \zeta, \frac{\partial c}{\partial t} \rangle_{\mathcal{B}} = 0 \tag{1.53}$$

where we have made use of the property $\nabla \zeta = 0$. Thus, total mass is conserved for all times.

2 Spatial discretization

To achieve a numerical solution for the various problems at hand, we apply a finite element framework to approximate the given fields. In particular, we consider Lagrange as well as NURBS based discretization schemes. The former scheme is well understood (see Belytschko et al. [5], Hughes [44] and Zienkiewicz et al. [86, 84, 85]), whereas the latter is subject to current research projects (see Corttrell et al. [18]).

2.1 Lagrange based discretization

Solid mechanics. Concerning the discretization in space, we apply displacement-based finite elements (cf. Hughes [44]). Accordingly, we introduce finite dimensional approximations of $\boldsymbol{\varphi}$ and $\delta\boldsymbol{\varphi}$ such that

$$\boldsymbol{\varphi}^{\mathrm{h}} = \sum_{A\in\omega} N^A(\boldsymbol{X})\boldsymbol{q}_A \quad \text{and} \quad \delta\boldsymbol{\varphi}^{\mathrm{h}} = \sum_{B\in\omega} N^A(\boldsymbol{X})\delta\boldsymbol{q}_A \tag{2.1}$$

Here, $N^A : \mathcal{B}_0^{\mathrm{h}} \to \mathbb{R}$ are polynomial global shape functions associated with nodes $A \in \omega = \{1, \cdots, n_{\mathrm{node}}\}$ corresponding to the isoparametric description of $\mathcal{B}_0^{\mathrm{h}}$. Moreover, $\boldsymbol{q}_A(t) = \boldsymbol{\varphi}^{\mathrm{h}}(\boldsymbol{X}_A, t)$ is the current position vector of the nodal point $\boldsymbol{X}_A \in \mathcal{B}_0^{\mathrm{h}}$. The configuration of each semi-discrete flexible body is characterized by its configuration vector, which can be composed consistently with its variations as follows

$$\boldsymbol{q}(t) = \begin{bmatrix} \boldsymbol{q}_1(t) \\ \vdots \\ \boldsymbol{q}_{n_{\mathrm{node}}}(t) \end{bmatrix} \quad \text{and} \quad \delta\boldsymbol{q}(t) = \begin{bmatrix} \delta\boldsymbol{q}_1(t) \\ \vdots \\ \delta\boldsymbol{q}_{n_{\mathrm{node}}}(t) \end{bmatrix} \tag{2.2}$$

Note that for simplicity of exposition we make use of the summation convention for repeated indices. The discrete counterpart of the first term in (1.7) can now be written as

$$\langle \delta\boldsymbol{\varphi}^{\mathrm{h}}, \rho_0 \ddot{\boldsymbol{\varphi}}^{\mathrm{h}} \rangle_{\mathcal{B}_0^{\mathrm{h}}} = \delta\boldsymbol{q}_A \cdot M^{AB} \ddot{\boldsymbol{q}}_B \tag{2.3}$$

where the coefficients of the consistent mass matrix

$$M^{AB} = \int\limits_{\mathcal{B}_0^{\mathrm{h}}} \rho_0 N^A N^B \, \mathrm{d}V \tag{2.4}$$

has been introduced. The kinetic energy assumes the form

$$T = \frac{1}{2}\dot{\boldsymbol{q}}_A \cdot M^{AB}\dot{\boldsymbol{q}}_B \tag{2.5}$$

where the system velocity vector $\dot{\boldsymbol{q}} = \boldsymbol{v}$ follows from differentiating (2.2) with respect to time.

The discretized versions of the deformation gradient and the deformation tensor are given by

$$\boldsymbol{F}^{\mathrm{h}} = \frac{\partial \boldsymbol{\varphi}^{\mathrm{h}}}{\partial \boldsymbol{X}} = \boldsymbol{q}_A \otimes \nabla N^A(\boldsymbol{X}) \tag{2.6}$$

and

$$\boldsymbol{C}^{\mathrm{h}} = \boldsymbol{q}_A \cdot \boldsymbol{q}_B \nabla N^A(\boldsymbol{X}) \otimes \nabla N^B(\boldsymbol{X}) \tag{2.7}$$

The discrete second term in (1.7) reads

$$\begin{aligned} \langle \boldsymbol{P}^{\mathrm{h}}, \nabla_{\boldsymbol{X}}\left(\delta\boldsymbol{\varphi}^{\mathrm{h}}\right)\rangle_{\mathcal{B}_0^{\mathrm{h}}} &= \delta\boldsymbol{q}_A \cdot \boldsymbol{q}_B \langle \nabla N^A(\boldsymbol{X}), \boldsymbol{\Sigma}^{\mathrm{h}} \nabla N^B(\boldsymbol{X})\rangle_{\mathcal{B}_0^{\mathrm{h}}} \\ &= \delta\boldsymbol{q}_A \cdot \int\limits_{\mathcal{B}_0^{\mathrm{h}}} S^{AB} \,\mathrm{d}V \boldsymbol{q}_B \end{aligned} \tag{2.8}$$

As previously stated, the second Piola-Kirchhoff stress tensor $\boldsymbol{\Sigma}^{\mathrm{h}} = 2\partial\Psi/\partial\boldsymbol{C}^{\mathrm{h}}$ is associated with the strain energy function

$$E^{\mathrm{int}}(\boldsymbol{q}) = \int\limits_{\mathcal{B}_0^{\mathrm{h}}} \Psi(\boldsymbol{C}^{\mathrm{h}}) \,\mathrm{d}V \tag{2.9}$$

The right hand side of (1.7) can be written as

$$\begin{aligned} \langle \rho_0 \bar{\boldsymbol{B}}, \delta\boldsymbol{\varphi}^{\mathrm{h}}\rangle_{\mathcal{B}_0^{\mathrm{h}}} + \langle \bar{\boldsymbol{T}}, \delta\boldsymbol{\varphi}^{\mathrm{h}}\rangle_{\partial\mathcal{B}_0^{\mathrm{h},\sigma}} &= \delta\boldsymbol{q}_A \cdot \left[\int\limits_{\mathcal{B}_0^{\mathrm{h}}} N^A \bar{\boldsymbol{B}} \,\mathrm{d}V + \int\limits_{\partial\mathcal{B}_0^{\mathrm{h},\sigma}} N^A \bar{\boldsymbol{T}} \,\mathrm{d}A\right] \\ &= \delta\boldsymbol{q}_A \cdot \boldsymbol{F}^{A,\mathrm{ext}} \end{aligned} \tag{2.10}$$

Summarized, we obtain for the balance of linear momentum

$$\delta\boldsymbol{q}_A \cdot \left[M^{AB}\dot{\boldsymbol{v}}_B + \int\limits_{\mathcal{B}_0^{\mathrm{h}}} S^{AB} \,\mathrm{d}V \boldsymbol{q}_B\right] = \delta\boldsymbol{q}_A \cdot \left[\boldsymbol{F}^{A,\mathrm{ext}}\right] \tag{2.11}$$

Thermomechanical systems. In a second step, we discretize the temperature field using the same shape functions as before

$$\theta^{\mathrm{h}} = \sum_{A\in\omega} N^A(\boldsymbol{X})\Theta_A, \quad \text{and} \quad \delta\theta^{\mathrm{h}} = \sum_{B\in\omega} N^B(\boldsymbol{X})\delta\Theta_B \tag{2.12}$$

where $\Theta_A \in \mathbb{R}$ denotes the temperature at node A. Consistent to (2.2) we introduce the system vectors $\boldsymbol{\Theta} = [\Theta_1, \ldots, \Theta_{n_{\mathrm{node}}}]$ and the variation thereof as $\delta\boldsymbol{\Theta} = [\delta\Theta_1, \ldots, \delta\Theta_{n_{\mathrm{node}}}]$. Accordingly, we obtain for the first term in $(1.20)_2$

$$\begin{aligned} \langle \delta\theta^{\mathrm{h}}, \theta^{\mathrm{h}}\dot{\eta}^{\mathrm{h}}\rangle_{\mathcal{B}_0^{\mathrm{h}}} &= \delta\Theta_A \int\limits_{\mathcal{B}_0^{\mathrm{h}}} \dot{\eta}^{\mathrm{h}} N^A N^B \,\mathrm{d}V \Theta_B \,\mathrm{d}V \\ &= \delta\Theta_A \Gamma^{AB}\Theta_B \end{aligned} \tag{2.13}$$

where, in view of $(1.12)_2$, the discrete entropy reads $\eta^{\mathrm{h}} = -\nabla_\theta\, \Psi(\boldsymbol{C}^{\mathrm{h}}, \theta^{\mathrm{h}})$. Furthermore, the discrete second term in (1.20) reads

$$\begin{aligned} \langle \boldsymbol{Q}, \nabla_{\boldsymbol{X}}\, (\delta\theta)\rangle_{\mathcal{B}_0^{\mathrm{h}}} &= -\delta\Theta_A \langle \nabla N^A, \widehat{\boldsymbol{K}}(\boldsymbol{C}^{\mathrm{h}}, \theta^{\mathrm{h}})\nabla N^B\rangle_{\mathcal{B}_0^{\mathrm{h}}} \\ &= -\delta\Theta_A \int\limits_{\mathcal{B}_0^{\mathrm{h}}} K^{AB} \,\mathrm{d}V \Theta_B \end{aligned} \tag{2.14}$$

The terms on the right side of $(1.20)_2$ can be written as

$$\begin{aligned} \langle \delta\theta, \bar{Q}\rangle_{\partial\mathcal{B}_0^{\mathrm{h},Q}} + \langle \delta\theta, \bar{R}\rangle_{\mathcal{B}_0^{\mathrm{h}}} &= \delta\Theta_A \left[\int\limits_{\partial\mathcal{B}_0^{\mathrm{h},Q}} N^A \bar{Q} \,\mathrm{d}A + \int\limits_{\mathcal{B}_0^{\mathrm{h}}} N^A \bar{R} \,\mathrm{d}V \right] \\ &= \delta\Theta_A Q^{\mathrm{h},A} \end{aligned} \tag{2.15}$$

which completes the spatial discretization process. In summary, we receive the following equations

$$\begin{aligned} \delta\boldsymbol{q}_A \cdot \left[M^{AB}\dot{\boldsymbol{v}}_B + \int\limits_{\mathcal{B}_0^{\mathrm{h}}} S^{AB} \,\mathrm{d}V \boldsymbol{q}_B \right] &= \delta\boldsymbol{q}_A \cdot \left[\boldsymbol{F}^{A,\mathrm{ext}} \right] \\ \delta\Theta_A \left[\Gamma^{AB}\Theta_B - \int\limits_{\mathcal{B}_0^{\mathrm{h}}} K^{AB} \,\mathrm{d}V \Theta_B \right] &= \delta\Theta_A Q^{\mathrm{h},A} \end{aligned} \tag{2.16}$$

Note that the second Piola-Kirchhoff stress tensor depends here on strains and temperature.

Fluid mechanics. Next, we discretize the fluid problem in space. Without prejudice to the generality of the formulation, a Q2Q1 Lagrangian finite element discretization is chosen as follows

$$\begin{aligned} \boldsymbol{v}^{\mathrm{h}} &= \sum_{A\in\omega} N^A \boldsymbol{v}_A; \quad \delta\boldsymbol{v}^{\mathrm{h}} = \sum_{A\in\omega} N^A \delta\boldsymbol{v}_A \\ p^{\mathrm{h}} &= \sum_{B\in\bar{\omega}} M^B p_B; \quad \delta p^{\mathrm{h}} = \sum_{B\in\bar{\omega}} M^B \delta p_B \end{aligned} \tag{2.17}$$

where $N^A(\boldsymbol{x}) : \mathcal{B}^{\mathrm{h}} \to \mathbb{R}$ are quadratic shape functions associated with nodes A and $M^B(\boldsymbol{x}) : \mathcal{B}^{\mathrm{h}} \to \mathbb{R}$ are linear shape functions associated with nodes B. This element is known to satisfy the LBB condition and provides optimal quadratic convergence of the velocity field (see Donea & Huerta [19]). The semi-discrete balance of momentum reads

$$\langle \rho^f(\dot{\boldsymbol{v}}^{\mathrm{h}} - \boldsymbol{g}^{\mathrm{h}}), \delta\boldsymbol{v}^{\mathrm{h}}\rangle_{\mathcal{B}^{\mathrm{h}}} + \langle \boldsymbol{\sigma}^f(\boldsymbol{v}^{\mathrm{h}}, p^{\mathrm{h}}), \nabla_{\boldsymbol{x}}(\delta\boldsymbol{v}^{\mathrm{h}})\rangle_{\mathcal{B}^{\mathrm{h}}} - \langle \boldsymbol{h}^{\mathrm{h}}, \delta\boldsymbol{v}^{\mathrm{h}}\rangle_{\partial\mathcal{B}^{\mathrm{h},\sigma}} = 0 \tag{2.18}$$

whereas we obtain for the incompressibility constraint

$$\langle \nabla_{\boldsymbol{x}} \cdot \boldsymbol{v}^{\mathrm{h}}, \delta p^{\mathrm{h}}\rangle_{\mathcal{B}^{\mathrm{h}}} = 0 \tag{2.19}$$

If necessary (i.e. for low order elements in conjunction with high Reynolds numbers), a stabilization technique for the underlying Galerkin approach can be applied (cf. Tezduyar [69, 71]) using extended test function spaces, defined as

$$\begin{aligned} \mathcal{V}^{\tilde{v}} &=: \{\delta\tilde{\boldsymbol{v}} \in \mathbb{H}^1(\mathcal{B}) \mid \delta\tilde{\boldsymbol{v}} = \delta\boldsymbol{v} + \gamma_{\mathrm{SUPG}}\boldsymbol{v}\cdot\nabla_{\boldsymbol{x}}(\delta\boldsymbol{v}) + \gamma_{\mathrm{PSPG}}\nabla_{\boldsymbol{x}}(\delta p)\} \\ \mathcal{V}^{\tilde{p}} &=: \{\delta\tilde{p} \in L_2(\mathcal{B}) \mid \delta\tilde{p} = \delta p + \gamma_{\mathrm{LSIC}}\nabla_{\boldsymbol{x}}\cdot(\delta\boldsymbol{v})\} \end{aligned} \tag{2.20}$$

where γ_{SUPG}, γ_{PSPG} and γ_{LSIC} are precalculated stabilization parameters. The modified semi-discrete balance of linear momentum reads

$$\begin{aligned} &\langle \rho^f(\dot{\boldsymbol{v}}^{\mathrm{h}} - \boldsymbol{g}^{\mathrm{h}}), \delta\boldsymbol{v}^{\mathrm{h}}\rangle_{\mathcal{B}^{\mathrm{h}}} + \langle \boldsymbol{\sigma}^f(\boldsymbol{v}^{\mathrm{h}}, p^{\mathrm{h}}), \nabla_{\boldsymbol{x}}(\delta\boldsymbol{v}^{\mathrm{h}})\rangle_{\mathcal{B}^{\mathrm{h}}} - \langle \boldsymbol{h}^{\mathrm{h}}, \delta\boldsymbol{v}^{\mathrm{h}}\rangle_{\partial\mathcal{B}^{\mathrm{h},\sigma}} + \\ &\quad \sum_e \gamma_{\mathrm{SUPG}}\langle \boldsymbol{\mathcal{R}}_v, (\boldsymbol{v}^{\mathrm{h}}\cdot\nabla_{\boldsymbol{x}})\delta\boldsymbol{v}^{\mathrm{h}}\rangle_{\mathcal{B}^{\mathrm{h}}} + \sum_e \gamma_{\mathrm{LSIC}}\langle \mathcal{R}_p, \nabla_{\boldsymbol{x}}\cdot\delta\boldsymbol{v}^{\mathrm{h}}\rangle_{\mathcal{B}^{\mathrm{h}}} = 0 \end{aligned} \tag{2.21}$$

and the kinematic constraint

$$\langle \nabla_{\boldsymbol{x}} \cdot \boldsymbol{v}^{\mathrm{h}}, \delta p^{\mathrm{h}}\rangle_{\mathcal{B}^{\mathrm{h}}} + \sum_e \gamma_{\mathrm{PSPG}}\langle \boldsymbol{\mathcal{R}}_v, \nabla_{\boldsymbol{x}}\delta p^{\mathrm{h}}\rangle_{\mathcal{B}^{\mathrm{h}}} = 0 \tag{2.22}$$

Here, $\boldsymbol{\mathcal{R}}_v$ and $\mathcal{R}_p$ denote the residuals of the original momentum and kinematic constraint equations, respectively.

2.2 NURBS based discretization

Inspired by developments in the context of isogeometric analysis (see Cottrell et al. [18] and the references therein for a comprehensive survey of this topic) we apply NURBS based shape functions for the approximation of displacement based finite elements in space

$$\boldsymbol{\varphi}^{\mathrm{h}} = \sum_{A\in\omega} R^A \boldsymbol{q}_A, \quad \delta\boldsymbol{\varphi}^{\mathrm{h}} = \sum_{A\in\omega} R^A \delta\boldsymbol{q}_A \tag{2.23}$$

where

$$R^A = R^{\mathfrak{i},\mathfrak{j},\mathfrak{k}}_{p,q,r}(\boldsymbol{\xi}) = \frac{N_{\mathfrak{i},p}(\xi) M_{\mathfrak{j},q}(\eta) L_{\mathfrak{k},r}(\zeta) w_{\mathfrak{i},\mathfrak{j},\mathfrak{k}}}{\sum_{\hat{\mathfrak{i}}=1}^{n} \sum_{\hat{\mathfrak{j}}=1}^{m} \sum_{\hat{\mathfrak{k}}=1}^{l} N_{\hat{\mathfrak{i}},p}(\xi) M_{\hat{\mathfrak{j}},q}(\eta) L_{\hat{\mathfrak{k}},r}(\zeta) w_{\hat{\mathfrak{i}},\hat{\mathfrak{j}},\hat{\mathfrak{k}}}} \tag{2.24}$$

Here, p, q, r denotes the order of the non-rational B-Spline shape functions N, M and L, recursively defined as follows

$$N_{\mathfrak{i},p} = \frac{\xi - \xi_{\mathfrak{i}}}{\xi_{\mathfrak{i}+p} - \xi_{\mathfrak{i}}} N_{\mathfrak{i},p-\mathfrak{i}}(\xi) + \frac{\xi_{\mathfrak{i}+p+1} - \xi}{\xi_{\mathfrak{i}+p+1} - \xi_{\mathfrak{i}+1}} N_{\mathfrak{i}+1,p+1}(\xi) \tag{2.25}$$

beginning with

$$N_{\mathfrak{i},0}(\xi) = \begin{cases} 1 & \text{if } \xi_{\mathfrak{i}} \leq \xi < \xi_{\mathfrak{i}+1} \\ 0 & \text{otherwise} \end{cases} \tag{2.26}$$

The definition for M and L follows analogously. Furthermore, $w_{\mathfrak{i},\mathfrak{j},\mathfrak{k}}$ are NURBS weights, for details see Piegl & Tiller [60]. The global index A for the shape functions is connected to the indices $\mathfrak{i} \in [1,\dots,n], \mathfrak{j} \in [1,\dots,m]$ and $\mathfrak{k} \in [1,\dots,l]$ in the parameter space. In particular, a connectivity array is used for implementation, similar to the location matrix defined in Hughes [44], such that the shape functions $R^A(\boldsymbol{\xi})$ are associated with the control points $A \in \omega^{(i)} = \{1,\dots,n_{\mathrm{node}}\}$, where, $n^{(i)}_{\mathrm{node}}$ denotes the total number of control points. Three so called knot vectors $\Xi = \{\xi_1, \xi_2, \dots, \xi_{n+p+1}\}$, $\mathcal{H} = \{\eta_1, \eta_2, \dots, \eta_{n+p+1}\}$ and $\mathcal{I} = \{\zeta_1, \zeta_2, \dots, \zeta_{n+p+1}\}$ represent a set of coordinates in the parameter space, which provide a definition for finite elements, such that a point $A : \mathfrak{i}, \mathfrak{j}, \mathfrak{k} \to \xi_{\mathfrak{i}}, \eta_{\mathfrak{j}}, \zeta_{\mathfrak{k}}$ in the parameter space addresses a node in the physical space, i.e. a corner of an element.

Remark: Details on the characteristics of the isogeometric approach such as continuity, explicit representation of specific shape functions and repeated knots, mesh generation and refinement can be found in Cottrell et al. [18] and the references therein. We will deal with this specific class of shape functions in a general way, such that the following methods like the domain decomposition can be applied without restrictions to all possible NURBS solids. Note that the control points $\boldsymbol{q}_A$ can be dealt with analogues to the nodes of Lagrange elements. We only have to take care about the fact that the control points can be, but do not have to be part of the geometry, i.e. of the curve, surface or solid.

The finite dimensional approximations of $\boldsymbol{v}$, $\delta\boldsymbol{v}$ and p, δp for the velocity and the pressure field of the fluid reads

$$\begin{aligned} \boldsymbol{v}^{\mathrm{h}} &= \sum_{A\in\omega} R^A \boldsymbol{v}_A; \quad \delta\boldsymbol{v}^{\mathrm{h}} = \sum_{A\in\omega} R^A \delta\boldsymbol{v}_A \\ p^{\mathrm{h}} &= \sum_{B\in\bar{\omega}} R^B p_B; \quad \delta p^{\mathrm{h}} = \sum_{B\in\bar{\omega}} R^B \delta p_B \end{aligned} \tag{2.27}$$

Note that the structure of the constitutive and balance equations in Section 2.1 remains unchanged, since we obtain e.g. for the deformation tensor

$$\boldsymbol{C}^{\mathrm{h}} = \boldsymbol{q}_A \cdot \boldsymbol{q}_B \nabla R^A(\boldsymbol{X}) \otimes \nabla R^B(\boldsymbol{X}) \tag{2.28}$$

where the derivative ∇R^A can be calculated in a straightforward manner

$$\nabla R^A = (\boldsymbol{J}^{-1})^T \frac{\partial R^A}{\partial \boldsymbol{\xi}}, \quad \boldsymbol{J} = \frac{\partial \boldsymbol{\varphi}^{\mathrm{h}}}{\partial \boldsymbol{\xi}} \tag{2.29}$$

and $\partial R^A/\partial \boldsymbol{\xi}$ follows directly from (2.24). The discretization of the velocity and pressure field of fluids as the discretization of the concentration field follows analogously.

Unsteady convective transport. The phase boundaries in the Cahn-Hilliard model are typically sharp layers which require a high spatial resolution. Taken into account, that the system has to be valid for arbitrary test functions, the semi-discrete system reads

$$\begin{gathered}\langle \dot{c}^h, R_A\rangle_{\mathcal{B}^{\mathrm{h}}} + \kappa\langle M\, \partial_c^2 \Psi^{\mathrm{con}}\, \nabla c^h \boldsymbol{D}^{\mathrm{T}}, \nabla R_A\rangle_{\mathcal{B}^{\mathrm{h}}} + \\ \kappa\langle \Delta c^h\, \partial_c M\, \nabla c^h \boldsymbol{D}^{\mathrm{T}}, \nabla R_A\rangle_{\mathcal{B}^{\mathrm{h}}} + \kappa\langle M\, \Delta c^h \boldsymbol{D}^{\mathrm{T}}, \nabla \otimes \nabla R_A\rangle_{\mathcal{B}^{\mathrm{h}}} = 0\end{gathered} \tag{2.30}$$

$\forall A \in \omega$. As mentioned before, we have to fulfill the boundary conditions (1.48) for all times. This is effected through the introduction of Lagrange multipliers $\bar{\lambda}$ associated with the surface. Accordingly, we introduce a suitable Lagrange multiplier space

$$\mathcal{M}^h = \{\bar{\lambda}^h \mid \bar{\lambda}^h \in C^0(\partial\mathcal{B}); \bar{\lambda}^h \in \mathbb{H}^1(\partial\mathcal{B})\}. \tag{2.31}$$

As shown in Hesch & Betsch [39] it is not necessary to retain the continuity of the underlying surface for the Lagrange multipliers. In particular, we apply standard Lagrange linear elements $\bar{\lambda}^h = \sum_{A\in\omega} \lambda_A \bar{N}_A$ to the Lagrange multiplier space, see Wohlmuth [76] for a comprehensive convergence analysis. Integration of the constraints yields for each node A on the surface

$$\Phi^A = \int_{\partial\mathcal{B}^{\mathrm{h}}} \bar{N}_A \nabla c^h \cdot \boldsymbol{n}\, \mathrm{d}A \tag{2.32}$$

By collecting all constraints in a vector $\boldsymbol{\Phi}$ and associated vector of Lagrange multipliers $\boldsymbol{\lambda}$ we end up with the saddle point problem

$$\begin{aligned}\langle \dot{c}^h, R_A\rangle_{\mathcal{B}^{\mathrm{h}}} + \kappa\langle M\, \partial_c^2 \Psi^{\mathrm{con}}\, \nabla c^h \boldsymbol{D}^{\mathrm{T}}, \nabla R_A\rangle_{\mathcal{B}^{\mathrm{h}}} + & \\ \kappa\langle \Delta c^h\, \partial_c M\, \nabla c^h \boldsymbol{D}^{\mathrm{T}}, \nabla R_A\rangle_{\mathcal{B}^{\mathrm{h}}} + \kappa\langle M\, \Delta c^h \boldsymbol{D}^{\mathrm{T}}, \nabla \otimes \nabla R_A\rangle_{\mathcal{B}^{\mathrm{h}}} &= \boldsymbol{\lambda} \nabla_{c_A} \boldsymbol{\Phi} \\ 0 &= \boldsymbol{\Phi}\end{aligned} \tag{2.33}$$

For large scale systems we have to avoid high condition numbers of the iteration matrix. Therefore, we can either apply an augmented Lagrange approach or we reduce the system to a minimum set of equations using a suitable null-space method, see Appendix D.

3 Temporal discretization

The previously introduced semi-discrete problem can now be discretized in time in order to obtain a full discrete set of non-linear algebraic equations. In particular, we aim at the development of structure preserving integrators for the solid and thermomechanical system. Furthermore, implicit time integration schemes are adapted to the fluid and transport systems, since they provide enhanced stability properties.

3.1 Solid mechanics

Consider a sequence of times $t_0, \dots, t_n, t_{n+1}, \dots$ and assume that the state at t_n, denoted by $\boldsymbol{\varphi}_n^{\mathrm{h}}$, is known. Then the goal is to approximate the state $\boldsymbol{\varphi}_{n+1}^{\mathrm{h}}$ at t_{n+1}, where the time-step size $\Delta t = t_{n+1} - t_n$ is prescribed. The full discrete approximation of (1.7) and (2.11), respectively, reads

$$\delta \boldsymbol{q}_A \cdot \left[M^{AB}(\boldsymbol{v}_{B,n+1} - \boldsymbol{v}_{B,n}) + \Delta t \int\limits_{\mathcal{B}_0^{\mathrm{h}}} S_{n,n+1}^{AB} \, \mathrm{d}V \boldsymbol{q}_{B,n+\frac{1}{2}} \right] = \Delta t \delta \boldsymbol{q}_A \cdot \left[\boldsymbol{F}_{n+\frac{1}{2}}^{A,\mathrm{ext}} \right] \tag{3.1}$$

The above equation is supplemented by the mid-point-type approximation to the kinematic relationship $(1.2)_1$ given by

$$\boldsymbol{\varphi}_{n+1}^{\mathrm{h}} - \boldsymbol{\varphi}_n^{\mathrm{h}} = \Delta t \boldsymbol{v}_{n+\frac{1}{2}}^{\mathrm{h}} \tag{3.2}$$

together with

$$\boldsymbol{\pi}_{n+\alpha}^{\mathrm{h}} = \rho_0 \boldsymbol{v}_{n+\alpha}^{\mathrm{h}} \quad \text{for} \quad \alpha \in \{0, \frac{1}{2}, 1\} \tag{3.3}$$

In the above formulas, $(\bullet)_{n+\frac{1}{2}} = \frac{1}{2}((\bullet)_{n+1} + (\bullet)_n)$ denotes the standard mid-point approximation. Moreover,

$$\delta \boldsymbol{q}_A \cdot \int\limits_{\mathcal{B}_0^{\mathrm{h}}} S_{n,n+1}^{AB} \, \mathrm{d}V \boldsymbol{q}_{B,n+\frac{1}{2}} = \delta \boldsymbol{q}_A \cdot \langle \nabla N^A, \boldsymbol{\Sigma}_{n,n+1}^{\mathrm{h}} \nabla N^B \rangle_{\mathcal{B}_0^{\mathrm{h}}} \boldsymbol{q}_{B,n+\frac{1}{2}} \tag{3.4}$$

where $\boldsymbol{\Sigma}_{n,n+1}^{\mathrm{h}}$ denotes a consistent algorithmic version of the discrete second Piola-Kirchhoff stress tensor, defined by

$$\boldsymbol{\Sigma}_{n,n+1}^{\mathrm{h}} = \nabla_{\boldsymbol{C}} \Psi(\boldsymbol{C}_{n+\frac{1}{2}}^{\mathrm{h}}) + \frac{\Psi(\boldsymbol{C}_{n+1}^{\mathrm{h}}) - \Psi(\boldsymbol{C}_n^{\mathrm{h}}) - \nabla_{\boldsymbol{C}} \Psi(\boldsymbol{C}_{n+\frac{1}{2}}^{\mathrm{h}}) : \Delta \boldsymbol{C}^{\mathrm{h}}}{\Delta \boldsymbol{C}^{\mathrm{h}} : \Delta \boldsymbol{C}^{\mathrm{h}}} \Delta \boldsymbol{C}^{\mathrm{h}} \tag{3.5}$$

Conservation properties. As shown in Betsch & Steinmann [13], the integration scheme is structure preserving, i.e. conserves algorithmically linear and angular momentum as well as energy and is of second order accuracy. First we verify conservation of linear momentum. Insertion of $\delta\boldsymbol{q}^A = \boldsymbol{\zeta}$ into (3.1) and subsequent summation yields

$$\boldsymbol{\zeta} \cdot (\boldsymbol{L}_{n+1} - \boldsymbol{L}_n) = \Delta t \sum_{A\in\omega} \boldsymbol{\zeta} \cdot \left[- \int\limits_{\mathcal{B}_0^{\mathrm{h}}} S^{AB}_{n,n+1} \,\mathrm{d}V \boldsymbol{q}_{B,n+\frac{1}{2}} + \boldsymbol{F}^{A,\mathrm{ext}}_{n+\frac{1}{2}} \right] \tag{3.6}$$

With regard to (2.8), (3.5) and (3.15), respectively, we can state

$$\boldsymbol{\zeta} \cdot \langle \left(\nabla \sum_{A\in\omega} N^A \right), \boldsymbol{\Sigma}^{\mathrm{h}}_{n,n+1} \nabla N^B \rangle_{\mathcal{B}_0^{\mathrm{h}}} \boldsymbol{q}_{B,n+\frac{1}{2}} = 0 \tag{3.7}$$

and obtain for the discrete counterpart of (1.21)

$$\boldsymbol{L}_{n+1} - \boldsymbol{L}_n = \Delta t \sum_{A\in\omega} \boldsymbol{F}^{A,\mathrm{ext}}_{n+\frac{1}{2}} \tag{3.8}$$

Next, we substitute $\delta\boldsymbol{q}_A = \boldsymbol{\zeta} \times \boldsymbol{q}_{A,n+\frac{1}{2}}$ into (3.1) and obtain

$$\boldsymbol{\zeta} \cdot (\boldsymbol{J}_{n+1} - \boldsymbol{J}_n) = \Delta t \boldsymbol{\zeta} \cdot \sum_{A\in\omega} \boldsymbol{q}_{A,n+\frac{1}{2}} \times \left[- \int\limits_{\mathcal{B}_0^{\mathrm{h}}} S^{AB}_{n,n+1} \,\mathrm{d}V \boldsymbol{q}_{B,n+\frac{1}{2}} + \boldsymbol{F}^{A,\mathrm{ext}}_{n+\frac{1}{2}} \right] \tag{3.9}$$

Due to the skew-symmetry of $\boldsymbol{q}_{A,n+\frac{1}{2}} \times \boldsymbol{q}_{B,n+\frac{1}{2}}$ and the symmetry of $S^{AB}_{n,n+1}$ we obtain the discrete counterpart of (1.22)

$$\boldsymbol{J}_{n+1} - \boldsymbol{J}_n = \Delta t \sum_{A\in\omega} \boldsymbol{q}_{A,n+\frac{1}{2}} \times \boldsymbol{F}^{A,\mathrm{ext}}_{n+\frac{1}{2}} \tag{3.10}$$

Finally, we substitute $\delta\boldsymbol{q}_A = \boldsymbol{v}_{A,n+\frac{1}{2}}$ in (3.1) and sum up the contributions of all nodes

$$T_{n+1} - T_n + \langle (\boldsymbol{q}_{A,n+1} - \boldsymbol{q}_{A,n}), S^{AB}_{n,n+1} \boldsymbol{q}_{B,n+\frac{1}{2}} \rangle_{\mathcal{B}_0^{\mathrm{h}}} = \Delta t \boldsymbol{v}_{A,n+\frac{1}{2}} \cdot \boldsymbol{F}^{A,\mathrm{ext}}_{n+\frac{1}{2}} \tag{3.11}$$

Rewriting the last equation as follows

$$T_{n+1} - T_n + \langle \boldsymbol{\Sigma}^{\mathrm{h}}_{n,n+1}, (\boldsymbol{C}^{\mathrm{h}}_{n+1} - \boldsymbol{C}^{\mathrm{h}}_n) \rangle_{\mathcal{B}_0^{\mathrm{h}}} = \Delta t P^{\mathrm{h,ext}}_{n,n+1} \tag{3.12}$$

and taking (3.5) into account we end up with

$$T_{n+1} - T_n + E_{n+1} - E_n = \Delta t P^{\mathrm{h,ext}}_{n,n+1} \tag{3.13}$$

which proves algorithmic conservation of energy.

3.2 Thermomechanical system

We next perform the discretization in time of the coupled thermoelastic problem under consideration. The algorithmic approximation to the weak form (2.16) is defined by

$$\begin{aligned} \delta\boldsymbol{q}_A \cdot \left[M^{AB}(\boldsymbol{v}_{B,n+1} - \boldsymbol{v}_{B,n}) + \Delta t \int\limits_{\mathcal{B}_0^{\mathrm{h}}} S^{AB}_{n,n+1}\,\mathrm{d}V \boldsymbol{q}_{B,n+\frac{1}{2}} \right] &= \Delta t \delta\boldsymbol{q}_A \cdot \left[\boldsymbol{F}^{A,\mathrm{ext}}_{n+\frac{1}{2}} \right] \\ \delta\Theta_A \left[\Gamma^{AB}_{n,n+1}\Theta_{B,n+\frac{1}{2}} - \Delta t \int\limits_{\mathcal{B}_0^{\mathrm{h}}} K^{AB}_{n,n+1}\,\mathrm{d}V \Theta_{B,n+\frac{1}{2}} \right] &= \Delta t \delta\Theta_A Q^{\mathrm{h},A}_{n,n+1} \end{aligned} \tag{3.14}$$

Similar to (3.4), $\boldsymbol{\Sigma}^{\mathrm{h}}_{n,n+1}$ denotes a consistent algorithmic version of the discrete second Piola-Kirchhoff stress tensor, defined by

$$\boldsymbol{\Sigma}^{\mathrm{h}}_{n,n+1} = \nabla_{\boldsymbol{C}}\,\Psi(\boldsymbol{C}^{\mathrm{h}}_{n+\frac{1}{2}}, \theta^{\mathrm{h}}_{n+\frac{1}{2}}) + \frac{e^{\mathrm{h}}_{n+1} - e^{\mathrm{h}}_{n} - \theta^{\mathrm{h}}_{n+\frac{1}{2}}\Delta\eta^{\mathrm{h}} - \nabla_{\boldsymbol{C}}\,\Psi(\boldsymbol{C}^{\mathrm{h}}_{n+\frac{1}{2}}, \theta^{\mathrm{h}}_{n+\frac{1}{2}}) : \Delta\boldsymbol{C}^{\mathrm{h}}}{\Delta\boldsymbol{C}^{\mathrm{h}} : \Delta\boldsymbol{C}^{\mathrm{h}}} \Delta\boldsymbol{C}^{\mathrm{h}} \tag{3.15}$$

where the inner energy in terms of the free Helmholtz energy reads

$$e_k = \Psi(\boldsymbol{C}^{\mathrm{h}}_k, \theta^{\mathrm{h}}_k) - \theta^{\mathrm{h}}_k \nabla_\theta\,\Psi(\boldsymbol{C}^{\mathrm{h}}_k, \theta^{\mathrm{h}}_k), \quad k \in \{n, n+1\} \tag{3.16}$$

Conservation properties. Next, we verify that the temporal discretization of the coupled thermoelastic system inherits the fundamental conservation properties of the underlying semi-discrete system. Verification of linear and angular momentum conservation follows exactly the procedure outlined in Section 3.1 (see also Hesch & Betsch [35]). Hence, we focus on the verification of the algorithmic conservation of energy. Replacing $\delta\boldsymbol{q}_A$ in $(3.14)_1$ with $\boldsymbol{v}_{A,n+\frac{1}{2}}$ and subsequent summation over all nodes yields

$$T_{n+1} - T_n + \langle(\boldsymbol{q}_{A,n+1} - \boldsymbol{q}_{A,n}), S^{AB}_{n,n+1}\boldsymbol{q}_{B,n+\frac{1}{2}}\rangle_{\mathcal{B}_0^{\mathrm{h}}} = \Delta t \boldsymbol{v}_{A,n+\frac{1}{2}} \cdot \boldsymbol{F}^{A,\mathrm{ext}}_{n+\frac{1}{2}} \tag{3.17}$$

The last equation can be rewritten as follows

$$T_{n+1} - T_n + \langle \boldsymbol{\Sigma}^{\mathrm{h}}_{n,n+1}, (\boldsymbol{C}^{\mathrm{h}}_{n+1} - \boldsymbol{C}^{\mathrm{h}}_n)\rangle_{\mathcal{B}_0^{\mathrm{h}}} = \Delta t P^{\mathrm{h,ext}}_{n,n+1} \tag{3.18}$$

Taking (3.15) into account, we obtain

$$T_{n+1} - T_n + \int\limits_{\mathcal{B}_0^{\mathrm{h}}} \left[e^{\mathrm{h}}_{n+1} - e^{\mathrm{h}}_n - \theta^{\mathrm{h}}_{n+\frac{1}{2}}(\eta^{\mathrm{h}}_{n+1} - \eta^{\mathrm{h}}_n) \right] \mathrm{d}V = \Delta t P^{\mathrm{h,ext}}_{n,n+1} \tag{3.19}$$

In a second step we set $\delta\theta_A = \zeta$ and obtain from $(3.14)_2$

$$\int\limits_{\mathcal{B}_0^{\mathrm{h}}} \left[\theta^{\mathrm{h}}_{n+\frac{1}{2}}(\eta^{\mathrm{h}}_{n+1} - \eta^{\mathrm{h}}_n) - \Delta t \left(\nabla \sum_{A\in\omega} N^A \right) \cdot \boldsymbol{K}^{\mathrm{h}}(\boldsymbol{C}^{\mathrm{h}}_{n+\frac{1}{2}}, \theta^{\mathrm{h}}_{n+\frac{1}{2}}) \nabla N^B \Theta_{B,n+\frac{1}{2}} \right] \mathrm{d}V = \Delta t Q^{\mathrm{h}}_{n,n+1} \tag{3.20}$$

Thus, we arrive at

$$T_{n+1} - T_n + E_{n+1} - E_n = \Delta t [P^{\mathrm{h,ext}}_{n,n+1} + Q^{\mathrm{h}}_{n,n+1}] \tag{3.21}$$

which proves algorithmic energy consistency.

3.3 Fluid mechanics

To approximate the state $(\boldsymbol{v}^{\mathrm{h}}_{n+1},\, p^{\mathrm{h}}_{n+1})$ we consider a similar mid-point type evaluation of the weak form in (2.18) and (2.19), and obtain

$$\begin{aligned}\langle \rho \left(\frac{\boldsymbol{v}^{\mathrm{h}}_{n+1} - \boldsymbol{v}^{\mathrm{h}}_{n}}{\Delta t} + (\boldsymbol{v}^{\mathrm{h}}_{n+1/2} \cdot \nabla_{\boldsymbol{x}}\,)\boldsymbol{v}^{\mathrm{h}}_{n+1/2} - \boldsymbol{g}^{\mathrm{h}}_{n+1/2} \right), \delta \boldsymbol{v}^{\mathrm{h}} \rangle_{\mathcal{B}^{\mathrm{h}}} + &\\ \langle \boldsymbol{\sigma}(\boldsymbol{v}^{\mathrm{h}}_{n+1/2}, p^{\mathrm{h}}_{n+1}), \nabla_{\boldsymbol{x}}\,(\delta \boldsymbol{v}^{\mathrm{h}}) \rangle_{\mathcal{B}^{\mathrm{h}}} - \langle \boldsymbol{h}^{\mathrm{h}}_{n+1/2}, \delta \boldsymbol{v}^{\mathrm{h}} \rangle_{\partial \mathcal{B}^{\mathrm{h},\sigma}} &= 0 \\ \langle \nabla_{\boldsymbol{x}}\, \cdot \boldsymbol{v}^{\mathrm{h}}_{n+1}, \delta p^{\mathrm{h}} \rangle_{\mathcal{B}^{\mathrm{h}}} &= 0\end{aligned} \tag{3.22}$$

Note that we evaluate the constraints at the end-point configuration and assume that the corresponding Lagrange multipliers p^{h}_{n+1} are constant within each time step. If the system requires the use of stabilization techniques, presented in (2.21) and (2.22), it yields

$$\begin{aligned}\langle \rho \left(\frac{\boldsymbol{v}^{\mathrm{h}}_{n+1} - \boldsymbol{v}^{\mathrm{h}}_{n}}{\Delta t} + (\boldsymbol{v}^{\mathrm{h}}_{n+1/2} \cdot \nabla_{\boldsymbol{x}}\,)\boldsymbol{v}^{\mathrm{h}}_{n+1/2} - \boldsymbol{g}^{\mathrm{h}}_{n+1/2} \right), \delta \boldsymbol{v}^{\mathrm{h}} \rangle_{\mathcal{B}^{\mathrm{h}}} + &\\ \langle \boldsymbol{\sigma}(\boldsymbol{v}^{\mathrm{h}}_{n+1/2}, p^{\mathrm{h}}_{n+1}), \nabla_{\boldsymbol{x}}\,(\delta \boldsymbol{v}^{\mathrm{h}}) \rangle_{\mathcal{B}^{\mathrm{h}}} - \langle \boldsymbol{h}^{\mathrm{h}}_{n+1/2}, \delta \boldsymbol{v}^{\mathrm{h}} \rangle_{\partial \mathcal{B}^{\mathrm{h},\sigma}} + &\\ \sum_e \gamma_{\mathrm{SUPG}} \langle \boldsymbol{\mathcal{R}}_v(\boldsymbol{v}^{\mathrm{h}}_{n+1/2}, p^{\mathrm{h}}_{n+1}), (\boldsymbol{v}^{\mathrm{h}}_{n+1/2} \cdot \nabla_{\boldsymbol{x}}\,) \delta \boldsymbol{v}^{\mathrm{h}} \rangle_{\mathcal{B}^{\mathrm{h}}} + &\\ \sum_e \gamma_{\mathrm{LSIC}} \langle \mathcal{R}_p(\boldsymbol{v}^{\mathrm{h}}_{n+1}), \nabla_{\boldsymbol{x}}\, \cdot \delta \boldsymbol{v}^{\mathrm{h}} \rangle_{\mathcal{B}^{\mathrm{h}}} &= 0 \\ \langle \nabla_{\boldsymbol{x}}\, \cdot \boldsymbol{v}^{\mathrm{h}}_{n+1/2}, \delta p^{\mathrm{h}} \rangle_{\mathcal{B}^{\mathrm{h}}} + &\\ \sum_e \gamma_{\mathrm{PSPG}} \langle \boldsymbol{\mathcal{R}}_v(\boldsymbol{v}^{\mathrm{h}}_{n+1/2}, p^{\mathrm{h}}_{n+1}), \nabla_{\boldsymbol{x}}\, \delta p^{\mathrm{h}} \rangle_{\mathcal{B}^{\mathrm{h}}} &= 0\end{aligned} \tag{3.23}$$

This mid-point type rule (see Betsch & Steinmann [14]) is of second order accuracy and robust for large time step sizes.

3.4 Unsteady convective transport

Adapting the previously introduced mid-point type rule to (2.33) yields

$$\begin{aligned}\langle \frac{c^h_{n+1} - c^h_n}{\Delta t}, R_A \rangle_{\mathcal{B}^{\mathrm{h}}} + \kappa \langle \big[M\, \partial^2_c \Psi^{\mathrm{con}}\, \nabla c^h \big]_{n+\frac{1}{2}} \boldsymbol{D}^{\mathrm{T}}, \nabla R_A \rangle_{\mathcal{B}^{\mathrm{h}}} + &\\ \kappa \langle \big[\Delta c^h\, \partial_c M\, \nabla c^h \big]_{n+\frac{1}{2}} \boldsymbol{D}^{\mathrm{T}}, \nabla R_A \rangle_{\mathcal{B}^{\mathrm{h}}} + \kappa \langle \big[M\, \Delta c^h \big]_{n+\frac{1}{2}} \boldsymbol{D}^{\mathrm{T}}, \nabla \otimes \nabla R_A \rangle_{\mathcal{B}^{\mathrm{h}}} &= \boldsymbol{\lambda} \nabla_{c_A} \boldsymbol{\Phi}_{n+\frac{1}{2}} \\ 0 &= \boldsymbol{\Phi}_{n+1}\end{aligned} \tag{3.24}$$

where we evaluate the mass diffusion equation at the mid-point configuration and the constraints at the end point.

Conservation properties. Conservation of mass for the full discrete system can be shown analogues to (1.53). As before, we replace the test functions $\delta c = \zeta$ and obtain

$$\int_{\mathcal{B}^{\mathrm{h}}} c_{n+1} \,\mathrm{d}V = \int_{\mathcal{B}^{\mathrm{h}}} c_n \,\mathrm{d}V \tag{3.25}$$

where we have again make use of the property $\nabla \zeta = 0$.

4 Domain decomposition

The goal of this section is to provide an adequate, Mortar based method for domain decomposition problems. This type of variationally consistent mesh-tying method has been developed by Bernadi et al. [9]. The extension of this method to linear elasticity problems can be found in Krause & Wohlmuth [50]. For full non-linear elasticity problems see Hesch & Betsch [34], whereas non-linear thermoelasticity is adressed in Hesch & Betsch [35]. Application to NURBS can be found in Hesch & Betsch [39].

4.1 Domain decomposition and Solids

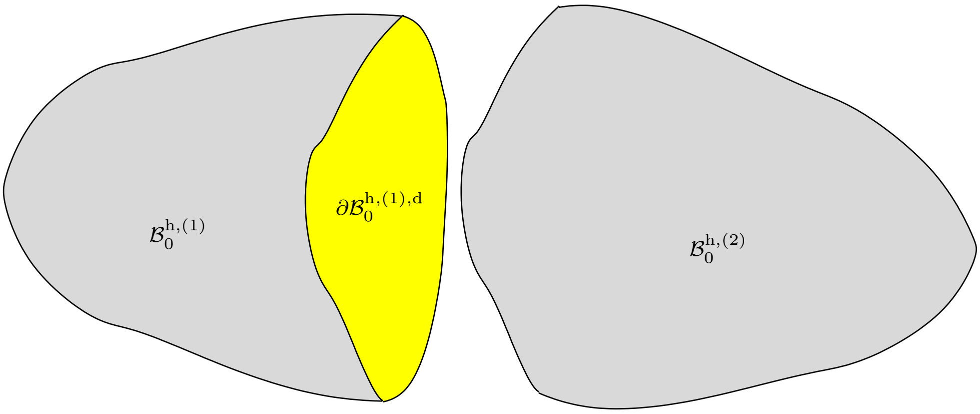

Figure 4.1: Decomposition of a body into two domains at the internal interface $\partial\mathcal{B}_0^{\mathrm{h},\mathrm{d}}$.

We consider a general non-linear mechanical system, artificially subdivided into several sub-domains (i), occupying the space $\mathcal{B}_0^{\mathrm{h},(i)} \subset \mathbb{R}^d$ in the reference configuration. The material surfaces $\partial\mathcal{B}_0^{\mathrm{h},(i)}$ are partitioned into the Dirichlet boundary $\partial\mathcal{B}_0^{\mathrm{h},(i),u}$, the Neumann boundary $\partial\mathcal{B}_0^{\mathrm{h},(i),\sigma}$ and the internal interface $\partial\mathcal{B}_0^{\mathrm{h},(i),d}$ between the sub-domains. We require that the three portions $\partial\mathcal{B}_0^{\mathrm{h},(i),u}$, $\partial\mathcal{B}_0^{\mathrm{h},(i),\sigma}$ and $\partial\mathcal{B}_0^{\mathrm{h},(i),d}$ satisfy

$$\partial\mathcal{B}_0^{\mathrm{h},(i),u} \cup \partial\mathcal{B}_0^{\mathrm{h},(i),\sigma} \cup \partial\mathcal{B}_0^{\mathrm{h},(i),d} = \partial\mathcal{B}_0^{\mathrm{h},(i)} \tag{4.1}$$

and

$$\partial\mathcal{B}_0^{\mathrm{h},(i),u} \cap \partial\mathcal{B}_0^{\mathrm{h},(i),\sigma} \cap \partial\mathcal{B}_0^{\mathrm{h},(i),d} = \emptyset \tag{4.2}$$

on each sub-domain. The contribution of body (i) to the balance of linear momentum for a large deformation contact problem can be expressed as follows

$$\begin{aligned}\langle \rho_R \ddot{\boldsymbol{\varphi}}^{\mathrm{h}}, \delta\boldsymbol{\varphi}^{\mathrm{h}}\rangle_{\mathcal{B}_0^{\mathrm{h},(i)}} + \langle \boldsymbol{P}^{\mathrm{h}}, \nabla_{\boldsymbol{X}} \left(\delta\boldsymbol{\varphi}^{\mathrm{h}}\right)\rangle_{\mathcal{B}_0^{\mathrm{h},(i)}} &= \\ \langle \rho_R \bar{\boldsymbol{B}}^{\mathrm{h}}, \delta\boldsymbol{\varphi}^{\mathrm{h}}\rangle_{\mathcal{B}_0^{\mathrm{h},(i)}} + \langle \bar{\boldsymbol{T}}^{\mathrm{h}}, \delta\boldsymbol{\varphi}^{\mathrm{h}}\rangle_{\partial\mathcal{B}_0^{\mathrm{h},(i),\sigma}} &+ \langle \boldsymbol{t}^{\mathrm{h}}, \delta\boldsymbol{\varphi}^{\mathrm{h}}\rangle_{\partial\mathcal{B}_0^{\mathrm{h},(i),d}}\end{aligned} \tag{4.3}$$

The discrete balance of linear momentum across the interface reads

$$\langle \boldsymbol{t}^{\mathrm{h},(1)}, (\delta\boldsymbol{\varphi}^{\mathrm{h},(1)} - \delta\boldsymbol{\varphi}^{\mathrm{h},(2)})\rangle_{\mathcal{B}_0^{\mathrm{h},(1),d}} = 0 \tag{4.4}$$

using the discrete tractions

$$\boldsymbol{t}^{\mathrm{h},(1)} = \sum_{A \in \tilde{\omega}^{(1)}} N^A \left(\boldsymbol{X}^{(1)}\right) \boldsymbol{\lambda}_A \tag{4.5}$$

Here, $N^A : \mathcal{B}_0^{\mathrm{h}} \to \mathbb{R}$ are linear shape functions associated with the nodes $A \in \tilde{\omega}^{(1)}$, where $\tilde{\omega}^{(1)}$ denotes the set of element nodes at the internal surface. Inserting (4.5) and (2.1) in (4.4) yields

$$\boldsymbol{\lambda}_A \cdot \left(n^{AB} \delta\boldsymbol{q}_B^{(1)} - n^{AC} \delta\boldsymbol{q}_C^{(2)}\right) = 0 \tag{4.6}$$

where n^{AB} and n^{AC} are the Mortar integrals, given by

$$\begin{aligned} n^{AB} &= \langle N^A, N^B\rangle_{\mathcal{B}_0^{\mathrm{h},(1),d}} \\ n^{AC} &= \langle N^A, N^C\rangle_{\mathcal{B}_0^{\mathrm{h},(1),d}} \end{aligned} \tag{4.7}$$

Next a segmentation process for the numerical evaluation of the Mortar integrals in (4.7) will be developed. Therefore, we have to split the internal surfaces into segments. Several efficient and powerful segmentation routines have been developed in the past (see Puso [62], Puso et al. [63] and Hesch & Betsch [34, 36]). To illustrate the procedure, we summarize the 4-step method developed Hesch in & Betsch [36] (see also Section 5.2):

1. Project orthogonally the nodes on the Mortar side to the opposing surface.
2. Project orthogonally the nodes on the non-Mortar side to the opposing surface.
3. Search for intersections between the edges.
4. Apply a Delaunay triangularization to each element on the Mortar side.

For each segment we obtain local coordinates $\boldsymbol{\xi}_{\mathrm{seg},K}^{(j)}$, $K \in [1,\, 2,\, 3]$ in the parameter space for each surface j, defining the vertices of the segment. Introducing linear, triangular shape functions M^K a linear transformation

$$\boldsymbol{\xi}_{\mathrm{seg}}^{(j),\mathrm{h}}(\boldsymbol{\eta}) = \sum_{K=1}^{3} M^K(\boldsymbol{\eta}) \boldsymbol{\xi}_{\mathrm{seg},K}^{(j)} \tag{4.8}$$

can be applied to parametrize the interface. The Mortar integrals for each segment can now be calculated by insertion of (4.8) in (4.7). Thus, we obtain for the segment contributions

$$\begin{aligned} n^{\kappa\beta} &= \langle N^{\kappa}(\boldsymbol{\xi}_{\mathrm{seg}}^{(1),\mathrm{h}}(\boldsymbol{\eta})), N^{\beta}(\boldsymbol{\xi}_{\mathrm{seg}}^{(1),\mathrm{h}}(\boldsymbol{\eta}))\rangle_{\mathcal{B}_0^{\mathrm{h},(1),d}} \\ n^{\kappa\zeta} &= \langle N^{\kappa}(\boldsymbol{\xi}_{\mathrm{seg}}^{(1),\mathrm{h}}(\boldsymbol{\eta})), N^{\zeta}(\boldsymbol{\xi}_{\mathrm{seg}}^{(2),\mathrm{h}}(\boldsymbol{\eta}))\rangle_{\mathcal{B}_0^{\mathrm{h},(1),d}} \end{aligned} \tag{4.9}$$

To apply a Gauss integration, the Jacobian J_{seg} of each segment is required

$$J_{\text{seg}} = \|\boldsymbol{A}_1(\boldsymbol{\xi}_{\text{seg}}^{(1),\text{h}}(\boldsymbol{\eta})) \times \boldsymbol{A}_2(\boldsymbol{\xi}_{\text{seg}}^{(1),\text{h}}(\boldsymbol{\eta}))\| \det(D\boldsymbol{\xi}(\boldsymbol{\eta})) \tag{4.10}$$

where $\boldsymbol{A}_\alpha(\boldsymbol{\xi}) = N^B_{,\alpha}(\boldsymbol{\xi})\boldsymbol{q}_B$ denotes the tangential vectors in the reference configuration. Eventually, we obtain

$$\begin{aligned} n^{\kappa\beta} &= \int\limits_\triangle N^\kappa(\boldsymbol{\xi}_{\text{seg}}^{(1),\text{h}}(\boldsymbol{\eta}))N^\beta(\boldsymbol{\xi}_{\text{seg}}^{(1),\text{h}}(\boldsymbol{\eta}))J_{\text{seg}}\,\text{d}\eta \\ n^{\kappa\zeta} &= \int\limits_\triangle N^\kappa(\boldsymbol{\xi}_{\text{seg}}^{(1),\text{h}}(\boldsymbol{\eta}))N^\zeta(\boldsymbol{\xi}_{\text{seg}}^{(2),\text{h}}(\boldsymbol{\eta}))J_{\text{seg}}\,\text{d}\eta \end{aligned} \tag{4.11}$$

In a last step, we collect the segment contributions

$$\boldsymbol{\Phi}^\kappa_{e,\text{seg}} = n^{\kappa\beta}\boldsymbol{q}^{(1)}_\beta - n^{\kappa\zeta}\boldsymbol{q}^{(2)}_\zeta \tag{4.12}$$

of each element e and assemble them into a global vector of constraints

$$\boldsymbol{\Phi}(\boldsymbol{q}) = \mathop{\mathbf{A}}_{e\in\epsilon^{(1)}} \bigcup_{\text{seg}} \begin{bmatrix} \boldsymbol{\Phi}^{\kappa=1}_{e,\text{seg}} \\ \vdots \\ \boldsymbol{\Phi}^{\kappa=4}_{e,\text{seg}} \end{bmatrix} \tag{4.13}$$

where $\epsilon^{(1)}$ denotes all elements on $\mathcal{B}_0^{\text{h},(1),d}$. For the implementation of the assembly, a location array $A = \text{LM}(\kappa, e)$ is needed to connect the segment contributions to a specific constraint, for details see Hesch & Betsch [33]. Note that the corresponding nodal force vector $\boldsymbol{f}^{(i),d,A}$ follows from

$$\delta\boldsymbol{q}^{(i)}_A \cdot \boldsymbol{f}^{(i),d,A} = \delta\boldsymbol{q}^{(i)}_A \cdot \nabla_{q_\text{A}}\,\boldsymbol{\Phi}(\boldsymbol{q}) \cdot \boldsymbol{\lambda}_A \tag{4.14}$$

Remark: The physical position of the Gauss points on both surfaces do not necessarily coincide with their orthogonal projections, although the corner nodes of the segments do. An alternative solution relies on the evaluation of the orthogonally projected Gauss points instead of the careful evaluation of the Mortar projections. More details on this discussion can be found in Puso et al. [63]. Furthermore, as shown in Puso [62], warped meshes can not be exactly integrated. Within our numerical tests, a 4 point Gauss integration has shown to be sufficient.

Next, we propose a reformulation of the Mortar constraints following the development in Hesch & Betsch [34] to retain conservation of both, linear and angular momentum. Therefore, we decompose the Lagrange multipliers into normal and tangential components

$$\boldsymbol{\lambda} = \lambda_N\boldsymbol{\nu}_{\text{seg}} + \lambda^\alpha\boldsymbol{a}_{\alpha,\text{seg}} \tag{4.15}$$

where

$$\boldsymbol{a}_{\alpha,\text{seg}} = \sum_A N^A_{,\alpha}(\boldsymbol{\xi}_{\text{seg}}^{(1),\text{h}}(\bar{\boldsymbol{\eta}}))\boldsymbol{q}_A \tag{4.16}$$

and

$$\boldsymbol{\nu}_{\text{seg}} = \frac{\boldsymbol{a}_{1,\text{seg}} \times \boldsymbol{a}_{2,\text{seg}}}{\|\boldsymbol{a}_{1,\text{seg}} \times \boldsymbol{a}_{2,\text{seg}}\|} \tag{4.17}$$

are evaluated at the mid-point $\bar{\boldsymbol{\eta}}$ of each segment. We assume that the normal and the tangential vectors remain constant throughout each segment, simplifying the evaluation of the Mortar integrals. The reformulated segment contributions of the Mortar constraints are given by

$$\bar{\boldsymbol{\Phi}}^{\kappa}_{e,\text{seg}} = \begin{bmatrix} \boldsymbol{\Phi}^{\kappa}_{e,\text{seg}} \cdot \boldsymbol{a}_1 \\ \boldsymbol{\Phi}^{\kappa}_{e,\text{seg}} \cdot \boldsymbol{a}_2 \\ \boldsymbol{\Phi}^{\kappa}_{e,\text{seg}} \cdot \boldsymbol{\nu} \end{bmatrix} - \bar{\boldsymbol{\Phi}}^{\kappa,\text{ref}}_{e,\text{seg}} \tag{4.18}$$

where $\bar{\boldsymbol{\Phi}}^{\kappa,\text{ref}}_{e,\text{seg}}$ denotes the segment contributions of the Mortar constraints evaluated in the reference configuration, computed once at problem initialization. This ensures that the constraints are fulfilled in the reference configuration. Note that if the mesh generation and refinement does not produce any gaps between the sub-domains and the position of the Gauss points on both surfaces coincide in the physical space, then $\bar{\boldsymbol{\Phi}}^{\kappa,\text{ref}}_{e,\text{seg}} = \mathbf{0}$.

Guided by the development in Hesch & Betsch [35] we introduce augmented coordinates $\boldsymbol{d}_A$ which equal the normal vector evaluated at each corner node of the elements, analogues to the Lagrange multipliers. To determine the value of the augmented coordinates, we apply additional constraints

$$\boldsymbol{\Phi}^{\text{aug}} = \begin{bmatrix} \boldsymbol{d}_A \cdot \boldsymbol{a}_1 \\ \boldsymbol{d}_A \cdot \boldsymbol{a}_2 \\ \boldsymbol{d}_A \cdot \boldsymbol{d}_A - 1 \end{bmatrix} \tag{4.19}$$

and interpolate the augmented coordinates using the linear shape functions introduced for the interpolation of the Lagrange multipliers

$$\boldsymbol{d}_{\text{seg}} = \sum_{A \in \tilde{\omega}^{(1)}} N^A(\boldsymbol{\xi}^{(1),\text{h}}_{\text{seg}}(\bar{\boldsymbol{\eta}}))\boldsymbol{d}_A \tag{4.20}$$

The reformulated Mortar constraints can be recast by employing the augmented coordinates to obtain

$$\tilde{\boldsymbol{\Phi}}^{\kappa}_{e,\text{seg}} = \begin{bmatrix} \boldsymbol{\Phi}^{\kappa}_{e,\text{seg}} \cdot \boldsymbol{a}_1 \\ \boldsymbol{\Phi}^{\kappa}_{e,\text{seg}} \cdot \boldsymbol{a}_2 \\ \boldsymbol{\Phi}^{\kappa}_{e,\text{seg}} \cdot \boldsymbol{d}_{\text{seg}} \end{bmatrix} - \bar{\boldsymbol{\Phi}}^{\kappa,\text{ref}}_{e,\text{seg}} \tag{4.21}$$

where $\bar{\boldsymbol{\Phi}}^{\kappa,\text{ref}}_{e,\text{seg}}$ remains unchanged.

Frame-indifference. For the verification of frame-indifference, we consider rigid motions of the form

$$\boldsymbol{q}^{\sharp}_A = \boldsymbol{c} + \boldsymbol{Q}\boldsymbol{q}_A \tag{4.22}$$

where $\boldsymbol{c} \in \mathbb{R}^3$ and $\boldsymbol{Q} \in SO(3)$ is a rotation tensor. It is easy to show that one gets for the convective base vectors

$$\boldsymbol{a}^{\sharp}_{\alpha} = \boldsymbol{Q}N^A_{,\alpha}\boldsymbol{q}_A = \boldsymbol{Q}\boldsymbol{a}_{\alpha} \tag{4.23}$$

and

$$\boldsymbol{\nu}^{\sharp} = \frac{\boldsymbol{Q}\boldsymbol{a}_1 \times \boldsymbol{Q}\boldsymbol{a}_2}{\|\boldsymbol{Q}\boldsymbol{a}_1 \times \boldsymbol{Q}\boldsymbol{a}_2\|} = \boldsymbol{Q}\boldsymbol{\nu} \tag{4.24}$$

Thus, for the constraints (4.18) follows immediately

$$\bar{\boldsymbol{\Phi}}^{\kappa}_{e,\text{seg}}(\boldsymbol{q}^{\sharp}) = \begin{bmatrix} \boldsymbol{\Phi}^{\kappa}_{e,\text{seg}} \cdot \boldsymbol{Q}^T\boldsymbol{Q}\boldsymbol{a}_1 \\ \boldsymbol{\Phi}^{\kappa}_{e,\text{seg}} \cdot \boldsymbol{Q}^T\boldsymbol{Q}\boldsymbol{a}_2 \\ \boldsymbol{\Phi}^{\kappa}_{e,\text{seg}} \cdot \boldsymbol{Q}^T\boldsymbol{Q}\boldsymbol{\nu} \end{bmatrix} - \bar{\boldsymbol{\Phi}}^{\kappa,\text{ref}}_{e,\text{seg}} = \bar{\boldsymbol{\Phi}}^{\kappa}_{e,\text{seg}}(\boldsymbol{q}) \tag{4.25}$$

provided that

$$\sum_{\beta} n^{\kappa\beta} - \sum_{\zeta} n^{\kappa\zeta} = 0 \tag{4.26}$$

is valid (for a detailed discussion see Puso [62]). With regard to (4.19) and (4.21) it is obvious that

$$\boldsymbol{\Phi}^{\text{aug}}(\boldsymbol{q}^{\sharp}, \boldsymbol{d}) = \boldsymbol{\Phi}^{\text{aug}}(\boldsymbol{q}, \boldsymbol{Q}^T\boldsymbol{d}) \tag{4.27}$$

and

$$\tilde{\boldsymbol{\Phi}}^{\kappa}_{e,\text{seg}}(\boldsymbol{q}^{\sharp}, \boldsymbol{d}) = \tilde{\boldsymbol{\Phi}}^{\kappa}_{e,\text{seg}}(\boldsymbol{q}, \boldsymbol{Q}^T\boldsymbol{d}) \tag{4.28}$$

For later use we substitute $\boldsymbol{q}^A_{\epsilon} = \boldsymbol{q}^A + \epsilon\boldsymbol{\zeta}$. Frame-indifference of the constraints, i.e. $\tilde{\boldsymbol{\Phi}}^{\kappa}_{e,\text{seg}}(\boldsymbol{q}_{\epsilon}, \boldsymbol{d}) = \tilde{\boldsymbol{\Phi}}^{\kappa}_{e,\text{seg}}(\boldsymbol{q}, \boldsymbol{d})$ implies translational invariance for arbitrary ϵ. Consequently,

$$\frac{\mathrm{d}}{\mathrm{d}\epsilon}\Big|_{\epsilon=0} \tilde{\boldsymbol{\Phi}}^{\kappa}_{e,\text{seg}}(\boldsymbol{q}_{\epsilon}, \boldsymbol{d}) = \boldsymbol{0} \tag{4.29}$$

for any $\boldsymbol{\zeta} \in \mathbb{R}^3$. Similarly, we substitute $\boldsymbol{q}^A_{\epsilon} = \exp(\epsilon\hat{\boldsymbol{\zeta}})\boldsymbol{q}^A$, where $\exp(\hat{\boldsymbol{\zeta}}) \in SO(3)$ denotes the exponential map of a skew-symmetric tensor $\hat{\boldsymbol{\zeta}}$, such that $\hat{\boldsymbol{\zeta}}\boldsymbol{a} = \boldsymbol{\zeta} \times \boldsymbol{a}$ for arbitrary $\boldsymbol{a} \in \mathbb{R}^3$ and receive

$$\frac{\mathrm{d}}{\mathrm{d}\epsilon}\Big|_{\epsilon=0} \tilde{\boldsymbol{\Phi}}^{\kappa}_{e,\text{seg}}(\exp(\epsilon\hat{\boldsymbol{\zeta}})\boldsymbol{q}, \boldsymbol{d}) - \tilde{\boldsymbol{\Phi}}^{\kappa}_{e,\text{seg}}(\boldsymbol{q}, \exp(-\epsilon\hat{\boldsymbol{\zeta}})\boldsymbol{d}) = \boldsymbol{0} \tag{4.30}$$

where we have made use of the rotational properties in (4.28). Note that the properties (4.29) and (4.30) hold for (4.19) as well.

Temporal discretization. Finally, we deal with the discretization in time of the finite-dimensional mechanical system under consideration. To this end we cast the discrete version of (4.3) into the form

$$\begin{aligned} \boldsymbol{M}\ddot{\boldsymbol{q}} &= -\nabla E(\boldsymbol{q}) - (\mathrm{D}_1\,\boldsymbol{\Phi}(\boldsymbol{q}, \boldsymbol{d}))^T\boldsymbol{\lambda} \\ \boldsymbol{0} &= (\mathrm{D}_2\,\boldsymbol{\Phi}(\boldsymbol{q}, \boldsymbol{d}))^T\boldsymbol{\lambda} \\ \boldsymbol{0} &= \boldsymbol{\Phi}(\boldsymbol{q}, \boldsymbol{d}) \end{aligned} \tag{4.31}$$

Here the operators D_1 and D_2 denote the derivative of the vector of constraints $\boldsymbol{\Phi}(\boldsymbol{q}, \boldsymbol{d})$ with respect to the first and the second slot. Furthermore, $\boldsymbol{q}$ consists of the different sub-domain contributions of $(2.2)_1$ and $\boldsymbol{M}$ consists of the contributions $M^{AB,(i)}$ corresponding to $\delta\boldsymbol{q}^{(i)}_A$

and $\boldsymbol{q}_B^{(i)}$. Similar, $\boldsymbol{\Phi}$ and $\boldsymbol{\lambda}$ are assembled from (4.19) and (4.21) in conjunction with (4.13). Note that the reformulated constraints (4.18) can be easily implemented using approach (4.31) by removing the augmented coordinates and replacing the constraints. Next, we apply an energy-momentum scheme (see Hesch & Betsch [34]) as follows

$$\begin{aligned} \boldsymbol{q}_{n+1} - \boldsymbol{q}_n =& \Delta t \boldsymbol{v}_{n+1/2} \\ \boldsymbol{M}(\boldsymbol{v}_{n+1} - \boldsymbol{v}_n) =& -\Delta t \overline{\nabla} E(\boldsymbol{q}_n, \boldsymbol{q}_{n+1}) \\ & - \Delta t (\mathrm{D}_1\, \boldsymbol{\Phi}(\boldsymbol{q}_{n+1/2}, \boldsymbol{d}_{n+1/2}))^T \boldsymbol{\lambda}_{n,n+1} \\ \boldsymbol{0} =& (\mathrm{D}_2\, \boldsymbol{\Phi}(\boldsymbol{q}_{n+1/2}, \boldsymbol{d}_{n+1/2}))^T \boldsymbol{\lambda}_{n,n+1} \\ \boldsymbol{0} =& \boldsymbol{\Phi}(\boldsymbol{q}_{n+1}, \boldsymbol{d}_{n+1}) \end{aligned} \tag{4.32}$$

where the Lagrange multipliers $\boldsymbol{\lambda} \rightarrow \boldsymbol{\lambda}_{n,n+1}$ remain constant within each time step.

Conservation properties. Assuming the absence of external forces we obtain for the linear momentum map $\boldsymbol{L}$ within each time-step

$$\begin{aligned} \boldsymbol{\zeta} \cdot (\boldsymbol{L}_{n+1} - \boldsymbol{L}_n) =& -\Delta t \boldsymbol{\zeta} \cdot \sum_{A \in \omega} \big[\overline{\nabla}_{\boldsymbol{q}_\mathrm{A}}\, E(\boldsymbol{q}_n, \boldsymbol{q}_{n+1}) \\ & + \nabla_{\boldsymbol{q}_\mathrm{A}}\, \boldsymbol{\Phi}(\boldsymbol{q}_{n+1/2}, \boldsymbol{d}_{n+1/2}) \boldsymbol{\lambda}_{n,n+1} \big] \end{aligned} \tag{4.33}$$

For the first term on the right hand side equals zero analogues to (3.7), whereas we obtain for the second term

$$-\Delta t \boldsymbol{\zeta} \cdot \sum_{A \in \omega} \nabla_{\boldsymbol{q}_\mathrm{A}}\, \boldsymbol{\Phi}(\boldsymbol{q}_{n+1/2}, \boldsymbol{d}_{n+1/2}) \boldsymbol{\lambda}_{n,n+1} = 0 \tag{4.34}$$

where we have made use of property (4.29). For the angular momentum map $\boldsymbol{J}$ we can state that

$$\begin{aligned} \boldsymbol{\zeta} \cdot (\boldsymbol{J}_{n+1} - \boldsymbol{J}_n) =& -\Delta t \boldsymbol{\zeta} \cdot \sum_{A \in \omega} \boldsymbol{q}_{A,n+1/2} \times \big[\overline{\nabla}_{\boldsymbol{q}_\mathrm{A}}\, E(\boldsymbol{q}_n, \boldsymbol{q}_{n+1}) \\ & + \nabla_{\boldsymbol{q}_\mathrm{A}}\, \boldsymbol{\Phi}(\boldsymbol{q}_{n+1/2}, \boldsymbol{d}_{n+1/2}) \boldsymbol{\lambda}_{n,n+1} \big] \end{aligned} \tag{4.35}$$

The first term vanishes due to the skew-symmetry of $\boldsymbol{q}_{A,n+1/2} \times \boldsymbol{q}_{B,n+1/2}$ and the symmetry of $\boldsymbol{\Sigma}^\mathrm{h}_{n,n+1}$. For the second term follows

$$\begin{aligned} \boldsymbol{\zeta} \cdot (\boldsymbol{J}_{n+1} - \boldsymbol{J}_n) &= -\Delta t \boldsymbol{\zeta} \cdot \sum_{A \in \omega} \boldsymbol{q}_{A,n+1/2} \times \nabla_{\boldsymbol{q}_\mathrm{A}}\, \boldsymbol{\Phi}(\boldsymbol{q}_{n+1/2}, \boldsymbol{d}_{n+1/2}) \boldsymbol{\lambda}_{n,n+1} \\ &= \Delta t \boldsymbol{\lambda}_{n,n+1} \cdot \sum_{A \in \omega} (\nabla_{\boldsymbol{q}_\mathrm{A}}\, \boldsymbol{\Phi}(\boldsymbol{q}_{n+1/2}, \boldsymbol{d}_{n+1/2}))^T \hat{\boldsymbol{q}}_{A,n+1/2} \boldsymbol{\zeta} \\ &= -\Delta t \boldsymbol{\lambda}_{n,n+1} \cdot \sum_{A \in \omega^{(1)}} (\nabla_{\boldsymbol{d}_\mathrm{A}}\, \boldsymbol{\Phi}(\boldsymbol{q}_{n+1/2}, \boldsymbol{d}_{n+1/2}))^T \hat{\boldsymbol{d}}_{A,n+1/2} \boldsymbol{\zeta} \\ &= \Delta t \boldsymbol{\zeta} \cdot \sum_{A \in \omega^{(1)}} \hat{\boldsymbol{d}}_{A,n+1/2} \nabla_{\boldsymbol{d}_\mathrm{A}}\, \boldsymbol{\Phi}(\boldsymbol{q}_{n+1/2}, \boldsymbol{d}_{n+1/2}) \boldsymbol{\lambda}_{n,n+1} \\ &= 0 \end{aligned} \tag{4.36}$$

where we have taken (4.30) and $(4.32)_3$ into account. Eventually, we verify algorithmic conservation of energy. Scalar multiplication of $(4.32)_2$ by $\boldsymbol{v}_{n+1/2}$ yields

$$\begin{aligned}\boldsymbol{v}_{n+1/2} \cdot \boldsymbol{M}(\boldsymbol{v}_{n+1} - \boldsymbol{v}_n) = &- (\boldsymbol{q}_{n+1} - \boldsymbol{q}_n) \cdot \overline{\nabla} E(\boldsymbol{q}_n, \boldsymbol{q}_{n+1}) \\ &+ (\boldsymbol{q}_{n+1} - \boldsymbol{q}_n) \cdot (\mathrm{D}_1\, \boldsymbol{\Phi}(\boldsymbol{q}_{n+1/2}, \boldsymbol{d}_{n+1/2}))^T \boldsymbol{\lambda}_{n,n+1}\end{aligned} \tag{4.37}$$

where we have taken $(4.32)_1$ into account. Due to the discrete gradient (3.5) we can recast the last equation as follows

$$\begin{aligned}T_{n+1} - T_n = &- (E(\boldsymbol{q}_{n+1}) - E(\boldsymbol{q}_n)) \\ &+ \boldsymbol{\lambda}_{n,n+1} \cdot \mathrm{D}_1\, \boldsymbol{\Phi}(\boldsymbol{q}_{n+1/2}, \boldsymbol{d}_{n+1/2})(\boldsymbol{q}_{n+1} - \boldsymbol{q}_n)\end{aligned} \tag{4.38}$$

For the last term we state that

$$\begin{aligned}\mathrm{D}_1\, \boldsymbol{\Phi}(\boldsymbol{q}_{n+1/2}, \boldsymbol{d}_{n+1/2})(\boldsymbol{q}_{n+1} - \boldsymbol{q}_n) + \mathrm{D}_2\, \boldsymbol{\Phi}(\boldsymbol{q}_{n+1/2}, \boldsymbol{d}_{n+1/2})(\boldsymbol{d}_{n+1} - \boldsymbol{d}_n) \\ = \boldsymbol{\Phi}(\boldsymbol{q}_{n+1}, \boldsymbol{d}_{n+1}) - \boldsymbol{\Phi}(\boldsymbol{q}_n, \boldsymbol{d}_n) = \mathbf{0}\end{aligned} \tag{4.39}$$

is valid, since the constraints are at most quadratic in $\boldsymbol{q}$ and $\boldsymbol{d}$ and we end up with

$$\begin{aligned}T_{n+1} - T_n + E_{n+1} - E_n = &- \boldsymbol{\lambda}_{n+1} \cdot \mathrm{D}_2\, \boldsymbol{\Phi}(\boldsymbol{q}_{n+1/2}, \boldsymbol{d}_{n+1/2})(\boldsymbol{d}_{n+1} - \boldsymbol{d}_n) \\ = &\, 0\end{aligned} \tag{4.40}$$

Thus, total energy is algorithmically conserved.

4.2 Domain decomposition and thermomechanical systems

Next, we to extend our previous developments to domain decomposition problems in thermoelasticity. The weak form of the coupling contributions reads

$$\langle \boldsymbol{t}^{\mathrm{h},(1)}, \left(\begin{bmatrix} \delta\boldsymbol{\varphi}^{\mathrm{h},(1)} \\ \delta\theta^{\mathrm{h},(1)} \end{bmatrix} - \begin{bmatrix} \delta\boldsymbol{\varphi}^{\mathrm{h},(2)} \\ \delta\theta^{\mathrm{h},(2)} \end{bmatrix} \right) \rangle_{\mathcal{B}_0^{\mathrm{h},(1),d}} = \boldsymbol{\lambda}_A \cdot \left(n^{AB} \begin{bmatrix} \delta\boldsymbol{q}_B^{(1)} \\ \delta\Theta_B^{(1)} \end{bmatrix} - n^{AC} \begin{bmatrix} \delta\boldsymbol{q}_C^{(2)} \\ \delta\Theta_C^{(2)} \end{bmatrix} \right) \tag{4.41}$$

where the Mortar integrals n^{AB} and n^{AC} are given in (4.7). The nodal Lagrange multipliers $\boldsymbol{\lambda}_A \in \mathbb{R}^4$ characterize the generalized forces of the Mortar mesh-tying constraint, given by

$$\boldsymbol{\Phi}^A_{\mathrm{mortar}}(\boldsymbol{q}, \boldsymbol{\Theta}) = n^{AB} \begin{bmatrix} \boldsymbol{q}_B^{(1)} \\ \Theta_B^{(1)} \end{bmatrix} - n^{AC} \begin{bmatrix} \boldsymbol{q}_C^{(2)} \\ \Theta_C^{(2)} \end{bmatrix} \tag{4.42}$$

To evaluate the Mortar integrals, we have to divide both sides of the discrete interface once again into segments. The arising segment contributions to the Mortar mesh-tying constraints are collected in the vector

$$\tilde{\boldsymbol{\Phi}}_{e,\mathrm{seg}}(\boldsymbol{q}, \boldsymbol{\Theta}) = \begin{bmatrix} \tilde{\boldsymbol{\Phi}}^{\kappa=1}_{e,\mathrm{seg}}(\boldsymbol{q}, \boldsymbol{\Theta}) \\ \vdots \\ \tilde{\boldsymbol{\Phi}}^{\kappa=4}_{e,\mathrm{seg}}(\boldsymbol{q}, \boldsymbol{\Theta}) \end{bmatrix} \tag{4.43}$$

where

$$\tilde{\boldsymbol{\Phi}}^{\kappa}_{e,\mathrm{seg}}(\boldsymbol{q},\boldsymbol{\Theta}) = n^{\kappa\beta}\begin{bmatrix}\boldsymbol{q}^{(1)}_{\beta}\\ \Theta^{(1)}_{\beta}\end{bmatrix} - n^{\kappa\zeta}\begin{bmatrix}\boldsymbol{q}^{(2)}_{\zeta}\\ \Theta^{(2)}_{\zeta}\end{bmatrix} \tag{4.44}$$

To perform the assembly of the contributions of all elements $e \in \bar{\epsilon}^{(1)}$ on the non-Mortar side, the connection between local and global node numbers is stored in the location array LM, so that $A = \mathrm{LM}(\kappa, e)$, for $A \in \bar{\omega}^{(1)}$, $\kappa \in \{1, \ldots, 4\}$ and $e \in \bar{\epsilon}^{(1)}$. Accordingly, the Mortar constraints follow from

$$\boldsymbol{\Phi}^{A}_{\mathrm{mortar}} \leftarrow \boldsymbol{\Phi}^{A}_{\mathrm{mortar}} + \boldsymbol{\Phi}^{\kappa}_{e} \tag{4.45}$$

Or equivalently

$$\boldsymbol{\Phi}_{\mathrm{mortar}}(\boldsymbol{q},\boldsymbol{\Theta}) = \underset{e\in\bar{\epsilon}^{(1)}}{\mathbf{A}}\,\tilde{\boldsymbol{\Phi}}_{e} = \underset{e\in\bar{\epsilon}^{(1)}}{\mathbf{A}}\bigcup_{\mathrm{seg}}\tilde{\boldsymbol{\Phi}}_{e,\mathrm{seg}} = \underset{e\in\bar{\epsilon}^{(1)}}{\mathbf{A}}\bigcup_{\mathrm{seg}}\begin{bmatrix}\tilde{\boldsymbol{\Phi}}^{\kappa=1}_{e,\mathrm{seg}}(\boldsymbol{q},\boldsymbol{\Theta})\\ \vdots\\ \tilde{\boldsymbol{\Phi}}^{\kappa=4}_{e,\mathrm{seg}}(\boldsymbol{q},\boldsymbol{\Theta})\end{bmatrix} \tag{4.46}$$

After adaptation of the previously introduce augmentation technique, we obtain the following modified constraint functions

$$\tilde{\boldsymbol{\Phi}}^{\kappa}_{e,\mathrm{seg}}(\boldsymbol{q},\boldsymbol{\Theta},\boldsymbol{d}) = \begin{bmatrix}\boldsymbol{\Phi}^{\kappa}_{e,\mathrm{seg}}(\boldsymbol{q},\boldsymbol{\Theta})\cdot\begin{bmatrix}\boldsymbol{a}_{1,\mathrm{seg}}\\ 0\end{bmatrix}\\ \boldsymbol{\Phi}^{\kappa}_{e,\mathrm{seg}}(\boldsymbol{q},\boldsymbol{\Theta})\cdot\begin{bmatrix}\boldsymbol{a}_{2,\mathrm{seg}}\\ 0\end{bmatrix}\\ \boldsymbol{\Phi}^{\kappa}_{e,\mathrm{seg}}(\boldsymbol{q},\boldsymbol{\Theta})\cdot\begin{bmatrix}\boldsymbol{d}_{\mathrm{seg}}\\ 0\end{bmatrix}\\ \boldsymbol{\Phi}^{\kappa}_{e,\mathrm{seg}}(\boldsymbol{q},\boldsymbol{\Theta})\cdot\begin{bmatrix}\boldsymbol{0}\\ 1\end{bmatrix}\end{bmatrix} \tag{4.47}$$

Collecting the above segment contributions into a system vector yields

$$\boldsymbol{\Phi}(\boldsymbol{q},\boldsymbol{\Theta},\boldsymbol{d}) = \begin{bmatrix}\boldsymbol{\Phi}^{\mathrm{aug}}_{A=1}(\boldsymbol{q},\boldsymbol{d})\\ \vdots\\ \boldsymbol{\Phi}^{\mathrm{aug}}_{A=n_{\mathrm{surf}}}(\boldsymbol{q},\boldsymbol{d})\\ \boldsymbol{\Phi}^{A=1}_{\mathrm{mortar}}(\boldsymbol{q},\boldsymbol{\Theta},\boldsymbol{d})\\ \vdots\\ \boldsymbol{\Phi}^{A=n_{\mathrm{surf}}}_{\mathrm{mortar}}(\boldsymbol{q},\boldsymbol{\Theta},\boldsymbol{d})\end{bmatrix} \tag{4.48}$$

The Lagrange multipliers corresponding to the coordinate augmentation and the Mortar constraints are collected in the system vector $\boldsymbol{\lambda}$. Overall we obtain seven constraints per node on the Mortar side.

Temporal discretization. We refer to previous developments in Section 3.2 for details on the thermoelastical system. As before, we evaluate the primary variables (position, temperature and augmented coordinates) using a mid-point type approximation, whereas the Lagrange multipliers $\boldsymbol{\lambda} \to \boldsymbol{\lambda}_{n,n+1}$ remain constant within each time step.

$$
\begin{aligned}
\delta \boldsymbol{q}_A \cdot \left[M^{AB}(\boldsymbol{v}_{B,n+1} - \boldsymbol{v}_{B,n}) + \Delta t \int\limits_{\mathcal{B}_0^{\mathrm{h}}} S^{AB}_{n,n+1} \, \mathrm{d}V \boldsymbol{q}_{B,n+\frac{1}{2}} \right] &= \\
\Delta t \delta \boldsymbol{q}_A \cdot \left[\boldsymbol{F}^{A,\mathrm{ext}}_{n+\frac{1}{2}} - \nabla_{\boldsymbol{q}^{\mathrm{A}}} \boldsymbol{\Phi}(\boldsymbol{q}_{n+\frac{1}{2}}, \boldsymbol{\Theta}_{n+\frac{1}{2}}, \boldsymbol{d}_{n+\frac{1}{2}}) \cdot \boldsymbol{\lambda}_{n,n+1} \right] & \\
\delta \Theta_A \left[\Gamma^{AB}_{n,n+1} \Theta_{B,n+\frac{1}{2}} - \Delta t \int\limits_{\mathcal{B}_0^{\mathrm{h}}} K^{AB}_{n,n+1} \, \mathrm{d}V \Theta_{B,n+\frac{1}{2}} \right] &= \\
\Delta t \delta \Theta_A \left[Q^{\mathrm{h},A}_{n,n+1} - \nabla_{\boldsymbol{\Theta}^{\mathrm{A}}} \boldsymbol{\Phi}(\boldsymbol{q}_{n+\frac{1}{2}}, \boldsymbol{\Theta}_{n+\frac{1}{2}}, \boldsymbol{d}_{n+\frac{1}{2}}) \cdot \boldsymbol{\lambda}_{n,n+1} \right] & \\
\nabla_{\boldsymbol{d}} \boldsymbol{\Phi}(\boldsymbol{q}_{n+\frac{1}{2}}, \boldsymbol{\Theta}_{n+\frac{1}{2}}, \boldsymbol{d}_{n+\frac{1}{2}}) \cdot \boldsymbol{\lambda}_{n,n+1} &= \boldsymbol{0} \\
\boldsymbol{\Phi}(\boldsymbol{q}_{n+1}, \boldsymbol{\Theta}_{n+1}, \boldsymbol{d}_{n+1}) &= \boldsymbol{0}
\end{aligned}
\tag{4.49}
$$

Since we do not change the energy-momentum consistent integrator used for the thermoelastic system, we will focus on the additional terms due to the constraints to verify the conservation properties.

Conservation properties. Proceeding along the lines of Section 4.1 (see (4.33)) and assuming the absence of external forces, we obtain for the constraint contributions

$$
\boldsymbol{\zeta} \cdot (\boldsymbol{L}_{n+1} - \boldsymbol{L}_n) = \Delta t \boldsymbol{\zeta} \cdot \sum_{A \in \omega} \left(-\nabla_{\boldsymbol{q}^{\mathrm{A}}} \boldsymbol{\Phi}(\boldsymbol{q}_{n+\frac{1}{2}}, \boldsymbol{\Theta}_{n+\frac{1}{2}}, \boldsymbol{d}_{n+\frac{1}{2}}) \cdot \boldsymbol{\lambda}_{n,n+1} \right) \tag{4.50}
$$

Frame-indifference of the vector of constraints $\boldsymbol{\Phi}$ has already been shown in detail in Section 4.1 for the purely mechanical case. It can be easily verified that

$$
\boldsymbol{\Phi}(\boldsymbol{q}_\epsilon, \boldsymbol{\Theta}_{n+\frac{1}{2}}, \boldsymbol{d}_{n+\frac{1}{2}}) = \boldsymbol{\Phi}(\boldsymbol{q}_{n+\frac{1}{2}}, \boldsymbol{\Theta}_{n+\frac{1}{2}}, \boldsymbol{d}_{n+\frac{1}{2}}) \tag{4.51}
$$

Here, $\boldsymbol{q}^A_\epsilon = \boldsymbol{q}^A_{n+\frac{1}{2}} + \epsilon \boldsymbol{\zeta}$, $\forall\, A \in \omega$ and $\epsilon \in \mathbb{R}$ is arbitrary. Equation (4.51) implies

$$
\left. \frac{\mathrm{d}}{\mathrm{d}\epsilon} \right|_{\epsilon=0} \boldsymbol{\Phi}(\boldsymbol{q}_\epsilon, \boldsymbol{\Theta}_{n+\frac{1}{2}}, \boldsymbol{d}_{n+\frac{1}{2}}) = \sum_{A \in \omega} \left[\nabla_{\boldsymbol{q}^{\mathrm{A}}} \boldsymbol{\Phi}(\boldsymbol{q}_{n+\frac{1}{2}}, \boldsymbol{\Theta}_{n+\frac{1}{2}}, \boldsymbol{d}_{n+\frac{1}{2}}) \right] \cdot \boldsymbol{\zeta} = 0 \tag{4.52}
$$

Insertion in (4.50) yields

$$
\boldsymbol{L}_{n+1} - \boldsymbol{L}_n = \boldsymbol{0} \tag{4.53}
$$

which confirms, that the constraints do not affect linear momentum conservation. Next we investigate the angular momentum conservation and obtain

$$
\boldsymbol{\zeta} \cdot (\boldsymbol{J}_{n+1} - \boldsymbol{J}_n) = \Delta t \boldsymbol{\zeta} \cdot \left(\sum_{A \in \omega} \boldsymbol{q}_{A,n+\frac{1}{2}} \times \left[-\nabla_{\boldsymbol{q}^{\mathrm{A}}} \boldsymbol{\Phi}(\boldsymbol{q}_{n+\frac{1}{2}}, \boldsymbol{\Theta}_{n+\frac{1}{2}}, \boldsymbol{d}_{n+\frac{1}{2}}) \cdot \boldsymbol{\lambda}_{n,n+1} \right] \right) \tag{4.54}
$$

Based on the results in Section 4.1 we can postulate for the domain decomposition constraints

$$\boldsymbol{\Phi}(\boldsymbol{q}_{\epsilon}, \boldsymbol{\Theta}_{n+\frac{1}{2}}, \boldsymbol{d}_{n+\frac{1}{2}}) = \boldsymbol{\Phi}(\boldsymbol{q}_{n+\frac{1}{2}}, \boldsymbol{\Theta}_{n+\frac{1}{2}}, \boldsymbol{d}_{\epsilon}) \tag{4.55}$$

where $\boldsymbol{q}_{\epsilon}^{A} = \exp(\epsilon\hat{\boldsymbol{\zeta}})\boldsymbol{q}_{n+\frac{1}{2}}^{A}$, $\forall\, A \in \omega$ and $\boldsymbol{d}_{\epsilon}^{A} = \exp(-\epsilon\hat{\boldsymbol{\zeta}})\boldsymbol{d}_{n+\frac{1}{2}}^{A}$, $\forall\, A \in \bar{\omega}^{(1)}$. Accordingly, we can write in analogy to (4.52)

$$\begin{aligned}\frac{\mathrm{d}}{\mathrm{d}\epsilon}\bigg|_{\epsilon=0}&\Big[\boldsymbol{\Phi}(\boldsymbol{q}_{\epsilon}, \boldsymbol{\Theta}_{n+\frac{1}{2}}, \boldsymbol{d}_{n+\frac{1}{2}}) - \boldsymbol{\Phi}(\boldsymbol{q}_{n+\frac{1}{2}}, \boldsymbol{\Theta}_{n+\frac{1}{2}}, \boldsymbol{d}_{\epsilon})\Big] = 0\\ \sum_{A\in\omega}&\Big[\nabla_{\boldsymbol{q}^{\mathrm{A}}}\,\boldsymbol{\Phi}(\boldsymbol{q}_{n+\frac{1}{2}}, \boldsymbol{\Theta}_{n+\frac{1}{2}}, \boldsymbol{d}_{n+\frac{1}{2}}) \cdot (\boldsymbol{\zeta} \times \boldsymbol{q}_{n+\frac{1}{2}}^{A}) -\\ &\nabla_{\boldsymbol{d}^{\mathrm{A}}}\,\boldsymbol{\Phi}(\boldsymbol{q}_{n+\frac{1}{2}}, \boldsymbol{\Theta}_{n+\frac{1}{2}}, \boldsymbol{d}_{n+\frac{1}{2}}) \cdot (\boldsymbol{\zeta} \times \boldsymbol{d}_{n+\frac{1}{2}}^{A})\Big] = 0\end{aligned} \tag{4.56}$$

Due to $(4.49)_3$ the last term in the square brackets of $(4.56)_2$ vanishes. Inserting the last equation into (4.54) yields

$$\boldsymbol{J}_{n+1} - \boldsymbol{J}_{n} = \boldsymbol{0} \tag{4.57}$$

which confirms, that the constraints do not affect angular momentum conservation as well. Eventually, we verify algorithmic energy consistency and restrict ourselves to the contributions of the constraints. In particular, we have to show that these contributions are workless. For the mechanical part, conservation of energy can be proven following the arguments in Section 4.1. Similar to result (3.21), in the present case we obtain

$$T_{n+1} - T_{n} + E_{n+1} - E_{n} = \Delta t\left[P_{n,n+1}^{\mathrm{h,ext}} + Q_{n,n+1}^{\mathrm{h}} - \sum_{A\in\omega}\nabla_{\boldsymbol{\Theta}^{\mathrm{A}}}\,\boldsymbol{\Phi}(\boldsymbol{q}_{n+\frac{1}{2}}, \boldsymbol{\Theta}_{n+\frac{1}{2}}, \boldsymbol{d}_{n+\frac{1}{2}}) \cdot \boldsymbol{\lambda}_{n,n+1}\right] \tag{4.58}$$

With regard to (4.42) we can rewrite the last term in the square brackets (4.58)

$$\begin{aligned}&\sum_{B\in\bar{\omega}}(\lambda_{A}^{4})_{n,n+1}n^{AB} - \sum_{C\in\bar{\omega}}(\lambda_{A}^{4})_{n,n+1}n^{AC} =\\ (\lambda_{A}^{4})_{n,n+1}&\left(\int\limits_{\partial\mathcal{B}^{\mathrm{h},(1),d}} N^{A}\left(\boldsymbol{X}^{(1)}\right)\,\mathrm{d}A - \int\limits_{\partial\mathcal{B}^{\mathrm{h},(1),d}} N^{A}\left(\boldsymbol{X}^{(1)}\right)\,\mathrm{d}A\right) = 0\end{aligned} \tag{4.59}$$

where we have made use of the property $\sum_{B} N^{B}\left(\boldsymbol{X}^{(1)}\right) = 1$. Taking into account the last result, (4.58) yields

$$T_{n+1} - T_{n} + E_{n+1} - E_{n} = \Delta t\left[P_{n,n+1}^{\mathrm{h,ext}} + Q_{n,n+1}^{\mathrm{h}}\right] \tag{4.60}$$

which confirm, that the constraints are workless.

Remark: The last statement depends crucially on the accuracy of the numerical evaluation of the Mortar integrals for each segment. Remarkably, the proof for linear momentum conservation in Puso [62] leads to the same conclusion. Our numerical experiments have shown, that a four point Gauss integration is sufficient.

4.3 Domain decomposition and isogeometric analysis

Next, we want to provide an adequate, Mortar based method for a nonconforming domain decomposition of NURBS based solids following the outlines in Hesch & Betsch [39]. The discrete balance of linear momentum across the interface reads

$$\langle \boldsymbol{t}^{\mathrm{h},(1)}, (\delta\boldsymbol{\varphi}^{\mathrm{h},(1)} - \delta\boldsymbol{\varphi}^{\mathrm{h},(2)})\rangle_{\mathcal{B}_0^{\mathrm{h},(1),d}} = 0 \tag{4.61}$$

where we have to define $\boldsymbol{t}^{(1),\mathrm{h}}$ for NURBS based interfaces which are usually of higher order. A brief discussion of higher order (in particular quadratic) interpolation in connection with Mortar contact methods can be found in Puso et al. [63] and in Fischer & Wriggers [20], a detailed analysis can be found in Hauret & Le Tallec [32]. In Hesch & Betsch [34, 35] the shape functions of the underlying displacement approximation are used to interpolate the Lagrange multipliers. Optimal convergence for higher order NURBS interpolation can only be achieved by using higher order interpolation of the Lagrange multiplier field, i.e. a quadratic interpolation of the Lagrange multipliers for cubic interpolation of the geometry. Higher order NURBS interpolation of the Lagrange multiplier field may become difficult, if the interface is not constructed by an open knot vector. In that case, the interpolation of the interface depends on a large set of control points, resulting in a large number of constraints which is inefficient and potentially overconstrained. A higher order Lagrangian interpolation is possible if additional nodes are placed on the interface. Here, we restrict ourself to linear shape functions due to the generality within the application, i.e. we can apply it to arbitrary h-, p- and k-refined bodies.
Note that this approach is potentially underconstrained for extremely coarse meshes in conjunction with higher order NURBS. In general, a one dimensional system has a knot vector with $n+p+1$ entries which correlates in our approach with the number of Lagrange multipliers reduced by the overall number of multiplicities.

Four corner nodes of each surface element of the interface, independent of the order of the underlying NURBS solid are given, such that we can always apply a linear interpolation of the Lagrange multipliers

$$\boldsymbol{t}^{(1),\mathrm{h}} = \sum_{A\in\tilde{\omega}^{(1)}} N^A \boldsymbol{\lambda}_A \tag{4.62}$$

Here, $N^A : \mathcal{B} \to \mathbb{R}$ are linear Lagrangian shape functions associated with the nodes $A \in \tilde{\omega}^{(1)}$, where $\tilde{\omega}^{(1)}$ denotes the set of element nodes (not the control nodes) at the physical surface. Inserting (4.62) and (2.23) in (4.61) yields

$$\boldsymbol{\lambda}_A \cdot \left(n^{AB}\delta\boldsymbol{q}_B^{(1)} - n^{AC}\delta\boldsymbol{q}_C^{(2)}\right) = 0 \tag{4.63}$$

where n^{AB} and n^{AC} are the Mortar integrals, given by

$$\begin{aligned} n^{AB} &= \langle N^A, R^B \rangle_{\mathcal{B}_0^{\mathrm{h},(1),d}} \\ n^{AC} &= \langle N^A, R^C \rangle_{\mathcal{B}_0^{\mathrm{h},(1),d}} \end{aligned} \tag{4.64}$$

The NURBS parametrization $\sum_B R^B \boldsymbol{q}_B$ and $\sum_C R^C \boldsymbol{q}_C$ of the respective interface surface can be derived from the adjacent volume element, as shown in Temizer et al. [68].

Remark: The presented linear interpolation of the Lagrange multipliers can be used independent of the order of the NURBS. As a result, the proposed method allows the combined use of Lagrangian and NURBS based shape functions. As shown in Hesch & Betsch [39] segmentation procedure for the evaluation of the Mortar integrals as well as the conservation properties of the resulting constraint formulation are identical to the results in Section 4.1.

4.4 Examples

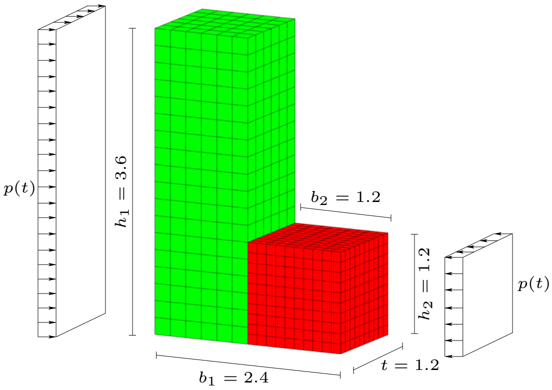

Figure 4.2: Initial mesh configuration of the L-shaped block.

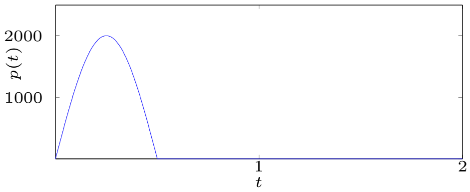

Figure 4.3: Time history of the pressure load.

Flying L-shaped block The first example deals with a continuum body which assumes the form of an L-shaped block in the stress-free initial configuration (see Figure 4.2). The block is divided into two parts which are independently meshed. In particular, the larger

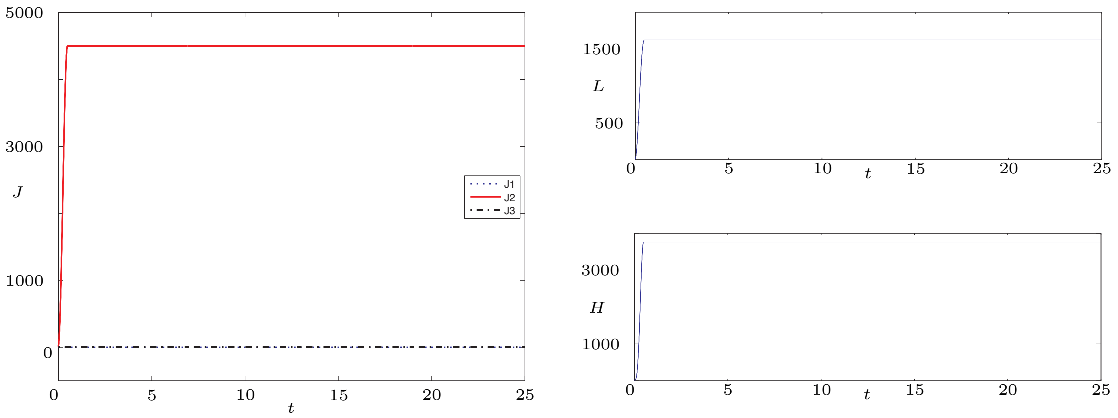

Figure 4.4: Total linear, angular momentum and total energy.

part consists of 648 elements ($18 \times 6 \times 6$), while the smaller small part comprises 1000 elements ($10 \times 10 \times 10$). Consequently, the two meshes do not conform on the interface. The model consists of 6786 degrees of freedom, the segmentation process generates 801 segments for 399 constraints. Therefore, 2403 additional constraints for the augmentation are needed. Hyperelastic constitutive behavior is assumed to be governed by a compressible Neo-Hooke material with associated stored energy function

$$W(\boldsymbol{C}) = \frac{\mu}{2}\left[\operatorname{tr}(\boldsymbol{C}) - 3\right] + \frac{\lambda}{2}(\ln(J))^2 - \mu \ln(J) \tag{4.65}$$

using $J = \sqrt{\det(\boldsymbol{C})}$. First, a quasi-rigid material behavior is investigated. The corresponding material constants are assumed to take the values $\lambda = 300000$, $\mu = 75000$ and $\rho = 100$, where λ and μ denote Lamé parameters and ρ is the density.

To initiate the motion, external pressure loads are acting on the block for $0 \leq t \leq 0.5$, see Figure 4.2. Figure 4.3 indicates the sinusoidal pressure load. In the simulations documented below a constant time step size of $\Delta t = 0.01$ has been used. For $t > 0.5$ the present example can be classified as autonomous Hamiltonian system with symmetry. Accordingly, the total energy, angular and linear momentum are conserved quantities for

Table 4.1: Material properties

Ogden model	$\mu_1 = 6.30 \cdot 10^5$	$\alpha_1 = 1.3$
	$\mu_2 = 0.012 \cdot 10^5$	$\alpha_2 = 5.0$
	$\mu_3 = -0.10 \cdot 10^5$	$\alpha_3 = -2.0$
Heat capacity	$c_0 = 1830$	
Density	$\rho_0 = 950$	
Linear expansion coefficient	$\alpha_0 = 22.333 \cdot 10^{-5}$	
Bulk modulus	$\kappa(\Theta_0) = 2.0 \cdot 10^8$	
Empirical coefficients	$\beta = 9.0$	
	$\gamma = 2.50$	
Thermal conductivity	$K_0(\Theta_0) = 0.15$	
Softening parameter	$\omega_K = 0.004$	

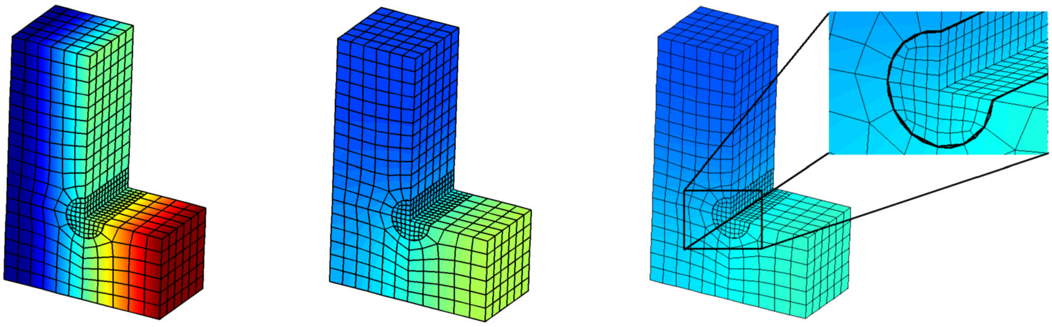

Figure 4.5: Temperature distribution at different times.

$t > 0.5$. The present energy-momentum scheme does indeed conserve these quantities. This can be observed from Figures 4.4.

Thermal domain decomposition problem This example utilizes the same geometry of a three-dimensional L-shape as before. As before, two subdomains of the L-shaped block have been meshed independently (see Figure 4.5). The larger subdomain consists of 840 elements, whereas the smaller subdomain consists of 675 elements. 1584 segments have to be computed for the domain decomposition interface. Additional 77 normal vectors with altogether 231 augmented coordinates as unknowns are used.

The data for the used Ogden model are similar to Holzapfel & Simo [41] and are summarized in Table 4.1. Enhanced assumed strain elements (see Appendix A for details) have been implemented as well. For all examples we define a stress free reference state in thermal equilibrium based on a homogeneous temperature field $\Theta_0 = 293.15$. Thus,

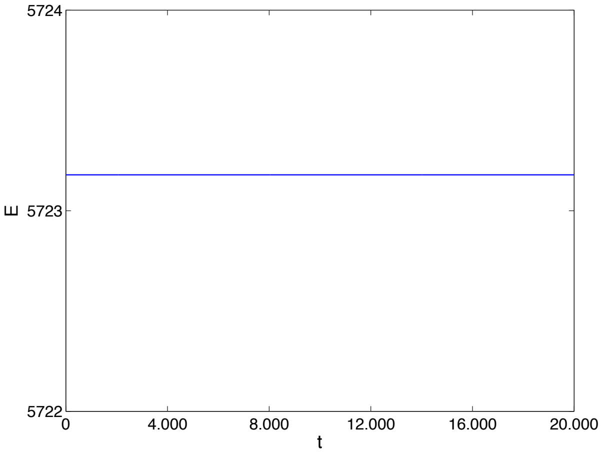

Figure 4.6: Energy over time).

the system consists of overall 9110 thermal, mechanical and augmented degrees of freedom in conjunction with 539 constraints (231 constraints for the augmented coordinates and

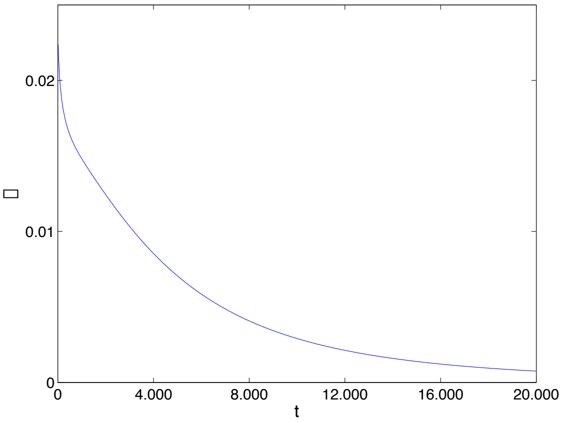

Figure 4.7: Entropy production over time.

308 for the mortar constraints). First we examine the influence of the mortar method on the pure heat conduction problem, i.e. we exclude all mechanical equations from the system and apply a linear distribution of temperature to the adiabatically isolated L-shape (cf. Figure 4.5, left). Figure 4.5, central shows the temperature distribution after 9900, whereas Figure 4.5, right shows the temperature distribution after 19800. At this time, thermodynamic equilibrium has nearly been reached. Figure 4.6 shows the total energy of the system over time.

As can be seen, energy is conserved, which reflects the first law of thermodynamics. The second law states, that the entropy production remains equal or greater zero, which can be observed in this particular example from Figure 4.7.

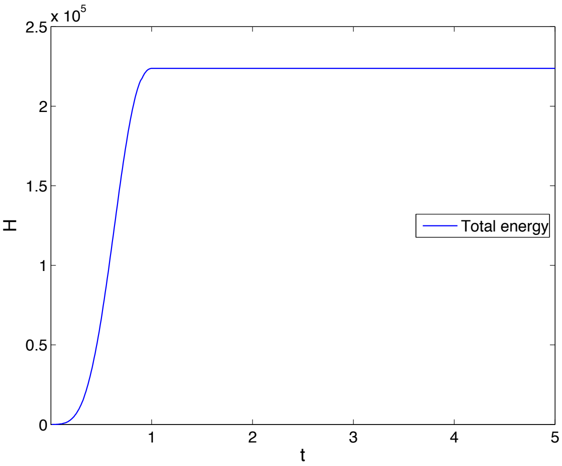

Figure 4.8: Energy over time.

We next deal with the completely coupled, transient thermoelastic problem using the same mechanical configuration as before. Again, after the load phase the adiabatically isolated

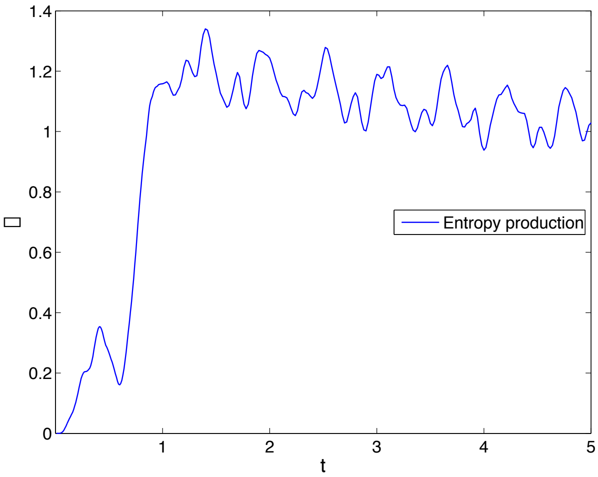

Figure 4.9: Entropy production over time.

system moves freely in space and the time step size has been set to $\Delta t = 0.02$. The proposed energy-momentum consistent scheme obeys the first law of thermodynamics, as shown in Figure 4.8. For the problem at hand, the entropy production is displayed in Figure 4.9.

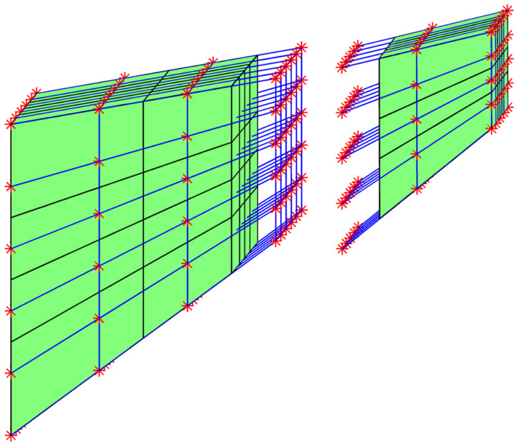

Figure 4.10: Decomposed and partially refined Cook's membrane.

Cook's membrane The last, static example deals with a decomposed and partially h-refined membrane structure, known as Cook's membrane. In particular we consider a 3d version of Cook's membrane with constant thickness $h = 10$. Fig. 4.10 shows the initial decomposed and refined mesh. The left part consists of $2 \times 4 \times 4$ and the right of $1 \times 3 \times 3$ quadratic elements. The $4 \times 6 \times 6$ and $3 \times 5 \times 5$ control points of the sub-domains are equidistant distributed to simplify mesh generation. The knot vectors are

$$\begin{aligned}\Xi^{(1)} &= [0,\ 0,\ 0,\ 1,\ 2,\ 3,\ 3]\\ \mathcal{H}^{(1)} &= [0,\ 0,\ 0,\ 1,\ 2,\ 3,\ 4,\ 4,\ 4]\\ \mathcal{I}^{(1)} &= [0,\ 0,\ 0,\ 1,\ 2,\ 3,\ 4,\ 4,\ 4]\end{aligned} \tag{4.66}$$

and

$$\begin{aligned}\Xi^{(2)} &= [0,\ 1,\ 2,\ 3,\ 3,\ 3]\\ \mathcal{H}^{(2)} &= [0,\ 0,\ 0,\ 1,\ 2,\ 3,\ 3,\ 3]\\ \mathcal{I}^{(2)} &= [0,\ 0,\ 0,\ 1,\ 2,\ 3,\ 3,\ 3]\end{aligned} \tag{4.67}$$

Here, the upper index refers to the left (1) and to the right (2) sub-domain. As before a compressible Neo-Hooke material model is applied using $\mu = 865.3846$ and $\lambda = 1298.1$. A Dirichlet boundary condition has been applied to the left side, whereas a Neumann boundary condition has been applied to the right side of the membrane. In particular, a surface load acts with a constant load $P = [0,\ -200,\ 500]$ on the specified surface. Fig. 4.11 displays the deformed configuration, whereas Fig. 4.12 shows the distribution of the norm of the Cauchy stresses of the left sub-domain. For comparison we have modified the KTS method (see Temizer et al. [68]*) using Lagrange multipliers instead of a penalty method and applied it to the problem at hand. The stress distribution of the left sub-domain is displayed in Fig. 4.13. Note that we have applied the Lagrange multipliers on the interface of the right sub-domain, such that we used 3 × 16 multipliers for the KTS as well as for the mortar method.

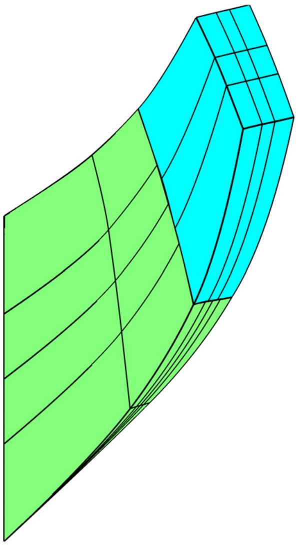

Figure 4.11: Deformed configuration of the membrane.

---

*The KTS method relies on an pointwise enforcement of the constraints.

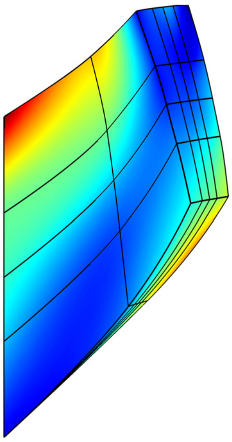

Figure 4.12: Deformed configuration and stress distribution of the left subdomain (mortar method).

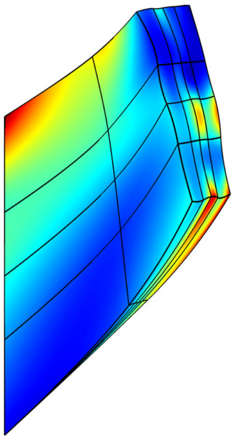

Figure 4.13: Deformed configuration and stress distribution of the left subdomain (KTS method).

5 Contact

The objective of this section is to develop time integration schemes for node-to-surface (NTS) as well as Mortar based contact methods. The concept of the NTS approach, originally introduced by Hallquist [30], has been subject of various papers published within the last thirty years. A survey of previous developments can be found in the textbooks written by Laursen [52] and Wriggers [77]. In contrast to that, the far more complex Mortar constraints (cf. Puso et al. [63], Hüeber & Wohlmuth [43], Popp et al. [61], Gitterle et al. [24], Tur et al. [72] and the references therein) are currently subject of intensive research. Energy conserving time integration schemes for unilateral contact problems have been developed previously within the framework of the NTS method (e.g. Laursen & Chawla [53], Armero & Petöcz [3], Laursen & Love [54] and Haikal & Hjelmstad [29]). The extension of the notion of a discrete gradient to contact problems has been developed by Hauret & Le Tallec [31] and Betsch & Hesch [11].

5.1 NTS method

For the large deformation problem under consideration we define the sets $\mathcal{B}^{(i)} \subset \mathbb{R}^3$, $i \in \{1, \ldots, k\}$, representing the reference configuration of the involved bodies. For convenience we restrict ourselves to a two body contact problem $i \in \{1, 2\}$ excluding self contact (see Benson & Hallquist [7] and Yang & Laursen [80]) without prejudice to the generality of the further development. The potential areas of contact are defined on the surfaces $\partial\mathcal{B}_0^{(i)}$, which are subdivided into the Dirichlet boundary $\partial\mathcal{B}_0^{(i),u}$ with prescribed displacements, the Neumann boundary $\partial\mathcal{B}_0^{(i),\sigma}$ with prescribed tractions and $\partial\mathcal{B}_0^{(i),c}$, the potential contact area. It is required that the different boundaries satisfy

$$\partial\mathcal{B}_0^{(i),u} \cup \partial\mathcal{B}_0^{(i),\sigma} \cup \partial\mathcal{B}_0^{(i),c} = \partial\mathcal{B}_0^{(i)} \tag{5.1}$$

and

$$\partial\mathcal{B}_0^{(i),u} \cap \partial\mathcal{B}_0^{(i),\sigma} \cap \partial\mathcal{B}_0^{(i),c} = \emptyset \tag{5.2}$$

The contribution of body (i) to the balance of linear momentum for a large deformation contact problem can be expressed as follows

$$\begin{aligned} &\langle \rho_R \ddot{\boldsymbol{\varphi}}^{\mathrm{h}}, \delta\boldsymbol{\varphi}^{\mathrm{h}} \rangle_{\mathcal{B}_0^{\mathrm{h},(i)}} + \langle \boldsymbol{P}^{\mathrm{h}}, \nabla_{\boldsymbol{X}} \left(\delta\boldsymbol{\varphi}^{\mathrm{h}}\right) \rangle_{\mathcal{B}_0^{\mathrm{h},(i)}} = \\ &\qquad \langle \rho_R \bar{\boldsymbol{B}}^{\mathrm{h}}, \delta\boldsymbol{\varphi}^{\mathrm{h}} \rangle_{\mathcal{B}_0^{\mathrm{h},(i)}} + \langle \bar{\boldsymbol{T}}^{\mathrm{h}}, \delta\boldsymbol{\varphi}^{\mathrm{h}} \rangle_{\partial\mathcal{B}_0^{\mathrm{h},(i),\sigma}} + \langle \boldsymbol{t}^{\mathrm{h}}, \delta\boldsymbol{\varphi}^{\mathrm{h}} \rangle_{\partial\mathcal{B}_0^{\mathrm{h},(i),c}} \end{aligned} \tag{5.3}$$

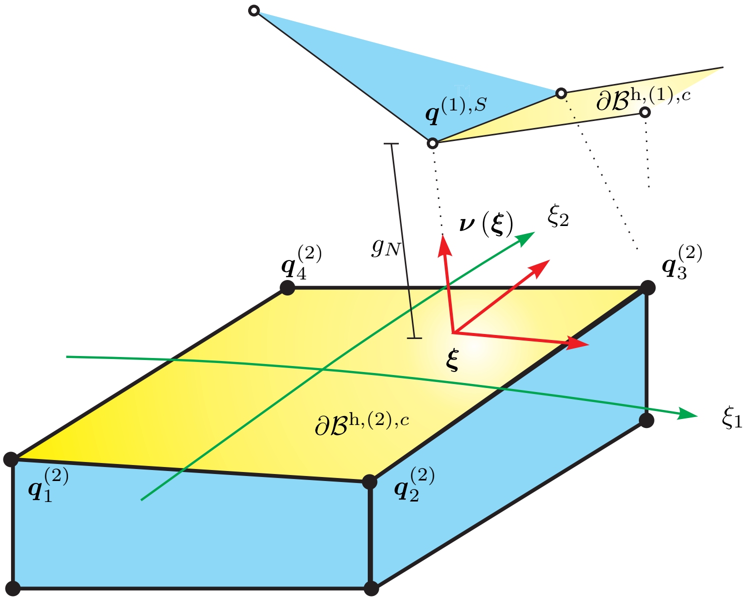

Figure 5.1: Initial configuration of the representative NTS element: Closest point projection of the node $\boldsymbol{q}^{(1),S}$ onto the surface $\partial\mathcal{B}^{\mathrm{h},(2),c}$.

Considering the balance of linear momentum across the current configuration of the contact area, we obtain

$$\langle \boldsymbol{t}^{\mathrm{h}}, (\delta\boldsymbol{\varphi}^{\mathrm{h},(1)} - \delta\boldsymbol{\varphi}^{\mathrm{h},(2)})\rangle_{\partial\mathcal{B}^{\mathrm{h},(1),c}} = 0 \tag{5.4}$$

In the case of frictionless contact only the normal component of $\boldsymbol{t}^{\mathrm{h},(1)}$, defined by $\boldsymbol{t}^{\mathrm{h},(1)} \cdot \boldsymbol{\nu}^{(1)} =: \lambda^{\mathrm{h}}$ is nonzero, where $\boldsymbol{\nu}^{(1)}$ denotes the outward unit normal vector on surface (1). Accordingly, (5.4) yields

$$\langle \lambda^{\mathrm{h}}\boldsymbol{\nu}, (\delta\boldsymbol{\varphi}^{\mathrm{h},(1)} - \delta\boldsymbol{\varphi}^{\mathrm{h},(2)})\rangle_{\partial\mathcal{B}^{\mathrm{h},(1),c}} = 0 \tag{5.5}$$

Next, we have to discretize the virtual work associated with the contact interface. First, we introduce the NTS method. This method constrains the system in such a way that the gap g_N remains greater or equal zero. The gap rests on the closest point projection of a node $\boldsymbol{q}^{(1),S}$, which is part of the slave side $\partial\mathcal{B}^{\mathrm{h},(1),c}$, onto the opposing master side $\partial\mathcal{B}^{\mathrm{h},(2),c}$ and measures the distance between $\boldsymbol{q}^{(1),S}$ and the projected point on $\partial\mathcal{B}^{\mathrm{h},(1),c}$. Thus, a typical constraint function depends on the set of relevant vectors

$$\eta_S = \{\bar{\boldsymbol{q}}_I^S\} = \{\boldsymbol{q}^{(1),S}, \boldsymbol{q}_1^{(2)}, \ldots, \boldsymbol{q}_4^{(2)}\} \tag{5.6}$$

The closest point projection yields

$$\boldsymbol{\varphi}^{\mathrm{h},(2)}(\boldsymbol{\xi}, t) = \sum_{C=1}^{4} \hat{N}^C(\boldsymbol{\xi})\boldsymbol{q}_c^{(2)}(t) \tag{5.7}$$

where the local convective coordinates $\boldsymbol{\xi} = (\xi_1, \xi_2)$ identify the projected point on $\partial\mathcal{B}^{\mathrm{h},(2),c}$ (see Wriggers et al. [78], Simo & Laursen [51] and Konyukhov & Schweizerhof [47, 48]).

Since we use isoparametric tri-linear solid elements, $\hat{N}^C(\boldsymbol{\xi})$ are standard bi-linear local shape functions.

The framework described in the following allows us to accomplish two major goals: The determination of the configuration dependent convective coordinates is simplified as does the construction of an energy-momentum scheme based on the notion of a discrete derivative in the sense of Gonzalez [27].

A measurement of the aforementioned distance between both surfaces can be established via the gap function $g_N^S(\boldsymbol{X},t)$, given by

$$g_N^S(\boldsymbol{X},t) = \left(\boldsymbol{q}^{(1),S} - \sum_{C=1}^{4} \hat{N}^C(\boldsymbol{\xi})\boldsymbol{q}_C^{(2)}\right) \cdot \boldsymbol{\nu}(\boldsymbol{\xi}) \tag{5.8}$$

Note, that the unit normal vector $\boldsymbol{\nu}(\boldsymbol{\xi})$ also depends on the convective coordinates. Now the impenetrability condition can be stated as

$$\Phi^S(\bar{\boldsymbol{q}}_I^S) = g_N^S(\boldsymbol{X},t) \leq 0 \tag{5.9}$$

The corresponding nodal force vector $\boldsymbol{f}^{\mathrm{c},A} = \boldsymbol{f}^{(1),\mathrm{c},A} + \boldsymbol{f}^{(2),\mathrm{c},A}$ can be written as

$$\delta\boldsymbol{q}_A \cdot \boldsymbol{f}^{\mathrm{c},A} = \delta\bar{\boldsymbol{q}}_A^S \cdot \lambda_S \nabla_{\boldsymbol{q}_\mathrm{A}} \Phi^S \tag{5.10}$$

where λ_S denotes the Lagrange multiplier and $\lambda_S\boldsymbol{\nu}(\boldsymbol{\xi})$ the corresponding traction in normal direction. Since we assume no adhesion, the tractions have to be positive, i.e. $\lambda_S \geq 0$. In combination with

$$\lambda_S(\boldsymbol{X},t) g_N^S(\boldsymbol{X},t) = 0 \tag{5.11}$$

we get the classical Kuhn-Tucker complementary conditions. These conditions separate the set of potential contact nodes $\bar{\omega}$ into an active set $\mathcal{A}$ and an inactive set $\mathcal{I}$, such that $\bar{\omega} = \mathcal{A} \cup \mathcal{I}$ and $\mathcal{A} \cap \mathcal{I} = \emptyset$. The discrete multiplier space can now be defined on the slave side as

$$\mathcal{C}^\mathrm{h} = \{\lambda^\mathrm{h} \in C^{-1}(\partial\mathcal{B}^{\mathrm{h},(1)}) |\, \lambda_S = 0,\ \forall\, \lambda_S \in \mathcal{I}\} \tag{5.12}$$

with

$$\lambda^\mathrm{h} = \sum_{A\in\bar{\omega}} N^A(\boldsymbol{X}_S)\lambda_A = \delta_S^A \lambda_A = \lambda_S \tag{5.13}$$

where δ_S^A denotes the classical Kronecker delta and $\boldsymbol{X}_S^{(1)}$ a material point on $\partial\mathcal{B}_0^{\mathrm{h},(1)}$ which coincides with the node S on $\partial\mathcal{B}^{\mathrm{h},(1)}$. For our approach we extend the already adapted coordinate augmentation technique. This technique leads to additional coordinates that can be appended to the set η_S of original coordinates

$$\eta_S^{\mathrm{aug}} = \eta_S \cup \{\boldsymbol{d}^S\} \cup \{\boldsymbol{f}^S\} \tag{5.14}$$

pertaining to the representative NTS element. In the present context the additional coordinates $\boldsymbol{d}^S \in \mathbb{R}^3$ play the role of the unit normal vector $\boldsymbol{\nu}$, whereas $\boldsymbol{f}^S \in \mathbb{R}^2$ stands for the convective coordinates $\boldsymbol{\xi}$. To link the new coordinates to the original ones the following five additional constraint functions are introduced

$$\boldsymbol{\Phi}^{\text{aug},S}(\bar{\boldsymbol{q}}^S, \boldsymbol{d}^S, \boldsymbol{f}^S) = \begin{bmatrix} \boldsymbol{d}^S \cdot \boldsymbol{a}_1(\boldsymbol{f}^S) \\ \boldsymbol{d}^S \cdot \boldsymbol{a}_2(\boldsymbol{f}^S) \\ \frac{1}{2}(\boldsymbol{d}^S \cdot \boldsymbol{d}^S - 1) \\ \left(\boldsymbol{q}^{(1),S} - \sum\limits_{C=1}^{4} \hat{N}^C(\boldsymbol{f}^S)\boldsymbol{q}_C^{(2)}\right) \cdot \boldsymbol{a}_1(\boldsymbol{f}^S) \\ \left(\boldsymbol{q}^{(1),S} - \sum\limits_{C=1}^{4} \hat{N}^C(\boldsymbol{f}^S)\boldsymbol{q}_C^{(2)}\right) \cdot \boldsymbol{a}_2(\boldsymbol{f}^S) \end{bmatrix} \tag{5.15}$$

The modified NTS constraints can now be expressed exclusively in terms of the set η_S^{aug}

$$\bar{\Phi}^S(\bar{\boldsymbol{q}}^S, \boldsymbol{d}^S, \boldsymbol{f}^S) = \left(\boldsymbol{q}^{(1),S} - \sum_{C=1}^{4} \hat{N}^C(\boldsymbol{f}^S)\boldsymbol{q}_C^{(2)}\right) \cdot \boldsymbol{d}^S \tag{5.16}$$

To simplify later developments, we collect the constraints (5.16) as well as the augmented constraints (5.15) and arrange them in a vector of constraint functions

$$\boldsymbol{g}^S(\bar{\boldsymbol{q}}^S, \boldsymbol{d}^S, \boldsymbol{f}^S) = \begin{bmatrix} \bar{\Phi}^S(\bar{\boldsymbol{q}}^S, \boldsymbol{d}^S, \boldsymbol{f}^S) \\ \boldsymbol{\Phi}^{\text{aug},S}(\bar{\boldsymbol{q}}^S, \boldsymbol{d}^S, \boldsymbol{f}^S) \end{bmatrix} \tag{5.17}$$

Frame-indifference. As before, rigid motions of the form

$$\bar{\boldsymbol{q}}_I^{S,\sharp} = \boldsymbol{c} + \boldsymbol{Q}\bar{\boldsymbol{q}}_I^S \tag{5.18}$$

are considered. It is easy to verify the following property

$$\begin{aligned} \boldsymbol{g}^S(\bar{\boldsymbol{q}}^{S,\sharp}, \boldsymbol{d}^S, \boldsymbol{f}^S) &= \begin{bmatrix} \left(\boldsymbol{q}^{(1),S} - \sum\limits_{C=1}^{4} \hat{N}^C \boldsymbol{q}_c^{(2)}\right) \cdot \boldsymbol{Q}^T\boldsymbol{d}^S \\ \boldsymbol{a}_1(\boldsymbol{f}_S) \cdot \boldsymbol{Q}^T\boldsymbol{d}_S \\ \boldsymbol{a}_2(\boldsymbol{f}_S) \cdot \boldsymbol{Q}^T\boldsymbol{d}_S \\ \frac{1}{2}((\boldsymbol{Q}^T\boldsymbol{d}_S) \cdot (\boldsymbol{Q}^T\boldsymbol{d}_S) - 1) \\ \left(\boldsymbol{q}^{(1),S} - \sum\limits_{C=1}^{4} \hat{N}^C(\boldsymbol{f}^S)\boldsymbol{q}_c^{(2)}\right) \cdot \boldsymbol{Q}^T\boldsymbol{Q}\boldsymbol{a}_1(\boldsymbol{f}_S) \\ \left(\boldsymbol{q}^{(1),S} - \sum\limits_{C=1}^{4} \hat{N}^C(\boldsymbol{f}^S)\boldsymbol{q}_c^{(2)}\right) \cdot \boldsymbol{Q}^T\boldsymbol{Q}\boldsymbol{a}_2(\boldsymbol{f}_S) \end{bmatrix} \\ &= \boldsymbol{g}^S(\bar{\boldsymbol{q}}^S, \boldsymbol{Q}^T\boldsymbol{d}^S, \boldsymbol{f}^S) \end{aligned} \tag{5.19}$$

where the characteristics of the shape functions ($\sum\limits_A N^A(\boldsymbol{X}) = 1$) have been used.

To show translational invariance we substitute $\boldsymbol{c} = \epsilon\boldsymbol{\zeta}$, $\boldsymbol{\zeta} \in \mathbb{R}^3$ and $\boldsymbol{Q} = \boldsymbol{I}$, where $\boldsymbol{I}$ denotes the identity matrix. Equation (5.19) implies, that

$$\boldsymbol{g}^S(\bar{\boldsymbol{q}}^S + \epsilon\boldsymbol{\zeta}, \boldsymbol{d}^S, \boldsymbol{f}^S) = \boldsymbol{g}^S(\bar{\boldsymbol{q}}^S, \boldsymbol{d}^S, \boldsymbol{f}^S) \tag{5.20}$$

holds for arbitrary $\epsilon \in \mathbb{R}$. Consequently,

$$\boldsymbol{0} = \left.\frac{\mathrm{d}}{\mathrm{d}\epsilon}\right|_{\epsilon=0} \boldsymbol{g}^S(\bar{\boldsymbol{q}}^S + \epsilon\boldsymbol{\zeta}, \boldsymbol{d}^S, \boldsymbol{f}^S) = \sum_I \left(\partial_{\bar{\boldsymbol{q}}_I^S} \boldsymbol{g}^S\right) \cdot \boldsymbol{\zeta} \tag{5.21}$$

which proves translational invariance. Substituting $\boldsymbol{c} = \boldsymbol{0}$ and $\boldsymbol{Q} = \exp(\epsilon\hat{\boldsymbol{\zeta}})$ into (5.19) yields

$$\boldsymbol{g}^S(\exp(\epsilon\hat{\boldsymbol{\zeta}})\bar{\boldsymbol{q}}^S, \boldsymbol{d}^S, \boldsymbol{f}^S) - \boldsymbol{g}^S(\bar{\boldsymbol{q}}^S, \exp(-\epsilon\hat{\boldsymbol{\zeta}})\boldsymbol{d}^S, \boldsymbol{f}^S) = \boldsymbol{0} \tag{5.22}$$

Accordingly, we end up with

$$\begin{aligned} \boldsymbol{0} = \left.\frac{\mathrm{d}}{\mathrm{d}\epsilon}\right|_{\epsilon=0} [\boldsymbol{g}^S(\exp(\epsilon\hat{\boldsymbol{\zeta}})\bar{\boldsymbol{q}}^S, \boldsymbol{d}^S, \boldsymbol{f}^S) - \boldsymbol{g}^S(\bar{\boldsymbol{q}}^S, \exp(-\epsilon\hat{\boldsymbol{\zeta}})\boldsymbol{d}^S, \boldsymbol{f}^S) &= \boldsymbol{0} \\ \sum_A \left(\partial_{\bar{\boldsymbol{q}}_A^S} \boldsymbol{g}^S\right) \cdot \hat{\boldsymbol{\zeta}}\bar{\boldsymbol{q}}_A^S + \left(\partial_{\boldsymbol{d}^S} \boldsymbol{g}^S\right) \cdot \hat{\boldsymbol{\zeta}}\boldsymbol{d}^S &= \boldsymbol{0} \\ \sum_A \left(\partial_{\bar{\boldsymbol{q}}_A^S} \boldsymbol{g}^S\right) \cdot (\boldsymbol{\zeta} \times \bar{\boldsymbol{q}}_A^S) + \left(\partial_{\boldsymbol{d}^S} \boldsymbol{g}^S\right) \cdot (\boldsymbol{\zeta} \times \boldsymbol{d}^S) &= \boldsymbol{0} \end{aligned} \tag{5.23}$$

for any vector $\boldsymbol{\zeta} \in \mathbb{R}^3$.

Translational and rotational invariance properties have to be in agreement with Cauchy's representation theorem, i.e. it has to be possible to rewrite the system in terms of appropriate invariants. In particular, we define three sets of invariants as follows[*]

$$\begin{aligned} \mathbb{S}(\eta_s^{\text{aug}}) &= \{(\bar{\boldsymbol{q}}_I^S - \boldsymbol{q}_1^{(2)}) \cdot (\bar{\boldsymbol{q}}_J^S - \boldsymbol{q}_1^{(2)}),\ 1 \leq I \leq J \leq 5\} \\ \tilde{\mathbb{S}}(\eta_s^{\text{aug}}) &= \{(\bar{\boldsymbol{q}}_I^S - \boldsymbol{q}_1^{(2)}) \cdot \boldsymbol{d}^S,\ I = 1, \ldots, 5\} \\ \bar{\mathbb{S}}(\eta_s^{\text{aug}}) &= \{\boldsymbol{d}^S \cdot \boldsymbol{d}^S\} \end{aligned} \tag{5.24}$$

and establish a fourth set composed of the augmented coordinates $\boldsymbol{f}^S$

$$\hat{\mathbb{S}}(\eta_s^{\text{aug}}) = \{f_\alpha^S,\ \alpha = 1, 2\} \tag{5.25}$$

---

[*] The invariance property of the last two sets can only be established, if the augmented constraints (5.19) are fulfilled.

Next, we rewrite the modified NTS constraints in terms of the above given invariants as follows

$$\begin{aligned}\bar{\Phi}^S(\bar{\boldsymbol{q}}^S, \boldsymbol{d}_S, \boldsymbol{f}_S) &= \left(\boldsymbol{q}^{(1),S} - \boldsymbol{q}_1^{(2)} - \sum_J N^J(\boldsymbol{f}^S)\boldsymbol{q}_J^{(2)} + \sum_J N^J(\boldsymbol{f}^S)\boldsymbol{q}_1^{(2)}\right) \cdot \boldsymbol{d}^S \\ &= (\boldsymbol{q}^{(1),S} - \boldsymbol{q}_1^{(2)}) \cdot \boldsymbol{d}^S - \sum_{J=2}^{4} N^J(\boldsymbol{f}^S)(\boldsymbol{q}_J^{(2)} - \boldsymbol{q}_1^{(2)}) \cdot \boldsymbol{d}^S\end{aligned} \tag{5.26}$$

Then we introduce a vector of invariants

$$\bar{\boldsymbol{\pi}}(\bar{\boldsymbol{q}}^S, \boldsymbol{d}^S, \boldsymbol{f}^S) = \begin{bmatrix}\pi_1\\ \pi_2\\ \pi_3\\ \pi_4\\ \pi_5\\ \pi_6\end{bmatrix} = \begin{bmatrix}(\boldsymbol{q}^{(1),S} - \boldsymbol{q}_1^{(2)}) \cdot \boldsymbol{d}^S\\ (\boldsymbol{q}_2^{(2)} - \boldsymbol{q}_1^{(2)}) \cdot \boldsymbol{d}^S\\ (\boldsymbol{q}_3^{(2)} - \boldsymbol{q}_1^{(2)}) \cdot \boldsymbol{d}^S\\ (\boldsymbol{q}_4^{(2)} - \boldsymbol{q}_1^{(2)}) \cdot \boldsymbol{d}^S\\ f_1^S\\ f_2^S\end{bmatrix} \tag{5.27}$$

and rewrite the modified NTS constraints (5.16) in the form

$$\tilde{\Phi}^S(\bar{\boldsymbol{\pi}}(\bar{\boldsymbol{q}}^S, \boldsymbol{d}^S, \boldsymbol{f}^S)) = \pi_1 - \sum_{I=2}^{4} N_I(\pi_5, \pi_6)\pi_I \tag{5.28}$$

Note that the augmented coordinates f_1^S and f_2^S play the role of linear invariants in (5.27). They do not depend explicitly on the configuration and the constraints $(5.15)_{4,5}$ used to calculate them are invariant as shown in (5.19). Following the same ideas, the additional constraints (5.15) can be written as

$$\tilde{\boldsymbol{\Phi}}^{\text{aug}}(\boldsymbol{\pi}(\bar{\boldsymbol{q}}^S, \boldsymbol{d}^S, \boldsymbol{f}^S)) = \begin{bmatrix}\sum\limits_{I=2}^{4} N_{I,\pi_5}(\pi_5, \pi_6)\pi_I\\ \sum\limits_{I=2}^{4} N_{I,\pi_6}(\pi_5, \pi_6)\pi_I\\ \frac{1}{2}(\pi_7 - 1)\\ \sum\limits_{I=2}^{4} N_{I,\pi_5}(\pi_5, \pi_6)\pi_{I+6} - K_1\\ \sum\limits_{I=2}^{4} N_{I,\pi_6}(\pi_5, \pi_6)\pi_{I+6} - K_2\end{bmatrix} \tag{5.29}$$

with

$$\begin{aligned}K_1 &= \sum_{I=2}^{4}\sum_{J=2}^{4} N_{I,\pi_5}(\pi_5, \pi_6)N_J(\pi_5, \pi_6)(\boldsymbol{q}_I^{(2)} - \boldsymbol{q}_1^{(2)}) \cdot (\boldsymbol{q}_J^{(2)} - \boldsymbol{q}_1^{(2)})\\ K_2 &= \sum_{I=2}^{4}\sum_{J=2}^{4} N_{I,\pi_6}(\pi_5, \pi_6)N_J(\pi_5, \pi_6)(\boldsymbol{q}_I^{(2)} - \boldsymbol{q}_1^{(2)}) \cdot (\boldsymbol{q}_J^{(2)} - \boldsymbol{q}_1^{(2)})\end{aligned} \tag{5.30}$$

This gives rise to the definition of the extended vector of invariants

$$\boldsymbol{\pi}(\bar{\boldsymbol{q}}^S, \boldsymbol{d}^S, \boldsymbol{f}^S) = \begin{bmatrix} \bar{\boldsymbol{\pi}} \\ \pi_7 \\ \pi_8 \\ \pi_9 \\ \pi_{10} \\ \pi_{11} \\ \pi_{12} \\ \pi_{13} \\ \pi_{14} \\ \pi_{15} \\ \pi_{16} \end{bmatrix} = \begin{bmatrix} \bar{\boldsymbol{\pi}} \\ \boldsymbol{d}^S \cdot \boldsymbol{d}^S \\ (\boldsymbol{q}_2^{(2)} - \boldsymbol{q}_1^{(2)}) \cdot (\boldsymbol{q}_S^{(1)} - \boldsymbol{q}_1^{(2)}) \\ (\boldsymbol{q}_3^{(2)} - \boldsymbol{q}_1^{(2)}) \cdot (\boldsymbol{q}_S^{(1)} - \boldsymbol{q}_1^{(2)}) \\ (\boldsymbol{q}_4^{(2)} - \boldsymbol{q}_1^{(2)}) \cdot (\boldsymbol{q}_S^{(1)} - \boldsymbol{q}_1^{(2)}) \\ (\boldsymbol{q}_2^{(2)} - \boldsymbol{q}_1^{(2)}) \cdot (\boldsymbol{q}_2^{(2)} - \boldsymbol{q}_1^{(2)}) \\ (\boldsymbol{q}_2^{(2)} - \boldsymbol{q}_1^{(2)}) \cdot (\boldsymbol{q}_3^{(2)} - \boldsymbol{q}_1^{(2)}) \\ (\boldsymbol{q}_2^{(2)} - \boldsymbol{q}_1^{(2)}) \cdot (\boldsymbol{q}_4^{(2)} - \boldsymbol{q}_1^{(2)}) \\ (\boldsymbol{q}_3^{(2)} - \boldsymbol{q}_1^{(2)}) \cdot (\boldsymbol{q}_3^{(2)} - \boldsymbol{q}_1^{(2)}) \\ (\boldsymbol{q}_3^{(2)} - \boldsymbol{q}_1^{(2)}) \cdot (\boldsymbol{q}_4^{(2)} - \boldsymbol{q}_1^{(2)}) \\ (\boldsymbol{q}_4^{(2)} - \boldsymbol{q}_1^{(2)}) \cdot (\boldsymbol{q}_4^{(2)} - \boldsymbol{q}_1^{(2)}) \end{bmatrix} \tag{5.31}$$

Finally, we can write

$$\tilde{\boldsymbol{g}}^S(\boldsymbol{\pi}(\bar{\boldsymbol{q}}^S, \boldsymbol{d}^S, \boldsymbol{f}^S)) = \boldsymbol{g}^S(\bar{\boldsymbol{q}}^S, \boldsymbol{d}^S, \boldsymbol{f}^S) \tag{5.32}$$

Of course, the fundamental properties defined previously are retained by the reformulated constraints. With regard to (5.21) we can state that

$$\boldsymbol{0} = \left.\frac{\mathrm{d}}{\mathrm{d}\epsilon}\right|_{\epsilon=0} \tilde{\boldsymbol{g}}^S(\boldsymbol{\pi}(\bar{\boldsymbol{q}}^S + \epsilon\boldsymbol{\zeta}, \boldsymbol{d}^S, \boldsymbol{f}^S)) = \partial_{\boldsymbol{\pi}}\tilde{\boldsymbol{g}}^S \cdot \sum_A \left(\partial_{\bar{\boldsymbol{q}}_A^S}\boldsymbol{\pi}\right) \cdot \boldsymbol{\zeta} \tag{5.33}$$

which is true a priori due to the construction of the vector of invariants. For the rotational part in (5.23) follows with regard to property (5.19) and (4.28)

$$\begin{aligned} \boldsymbol{0} = \left.\frac{\mathrm{d}}{\mathrm{d}\epsilon}\right|_{\epsilon=0} [\tilde{\boldsymbol{g}}^S(\boldsymbol{\pi}(\exp(\hat{\boldsymbol{\zeta}})\bar{\boldsymbol{q}}^S, \boldsymbol{d}^S, \boldsymbol{f}^S)) - \tilde{\boldsymbol{g}}^S(\boldsymbol{\pi}(\bar{\boldsymbol{q}}^S, \exp(-\epsilon\hat{\boldsymbol{\zeta}})\boldsymbol{d}^S, \boldsymbol{f}^S)) &= \boldsymbol{0} \\ \partial_{\boldsymbol{\pi}}\tilde{\boldsymbol{g}}^S \cdot \left[\sum_A (\partial_{\bar{\boldsymbol{q}}_A^S}\boldsymbol{\pi}) \cdot \hat{\boldsymbol{\zeta}}\bar{\boldsymbol{q}}_A^S + (\partial_{\boldsymbol{d}^S}\boldsymbol{\pi}) \cdot \hat{\boldsymbol{\zeta}}\boldsymbol{d}^S\right] &= \boldsymbol{0} \\ \partial_{\boldsymbol{\pi}}\tilde{\boldsymbol{g}}^S \cdot \left[\sum_A (\partial_{\bar{\boldsymbol{q}}_A^S}\boldsymbol{\pi}) \cdot (\boldsymbol{\zeta} \times \bar{\boldsymbol{q}}_A^S) + (\partial_{\boldsymbol{d}^S}\boldsymbol{\pi}) \cdot (\boldsymbol{\zeta} \times \boldsymbol{d}^S)\right] &= \boldsymbol{0} \end{aligned} \tag{5.34}$$

which is also true a priori due to the construction of the vector of invariants.

Temporal discretization. Next, we want to perform an energy and momentum conserving time discretization of the semidiscrete system at hand. This approach is in contrast to the established energy-momentum schemes developed for unilateral contact constraints. In Laursen & Chawla [53] (and similarly in Armero & Petöcz [3]) an algorithmic gap rate has been defined in exchange of the original constraints. This ensures conservation of energy as well as conservation of the momentum maps by sacrificing the exact fulfillment of the constraints. In Laursen & Love [54] a velocity update procedure has been proposed to ensure the conservation properties. In contrast to the algorithmic gap rate approach as well as the method proposed in this paper the velocity update algorithm can display only first-order accuracy in time (see also Simo et al. [67]). Within our approach, the fully discretized equations of motion are given by

$$\begin{aligned}
\boldsymbol{q}_{n+1} - \boldsymbol{q}_n =& \Delta t \boldsymbol{v}_{n+\frac{1}{2}} \\
\boldsymbol{M}\left(\boldsymbol{v}_{n+1} - \boldsymbol{v}_n\right) =& -\Delta t \overline{\nabla} E(\boldsymbol{q}_n, \boldsymbol{q}_{n+1}) \\
& - \Delta t \sum_{S \in \bar{\omega}} (D_1 \boldsymbol{\pi}(\bar{\boldsymbol{q}}^S_{n+\frac{1}{2}}, \boldsymbol{d}^S_{n+\frac{1}{2}}, \boldsymbol{f}^S_{n+\frac{1}{2}}))^T \overline{\overline{\overline{\nabla}}}_\pi \, \tilde{\boldsymbol{g}}^S(\boldsymbol{\pi}_n, \boldsymbol{\pi}_{n+1}) \cdot \boldsymbol{\lambda}_S \\
\boldsymbol{0} =& \sum_{S \in \bar{\omega}} (D_2 \boldsymbol{\pi}(\bar{\boldsymbol{q}}^S_{n+\frac{1}{2}}, \boldsymbol{d}^S_{n+\frac{1}{2}}, \boldsymbol{f}^S_{n+\frac{1}{2}}))^T \overline{\overline{\overline{\nabla}}}_\pi \, \tilde{\boldsymbol{g}}^S(\boldsymbol{\pi}_n, \boldsymbol{\pi}_{n+1}) \cdot \boldsymbol{\lambda}_S \\
\boldsymbol{0} =& \sum_{S \in \bar{\omega}} (D_3 \boldsymbol{\pi}(\bar{\boldsymbol{q}}^S_{n+\frac{1}{2}}, \boldsymbol{d}^S_{n+\frac{1}{2}}, \boldsymbol{f}^S_{n+\frac{1}{2}}))^T \overline{\overline{\overline{\nabla}}}_\pi \, \tilde{\boldsymbol{g}}^S(\boldsymbol{\pi}_n, \boldsymbol{\pi}_{n+1}) \cdot \boldsymbol{\lambda}_S \\
\boldsymbol{0} =& \begin{bmatrix} \tilde{\boldsymbol{g}}^{S=1}(\boldsymbol{\pi}(\bar{\boldsymbol{q}}^S_{n+1}, \boldsymbol{d}^S_{n+1}, \boldsymbol{f}^S_{n+1})) \\ \vdots \\ \tilde{\boldsymbol{g}}^{S=n_{\text{surf}}}(\boldsymbol{\pi}(\bar{\boldsymbol{q}}^S_{n+1}, \boldsymbol{d}^S_{n+1}, \boldsymbol{f}^S_{n+1})) \end{bmatrix}
\end{aligned} \tag{5.35}$$

Here, we use the abbreviation $\boldsymbol{\lambda}_S := \boldsymbol{\lambda}_{S,n,n+1}$ to simplify the notation. Furthermore, the discrete gradient of the internal energy (in absence of additional external energy) $\overline{\nabla} V(\boldsymbol{q}_n, \boldsymbol{q}_{n+1})$ facilitates conservation of energy and both momentum maps by design. We refer to Betsch & Steinmann [13] and the references therein for further details of energy-momentum conserving schemes in the context of non-linear elastodynamics. Additionally, $\overline{\overline{\overline{\nabla}}}_\pi \, \tilde{\boldsymbol{g}}^S(\boldsymbol{\pi}_n, \boldsymbol{\pi}_{n+1})$ denotes a discrete gradient of the constraint functions, defined as (see Gonzalez [26])

$$\overline{\overline{\overline{\nabla}}}_\pi \, \tilde{\boldsymbol{g}}^S(\boldsymbol{\pi}_n, \boldsymbol{\pi}_{n+1}) = \nabla_\pi \, \tilde{\boldsymbol{g}}^S(\boldsymbol{\pi}_{n+\frac{1}{2}}) + \frac{\tilde{\boldsymbol{g}}^S(\boldsymbol{\pi}_{n+1}) - \tilde{\boldsymbol{g}}^S(\boldsymbol{\pi}_n) - \nabla_\pi \, \tilde{\boldsymbol{g}}^S(\boldsymbol{\pi}_{n+\frac{1}{2}}) \cdot \Delta\boldsymbol{\pi}}{\|\Delta\boldsymbol{\pi}\|^2} \Delta\boldsymbol{\pi} \tag{5.36}$$

In this connection, the abbreviations $\Delta\boldsymbol{\pi} = \boldsymbol{\pi}_{n+1} - \boldsymbol{\pi}_n$, $\boldsymbol{\pi}_n = \boldsymbol{\pi}(\bar{\boldsymbol{q}}^S_{I,n}, \boldsymbol{d}^S_n, \boldsymbol{f}^S_n)$ and $\boldsymbol{\pi}_{n+1} = \boldsymbol{\pi}(\bar{\boldsymbol{q}}^S_{I,n+1}, \boldsymbol{d}^S_{n+1}, \boldsymbol{f}^S_{n+1})$ have been employed.

Conservation properties. We omit the verification of conservation of linear momentum due to the translational invariance of the constraints and demonstrate exemplarily the verification of conservation of angular momentum. Since the angular momentum map $\boldsymbol{J}(\boldsymbol{q}, \boldsymbol{v})$ is a quadratic function of $(\boldsymbol{q}, \boldsymbol{v})$ we can state that

$$\begin{aligned}
&\boldsymbol{J}_{n+1} - \boldsymbol{J}_n \\
&= \left(D_1 \boldsymbol{J}\left(\boldsymbol{q}_{n+\frac{1}{2}}, \boldsymbol{v}_{n+\frac{1}{2}}\right)\right)(\boldsymbol{q}_{n+1} - \boldsymbol{q}_n) + \left(D_2 \boldsymbol{J}\left(\boldsymbol{q}_{n+\frac{1}{2}}, \boldsymbol{v}_{n+\frac{1}{2}}\right)\right)(\boldsymbol{v}_{n+1} - \boldsymbol{v}_n) \\
&= -\sum_{A,B} M^{AB} \boldsymbol{v}_{B_{n+\frac{1}{2}}} \times \left(\boldsymbol{q}_{A_{n+1}} - \boldsymbol{q}_{A_n}\right) + \sum_{A,B} M^{AB} \boldsymbol{q}_{B_{n+\frac{1}{2}}} \times \left(\boldsymbol{v}_{A_{n+1}} - \boldsymbol{v}_{A_n}\right)
\end{aligned} \tag{5.37}$$

Scalar multiplication of the last equation with an arbitrary vector $\boldsymbol{\zeta}$ and subsequently substituting from $(5.35)_1$ and $(5.35)_2$ yields

$$\begin{aligned}
&\boldsymbol{\zeta}\cdot(\boldsymbol{J}_{n+1}-\boldsymbol{J}_n)=\\
&\quad-\Delta t\boldsymbol{\zeta}\cdot\sum_B \boldsymbol{q}_{B_{n+\frac{1}{2}}}\times\left(\sum_{S\in\bar{\omega}}(\partial_{\boldsymbol{q}_B}\boldsymbol{\pi}(\bar{\boldsymbol{q}}^S_{n+\frac{1}{2}},\boldsymbol{d}^S_{n+\frac{1}{2}},\boldsymbol{f}^S_{n+\frac{1}{2}}))^T\overline{\overline{\nabla}}_{\pi}\,\tilde{\boldsymbol{g}}^S(\boldsymbol{\pi}_n,\boldsymbol{\pi}_{n+1})\cdot\boldsymbol{\lambda}_S\right)\\
&\quad=\Delta t\sum_{S\in\bar{\omega}}\boldsymbol{\lambda}_S\cdot\sum_B(\partial_{\boldsymbol{q}_B}\boldsymbol{\pi}(\bar{\boldsymbol{q}}^S_{n+\frac{1}{2}},\boldsymbol{d}^S_{n+\frac{1}{2}},\boldsymbol{f}^S_{n+\frac{1}{2}}))^T\overline{\overline{\nabla}}_{\pi}\,\tilde{\boldsymbol{g}}^S(\boldsymbol{\pi}_n,\boldsymbol{\pi}_{n+1})\cdot\widehat{\boldsymbol{q}}_{B,n+\frac{1}{2}}\boldsymbol{\zeta}
\end{aligned}\tag{5.38}$$

Again, we incorporate the relation (5.34)

$$\begin{aligned}
\sum_A(\partial_{\boldsymbol{q}_A}\boldsymbol{\pi}(\bar{\boldsymbol{q}}^S_{n+\frac{1}{2}},\boldsymbol{d}^S_{n+\frac{1}{2}},\boldsymbol{f}^S_{n+\frac{1}{2}}))^T\overline{\overline{\nabla}}_{\pi}\,\tilde{\boldsymbol{g}}^S(\boldsymbol{\pi}_n,\boldsymbol{\pi}_{n+1})\cdot\hat{\boldsymbol{q}}_{A,n+\frac{1}{2}}\boldsymbol{\zeta}+&\\
\partial_{\boldsymbol{d}^S}\boldsymbol{\pi}(\bar{\boldsymbol{q}}^S_{n+\frac{1}{2}},\boldsymbol{d}^S_{n+\frac{1}{2}},\boldsymbol{f}^S_{n+\frac{1}{2}}))^T\overline{\overline{\nabla}}_{\pi}\,\tilde{\boldsymbol{g}}^S(\boldsymbol{\pi}_n,\boldsymbol{\pi}_{n+1})\cdot\hat{\boldsymbol{d}}^S_{n+\frac{1}{2}}\boldsymbol{\zeta}&=0
\end{aligned}\tag{5.39}$$

into the last equation

$$\begin{aligned}
&\boldsymbol{\zeta}\cdot(\boldsymbol{J}_{n+1}-\boldsymbol{J}_n)=\\
&\quad=-\Delta t\sum_{S\in\bar{\omega}}\boldsymbol{\lambda}_S\cdot\partial_{\boldsymbol{d}^S}\boldsymbol{\pi}(\bar{\boldsymbol{q}}^S_{n+\frac{1}{2}},\boldsymbol{d}^S_{n+\frac{1}{2}},\boldsymbol{f}^S_{n+\frac{1}{2}}))^T\overline{\overline{\nabla}}_{\pi}\,\tilde{\boldsymbol{g}}^S(\boldsymbol{\pi}_n,\boldsymbol{\pi}_{n+1})\cdot\widehat{\boldsymbol{d}}^S_{n+\frac{1}{2}}\boldsymbol{\zeta}\\
&\quad=\Delta t\boldsymbol{\zeta}\cdot\sum_{S\in\bar{\omega}}\boldsymbol{d}^S_{n+\frac{1}{2}}\times\partial_{\boldsymbol{d}^S}\boldsymbol{\pi}(\bar{\boldsymbol{q}}^S_{I,n+\frac{1}{2}},\boldsymbol{d}^S_{n+\frac{1}{2}},\boldsymbol{f}^S_{n+\frac{1}{2}}))^T\overline{\overline{\nabla}}_{\pi}\,\tilde{\boldsymbol{g}}^S(\boldsymbol{\pi}_n,\boldsymbol{\pi}_{n+1})\cdot\boldsymbol{\lambda}_S\\
&\quad=0
\end{aligned}\tag{5.40}$$

Eventually, we verify algorithmic conservation of energy. Two sources for the lack of energy conservation have to be considered: a) The nonlinearity of the constraints and b) the discretization error in time due to the active set strategy (cf. Hesch & Betsch [33]). We will deal with the former first and then explain solution strategies for the latter at the end of this section.

For the verification of algorithmic conservation of energy we have to show that the net power input to the system within each time step is zero. Scalar multiplication of $(5.35)_2$ with $\boldsymbol{v}_{n+\frac{1}{2}}$ yields

$$\begin{aligned}
\boldsymbol{v}_{n+\frac{1}{2}}\cdot\boldsymbol{M}\,(\boldsymbol{v}_{n+1}-\boldsymbol{v}_n)&=-\overline{\nabla}E(\boldsymbol{q}_n,\boldsymbol{q}_{n+1})(\boldsymbol{q}_{n+1}-\boldsymbol{q}_n)\\
&-(\boldsymbol{q}_{n+1}-\boldsymbol{q}_n)\cdot\sum_{S\in\bar{\omega}}(D_1\boldsymbol{\pi}(\bar{\boldsymbol{q}}^S_{n+\frac{1}{2}},\boldsymbol{d}^S_{n+\frac{1}{2}},\boldsymbol{f}^S_{n+\frac{1}{2}}))^T\overline{\overline{\nabla}}_{\pi}\,\tilde{\boldsymbol{g}}^S(\boldsymbol{\pi}_n,\boldsymbol{\pi}_{n+1})\cdot\boldsymbol{\lambda}_S
\end{aligned}\tag{5.41}$$

The last equation can be recast in the form

$$\begin{aligned}
T_{n+1}-T_n&=-[E(\boldsymbol{q}_{n+1})-E(\boldsymbol{q}_n)]\\
&+\boldsymbol{\lambda}_S\cdot\sum_{S\in\bar{\omega}}(D_1\boldsymbol{\pi}(\bar{\boldsymbol{q}}^S_{n+\frac{1}{2}},\boldsymbol{d}^S_{n+\frac{1}{2}},\boldsymbol{f}^S_{n+\frac{1}{2}}))^T\overline{\overline{\nabla}}_{\pi}\,\tilde{\boldsymbol{g}}^S(\boldsymbol{\pi}_n,\boldsymbol{\pi}_{n+1})\cdot(\boldsymbol{q}_{n+1}-\boldsymbol{q}_n)
\end{aligned}\tag{5.42}$$

where the directionality property of the discrete derivative (see Gonzalez [26]) has been employed. To show that the last term in (5.42) equals zero, we have to consider the consistency condition in the discrete setting, i.e. to prove that

$$\begin{aligned}&\Big[(\bar{\boldsymbol{q}}^S_{I,n+1} - \bar{\boldsymbol{q}}^S_{I,n}) \cdot (D_1\boldsymbol{\pi}(\bar{\boldsymbol{q}}^S_{,n+\frac{1}{2}}, \boldsymbol{d}^S_{n+\frac{1}{2}}, \boldsymbol{f}^S_{n+\frac{1}{2}}))^T + \\ &(\boldsymbol{d}^S_{n+1} - \boldsymbol{d}^S_{n}) \cdot (D_2\boldsymbol{\pi}(\bar{\boldsymbol{q}}^S_{n+\frac{1}{2}}, \boldsymbol{d}^S_{n+\frac{1}{2}}, \boldsymbol{f}^S_{n+\frac{1}{2}}))^T + \\ &(\boldsymbol{f}^S_{n+1} - \boldsymbol{f}^S_{n}) \cdot (D_3\boldsymbol{\pi}(\bar{\boldsymbol{q}}^S_{n+\frac{1}{2}}, \boldsymbol{d}^S_{n+\frac{1}{2}}, \boldsymbol{f}^S_{n+\frac{1}{2}}))^T\Big] \cdot \overline{\overline{\nabla}}_{\pi}\, \tilde{\boldsymbol{g}}^S(\boldsymbol{\pi}_n, \boldsymbol{\pi}_{n+1}) = 0\end{aligned} \tag{5.43}$$

holds. Due to the specific structure of the invariants (cf. (5.31)), we can recast (5.43) as follows

$$(\boldsymbol{\pi}_{n+1} - \boldsymbol{\pi}_n) \cdot \overline{\overline{\nabla}}_{\pi}\, \tilde{\boldsymbol{g}}^S(\boldsymbol{\pi}_n, \boldsymbol{\pi}_{n+1}) = 0 \tag{5.44}$$

In consequence of the discrete gradient (5.36) the last equation can be written as

$$\tilde{\boldsymbol{g}}^S_{n+1} - \tilde{\boldsymbol{g}}^S_{n} = 0 \tag{5.45}$$

Insertion into (5.42) yields

$$\begin{aligned}T_{n+1} - T_n + E_{n+1} - E_n = \\ -\sum_{S\in\bar{\omega}} \boldsymbol{\lambda}_S \cdot \Big(&D_2\boldsymbol{\pi}(\bar{\boldsymbol{q}}^S_{n+\frac{1}{2}}, \boldsymbol{d}^S_{n+\frac{1}{2}}, \boldsymbol{f}^S_{n+\frac{1}{2}}))^T \overline{\overline{\nabla}}_{\pi}\, \tilde{\boldsymbol{g}}^S(\boldsymbol{\pi}_n, \boldsymbol{\pi}_{n+1}) \cdot (\boldsymbol{d}^S_{n+1} - \boldsymbol{d}^S_{n}) + \\ &D_3\boldsymbol{\pi}(\bar{\boldsymbol{q}}^S_{n+\frac{1}{2}}, \boldsymbol{d}^S_{n+\frac{1}{2}}, \boldsymbol{f}^S_{n+\frac{1}{2}}))^T \overline{\overline{\nabla}}_{\pi}\, \tilde{\boldsymbol{g}}^S(\boldsymbol{\pi}_n, \boldsymbol{\pi}_{n+1}) \cdot (\boldsymbol{f}^S_{n+1} - \boldsymbol{f}^S_{n})\Big) \\ &= 0\end{aligned} \tag{5.46}$$

where $(5.35)_3$ and $(5.35)_4$ have been taken into account. Accordingly, algorithmic conservation of energy is facilitated if the discrete persistency condition $\boldsymbol{\lambda}_S \cdot (\tilde{\boldsymbol{g}}^S_{n+1} - \tilde{\boldsymbol{g}}^S_{n}) = 0$ is fulfilled.

The active set strategy (see Hüber & Wohlmuth [42] and the references therein for details) separates the set of constraints into the active and inactive set within each time step. A constraint, moving from the inactive into the active set violates the constraint requirements at time t_n in general. This also violates the consistency condition and (5.45), respectively. Different possibilities are given to deal with the problem at hand (cf. Hesch & Betsch [33]). First of all, energy-momentum schemes have been developed to overcome numerical instabilities in nonlinear elastodynamics (see Simo & Tarnow [66]). This requirement is fulfilled by the proposed approach independent of the violation of the consistency condition, so there is no need to correct this kind of artificial energy. If necessary (e.g. for the numerical verification of energy conservation), the consistency condition itself can be used by replacing the original constraint function according to

$$\tilde{\boldsymbol{g}}^S_{n+1} \rightarrow \tilde{\boldsymbol{g}}^S_{n+1} - \tilde{\boldsymbol{g}}^S_{n} \tag{5.47}$$

so that condition (5.45) is always satisfied.

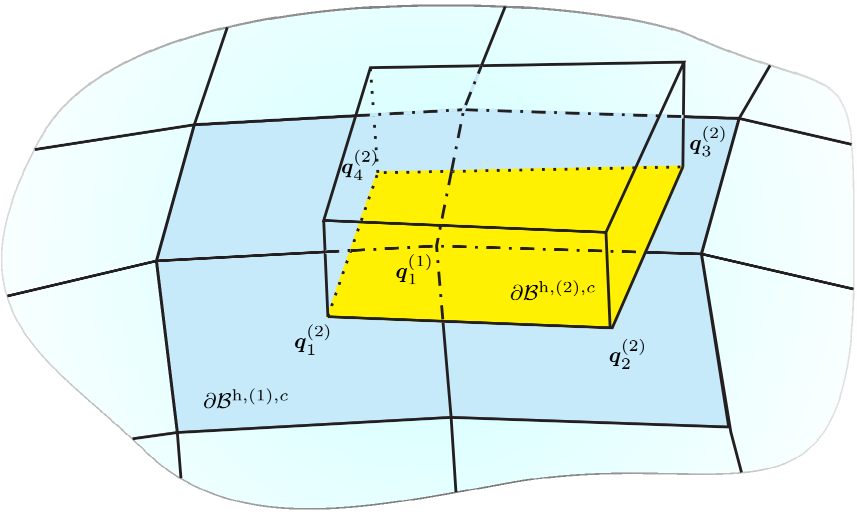

Figure 5.2: Three dimensional segmentation problem.

5.2 Mortar method

In contrast to the NTS-method, we interpolate now the tractions using the shape functions N^A of the underlying discrete surface on the non-Mortar side. Accordingly,

$$\boldsymbol{t}^{\mathrm{h},(1)} = \sum_{A=\bar{\omega}^{(1)}} N^A\left(\boldsymbol{X}^{(1)}\right)\boldsymbol{t}_A^{(1)} \tag{5.48}$$

If we substitute the shape functions of the underlying geometry and (5.48) into (5.4) we obtain the discrete contact virtual work

$$G^c = \boldsymbol{n}^B \cdot \delta\boldsymbol{q}_B^{(1)} - \boldsymbol{n}^C \cdot \delta\boldsymbol{q}_C^{(2)} \tag{5.49}$$

where the abbreviations

$$\boldsymbol{n}^B = \langle \boldsymbol{t}_A N^A, N^B \rangle_{\partial\mathcal{B}^{\mathrm{h},(1),c}} \tag{5.50}$$

and

$$\boldsymbol{n}^C = \langle \boldsymbol{t}_A N^A, N^C \rangle_{\partial\mathcal{B}^{\mathrm{h},(1),c}} \tag{5.51}$$

have been used. The Cauchy tractions are decomposed into the normal and the tangential part

$$\boldsymbol{t}_A = \boldsymbol{t}_A^N + \boldsymbol{t}_A^F, \quad \text{with} \quad \boldsymbol{t}_A^N = \lambda_A \boldsymbol{\nu}, \quad \boldsymbol{t}^F \cdot \boldsymbol{\nu} = 0 \tag{5.52}$$

Since we restrict ourselves for now to frictionless sliding, we assume $\boldsymbol{t}^F = \boldsymbol{0}$. The Mortar constraints in normal directions can now be written as follows

$$\Phi^A = \boldsymbol{n}^{AB} \cdot \boldsymbol{q}_B^{(1)} - \boldsymbol{n}^{AC} \cdot \boldsymbol{q}_C^{(2)} \tag{5.53}$$

where

$$\boldsymbol{n}^{AB} = \langle \boldsymbol{\nu} N^A, N^B \rangle_{\partial\mathcal{B}^{\mathrm{h},(1),c}} \tag{5.54}$$

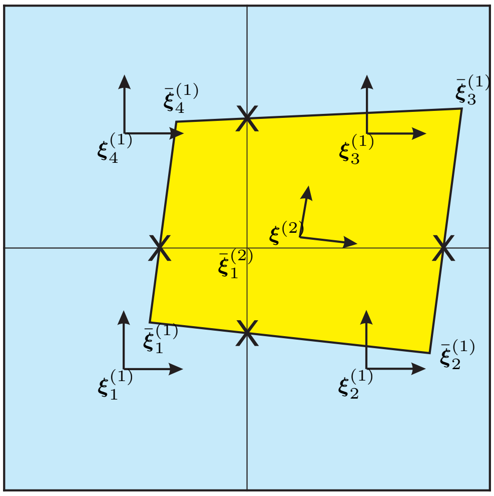

Figure 5.3: Orthogonal projection of the vertices and edges.

and

$$\boldsymbol{n}^{AC} = \langle \boldsymbol{\nu} N^A, N^C \rangle_{\partial \mathcal{B}^{\mathrm{h},(1),c}} \tag{5.55}$$

are referred to as Mortar integrals. The evaluation of the Mortar integrals (5.54) is based on a segmentation process, as shown before in Section 4.1. We recast the necessary steps in the following in detail, since we have to define appropriate augmented constraints to rewrite the system in terms of invariants:

1. Loop over all nodes $\boldsymbol{q}_I^{(2)}$ on the Mortar side.
   We determine the convective coordinates $\bar{\boldsymbol{\xi}}_I^{(1)}$ corresponding to the vertices $\boldsymbol{q}_I^{(2)}$ by solving the non-linear equations

   $$\boldsymbol{\Phi}_{\mathrm{Aug}_1,I} = \begin{bmatrix} \sum\limits_{J=1}^{4} N_{J,\bar{\xi}_{I,1}^{(1)}}\left(\bar{\boldsymbol{\xi}}_I^{(1)}\right)\boldsymbol{q}_J^{(1)} \cdot \left(\boldsymbol{q}_I^{(2)} - \sum\limits_{L=1}^{4} N_L\left(\bar{\boldsymbol{\xi}}_I^{(1)}\right)\boldsymbol{q}_L^{(1)}\right) \\ \sum\limits_{J=1}^{4} N_{J,\bar{\xi}_{I,2}^{(1)}}\left(\bar{\boldsymbol{\xi}}_I^{(1)}\right)\boldsymbol{q}_J^{(1)} \cdot \left(\boldsymbol{q}_I^{(2)} - \sum\limits_{L=1}^{4} N_L\left(\bar{\boldsymbol{\xi}}_I^{(1)}\right)\boldsymbol{q}_L^{(1)}\right) \end{bmatrix} \equiv \boldsymbol{0} \tag{5.56}$$

   with respect to the convective coordinates using a standard Newton method. Here, $N_{J,\bar{\xi}_{I,\alpha}^{(1)}}(\bar{\boldsymbol{\xi}}_I^{(1)})$ denotes the derivative of the shape function with respect to $\bar{\boldsymbol{\xi}}_{I,\alpha}^{(1)}$.
2. Loop over all nodes $\boldsymbol{q}_I^{(1)}$ on the non-Mortar side, see Figure 5.2.
   We determine convective coordinates $\bar{\boldsymbol{\xi}}_I^{(2)}$ corresponding to the relevant nodes on the Mortar side. To deal with arbitrary curved surfaces, we project the nodes to the projected surfaces defined by the nodes $\bar{\boldsymbol{q}}_I^{(1)} = \sum\limits_{L} N_L\left(\bar{\boldsymbol{\xi}}_I^{(1)}\right)\boldsymbol{q}_L^{(1)}$ instead of the original surface defined by the nodes $\boldsymbol{q}_I^{(2)}$. Once again, we use a Newton method to

solve the non-linear equations

$$\boldsymbol{\Phi}_{\mathrm{Aug}_2,I} = \begin{bmatrix} \sum\limits_{J=1}^{4} N_{J,\bar{\xi}^{(2)}_{I,1}}\left(\bar{\boldsymbol{\xi}}^{(2)}_I\right)\bar{\boldsymbol{q}}^{(1)}_J \cdot \left(\boldsymbol{q}^{(1)}_I - \sum\limits_{K=1}^{4} N_K\left(\bar{\boldsymbol{\xi}}^{(2)}_I\right)\bar{\boldsymbol{q}}^{(1)}_K\right) \\ \sum\limits_{J=1}^{4} N_{J,\bar{\xi}^{(2)}_{I,2}}\left(\bar{\boldsymbol{\xi}}^{(2)}_I\right)\bar{\boldsymbol{q}}^{(1)}_J \cdot \left(\boldsymbol{q}^{(1)}_I - \sum\limits_{K=1}^{4} N_K\left(\bar{\boldsymbol{\xi}}^{(2)}_I\right)\bar{\boldsymbol{q}}^{(1)}_K\right) \end{bmatrix} \equiv \mathbf{0} \tag{5.57}$$

with respect to the convective coordinates $\bar{\boldsymbol{\xi}}^{(2)}_I$.

3. Loop over all edges on the non-Mortar side.
   To determine the projected intersections between the edges, we create a list of all edges of all surface elements on the Mortar side and span on each edge, corresponding to the nodes $\boldsymbol{q}^{(1)}_K$, $K \in \{1, 2\}$, a surface using a normal field[†], defined by $\boldsymbol{d}_K$ at both nodes $\boldsymbol{q}^{(1)}_K$. Then we create a second list of all edges of the projected mesh. A specific line on the projected mesh can be determined using the projected nodes $\bar{\boldsymbol{q}}^{(1)}_J = \sum\limits_{L} N_L\left(\bar{\boldsymbol{\xi}}^{(1)}_J\right)\boldsymbol{q}^{(1)}_L$, $J \in \{1, 2\}$. Next, we search for the intersection between each projected line and each possible surface. The corresponding convective coordinates $\tilde{\xi}_{I,1}$ and $\tilde{\xi}_{I,2}$ (as well as $\tilde{\xi}_{I,3}$ which is not needed in the sequel) follow from

   $$\boldsymbol{\Phi}_{\mathrm{Aug}_3,I} = \sum_{I=1}^{2} \hat{N}_J\left(\tilde{\xi}_{I,1}\right)\bar{\boldsymbol{q}}^{(1)}_J - \sum_{K=1}^{2} \hat{N}_K\left(\tilde{\xi}_{I,2}\right)\left(\boldsymbol{q}^{(1)}_K + \boldsymbol{d}^{(1)}_K\tilde{\xi}_{I,3}\right) \equiv \mathbf{0} \tag{5.58}$$

   Note that in the above considerations the shape functions $\hat{N}_J\left(\tilde{\xi}_{I,i}\right)$, $i \in \{1, 2\}$ on the edges are one dimensional.
4. Delaunay triangularization of each element on the Mortar side.
   Based on the results of the first three steps we apply a Delaunay triangularization. Note that several constraints (i.e. specification of nodes, which must be connected) have to be predetermined.

For later use and guided by previous developments in [37] we introduce a global vector of coordinates $\boldsymbol{f}$, collecting all convective coordinates, determined by (5.56), (5.57) and (5.58).

After we have located all segments, we calculate the segment contributions to the Mortar constraints (5.53). As shown in Section 4.1 we introduce for each segment a linear transformation $\boldsymbol{\eta} \to \tilde{\boldsymbol{\xi}}^{(i)}_{\mathrm{seg}}$ via

$$\tilde{\boldsymbol{\xi}}^{(i)}_{\mathrm{seg}}(\boldsymbol{\eta}) = \sum_{K=1}^{3} M^K(\boldsymbol{\eta})\boldsymbol{\xi}^{(i)}_{\mathrm{seg},K} \tag{5.59}$$

where $\boldsymbol{\xi}^{(i)}_{\mathrm{seg},K}$ denote the convective coordinates determined previously. For each segment we specify the associated convective coordinates and collect them in the set $\eta_{\mathrm{conv}} = \{\boldsymbol{f}_{\mathrm{seg}}\} =$

[†] Different definitions of a normal vector on a discrete surface are possible, see e.g. Yang et al. [81]. We use an averaged normal composed of the normals of the adjacent elements.

$\{\boldsymbol{\xi}^{(i)}_{\mathrm{seg},K}\}$, $i \in \{1, 2\}$, $K \in \{1, 2, 3\}$. In accordance with the results of the segmentation algorithm, linear triangular shape functions M^K are used. The approximations of the geometry and of the Cauchy tractions can now be recast in the form

$$\boldsymbol{t}^{(1)}_{\mathrm{seg}} = \sum_{\kappa} N^{\kappa}\left(\tilde{\boldsymbol{\xi}}^{(1)}_{\mathrm{seg}}(\boldsymbol{\eta})\right)\boldsymbol{t}_{\kappa} \tag{5.60}$$

$$\boldsymbol{q}^{(1)}_{\mathrm{seg}} = \sum_{\beta} N^{\beta}\left(\tilde{\boldsymbol{\xi}}^{(1)}_{\mathrm{seg}}(\boldsymbol{\eta})\right)\boldsymbol{q}^{(1)}_{\beta} \tag{5.61}$$

$$\boldsymbol{q}^{(2)}_{\mathrm{seg}} = \sum_{\zeta} N^{\zeta}\left(\tilde{\boldsymbol{\xi}}^{(2)}_{\mathrm{seg}}(\boldsymbol{\eta})\right)\boldsymbol{q}^{(2)}_{\zeta} \tag{5.62}$$

For the application of a numerical quadrature rule, the Jacobian

$$J_{\mathrm{seg}} = \left\|\boldsymbol{a}_1\left(\tilde{\boldsymbol{\xi}}^{(1)}_{\mathrm{seg}}(\boldsymbol{\eta})\right)\times\boldsymbol{a}_2\left(\tilde{\boldsymbol{\xi}}^{(1)}_{\mathrm{seg}}(\boldsymbol{\eta})\right)\right\|\det(D\boldsymbol{\xi}(\boldsymbol{\eta})) \tag{5.63}$$

is required, where the tangential vectors $\boldsymbol{a}_\alpha$ are calculated via

$$\boldsymbol{a}_\alpha = \sum_{\kappa} N^{\kappa}_{,\xi^{(1)}_\alpha}\left(\tilde{\boldsymbol{\xi}}^{(1)}_{\mathrm{seg}}(\boldsymbol{\eta})\right)\boldsymbol{q}^{(1)}_{\kappa} \tag{5.64}$$

Based on the tangential vectors, we specify a unit normal vector $\boldsymbol{\nu}$

$$\boldsymbol{\nu} = \frac{\boldsymbol{a}_1\left(\tilde{\boldsymbol{\xi}}^{(1)}_{\mathrm{seg}}(\boldsymbol{\eta})\right)\times\boldsymbol{a}_2\left(\tilde{\boldsymbol{\xi}}^{(1)}_{\mathrm{seg}}(\boldsymbol{\eta})\right)}{\left\|\boldsymbol{a}_1\left(\tilde{\boldsymbol{\xi}}^{(1)}_{\mathrm{seg}}(\boldsymbol{\eta})\right)\times\boldsymbol{a}_2\left(\tilde{\boldsymbol{\xi}}^{(1)}_{\mathrm{seg}}(\boldsymbol{\eta})\right)\right\|} \tag{5.65}$$

Then we cut the norm from both, the Jacobian and the normal vector and receive

$$\bar{J}_{\mathrm{seg}} = \det(D\boldsymbol{\xi}(\boldsymbol{\eta})), \quad \bar{\boldsymbol{\nu}} = \boldsymbol{a}_1\left(\tilde{\boldsymbol{\xi}}^{(1)}_{\mathrm{seg}}(\boldsymbol{\eta})\right)\times\boldsymbol{a}_2\left(\tilde{\boldsymbol{\xi}}^{(1)}_{\mathrm{seg}}(\boldsymbol{\eta})\right) \tag{5.66}$$

To prevent expensive calculations we propose at this point a simplification and assume that $\bar{\boldsymbol{\nu}}$ remains constant in each segment, i.e. we evaluate the normal vector at a specific, constant position within the segment[‡]. Then we can rewrite the constraints on segment level as follows

$$\Phi^{\kappa}_{\mathrm{seg}} = \bar{\boldsymbol{\nu}}\cdot\left[\bar{n}^{\kappa\beta}\boldsymbol{q}^{(1)}_{\beta} - \bar{n}^{\kappa\zeta}\boldsymbol{q}^{(2)}_{\zeta}\right] \tag{5.67}$$

using the Mortar integrals

$$\begin{aligned}\bar{n}^{\kappa\beta}(\boldsymbol{f}_{\mathrm{seg}}) &= \int_{\triangle} N^{\kappa}\left(\tilde{\boldsymbol{\xi}}^{(1)}_{\mathrm{seg}}(\boldsymbol{\eta})\right)N^{\beta}\left(\tilde{\boldsymbol{\xi}}^{(1)}_{\mathrm{seg}}(\boldsymbol{\eta})\right)\bar{J}_{\mathrm{seg}}\,\mathrm{d}\eta \\ \bar{n}^{\kappa\zeta}(\boldsymbol{f}_{\mathrm{seg}}) &= \int_{\triangle} N^{\kappa}\left(\tilde{\boldsymbol{\xi}}^{(1)}_{\mathrm{seg}}(\boldsymbol{\eta})\right)N^{\zeta}\left(\tilde{\boldsymbol{\xi}}^{(2)}_{\mathrm{seg}}(\boldsymbol{\eta})\right)\bar{J}_{\mathrm{seg}}\,\mathrm{d}\eta\end{aligned} \tag{5.68}$$

[‡] It is important to note that the normal vector still depends on the current configuration of the surface, only its relative position on the surface remains constant.

which we evaluate using a standard Gauss quadrature (cf. Hesch & Betsch [34] and Puso [62]).

Once we have determined all segment contributions, we have to assemble the Mortar constraints. Therefore, we arrange the constraint functions in a global vector of constraints $\boldsymbol{\Phi}(\boldsymbol{q})$ in correspondence to the Lagrange multipliers, which are related to the nodal points on the non-Mortar side

$$\sum_{A\in\bar{\omega}^{(1)}} \lambda_A \Phi^A(\boldsymbol{q},\boldsymbol{f}) = \boldsymbol{\lambda}\cdot\boldsymbol{\Phi}(\boldsymbol{q},\boldsymbol{f}) \tag{5.69}$$

Since each constraint will be assembled out of a variable number of segments, where each triangular segment relies on the four vertices of e_1 with local node number $\kappa \in \{1, \ldots, 4\}$, we need a connection between the local node numbers and the global location within the vector of constraints $\boldsymbol{\Phi}(\boldsymbol{q})$. Analogues to the approach in Section 4.1 we introduce a location array LM, so that $A = \mathrm{LM}(\kappa,\, e_1)$ and use this location array for the assembly of the segment contributions

$$\begin{aligned}\boldsymbol{\Phi}_{\mathrm{mortar}}(\boldsymbol{q},\boldsymbol{f}) &= \mathop{\mathbf{A}}_{e_1\in\bar{\epsilon}^{(1)}} \boldsymbol{\Phi}_{e_1}(\boldsymbol{q},\boldsymbol{f}) \\ &= \mathop{\mathbf{A}}_{e_1\in\bar{\epsilon}^{(1)}} \bigcup_{\mathrm{seg}} \boldsymbol{\Phi}_{e_1,\mathrm{seg}}(\boldsymbol{q}_{\mathrm{seg}},\boldsymbol{f}_{\mathrm{seg}}) = \mathop{\mathbf{A}}_{e_1\in\bar{\epsilon}^{(1)}} \bigcup_{\mathrm{seg}} \begin{bmatrix} \Phi^{\kappa=1}_{e_1,\mathrm{seg}}(\boldsymbol{q}_{\mathrm{seg}},\boldsymbol{f}_{\mathrm{seg}}) \\ \vdots \\ \Phi^{\kappa=4}_{e_1,\mathrm{seg}}(\boldsymbol{q}_{\mathrm{seg}},\boldsymbol{f}_{\mathrm{seg}}) \end{bmatrix}\end{aligned} \tag{5.70}$$

where $\boldsymbol{q}_{\mathrm{seg}}$ is defined by the set of relevant vectors $\eta_{\mathrm{seg}} = \{\boldsymbol{q}_{\mathrm{seg}}\} = \{\boldsymbol{q}_I^{(1)}, \boldsymbol{q}_J^{(2)}\}$, $\forall\, I, J \in [1, \ldots, 4]$.

Regarding Cauchy's representation theorem, we can rewrite the constraints in terms of invariants. For the later application of the concept of a discrete gradient to conserve the total energy, we have to reformulate the constraints in terms of invariants, which are at most quadratic. Therefore, as outlined in Section 4.1, we replace the normal vector for each segment by augmented coordinates $\boldsymbol{d}_{\mathrm{seg}}$ in the Mortar constraints

$$\Phi^{\kappa}_{\mathrm{seg}}(\boldsymbol{q}_{\mathrm{seg}},\boldsymbol{f}_{\mathrm{seg}},\boldsymbol{d}_{\mathrm{seg}}) = \boldsymbol{d}_{\mathrm{seg}} \cdot \left[\bar{n}^{\kappa\beta}(\boldsymbol{f}_{\mathrm{seg}})\boldsymbol{q}^{(1)}_{\beta} - \bar{n}^{\kappa\zeta}(\boldsymbol{f}_{\mathrm{seg}})\boldsymbol{q}^{(2)}_{\zeta}\right] \tag{5.71}$$

Note that the additional constraints

$$\boldsymbol{\Phi}^{\mathrm{normal}}_{\mathrm{seg}} = \begin{bmatrix} \boldsymbol{d}_{\mathrm{seg}} \cdot \boldsymbol{a}_1 \\ \boldsymbol{d}_{\mathrm{seg}} \cdot \boldsymbol{a}_2 \\ \boldsymbol{d}_{\mathrm{seg}} \cdot \boldsymbol{d}_{\mathrm{seg}} - \|\boldsymbol{a}_1 \times \boldsymbol{a}_2\|^2 \end{bmatrix} \tag{5.72}$$

are necessary to determine the actual value of the augmented coordinates. Next, we rewrite the Mortar constraints (5.71) in terms of invariants. Therefore, we introduce the following sets

$$\begin{aligned}\bar{\mathbb{S}}(\eta_{\mathrm{aug}}) &= \{(\boldsymbol{q}^{(1)}_I - \boldsymbol{q}^{(1)}_1)\cdot(\boldsymbol{q}^{(i)}_J - \boldsymbol{q}^{(1)}_1),\, i \in \{1,\,2\},\, I, J \in \{1,\,2,\,3,\,4\}\} \\ \tilde{\mathbb{S}}(\eta_{\mathrm{aug}}) &= \{(\boldsymbol{q}^{(i)}_I - \boldsymbol{q}^{(1)}_1)\cdot \boldsymbol{d}_{\mathrm{seg}},\, i \in \{1,\,2\},\, I \in \{1,\,2,\,3,\,4\}\} \\ \mathring{\mathbb{S}}(\eta_{\mathrm{aug}}) &= \{\boldsymbol{d}_{\mathrm{seg}} \cdot \boldsymbol{d}_{\mathrm{seg}}\} \\ \hat{\mathbb{S}}(\eta_{\mathrm{aug}}) &= \{\boldsymbol{f}_{\mathrm{seg}}\}\end{aligned} \tag{5.73}$$

and define a vector of possible invariants

$$\boldsymbol{\pi} = \begin{bmatrix} \bar{\boldsymbol{\pi}}^{(i)} \in \bar{\mathbb{S}}(\eta_{\text{aug}}) \\ \tilde{\boldsymbol{\pi}}^{(i)} \in \tilde{\mathbb{S}}(\eta_{\text{aug}}) \\ \mathring{\pi} \in \mathring{\mathbb{S}}(\eta_{\text{aug}}) \\ \hat{\boldsymbol{\pi}} \in \hat{\mathbb{S}}(\eta_{\text{aug}}) \end{bmatrix} \tag{5.74}$$

Note that we have chosen $\boldsymbol{q}_1^{(1)}$ such that all terms with $I = 1$ in (5.73) vanish. Other choices using a different number of invariants are possible. To rewrite (5.71) in terms of the invariants (5.74) we rearrange the constraints as follows

$$\Phi^{\kappa}_{\text{seg}}(\boldsymbol{q}_{\text{seg}}, \boldsymbol{f}_{\text{seg}}, \boldsymbol{d}_{\text{seg}}) = \bar{n}^{\kappa\beta}(\boldsymbol{f}_{\text{seg}})\boldsymbol{d}_{\text{seg}} \cdot \boldsymbol{q}^{(1)}_{\beta} - \bar{n}^{\kappa\zeta}(\boldsymbol{f}_{\text{seg}})\boldsymbol{d}_{\text{seg}} \cdot \boldsymbol{q}^{(2)}_{\zeta} \tag{5.75}$$

As shown in Puso [62], linear momentum can not be exactly conserved due to the inexact numerical evaluation of the Mortar integrals. This drawback can be removed by assuming that

$$\sum_{\beta} \bar{n}^{\kappa\beta}\boldsymbol{q}_1^{(1)} - \sum_{\zeta} \bar{n}^{\kappa\zeta}\boldsymbol{q}_1^{(1)} = \mathbf{0} \tag{5.76}$$

holds exactly. Note that the evaluation of the Mortar integrals (5.68) by means of quadrature rules violates condition (5.76) in general. Inserting (5.76) in (5.75) yields

$$\Phi^{\kappa}_{\text{seg}}(\boldsymbol{q}_{\text{seg}}, \boldsymbol{f}_{\text{seg}}, \boldsymbol{d}_{\text{seg}}) = \bar{n}^{\kappa\beta}(\boldsymbol{f}_{\text{seg}})(\boldsymbol{q}^{(1)}_{\beta} - \boldsymbol{q}^{(1)}_{1}) \cdot \boldsymbol{d}_{\text{seg}} - \bar{n}^{\kappa\zeta}(\boldsymbol{f}_{\text{seg}})(\boldsymbol{q}^{(2)}_{\zeta} - \boldsymbol{q}^{(1)}_{1}) \cdot \boldsymbol{d}_{\text{seg}} \tag{5.77}$$

Applying the sets of invariants (5.73) the Mortar constraints (5.71) can now be written as follows

$$\Phi^{\kappa}_{\text{seg}}(\boldsymbol{\pi}) = \bar{n}^{\kappa\beta}(\hat{\boldsymbol{\pi}})\tilde{\pi}^{(1)}_{\beta} - \bar{n}^{\kappa\zeta}(\hat{\boldsymbol{\pi}})\tilde{\pi}^{(2)}_{\zeta} \tag{5.78}$$

The additional constraints (5.72) used to determine the actual values of the augmented coordinates $\boldsymbol{d}_{\text{seg}}$ have also to be rewritten in terms of invariants

$$\boldsymbol{\Phi}^{\text{normal}}_{\text{seg}}(\boldsymbol{\pi}) = \begin{bmatrix} \sum\limits_{I=1}^{4} N_{I,\xi_1^{(1)}}\tilde{\pi}^{(1)}_I \\ \sum\limits_{I=1}^{4} N_{I,\xi_2^{(1)}}\tilde{\pi}^{(1)}_I \\ \mathring{\pi} - K \end{bmatrix} \tag{5.79}$$

with

$$K = \left[\left(N_{I,\xi_1^{(1)}} N_{J,\xi_1^{(1)}} \bar{\pi}^{(1)}_{I,J}\right)\left(N_{I,\xi_2^{(1)}} N_{J,\xi_2^{(1)}} \bar{\pi}^{(1)}_{I,J}\right) - \left(N_{I,\xi_1^{(1)}} N_{J,\xi_2^{(1)}} \bar{\pi}^{(1)}_{I,J}\right)^2\right] \tag{5.80}$$

Note that the constraints $\boldsymbol{\Phi}_{\text{Aug}_3}$ in (5.58) have to be modified as follows

$$\boldsymbol{\Phi}^{\text{ed}_{IJ}}_{\text{Aug}_3} = \begin{bmatrix} \boldsymbol{d}_1^{(1)} \cdot \left[\sum\limits_{I=1}^{2} \hat{N}_I\left(\tilde{\xi}_1\right)\bar{\boldsymbol{q}}_I^{(1)} - \sum\limits_{J=1}^{2} \hat{N}_J\left(\tilde{\xi}_2\right)\left(\boldsymbol{q}_J^{(1)} + \boldsymbol{d}_J^{(1)}\tilde{\xi}_3\right)\right] \\ (\boldsymbol{q}_1^{(1)} - \boldsymbol{q}_2^{(1)}) \cdot \left[\sum\limits_{I=1}^{2} \hat{N}_I\left(\tilde{\xi}_1\right)\bar{\boldsymbol{q}}_I^{(1)} - \sum\limits_{J=1}^{2} \hat{N}_J\left(\tilde{\xi}_2\right)\left(\boldsymbol{q}_J^{(1)} + \boldsymbol{d}_J^{(1)}\tilde{\xi}_3\right)\right] \\ (\bar{\boldsymbol{q}}_1^{(1)} - \bar{\boldsymbol{q}}_2^{(1)}) \cdot \left[\sum\limits_{I=1}^{2} \hat{N}_I\left(\tilde{\xi}_1\right)\bar{\boldsymbol{q}}_I^{(1)} - \sum\limits_{J=1}^{2} \hat{N}_J\left(\tilde{\xi}_2\right)\left(\boldsymbol{q}_J^{(1)} + \boldsymbol{d}_J^{(1)}\tilde{\xi}_3\right)\right] \end{bmatrix} \tag{5.81}$$

As will be shown in the following, the pre-multiplication of the original, nonlinear constraints using a local basis composed of $\boldsymbol{d}_J^{(1)}$, $(\boldsymbol{q}_1^{(1)} - \boldsymbol{q}_2^{(1)})$ and $(\bar{\boldsymbol{q}}_1^{(1)} - \bar{\boldsymbol{q}}_2^{(1)})$ is necessary for the conservation of angular momentum[§]. Collecting all constraints in one global vector yields

$$\boldsymbol{\Phi}(\boldsymbol{\pi}(\boldsymbol{q},\boldsymbol{f},\boldsymbol{d})) = \begin{bmatrix} \boldsymbol{\Phi}_{\text{mortar}}(\boldsymbol{\pi}(\boldsymbol{q},\boldsymbol{f},\boldsymbol{d})) \\ \boldsymbol{\Phi}_{\text{normal}}(\boldsymbol{\pi}(\boldsymbol{q},\boldsymbol{f},\boldsymbol{d})) \\ \boldsymbol{\Phi}_{\text{Aug}_1}(\boldsymbol{\pi}(\boldsymbol{q},\boldsymbol{f},\boldsymbol{d})) \\ \boldsymbol{\Phi}_{\text{Aug}_2}(\boldsymbol{\pi}(\boldsymbol{q},\boldsymbol{f},\boldsymbol{d})) \\ \boldsymbol{\Phi}_{\text{Aug}_3}(\boldsymbol{\pi}(\boldsymbol{q},\boldsymbol{f},\boldsymbol{d})) \end{bmatrix} \tag{5.82}$$

Remark: The original constraint (5.67) can be rewritten in terms of invariants, which are at most cubic

$$\breve{\boldsymbol{\pi}}_{\text{seg}} = \begin{bmatrix} (\boldsymbol{a}_1 \times \boldsymbol{a}_2)\cdot(\boldsymbol{q}_\beta^{(1)} - \boldsymbol{q}_1^{(1)}) \\ (\boldsymbol{a}_1 \times \boldsymbol{a}_2)\cdot(\boldsymbol{q}_\zeta^{(2)} - \boldsymbol{q}_1^{(1)}) \\ \boldsymbol{f}_{\text{seg}} \end{bmatrix}, \quad \forall \beta,\zeta \in \{1,\dots,4\} \tag{5.83}$$

The segment contributions to the Mortar constraints based on (5.83) can now be written as follows

$$\breve{\Phi}^{\kappa}_{\text{seg}}(\boldsymbol{\pi}) = \bar{n}^{\kappa\beta}(\breve{\boldsymbol{\pi}})\breve{\pi}^{(1)}_{\beta} - \bar{n}^{\kappa\zeta}(\breve{\boldsymbol{\pi}})\breve{\pi}^{(2)}_{\zeta} \tag{5.84}$$

After the assembly procedure (see (5.70)) we obtain the reformulated Mortar constraints $\breve{\boldsymbol{\Phi}}_{\text{mortar}}(\breve{\boldsymbol{\pi}}(\boldsymbol{q},\boldsymbol{f},\boldsymbol{d}))$. Note, however, that cubic invariants prevent the application of the concept of a discrete gradient in the sense of Gonzalez [27].

Frame-indifference. As before, we postulate the invariance of the strain energy function $V(\boldsymbol{q})$ (cf. Betsch & Steinmann [13]) and concentrate our investigations on the constraint functions. To verify the frame-indifference, rigid body motions

$$\boldsymbol{q}^{\sharp}_{I,\text{seg}} = \boldsymbol{c} + \boldsymbol{Q}\boldsymbol{q}_{I,\text{seg}} \tag{5.85}$$

analogues to (5.18) are considered. Due to the definition of the sets in (5.73) and the demonstrated reformulation of the segment contributions in terms of invariants (5.78) we can state that

$$\Phi^{\kappa}_{\text{seg}}(\boldsymbol{\pi}(\boldsymbol{c} + \boldsymbol{Q}\boldsymbol{q}_{I,\text{seg}}, \boldsymbol{f}_{\text{seg}}, \boldsymbol{d}_{\text{seg}})) - \Phi^{\kappa}_{\text{seg}}(\boldsymbol{\pi}(\boldsymbol{q}_{\text{seg}}, \boldsymbol{f}_{\text{seg}}, \boldsymbol{Q}^T\boldsymbol{d}_{\text{seg}})) = 0 \tag{5.86}$$

Next, we substitute $\boldsymbol{c} = \epsilon\boldsymbol{\zeta}$ and $\boldsymbol{Q} = \boldsymbol{I}$. Accordingly, we receive for the translational part

$$0 = \left.\frac{\mathrm{d}}{\mathrm{d}\epsilon}\right|_{\epsilon=0} \Phi^{\kappa}_{\text{seg}}(\boldsymbol{\pi}(\boldsymbol{q}_{I,\text{seg}} + \epsilon\boldsymbol{\zeta}, \boldsymbol{f}_{\text{seg}}, \boldsymbol{d}_{\text{seg}})) = D\Phi^{\kappa}_{\text{seg}}(\boldsymbol{\pi})) \cdot \sum_I \partial_{\boldsymbol{q}_{I,\text{seg}}}\boldsymbol{\pi}(\boldsymbol{q}_{\text{seg}}, \boldsymbol{f}_{\text{seg}}, \boldsymbol{d}_{\text{seg}}) \cdot \boldsymbol{\zeta} = 0 \tag{5.87}$$

[§] Other local bases are possible.

For the rotational part, we substitute $\boldsymbol{c} = \boldsymbol{0}$ and $\boldsymbol{Q} = \exp(\epsilon\hat{\boldsymbol{\zeta}})$, and receive

$$\begin{aligned}
0 =& \frac{\mathrm{d}}{\mathrm{d}\epsilon}\bigg|_{\epsilon=0} \Phi^{\kappa}_{\text{seg}}(\boldsymbol{\pi}(\exp(\epsilon\hat{\boldsymbol{\zeta}})\boldsymbol{q}_{I,\text{seg}}, \boldsymbol{f}_{\text{seg}}, \boldsymbol{d}_{\text{seg}})) - \Phi^{\kappa}_{\text{seg}}(\boldsymbol{\pi}(\boldsymbol{q}_{\text{seg}}, \boldsymbol{f}_{\text{seg}}, \exp(-\epsilon\hat{\boldsymbol{\zeta}})\boldsymbol{d}_{\text{seg}})) \\
=& D\Phi^{\kappa}_{\text{seg}}(\boldsymbol{\pi})) \cdot \sum_{I} \Big[\partial_{\boldsymbol{q}_{I,\text{seg}}}\boldsymbol{\pi}(\boldsymbol{q}_{\text{seg}}, \boldsymbol{f}_{\text{seg}}, \boldsymbol{d}_{\text{seg}}) \cdot (\boldsymbol{\zeta} \times \boldsymbol{q}_{I,\text{seg}}) \\
&+ \partial_{\boldsymbol{d}_{\text{seg}}}\boldsymbol{\pi}(\boldsymbol{q}_{\text{seg}}, \boldsymbol{f}_{\text{seg}}, \boldsymbol{d}_{\text{seg}}) \cdot (\boldsymbol{\zeta} \times \boldsymbol{d}_{\text{seg}})\Big]
\end{aligned} \tag{5.88}$$

Since we rewrite the additional constraints (5.72), (5.56), (5.57) and (5.58) in terms of the same invariants, analogues properties are also valid for them.

Temporal discretization. To solve the semidiscrete system at hand, we have to implement an appropriate time stepping scheme. Three approaches for the discretization in time with different degrees of complexity are considered below.

1. The most complex approach rests on the configuration dependency of the Mortar integrals. For a typical time step $[t_n, t_{n+1}]$ of length Δt the equations of motion (5.3) can be recast in the form[¶]

$$\begin{aligned}
\boldsymbol{q}_{n+1} - \boldsymbol{q}_n =& \Delta t \boldsymbol{v}_{n+\frac{1}{2}} \\
\boldsymbol{M}(\boldsymbol{v}_{n+1} - \boldsymbol{v}_n) =& -\Delta t \overline{\nabla} E(\boldsymbol{q}_n, \boldsymbol{q}_{n+1}) \\
& - \Delta t (D_1\boldsymbol{\pi}(\boldsymbol{q}_{n+\frac{1}{2}}, \boldsymbol{d}_{n+\frac{1}{2}}, \boldsymbol{f}_{n+\frac{1}{2}}))^T \overline{\overline{\nabla}}_{\pi}\, \boldsymbol{\Phi}(\boldsymbol{\pi}_n, \boldsymbol{\pi}_{n+1}) \cdot \boldsymbol{\lambda}_{n,n+1} \\
\boldsymbol{0} =& (D_2\boldsymbol{\pi}(\boldsymbol{q}_{n+\frac{1}{2}}, \boldsymbol{d}_{n+\frac{1}{2}}, \boldsymbol{f}_{n+\frac{1}{2}}))^T \overline{\overline{\nabla}}_{\pi}\, \boldsymbol{\Phi}(\boldsymbol{\pi}_n, \boldsymbol{\pi}_{n+1}) \cdot \boldsymbol{\lambda}_{n,n+1} \\
\boldsymbol{0} =& (D_3\boldsymbol{\pi}(\boldsymbol{q}_{n+\frac{1}{2}}, \boldsymbol{d}_{n+\frac{1}{2}}, \boldsymbol{f}_{n+\frac{1}{2}}))^T \overline{\overline{\nabla}}_{\pi}\, \boldsymbol{\Phi}(\boldsymbol{\pi}_n, \boldsymbol{\pi}_{n+1}) \cdot \boldsymbol{\lambda}_{n,n+1} \\
\boldsymbol{0} =& \boldsymbol{\Phi}(\boldsymbol{\pi}(\boldsymbol{q}_{n+1}, \boldsymbol{d}_{n+1}, \boldsymbol{f}_{n+1}))
\end{aligned} \tag{5.89}$$

   The equivariant discrete gradient of the constraints $\overline{\overline{\nabla}}_{\pi}\, \boldsymbol{\Phi}(\boldsymbol{\pi}_n, \boldsymbol{\pi}_{n+1})$ consists on the one hand of the segment contributions

$$\begin{aligned}
\overline{\overline{\nabla}}_{\pi}\, \Phi^{\kappa}_{\text{seg}}(\boldsymbol{\pi}_n, \boldsymbol{\pi}_{n+1}) =& \nabla\Phi^{\kappa}_{\text{seg}}(\boldsymbol{\pi}_{n+\frac{1}{2}}) + \\
& \frac{\Phi^{\kappa}_{\text{seg}}(\boldsymbol{\pi}_{n+1}) - \Phi^{\kappa}_{\text{seg}}(\boldsymbol{\pi}_n) - \nabla\Phi^{\kappa}_{\text{seg}}(\boldsymbol{\pi}_{n+\frac{1}{2}})\Delta\boldsymbol{\pi}}{\|\Delta\boldsymbol{\pi}\|^2}\Delta\boldsymbol{\pi}
\end{aligned} \tag{5.90}$$

   where $\Delta\boldsymbol{\pi} = \boldsymbol{\pi}_{n+1} - \boldsymbol{\pi}_n$. On the other hand, $\overline{\overline{\nabla}}_{\pi}\, \boldsymbol{\Phi}(\boldsymbol{\pi}_n, \boldsymbol{\pi}_{n+1})$ consists of the contributions of the reformulated constraints $(4.48)_{2-5}$, using the same vector of invariants and the same definition for the discrete gradient.
2. A tremendous decrease of the size and the complexity of the system can be achieved by evaluating the convective coordinates $\boldsymbol{f}$ only at time t_n. The equations of motion

---

[¶] Here, D_{1-3} denotes the derivative with respect to the $1-3$ slot.

can now be recast in the form

$$\begin{aligned} \boldsymbol{q}_{n+1} - \boldsymbol{q}_n =& \Delta t \boldsymbol{v}_{n+\frac{1}{2}} \\ \boldsymbol{M}(\boldsymbol{v}_{n+1} - \boldsymbol{v}_n) =& - \Delta t \overline{\nabla} E(\boldsymbol{q}_n, \boldsymbol{q}_{n+1}) \\ & - \Delta t (D_1 \boldsymbol{\pi}(\boldsymbol{q}_{n+\frac{1}{2}}, \boldsymbol{d}_{n+\frac{1}{2}}, \boldsymbol{f}_n))^T \overline{\overline{\overline{\nabla}}}_{\pi} \, \boldsymbol{\Phi}(\boldsymbol{\pi}_n, \boldsymbol{\pi}_{n+1}) \cdot \boldsymbol{\lambda}_{n,n+1} \\ \boldsymbol{0} =& (D_2 \boldsymbol{\pi}(\boldsymbol{q}_{n+\frac{1}{2}}, \boldsymbol{d}_{n+\frac{1}{2}}, \boldsymbol{f}_n))^T \overline{\overline{\overline{\nabla}}}_{\pi} \, \boldsymbol{\Phi}(\boldsymbol{\pi}_n, \boldsymbol{\pi}_{n+1}) \cdot \boldsymbol{\lambda}_{n,n+1} \\ \boldsymbol{0} =& \boldsymbol{\Phi}(\boldsymbol{\pi}(\boldsymbol{q}_{n+1}, \boldsymbol{d}_{n+1}, \boldsymbol{f}_n)) \end{aligned} \tag{5.91}$$

Here, the constraints are assembled as follows

$$\boldsymbol{\Phi}(\boldsymbol{\pi}(\boldsymbol{q}_{n+1}, \boldsymbol{d}_{n+1}, \boldsymbol{f}_n)) = \begin{bmatrix} \boldsymbol{\Phi}_{\text{mortar}}(\boldsymbol{\pi}(\boldsymbol{q}_{n+1}, \boldsymbol{d}_{n+1}, \boldsymbol{f}_n)) \\ \boldsymbol{\Phi}_{\text{normal}}(\boldsymbol{\pi}(\boldsymbol{q}_{n+1}, \boldsymbol{d}_{n+1}, \boldsymbol{f}_n)) \end{bmatrix} \tag{5.92}$$

Note that the segments have to be generated merely once for each time step and are held constant until the next time step.

3. A further decrease of the size and the complexity of the system can be achieved by eliminating the augmentation of the normal vector and sacrificing exact conservation of energy. In particular, we retain the augmented coordinates $\boldsymbol{f}_n$ and make use of the cubic invariants $\breve{\boldsymbol{\pi}}$ (see (5.83)) instead of the quadratic invarinats

$$\begin{aligned} \boldsymbol{q}_{n+1} - \boldsymbol{q}_n =& \Delta t \boldsymbol{v}_{n+\frac{1}{2}} \\ \boldsymbol{M}(\boldsymbol{v}_{n+1} - \boldsymbol{v}_n) =& - \Delta t \overline{\nabla} E(\boldsymbol{q}_n, \boldsymbol{q}_{n+1}) \\ & - \Delta t (D_1 \breve{\boldsymbol{\pi}}(\boldsymbol{q}_{n+\frac{1}{2}}, \boldsymbol{f}_n))^T \nabla_{\breve{\pi}} \, \boldsymbol{\Phi}(\breve{\boldsymbol{\pi}}_n, \breve{\boldsymbol{\pi}}_{n+1}) \cdot \boldsymbol{\lambda}_{n,n+1} \\ \boldsymbol{0} =& \breve{\boldsymbol{\Phi}}_{\text{mortar}}(\breve{\boldsymbol{\pi}}(\boldsymbol{q}_{n+1}, \boldsymbol{f}_n)) \end{aligned} \tag{5.93}$$

Conservation properties. Again we focus on the constraint contributions and start with the conservation properties of the momentum maps for the first approach

$$\begin{aligned} \boldsymbol{\zeta} \cdot (\boldsymbol{L}_{n+1} - \boldsymbol{L}_n) &= \boldsymbol{\zeta} \cdot \sum_{A \in \bar{\omega}} \big(\boldsymbol{p}_{A,n+1} - \boldsymbol{p}_{A,n}\big) \\ &= \boldsymbol{\zeta} \cdot \sum_{A \in \bar{\omega}} (\partial_{\boldsymbol{q}_A} \boldsymbol{\pi}(\boldsymbol{q}_{n+\frac{1}{2}}, \boldsymbol{d}_{n+\frac{1}{2}}, \boldsymbol{f}_{n+\frac{1}{2}}))^T \overline{\overline{\overline{\nabla}}}_{\pi} \, \boldsymbol{\Phi}(\boldsymbol{\pi}_n, \boldsymbol{\pi}_{n+1}) \cdot \boldsymbol{\lambda}_{n,n+1} \\ &= 0 \end{aligned} \tag{5.94}$$

and

$$\begin{aligned} \boldsymbol{\zeta} \cdot (\boldsymbol{J}_{n+1} - \boldsymbol{J}_n) &= \boldsymbol{\zeta} \cdot \sum_{A \in \omega} \Big[\big(\boldsymbol{q}_{A,n+1} - \boldsymbol{q}_{A,n}\big) \times \boldsymbol{p}_{A,n+\frac{1}{2}} + \boldsymbol{q}_{A,n+\frac{1}{2}} \times \big(\boldsymbol{p}_{n+1} - \boldsymbol{p}_n\big)\Big] \\ &= -\Delta t \boldsymbol{\zeta} \cdot \sum_{A \in \omega} \Big[\boldsymbol{q}_{A,n+\frac{1}{2}} \times (\partial_{\boldsymbol{q}_A} \boldsymbol{\pi}(\boldsymbol{q}_{n+\frac{1}{2}}, \boldsymbol{d}_{n+\frac{1}{2}}, \boldsymbol{f}_{n+\frac{1}{2}}))^T \overline{\overline{\overline{\nabla}}}_{\pi} \, \boldsymbol{\Phi}(\boldsymbol{\pi}_n, \boldsymbol{\pi}_{n+1}) \cdot \boldsymbol{\lambda}_{n,n+1}\Big] \\ &= -\Delta t \boldsymbol{\lambda}_{n,n+1} \cdot \Big(\overline{\overline{\overline{\nabla}}}_{\pi} \, \boldsymbol{\Phi}(\boldsymbol{\pi}_n, \boldsymbol{\pi}_{n+1})\Big)^T \cdot \sum_{A \in \omega} (\partial_{\boldsymbol{q}_A} \boldsymbol{\pi}(\boldsymbol{q}_{n+\frac{1}{2}}, \boldsymbol{d}_{n+\frac{1}{2}}, \boldsymbol{f}_{n+\frac{1}{2}})) \cdot \hat{\boldsymbol{q}}_{A,n+\frac{1}{2}} \boldsymbol{\zeta} \end{aligned} \tag{5.95}$$

With regard to (5.88) we can state

$$\begin{aligned}\left(\overline{\overline{\nabla}}_\pi\, \boldsymbol{\Phi}(\boldsymbol{\pi}_n, \boldsymbol{\pi}_{n+1})\right)^T \cdot \Bigg[\sum_{A\in\bar{\omega}} (\partial_{\boldsymbol{q}_A}\boldsymbol{\pi}(\boldsymbol{q}_{n+\frac{1}{2}}, \boldsymbol{d}_{n+\frac{1}{2}}, \boldsymbol{f}_{n+\frac{1}{2}})) \cdot \hat{\boldsymbol{q}}_{A,n+\frac{1}{2}}\boldsymbol{\zeta} - \\ \sum_{B\in\omega_{\text{seg}}} (\partial_{\boldsymbol{d}_B}\boldsymbol{\pi}(\boldsymbol{q}_{n+\frac{1}{2}}, \boldsymbol{d}_{n+\frac{1}{2}}, \boldsymbol{f}_{n+\frac{1}{2}})) \cdot \hat{\boldsymbol{d}}_{B,n+\frac{1}{2}}\boldsymbol{\zeta}\Bigg] = \boldsymbol{0}\end{aligned} \tag{5.96}$$

and rewrite the last equation

$$\begin{aligned}&\boldsymbol{\zeta}\cdot(\boldsymbol{J}_{n+1} - \boldsymbol{J}_n)\\ &\quad=\Delta t\boldsymbol{\lambda}_{n,n+1}\cdot\left(\overline{\overline{\nabla}}_\pi\, \boldsymbol{\Phi}(\boldsymbol{\pi}_n, \boldsymbol{\pi}_{n+1})\right)^T \cdot \sum_{B\in\omega_{\text{seg}}}\left[(\partial_{\boldsymbol{d}_B}\boldsymbol{\pi}(\boldsymbol{q}_{n+\frac{1}{2}}, \boldsymbol{d}_{n+\frac{1}{2}}, \boldsymbol{f}_{n+\frac{1}{2}})) \cdot \hat{\boldsymbol{d}}_{B,n+\frac{1}{2}}\boldsymbol{\zeta}\right]\\ &\quad=\Delta t\boldsymbol{\zeta}\cdot\sum_{B\in\omega_{\text{seg}}}\boldsymbol{d}_{B,n+\frac{1}{2}}\times(\partial_{\boldsymbol{d}_B}\boldsymbol{\pi}(\boldsymbol{q}_{n+\frac{1}{2}}, \boldsymbol{d}_{n+\frac{1}{2}}, \boldsymbol{f}_{n+\frac{1}{2}}))^T\overline{\overline{\nabla}}_\pi\, \boldsymbol{\Phi}(\boldsymbol{\pi}_n, \boldsymbol{\pi}_{n+1})\cdot\boldsymbol{\lambda}_{n,n+1}\\ &\quad=0\end{aligned} \tag{5.97}$$

Next, we verify algorithmic conservation of energy. Since the original system deals with inequality constraints, an additional error in energy arises due to the application of the active set strategy. As shown in Hesch & Betsch [37], this error is negligible and can be treated as described in the afore mentioned paper. For the algorithmic conservation of energy the net power input to the system within each time step has to be zero. After a few calculations we receive

$$T_{n+1} - T_n + E_{n+1} - E_n = \boldsymbol{\lambda}_{n,n+1}\cdot D_1\boldsymbol{\pi}(\boldsymbol{q}_{n+\frac{1}{2}}, \boldsymbol{d}_{n+\frac{1}{2}}, \boldsymbol{f}_{n+\frac{1}{2}}))^T\overline{\overline{\nabla}}_\pi\, \boldsymbol{\Phi}(\boldsymbol{\pi}_n, \boldsymbol{\pi}_{n+1})\cdot(\boldsymbol{q}_{n+1} - \boldsymbol{q}_n) \tag{5.98}$$

Introducing the discrete consistency condition

$$\begin{aligned}D_1\boldsymbol{\pi}(\boldsymbol{q}_{n+\frac{1}{2}}, \boldsymbol{d}_{n+\frac{1}{2}}, \boldsymbol{f}_{n+\frac{1}{2}}))^T\overline{\overline{\nabla}}_\pi\, \boldsymbol{\Phi}(\boldsymbol{\pi}_n, \boldsymbol{\pi}_{n+1})(\boldsymbol{q}_{n+1} - \boldsymbol{q}_n)+&\\ D_2\boldsymbol{\pi}(\boldsymbol{q}_{n+\frac{1}{2}}, \boldsymbol{d}_{n+\frac{1}{2}}, \boldsymbol{f}_{n+\frac{1}{2}}))^T\overline{\overline{\nabla}}_\pi\, \boldsymbol{\Phi}(\boldsymbol{\pi}_n, \boldsymbol{\pi}_{n+1})(\boldsymbol{d}_{n+1} - \boldsymbol{d}_n)+&\\ D_3\boldsymbol{\pi}(\boldsymbol{q}_{n+\frac{1}{2}}, \boldsymbol{d}_{n+\frac{1}{2}}, \boldsymbol{f}_{n+\frac{1}{2}}))^T\overline{\overline{\nabla}}_\pi\, \boldsymbol{\Phi}(\boldsymbol{\pi}_n, \boldsymbol{\pi}_{n+1})(\boldsymbol{f}_{n+1} - \boldsymbol{f}_n) =&\\ \overline{\overline{\nabla}}_\pi\, \boldsymbol{\Phi}(\boldsymbol{\pi}_n, \boldsymbol{\pi}_{n+1})(\boldsymbol{\pi}_{n+1} - \boldsymbol{\pi}_n) =&\\ \boldsymbol{\Phi}(\boldsymbol{\pi}_{n+1}) - \boldsymbol{\Phi}(\boldsymbol{\pi}_n) =&\boldsymbol{0}\end{aligned} \tag{5.99}$$

we can show that

$$\begin{aligned}&T_{n+1} - T_n + E_{n+1} - E_n =\\ &\quad-\boldsymbol{\lambda}_{n,n+1}\cdot\Big[D_2\boldsymbol{\pi}(\boldsymbol{q}_{n+\frac{1}{2}}, \boldsymbol{d}_{n+\frac{1}{2}}, \boldsymbol{f}_{n+\frac{1}{2}}))^T\overline{\overline{\nabla}}_\pi\, \boldsymbol{\Phi}(\boldsymbol{\pi}_n, \boldsymbol{\pi}_{n+1})(\boldsymbol{d}_{n+1} - \boldsymbol{d}_n)+\\ &\quad D_3\boldsymbol{\pi}(\boldsymbol{q}_{n+\frac{1}{2}}, \boldsymbol{d}_{n+\frac{1}{2}}, \boldsymbol{f}_{n+\frac{1}{2}}))^T\overline{\overline{\nabla}}_\pi\, \boldsymbol{\Phi}(\boldsymbol{\pi}_n, \boldsymbol{\pi}_{n+1})(\boldsymbol{f}_{n+1} - \boldsymbol{f}_n)\Big]\\ &=0\end{aligned} \tag{5.100}$$

is valid. Thus, total energy is conserved. Similarly, the second approach yields for the momentum maps

$$\begin{aligned}\boldsymbol{\zeta}\cdot(\boldsymbol{L}_{n+1}-\boldsymbol{L}_n) &= \boldsymbol{\zeta}\cdot\sum_{A\in\bar{\omega}}\big(\boldsymbol{p}_{A,n+1}-\boldsymbol{p}_{A,n}\big)\\ &= \boldsymbol{\zeta}\cdot\sum_{A\in\bar{\omega}}(\partial_{\boldsymbol{q}_A}\boldsymbol{\pi}(\boldsymbol{q}_{n+\frac{1}{2}},\boldsymbol{d}_{n+\frac{1}{2}},\boldsymbol{f}_n))^T\overline{\overline{\nabla}}_{\pi}\,\boldsymbol{\Phi}(\boldsymbol{\pi}_n,\boldsymbol{\pi}_{n+1})\cdot\boldsymbol{\lambda}_{n,n+1}\\ &= 0\end{aligned}\tag{5.101}$$

and

$$\begin{aligned}\boldsymbol{\zeta}\cdot(\boldsymbol{J}_{n+1}-\boldsymbol{J}_n) &= \boldsymbol{\zeta}\cdot\sum_{A\in\omega}\Big[\big(\boldsymbol{q}_{A,n+1}-\boldsymbol{q}_{A,n}\big)\times\boldsymbol{p}_{A,n+\frac{1}{2}}+\boldsymbol{q}_{A,n+\frac{1}{2}}\times\big(\boldsymbol{p}_{n+1}-\boldsymbol{p}_n\big)\Big]\\ &= -\Delta t\boldsymbol{\zeta}\cdot\sum_{A\in\omega}\Big[\boldsymbol{q}_{A,n+\frac{1}{2}}\times(\partial_{\boldsymbol{q}_A}\boldsymbol{\pi}(\boldsymbol{q}_{n+\frac{1}{2}},\boldsymbol{d}_{n+\frac{1}{2}},\boldsymbol{f}_n))^T\overline{\overline{\nabla}}_{\pi}\,\boldsymbol{\Phi}(\boldsymbol{\pi}_n,\boldsymbol{\pi}_{n+1})\cdot\boldsymbol{\lambda}_{n,n+1}\Big]\\ &= -\Delta t\boldsymbol{\lambda}_{n,n+1}\cdot\Big(\overline{\overline{\nabla}}_{\pi}\,\boldsymbol{\Phi}(\boldsymbol{\pi}_n,\boldsymbol{\pi}_{n+1})\Big)^T\cdot\sum_{A\in\omega}(\partial_{\boldsymbol{q}_A}\boldsymbol{\pi}(\boldsymbol{q}_{n+\frac{1}{2}},\boldsymbol{d}_{n+\frac{1}{2}},\boldsymbol{f}_n))\cdot\hat{\boldsymbol{q}}_{A,n+\frac{1}{2}}\boldsymbol{\zeta}\end{aligned}\tag{5.102}$$

With regard to (5.88) we obtain immediately

$$\begin{aligned}&\Big(\overline{\overline{\nabla}}_{\pi}\,\boldsymbol{\Phi}(\boldsymbol{\pi}_n,\boldsymbol{\pi}_{n+1})\Big)^T\cdot\Bigg[\sum_{A\in\bar{\omega}}(\partial_{\boldsymbol{q}_A}\boldsymbol{\pi}(\boldsymbol{q}_{n+\frac{1}{2}},\boldsymbol{d}_{n+\frac{1}{2}},\boldsymbol{f}_n))\cdot\hat{\boldsymbol{q}}_{A,n+\frac{1}{2}}\boldsymbol{\zeta}-\\ &\qquad\qquad\sum_{B\in\omega_{\text{seg}}}(\partial_{\boldsymbol{d}_B}\boldsymbol{\pi}(\boldsymbol{q}_{n+\frac{1}{2}},\boldsymbol{d}_{n+\frac{1}{2}},\boldsymbol{f}_n))\cdot\hat{\boldsymbol{d}}_{B,n+\frac{1}{2}}\boldsymbol{\zeta}\Bigg]=\boldsymbol{0}\end{aligned}\tag{5.103}$$

and rewrite equation (5.102) as follows

$$\begin{aligned}&\boldsymbol{\zeta}\cdot(\boldsymbol{J}_{n+1}-\boldsymbol{J}_n)\\ &\quad=\Delta t\boldsymbol{\lambda}_{n,n+1}\cdot\Big(\overline{\overline{\nabla}}_{\pi}\,\boldsymbol{\Phi}(\boldsymbol{\pi}_n,\boldsymbol{\pi}_{n+1})\Big)^T\cdot\sum_{B\in\omega_{\text{seg}}}\Big[(\partial_{\boldsymbol{d}_B}\boldsymbol{\pi}(\boldsymbol{q}_{n+\frac{1}{2}},\boldsymbol{d}_{n+\frac{1}{2}},\boldsymbol{f}_n))\cdot\hat{\boldsymbol{d}}_{B,n+\frac{1}{2}}\boldsymbol{\zeta}\Big]\\ &\quad=\Delta t\boldsymbol{\zeta}\cdot\sum_{B\in\omega_{\text{seg}}}\boldsymbol{d}_{B,n+\frac{1}{2}}\times(\partial_{\boldsymbol{d}_B}\boldsymbol{\pi}(\boldsymbol{q}_{n+\frac{1}{2}},\boldsymbol{d}_{n+\frac{1}{2}},\boldsymbol{f}_n))^T\overline{\overline{\nabla}}_{\pi}\,\boldsymbol{\Phi}(\boldsymbol{\pi}_n,\boldsymbol{\pi}_{n+1})\cdot\boldsymbol{\lambda}_{n,n+1}\\ &\quad=0\end{aligned}\tag{5.104}$$

Again, both momentum maps are algorithmically conserved. For the total energy we get

$$T_{n+1}-T_n+E_{n+1}-E_n=\boldsymbol{\lambda}_{n,n+1}\cdot D_1\boldsymbol{\pi}(\boldsymbol{q}_{n+\frac{1}{2}},\boldsymbol{d}_{n+\frac{1}{2}},\boldsymbol{f}_n))^T\overline{\overline{\nabla}}_{\pi}\,\boldsymbol{\Phi}(\boldsymbol{\pi}_n,\boldsymbol{\pi}_{n+1})\cdot(\boldsymbol{q}_{n+1}-\boldsymbol{q}_n)\tag{5.105}$$

The discrete consistency condition reads

$$\begin{aligned}D_1\boldsymbol{\pi}(\boldsymbol{q}_{n+\frac{1}{2}},\boldsymbol{d}_{n+\frac{1}{2}},\boldsymbol{f}_n))^T\overline{\overline{\nabla}}_{\pi}\,\boldsymbol{\Phi}(\boldsymbol{\pi}_n,\boldsymbol{\pi}_{n+1})(\boldsymbol{q}_{n+1}-\boldsymbol{q}_n)+&\\ D_2\boldsymbol{\pi}(\boldsymbol{q}_{n+\frac{1}{2}},\boldsymbol{d}_{n+\frac{1}{2}},\boldsymbol{f}_n))^T\overline{\overline{\nabla}}_{\pi}\,\boldsymbol{\Phi}(\boldsymbol{\pi}_n,\boldsymbol{\pi}_{n+1})(\boldsymbol{d}_{n+1}-\boldsymbol{d}_n)=&\\ \overline{\overline{\nabla}}_{\pi}\,\boldsymbol{\Phi}(\boldsymbol{\pi}_n,\boldsymbol{\pi}_{n+1})(\boldsymbol{\pi}_{n+1}-\boldsymbol{\pi}_n)=&\\ \boldsymbol{\Phi}(\boldsymbol{\pi}_{n+1})-\boldsymbol{\Phi}(\boldsymbol{\pi}_n)=&\boldsymbol{0}\end{aligned}\tag{5.106}$$

and insertion in (5.105) yields

$$T_{n+1}-T_n+E_{n+1}-E_n = -\boldsymbol{\lambda}_{n,n+1}\cdot\Big[D_2\boldsymbol{\pi}(\boldsymbol{q}_{n+\frac{1}{2}},\boldsymbol{d}_{n+\frac{1}{2}},\boldsymbol{f}_n))^T\overline{\overline{\nabla}}_{\pi}\,\boldsymbol{\Phi}(\boldsymbol{\pi}_n,\boldsymbol{\pi}_{n+1})(\boldsymbol{d}_{n+1}-\boldsymbol{d}_n)\Big] = 0 \tag{5.107}$$

Thus, total energy is conserved. Furthermore, we can show for the third approach that

$$\begin{aligned}\boldsymbol{\zeta}\cdot(\boldsymbol{L}_{n+1}-\boldsymbol{L}_n) &= \boldsymbol{\zeta}\cdot\sum_{A\in\bar{\omega}}\big(\boldsymbol{p}_{A,n+1}-\boldsymbol{p}_{A,n}\big)\\ &= \boldsymbol{\zeta}\cdot\sum_{A\in\bar{\omega}}(\partial_{\boldsymbol{q}_A}\breve{\boldsymbol{\pi}}(\boldsymbol{q}_{n+\frac{1}{2}},\boldsymbol{f}_n))^T\nabla_{\breve{\pi}}\,\breve{\boldsymbol{\Phi}}(\breve{\boldsymbol{\pi}}_n,\breve{\boldsymbol{\pi}}_{n+1})\cdot\boldsymbol{\lambda}_{n,n+1}\\ &= 0\end{aligned} \tag{5.108}$$

and

$$\begin{aligned}\boldsymbol{\zeta}\cdot(\boldsymbol{J}_{n+1}-\boldsymbol{J}_n) = \boldsymbol{\zeta}\cdot\sum_{A\in\omega}&\Big[\big(\boldsymbol{q}_{A,n+1}-\boldsymbol{q}_{A,n}\big)\times\boldsymbol{p}_{A,n+\frac{1}{2}}+\boldsymbol{q}_{A,n+\frac{1}{2}}\times\big(\boldsymbol{p}_{n+1}-\boldsymbol{p}_n\big)\Big]\\ = -\Delta t\boldsymbol{\zeta}\cdot\sum_{A\in\omega}&\Big[\boldsymbol{q}_{A,n+\frac{1}{2}}\times(\partial_{\boldsymbol{q}_A}\breve{\boldsymbol{\pi}}(\boldsymbol{q}_{n+\frac{1}{2}},\boldsymbol{f}_n))^T\nabla_{\breve{\pi}}\,\breve{\boldsymbol{\Phi}}(\breve{\boldsymbol{\pi}}_n,\breve{\boldsymbol{\pi}}_{n+1})\cdot\boldsymbol{\lambda}_{n,n+1}\Big]\\ = -\Delta t\boldsymbol{\lambda}_{n,n+1}\cdot&\Big(\nabla_{\breve{\pi}}\,\breve{\boldsymbol{\Phi}}(\breve{\boldsymbol{\pi}}_n,\breve{\boldsymbol{\pi}}_{n+1})\Big)^T\cdot\sum_{A\in\omega}(\partial_{\boldsymbol{q}_A}\breve{\boldsymbol{\pi}}(\boldsymbol{q}_{n+\frac{1}{2}},\boldsymbol{f}_n))\cdot\hat{\boldsymbol{q}}_{A,n+\frac{1}{2}}\boldsymbol{\zeta}\\ = 0&\end{aligned} \tag{5.109}$$

Accordingly, both momentum maps are algorithmically conserved. Since we can not apply the concept of a discrete gradient, total energy is not conserved.

5.3 Frictional contact

Next, we focus on frictional contact problems (see Franke et al. [21]). As before, we establish the definition of the closest point projection

$$\|\boldsymbol{\varphi}^{(1)}(\boldsymbol{X}^{(1)})-\boldsymbol{\varphi}^{(2)}(\bar{\boldsymbol{X}}^{(2)}(\boldsymbol{X}^{(1)}))\|\rightarrow\min \tag{5.110}$$

where $\boldsymbol{\varphi}^{(2)}(\bar{\boldsymbol{X}}^{(2)}(\boldsymbol{X}^{(1)}))$ is the closest point to $\boldsymbol{\varphi}^{(1)}(\boldsymbol{X}^{(1)})$. The projection is characterized by the convective coordinates

$$\bar{\boldsymbol{\varphi}}^{(2)} := \boldsymbol{\varphi}^{(2)}(\bar{\boldsymbol{\xi}}),\quad \bar{\boldsymbol{\xi}} = [\bar{\xi}^1,\bar{\xi}^2] \tag{5.111}$$

where $\bar{\xi}^\alpha$ are calculated from (5.110). We further introduce tangent vectors

$$\boldsymbol{a}_\alpha := \boldsymbol{\varphi}^{(2)}_{,\alpha}(\bar{\boldsymbol{\xi}}) \tag{5.112}$$

where $(\bullet)_{,\alpha}$ denotes the derivative with respect to ξ^α. Note that the vectors $\boldsymbol{a}_\alpha$ are directed tangentially along the coordinate curves ξ^α at $\bar{\boldsymbol{\varphi}}^{(2)}$. Associated dual vectors are defined by

$$\boldsymbol{a}^\alpha = m^{\alpha\beta}\boldsymbol{a}_\beta \tag{5.113}$$

where $m^{\alpha\beta} = (m_{\alpha\beta})^{-1}$ is the inverse of the metric $m_{\alpha\beta} = \boldsymbol{a}_\alpha \cdot \boldsymbol{a}_\beta$. The definition of the gap function as well as the corresponding Karush-Kuhn-Tucker conditions in normal direction remains, such that we can decompose the contact traction in (5.4) into the normal and the tangential part

$$\boldsymbol{t}^{\mathrm{h}} = t_N\,\boldsymbol{n} + \boldsymbol{t}_T \tag{5.114}$$

and require that $\boldsymbol{t}_T \cdot \boldsymbol{n} = 0$ and $\boldsymbol{t}_T = t_{T_\alpha}\boldsymbol{a}^\alpha$. The corresponding frictional constitutive law to define the tractions t_{T_α} will be dealt with in the appendix.

Summarizing, the contact contribution to the virtual work can now be written in the form

$$G^c(\boldsymbol{\varphi}, \delta\boldsymbol{\varphi}) = \langle \left[\delta\boldsymbol{\varphi}^{(1)} - \delta\bar{\boldsymbol{\varphi}}^{(2)}\right], [t_N\,\boldsymbol{n} + t_{T_\alpha}\boldsymbol{a}^\alpha] \rangle_{\partial\mathcal{B}^{\mathrm{h},(1),c}} \tag{5.115}$$

The last statement depends crucially on the variation of the convective coordinates $\bar{\boldsymbol{\xi}}$ on which we will focus next. In particular, we outline the most common approach, referred to as the *direct approach* in the following (see [47]) and present subsequently a new augmentation technique for the description of the frictional kinematics.

Direct approach The convective coordinates $\bar{\boldsymbol{\xi}} = [\bar{\xi}^1, \bar{\xi}^2]$ can be obtained from the solution of the minimum distance problem (5.110). Correspondingly, the orthogonality condition

$$\left(\boldsymbol{\varphi}^{(1)} - \bar{\boldsymbol{\varphi}}^{(2)}\right) \cdot \boldsymbol{a}_\alpha = 0, \quad \forall \alpha \in \{1,\, 2\} \tag{5.116}$$

has to be valid. Computing the time derivative of the last equation yields

$$(\dot{\boldsymbol{\varphi}}^{(1)} - \dot{\bar{\boldsymbol{\varphi}}}^{(2)} - \boldsymbol{a}_\beta \dot{\bar{\xi}}^\beta) \cdot \boldsymbol{a}_\alpha + \left(\boldsymbol{\varphi}^{(1)} - \bar{\boldsymbol{\varphi}}^{(2)}\right) \cdot \left(\dot{\boldsymbol{a}}_\alpha + \boldsymbol{a}_{\alpha\beta}\dot{\bar{\xi}}^\beta\right) = 0 \tag{5.117}$$

Using the unit length of the normal vector, i.e. $\boldsymbol{n} \cdot \boldsymbol{n} = 1$ together with $(\boldsymbol{\varphi}^{(1)} - \bar{\boldsymbol{\varphi}}^{(2)}) = g\boldsymbol{n}$, we can rearrange the terms in (5.117) and obtain the rate of change of the convective coordinates

$$\dot{\bar{\xi}}^\beta = A^{\alpha\beta}\;\left[\left(\dot{\boldsymbol{\varphi}}^{(1)} - \dot{\bar{\boldsymbol{\varphi}}}^{(2)}\right) \cdot \boldsymbol{a}_\alpha + g\,\boldsymbol{n} \cdot \dot{\bar{\boldsymbol{\varphi}}}^{(2)}_{,\alpha}\right] \tag{5.118}$$

where $A^{\alpha\beta}$ denotes the inverse of $A_{\alpha\beta} := m_{\alpha\beta} - g\,h_{\alpha\beta}$ and $h_{\alpha\beta} = \boldsymbol{a}_{\alpha\beta} \cdot \boldsymbol{n}$ is the curvature of the surface. Replacing the velocity by the variation yields

$$\delta\bar{\xi}^\beta = A^{\alpha\beta}\;\left[\left(\delta\boldsymbol{\varphi}^{(1)} - \delta\bar{\boldsymbol{\varphi}}^{(2)}\right) \cdot \boldsymbol{a}_\alpha + g\,\boldsymbol{n} \cdot \delta\bar{\boldsymbol{\varphi}}^{(2)}_{,\alpha}\right] \tag{5.119}$$

Assuming that $g = 0$ is valid at the contact interface, the variation of $\bar{\xi}^\alpha$ boils down to

$$\delta\bar{\xi}^\alpha = \left(\delta\boldsymbol{\varphi}^{(1)} - \delta\bar{\boldsymbol{\varphi}}^{(2)}\right) \cdot \boldsymbol{a}^\alpha \tag{5.120}$$

Accordingly, the virtual work expression (5.115) can be recast in the form

$$G^c(\boldsymbol{\varphi}, \delta\boldsymbol{\varphi}) = \int\limits_{\partial\mathcal{B}^{\mathrm{h},(1),c}} \left(t_N \delta g + t_{T_\alpha}\delta\bar{\xi}^\alpha\right)\;\mathrm{d}A \tag{5.121}$$

The majority of previous works dealing with large deformation frictional contact problems rely on (5.121) (see Wriggers [77]). Note that statement (5.121) holds true if (5.119) is used instead of (5.120), since the additional terms to be considered only redefine the tractions t_{T_α} in tangential direction.

Coordinate augmentation technique Following the arguments in Hesch & Betsch [37] we extend a specific coordinate augmentation technique to frictional contact problems. This technique relies on the introduction of additional coordinates $\mathfrak{f} = [f^1,\ f^2] \in \mathbb{R}^2$ which represent the convective coordinates $[\xi^1,\ \xi^2]$. To link the new coordinates to the original ones, we introduce two constraint functions

$$\boldsymbol{\Phi}^{\text{aug}}(\boldsymbol{\varphi},\mathfrak{f}) = \begin{bmatrix} \left(\boldsymbol{\varphi}^{(1)} - \boldsymbol{\varphi}^{(2)}(\mathfrak{f})\right) \cdot \boldsymbol{a}_1(\mathfrak{f}) \\ \left(\boldsymbol{\varphi}^{(1)} - \boldsymbol{\varphi}^{(2)}(\mathfrak{f})\right) \cdot \boldsymbol{a}_2(\mathfrak{f}) \end{bmatrix} \tag{5.122}$$

and require that $\boldsymbol{\Phi}^{\text{aug}} = \boldsymbol{0}$. Similar to definition (5.112) for the tangent vectors, in (5.122), $\boldsymbol{a}_\alpha(\mathfrak{f}) = \boldsymbol{\varphi}^{(2)}_{,\alpha}(\mathfrak{f})$ for $\alpha = 1, 2$. Analogous to the definition of the gap function in the previous Section we introduce

$$\tilde{g}(\boldsymbol{\varphi},\mathfrak{f}) = \left(\boldsymbol{\varphi}^{(1)} - \boldsymbol{\varphi}^{(2)}(\mathfrak{f})\right) \cdot \tilde{\boldsymbol{n}}(\mathfrak{f}) \tag{5.123}$$

The contact contribution to the virtual work can now be determined along the lines of the direct approach. Accordingly, similar to (5.121), we obtain

$$G^c(\boldsymbol{\varphi},\mathfrak{f},\delta\boldsymbol{\varphi},\delta\mathfrak{f}) = \int\limits_{\Gamma_c^{(1)}} \left(t_N \delta\tilde{g} + t_{T_\alpha}\delta f^\alpha)\right)\ \mathrm{d}A \tag{5.124}$$

where $\delta\tilde{g} = (\delta\boldsymbol{\varphi}^{(1)} - \delta\boldsymbol{\varphi}^{(2)}(\mathfrak{f})) \cdot \tilde{\boldsymbol{n}}(\mathfrak{f})$. It is important to realize that the augmented coordinates $\mathfrak{f}$ are to be viewed as primary variables on an equal footing with the original variables $\boldsymbol{\varphi}$. Consequently, the newly proposed augmentation technique strongly affects the discretization in space and time. Indeed, it will be shown in the sequel that the newly proposed augmentation technique simplifies the implementation significantly when compared to the direct approach.

Spatial discretization Analogous to the approximations of the solution and the test space in 2.1 we define the following approximations at the contact boundaries

$$\boldsymbol{\varphi}_c^{(i),h} = \sum_{I\in\bar{\omega}} \hat{N}^I \boldsymbol{q}_I^{(i)}, \quad \delta\boldsymbol{\varphi}_c^{(i),h} = \sum_{J\in\bar{\omega}} \hat{N}^J\, \delta\boldsymbol{q}_J^{(i)} \tag{5.125}$$

where $\hat{N}_I$ denote bilinear shape functions at the corresponding node $I \in \bar{\omega}$, representing the set of all nodes on the contact interface. Using the direct approach, we have to compute the convected coordinates $\bar{\xi}^1, \bar{\xi}^2$ internally within each NTS element A by solving

$$\begin{bmatrix} \left(\boldsymbol{q}_s^{(1)} - \boldsymbol{q}_s^{(2)}(\bar{\xi}^1,\bar{\xi}^2)\right) \cdot \boldsymbol{a}_1(\bar{\xi}^1,\bar{\xi}^2) \\ \left(\boldsymbol{q}_s^{(1)} - \boldsymbol{q}_s^{(2)}(\bar{\xi}^1,\bar{\xi}^2)\right) \cdot \boldsymbol{a}_2(\bar{\xi}^1,\bar{\xi}^2) \end{bmatrix} = \boldsymbol{0} \tag{5.126}$$

for the convective coordinates using a Newton-Raphson iteration. The discrete nodal gap function g_s^h reads

$$g_s^h(\boldsymbol{q}_A) = \left(\boldsymbol{q}_s^{(1)} - \boldsymbol{q}_s^{(2)}(\bar{\xi}^1,\bar{\xi}^2)\right) \cdot \boldsymbol{n}(\bar{\xi}^1,\bar{\xi}^2) \tag{5.127}$$

using the set of nodes $\eta_{NTS} := \{\boldsymbol{q}_A\} = \{\boldsymbol{q}_s^{(1)},\ \boldsymbol{q}_1^{(2)},\ \boldsymbol{q}_2^{(2)},\ \boldsymbol{q}_3^{(2)},\ \boldsymbol{q}_4^{(2)}\}$. Employing the discrete nodal gap function we can define the constraint function in normal direction

$$\bar{\Phi}^{\mathrm{n}}(\boldsymbol{q}_A) = \int\limits_{\Gamma_c^{(1)}} g_s^h \,\mathrm{d}A \tag{5.128}$$

along with the Lagrange multipliers $\bar{\lambda}^n$ which can be viewed as discrete counterpart of the normal traction t_N. The corresponding tangential tractions are dealt with in Appendix C for the case of Coulombs law. Similar to the kinematic relationship (5.119), the variation of the convective coordinates in the discrete setting reads

$$\delta \bar{\xi}_s^{\alpha,h} = A^{\alpha\beta}\left[\left(\delta \boldsymbol{q}_s^{(1)} - \delta \bar{\boldsymbol{q}}_s^{(2)}\right)\cdot \boldsymbol{a}_\beta + g^h \boldsymbol{n}\cdot \delta \boldsymbol{a}_\beta\right] \tag{5.129}$$

If we assume that the gap is zero, we obtain

$$\delta \bar{\xi}_s^{\alpha,h} = A^{\alpha\beta}\left(\delta \boldsymbol{q}_s^{(1)} - \delta \bar{\boldsymbol{q}}_s^{(2)}\right)\cdot \boldsymbol{a}_\beta \tag{5.130}$$

and the corresponding discrete virtual contact work for a single NTS element reads

$$G_s^{c,h} = \int\limits_{\Gamma_c^{(1)}} \left(t_N \delta g_s^h + t_{T_\alpha}\delta \bar{\xi}_s^{\alpha,h}\right)\,\mathrm{d}A \tag{5.131}$$

Next, we rearrange the frictional contributions using a single vector $\delta \boldsymbol{q}\cdot \boldsymbol{f}^{\mathrm{fric}}$. Furthermore, we collect all normal constraints in a single vector $\boldsymbol{\Phi}^n(\boldsymbol{q})$ and assemble the associated Lagrange multipliers in the vector $\boldsymbol{\lambda}^{\mathrm{n}}$. Then, the semi-discrete equations of motion reads

$$\begin{aligned}\boldsymbol{0} &= \boldsymbol{M}\ddot{\boldsymbol{q}} + \nabla_{\boldsymbol{q}} V(\boldsymbol{q}) + \nabla_{\boldsymbol{q}}\left(\boldsymbol{\Phi}^{\mathrm{n}}(\boldsymbol{q})\cdot \boldsymbol{\lambda}^{\mathrm{n}}\right) + \boldsymbol{f}^{\mathrm{fric}}(\boldsymbol{q})\\ \boldsymbol{0} &= \boldsymbol{\Phi}^{\mathrm{n}}(\boldsymbol{q})\end{aligned} \tag{5.132}$$

Coordinate augmentation technique Next we apply the coordinate augmentation technique described in Section 5.3 to the NTS element. In contrast to the direct approach, we calculate the convective coordinates on a global level, i.e. we do not solve the algebraic system of equations in (5.126) internally, but enforce them as additional constraints

$$\bar{\boldsymbol{\Phi}}^{\mathrm{aug}}(\boldsymbol{q}_A, \mathfrak{f}_A) = \begin{bmatrix}\left(\boldsymbol{q}^{(1)} - \boldsymbol{q}^{(2)}(\mathfrak{f}_A)\right)\cdot \boldsymbol{a}_1(\mathfrak{f}_A)\\ \left(\boldsymbol{q}^{(1)} - \boldsymbol{q}^{(2)}(\mathfrak{f}_A)\right)\cdot \boldsymbol{a}_2(\mathfrak{f}_A)\end{bmatrix} \tag{5.133}$$

Here, we make use of a vector $\mathfrak{f}_A \in \mathbb{R}^2$ for each NTS element, representing the convective coordinates $[\bar{\xi}^1,\ \bar{\xi}^2]$. The associated Lagrange multipliers are given by $\bar{\boldsymbol{\lambda}}^{\mathrm{aug}}$. In addition to that, the constraints in normal direction are given by

$$\bar{\Phi}^{\mathrm{n}}(\boldsymbol{q}_A, \mathfrak{f}_A) = \left(\boldsymbol{q}_s^{(1)} - \boldsymbol{q}_s^{(2)}(\mathfrak{f}_A)\right)\cdot \boldsymbol{n}(\mathfrak{f}_A) \tag{5.134}$$

As before, we collect all data in global vectors, i.e. we collect all augmented coordinates in a single vector $\mathfrak{f} \in \mathbb{R}^l$, where l denotes the number of all convective coordinates. Furthermore, the augmented constraints (5.133) are arranged in a single vector $\boldsymbol{\Phi}^{\text{aug}}(\boldsymbol{q},\mathfrak{f}) \in \mathbb{R}^l$ and the associated Lagrange multipliers in a single vector $\boldsymbol{\lambda}^{\text{aug}} \in \mathbb{R}^l$. The semi-discrete equations of motion can now be written as follows

$$\begin{aligned} \mathbf{0} &= \boldsymbol{M}\ddot{\boldsymbol{q}} + \nabla_{\boldsymbol{q}}\, V(\boldsymbol{q}) + \nabla_{\boldsymbol{q}}\left(\boldsymbol{\Phi}(\boldsymbol{q},\mathfrak{f})\cdot\boldsymbol{\lambda}\right) \\ \mathbf{0} &= \nabla_{\mathfrak{f}}\left(\boldsymbol{\Phi}(\boldsymbol{q},\mathfrak{f})\cdot\boldsymbol{\lambda}\right) + \boldsymbol{f}^{\text{aug}}(\boldsymbol{q},\mathfrak{f}) \\ \mathbf{0} &= \boldsymbol{\Phi}(\boldsymbol{q},\mathfrak{f}) \end{aligned} \tag{5.135}$$

where $\boldsymbol{\Phi}(\boldsymbol{q},\mathfrak{f}) = [\boldsymbol{\Phi}^{\text{aug}},\, \boldsymbol{\Phi}^{\text{n}}]^T \in \mathbb{R}^m$ and $\boldsymbol{\lambda} = [\boldsymbol{\lambda}^{\text{aug}},\, \boldsymbol{\lambda}^{\text{n}}]^T \in \mathbb{R}^m$. Furthermore, $\boldsymbol{f}^{\text{aug}}(\boldsymbol{q},\mathfrak{f}) = [t_{T_1},\dots,t_{T_n}]^T \in \mathbb{R}^l$ combines the frictional tractions in a single vector.

To implement the newly proposed method in an efficient way, we eliminate the additional Lagrange multipliers $\boldsymbol{\lambda}^{\text{aug}}$ using the algebraic condition $(5.135)_2$. For a single NTS element, this condition reads

$$\nabla_{\mathfrak{f}_{\text{A}}}\left(\bar{\boldsymbol{\Phi}}^{\text{aug}}\cdot\bar{\boldsymbol{\lambda}}^{\text{aug}}\right) + \nabla_{\mathfrak{f}_{\text{A}}}\,\bar{\Phi}^n\bar{\lambda}^n + \bar{\boldsymbol{f}}^{\text{aug}} = \mathbf{0} \tag{5.136}$$

where $\bar{\boldsymbol{f}}^{\text{aug}} = [t_{T_1},\, t_{T_2}]^T \in \mathbb{R}^2$ represents the tangential tractions of the corresponding NTS element. The Lagrange multipliers can now be calculated analytically as follows

$$\bar{\boldsymbol{\lambda}}^{\text{aug}} = -\left(\nabla_{\mathfrak{f}_{\text{A}}}\,\bar{\boldsymbol{\Phi}}^{\text{aug}}\right)^{-1}\cdot\left(\nabla_{\mathfrak{f}_{\text{A}}}\,\bar{\Phi}^n\bar{\lambda}^n + \bar{\boldsymbol{f}}^{\text{aug}}\right) \tag{5.137}$$

Accordingly, on the level of each NTS element, the Lagrange multipliers associated with the augmented coordinates can be expressed in terms of the extended set of coordinates $\boldsymbol{q}_A$, $\mathfrak{f}_A$ and the contact traction $\bar{\lambda}^n$ in normal direction. Using (5.137) for each NTS element the vector $\bar{\boldsymbol{\lambda}}^{\text{aug}}$ of Lagrange multipliers can be eliminated from the semi-discrete equations of motion (5.135). Accordingly, we arrive at

$$\begin{aligned} \mathbf{0} &= \boldsymbol{M}\ddot{\boldsymbol{q}} + \nabla_{\boldsymbol{q}}\, V(\boldsymbol{q}) + \left(\mathfrak{P}\nabla_{\mathfrak{f}}\,\boldsymbol{\Phi}^n(\boldsymbol{q},\mathfrak{f}) + \nabla_{\boldsymbol{q}}\,\boldsymbol{\Phi}^n(\boldsymbol{q},\mathfrak{f})\right)\cdot\boldsymbol{\lambda}^n + \mathfrak{P}\boldsymbol{f}^{\text{aug}}(\boldsymbol{q},\mathfrak{f}) \\ \mathbf{0} &= \boldsymbol{\Phi}(\boldsymbol{q},\mathfrak{f}) \end{aligned} \tag{5.138}$$

where the block diagonal matrix $\mathfrak{P} = \operatorname{diag}(\bar{\mathfrak{P}}_1,\, \dots,\, \bar{\mathfrak{P}}_n)$ consists of the local projection matrix

$$\bar{\mathfrak{P}} = -\nabla_{q_{\text{A}}}\,\bar{\boldsymbol{\Phi}}^{\text{aug}}\left(\nabla_{\mathfrak{f}_{\text{A}}}\,\bar{\boldsymbol{\Phi}}^{\text{aug}}\right)^{-1} \tag{5.139}$$

for each NTS element. Note that $\nabla_{\mathfrak{f}}\,\boldsymbol{\Phi}^n = \mathbf{0}$ is valid at the solution point and we obtain the simplified system

$$\begin{aligned} \mathbf{0} &= \boldsymbol{M}\ddot{\boldsymbol{q}} + \nabla_{\boldsymbol{q}}\, V(\boldsymbol{q}) + \nabla_{\boldsymbol{q}}\left(\boldsymbol{\Phi}^n(\boldsymbol{q},\mathfrak{f})\cdot\boldsymbol{\lambda}^n\right) + \mathfrak{P}\boldsymbol{f}^{\text{aug}}(\boldsymbol{q},\mathfrak{f}) \\ \mathbf{0} &= \boldsymbol{\Phi}(\boldsymbol{q},\mathfrak{f}) \end{aligned} \tag{5.140}$$

The last set of equations defines the residual $[\boldsymbol{R}_q,\, \boldsymbol{\Phi}]\text{T}$, which we have to solve with respect to $\boldsymbol{q} \in \mathbb{R}^n$, $\mathfrak{f} \in \mathbb{R}^l$ and $\boldsymbol{\lambda}^n \in \mathbb{R}^{m-l}$. This first reduction step can be written in matrix notation using the modified projection matrix

$$\widetilde{\boldsymbol{\mathcal{P}}} = \begin{bmatrix} \boldsymbol{I}^{n\times n} & \mathfrak{P} & \mathbf{0}^{n\times m} \\ \mathbf{0}^{m\times n} & \mathbf{0}^{m\times l} & \boldsymbol{I}^{m\times m} \end{bmatrix} \in \mathbb{R}^{(n+m)\times(n+l+m)} \tag{5.141}$$

where n denotes the number of degrees of freedom of the configuration $\boldsymbol{q}$, m the number of constraints $\boldsymbol{\Phi} = [\boldsymbol{\Phi}^{\mathrm{aug}}, \boldsymbol{\Phi}^{\mathrm{n}}]$ and l the number of augmented coordinates $\mathfrak{f}$. Premultiplication of (5.135) by the projection matrix in (5.141) yields (5.140).

In a second step, we eliminate the augmented coordinates within the Newton-Raphson iteration

$$\begin{bmatrix} \boldsymbol{K}_{qq} & \boldsymbol{K}_{q\mathfrak{f}} & \nabla_{\boldsymbol{q}}\, \boldsymbol{\Phi}^n \\ \nabla_{\boldsymbol{q}}{}^T \boldsymbol{\Phi} & \nabla_{\mathfrak{f}}{}^T \boldsymbol{\Phi} & \boldsymbol{0} \end{bmatrix} \cdot \begin{bmatrix} \Delta \boldsymbol{q} \\ \Delta \mathfrak{f} \\ \Delta \boldsymbol{\lambda}^n \end{bmatrix} = \begin{bmatrix} \boldsymbol{R}_q \\ \boldsymbol{\Phi} \end{bmatrix} \tag{5.142}$$

used to solve (5.140). Here, $\boldsymbol{K}_{qq}$ and $\boldsymbol{K}_{q\mathfrak{f}}$ denotes the derivative of $\boldsymbol{R}_{\boldsymbol{q}}$ with respect to $\boldsymbol{q}$ and $\mathfrak{f}$, respectively. Next, we extract the equations for the augmented constraints of a single NTS element from (5.142)

$$\nabla_{\boldsymbol{q}_{\mathrm{A}}}{}^T \bar{\boldsymbol{\Phi}}^{\mathrm{aug}} \Delta \boldsymbol{q}_A + \nabla_{\mathfrak{f}_{\mathrm{A}}}{}^T \bar{\boldsymbol{\Phi}}^{\mathrm{aug}} \Delta \mathfrak{f}_A = \bar{\boldsymbol{\Phi}}^{\mathrm{aug}} \tag{5.143}$$

and solve this last equation with respect to $\Delta\mathfrak{f}_A$, such that we obtain

$$\begin{aligned} \Delta \mathfrak{f}_A &= \left(\nabla_{\mathfrak{f}_{\mathrm{A}}}{}^T \bar{\boldsymbol{\Phi}}^{\mathrm{aug}}\right)^{-1} \bar{\boldsymbol{\Phi}}^{\mathrm{aug}} - \left(\nabla_{\mathfrak{f}_{\mathrm{A}}}{}^T \bar{\boldsymbol{\Phi}}^{\mathrm{aug}}\right)^{-1} \nabla_{\boldsymbol{q}_{\mathrm{A}}}{}^T \bar{\boldsymbol{\Phi}}^{\mathrm{aug}} \Delta \boldsymbol{q}_A \\ &= \left(\nabla_{\mathfrak{f}_{\mathrm{A}}}{}^T \bar{\boldsymbol{\Phi}}^{\mathrm{aug}}\right)^{-1} \bar{\boldsymbol{\Phi}}^{\mathrm{aug}} + \bar{\boldsymbol{\mathfrak{P}}}^T \Delta \boldsymbol{q}_A \end{aligned} \tag{5.144}$$

Insertion in (5.142) yields the reduced system

$$\begin{bmatrix} \boldsymbol{K}_{qq} + \boldsymbol{K}_{q\mathfrak{f}} \boldsymbol{\mathfrak{P}}^T & \nabla_{\boldsymbol{q}}\, \boldsymbol{\Phi}^n \\ \nabla_{\boldsymbol{q}}{}^T \boldsymbol{\Phi}^n & \boldsymbol{0} \end{bmatrix} \cdot \begin{bmatrix} \Delta \boldsymbol{q} \\ \Delta \boldsymbol{\lambda}^n \end{bmatrix} = \begin{bmatrix} \boldsymbol{R}_q - \boldsymbol{K}_{q\mathfrak{f}} \left(\nabla_{\mathfrak{f}}{}^T \bar{\boldsymbol{\Phi}}^{\mathrm{aug}}\right)^{-1} \boldsymbol{\Phi}^{\mathrm{aug}} \\ \boldsymbol{\Phi}^n \end{bmatrix} \tag{5.145}$$

The last reduction step can also be written in matrix notation using

$$\bar{\boldsymbol{\mathcal{P}}} = \begin{bmatrix} \boldsymbol{I}^{n\times n} & \boldsymbol{\mathfrak{P}} & \boldsymbol{0}^{n\times(m-l)} \\ \boldsymbol{0}^{(m-l)\times n} & \boldsymbol{0}^{(m-l)\times l} & \boldsymbol{I}^{(m-l)\times(m-l)} \end{bmatrix} \in \mathbb{R}^{(n+m-l)\times(n+m)} \tag{5.146}$$

It is important to remark, that the whole reduction procedure can be carried out on element level for each single NTS-element, since $\boldsymbol{\mathfrak{P}}$ is block diagonal. The convective coordinates can be recovered using (5.144). The consistent linearization can now be carried out in two different ways:

1. As shown in (5.142) we have to linearize $(5.140)_1$ with respect to the configuration $\boldsymbol{q}$ and the augmented coordinates $\mathfrak{f}$. The involved constraints (5.133) and (5.134) are at most quadratic in the configuration and in the augmented coordinates, thus the only terms of higher order to be derived depend on the used constitutive law $\boldsymbol{f}^{\mathrm{aug}}$ (this derivative is always necessary) and the 2×2 inverse matrix $(\nabla_{\mathfrak{f}_{\mathrm{A}}}{}^T \bar{\boldsymbol{\Phi}}^{\mathrm{aug}})^{-1}$, i.e. we have to linearize $\boldsymbol{\mathfrak{P}}$.
2. In (5.140) we have used the projection matrix $\widetilde{\boldsymbol{\mathcal{P}}}$ to obtain a new residual, which we have to linearize to obtain the $(n + m) \times (n + m)$ matrix in (5.142). Alternatively we can pre-multiply the full linearized original system (5.135) by $\widetilde{\boldsymbol{\mathcal{P}}}$ and obtain

$$\begin{bmatrix} \boldsymbol{K}^o_{qq} + \boldsymbol{\mathfrak{P}} \boldsymbol{K}^o_{\mathfrak{f}q} & \boldsymbol{K}^o_{q\mathfrak{f}} + \boldsymbol{\mathfrak{P}} \boldsymbol{K}^o_{\mathfrak{f}\mathfrak{f}} & \nabla_{\boldsymbol{q}}\, \boldsymbol{\Phi} + \boldsymbol{\mathfrak{P}} \nabla_{\mathfrak{f}}\, \boldsymbol{\Phi} \\ \nabla_{\boldsymbol{q}}{}^T \boldsymbol{\Phi} & \nabla_{\mathfrak{f}}{}^T \boldsymbol{\Phi} & \boldsymbol{0} \end{bmatrix} \cdot \begin{bmatrix} \Delta \boldsymbol{q} \\ \Delta \mathfrak{f} \\ \Delta \boldsymbol{\lambda} \end{bmatrix} = \widetilde{\boldsymbol{\mathcal{P}}} \begin{bmatrix} \boldsymbol{R}^o_q \\ \boldsymbol{R}^o_{\mathfrak{f}} \\ \boldsymbol{\Phi} \end{bmatrix} \tag{5.147}$$

where terms labeled by the upper index $(\bullet)^o$ represent the contributions arising from $(5.135)_1$ and $(5.135)_2$. Next, we remove $\Delta\boldsymbol{\lambda}^{\text{aug}}$ and the corresponding columns from the system, since we solve directly for $\boldsymbol{\lambda}^{\text{aug}}$ using (5.137). The second reduction step follows as before, now avoiding the linearization of $\boldsymbol{\mathfrak{P}}$. Note, that we take again advantage of its blockdiagonal structure, such that all steps can be carried for each contact element.

The linearization is extremely simplified, compared with traditional methods, where we need to calculate the linearization of the variation of the convective coordinates (cf. Laursen [52])

$$\begin{aligned}\Delta\,\delta\bar{\xi}^{\alpha} =& A^{\alpha\beta}\Big[-\boldsymbol{a}_{\beta}\left(\delta\bar{\xi}^{\gamma}\,\Delta\bar{\boldsymbol{\varphi}}^{(2)}_{,\gamma} + \delta\bar{\boldsymbol{\varphi}}^{(2)}_{,\gamma}\,\Delta\bar{\xi}^{\gamma}\right) - \left(\boldsymbol{a}_{\beta}\cdot\boldsymbol{a}_{\gamma\delta} - g\,\boldsymbol{n}\cdot\boldsymbol{a}_{\beta\gamma\delta}\right)\delta\bar{\xi}^{\gamma}\,\Delta\bar{\xi}^{\delta} + \\ & g\left(\delta\bar{\boldsymbol{\varphi}}_{,\beta\gamma}\,\Delta\bar{\xi}^{\gamma} + \Delta\bar{\boldsymbol{\varphi}}_{,\beta\gamma}\,\delta\bar{\xi}^{\gamma}\right)\boldsymbol{n} - \left(\delta\bar{\boldsymbol{\varphi}}^{(2)}_{,\beta} + \boldsymbol{a}_{\beta\gamma}\,\delta\bar{\xi}^{\gamma}\right)\cdot\boldsymbol{a}_{\delta}\,\Delta\bar{\xi}^{\delta} - \\ & \left(\Delta\bar{\boldsymbol{\varphi}}^{(2)}_{,\beta} + \boldsymbol{a}_{\beta\gamma}\,\Delta\bar{\xi}^{\gamma}\right)\cdot\boldsymbol{a}_{\delta}\,\delta\bar{\xi}^{\delta} + \left(\delta\boldsymbol{\varphi}^{(1)} - \delta\bar{\boldsymbol{\varphi}}^{(2)}\right)\left(\Delta\bar{\boldsymbol{\varphi}}^{(2)}_{,\beta} + \boldsymbol{a}_{\beta\gamma}\,\Delta\bar{\xi}^{\gamma}\right) + \\ & \left(\Delta\boldsymbol{\varphi}^{(1)} - \Delta\bar{\boldsymbol{\varphi}}^{(2)}\right)\left(\delta\bar{\boldsymbol{\varphi}}^{(2)}_{,\beta} + \boldsymbol{a}_{\beta\gamma}\,\delta\bar{\xi}^{\gamma}\right)\Big]\end{aligned} \tag{5.148}$$

where $\Delta\bar{\xi}$ has the same structure as $\delta\bar{\xi}$, given in (5.119).

Conservation properties The conservation properties of the underlying mechanical system are well known, so we concentrate on the contact contributions. Reconsider the virtual work contributions of a single contact element

$$\begin{aligned}G^{c,h}(\boldsymbol{q},\delta\boldsymbol{q}) = \int\limits_{\Gamma_c^{(1)}} & t_N\boldsymbol{n}\cdot(\delta\boldsymbol{q}_s^{(1)} - \delta\boldsymbol{q}_s^{(2)}) + \\ & t_{T_\alpha}A^{\alpha\beta}\left[(\delta\boldsymbol{q}_s^{(1)} - \delta\boldsymbol{q})_s^{(1)}\cdot\boldsymbol{a}_{\beta} + g^h\boldsymbol{n}\cdot\delta\boldsymbol{a}_{\beta}\right]\,\mathrm{d}A = 0\end{aligned} \tag{5.149}$$

where we make use of (5.131) along with (5.127) and (5.129). The conservation of linear momentum may be verified by substituting $\delta\boldsymbol{q}_I = \boldsymbol{\zeta}$ into the global virtual work of the constraint forces

$$\begin{aligned}G^{c,h}(\boldsymbol{q},[\boldsymbol{\zeta}]) = \int\limits_{\Gamma_c^{(1)}} & t_N\boldsymbol{n}\cdot(\boldsymbol{\zeta}-\boldsymbol{\zeta}) + \\ & t_{T_\alpha}A^{\alpha\beta}\left[(\boldsymbol{\zeta}-\boldsymbol{\zeta})\cdot\boldsymbol{a}_{\beta} + g^h\boldsymbol{n}\cdot\sum_I \hat{N}^I_{,\beta}\boldsymbol{\zeta}\right]\,\mathrm{d}A = 0\end{aligned} \tag{5.150}$$

using the direct approach in (5.129). To verify conservation of angular momentum, we substitute $\delta\boldsymbol{q}_I = \boldsymbol{\zeta} \times \boldsymbol{q}_I$ and obtain

$$\begin{aligned} G^{c,h}(\boldsymbol{q}, [\boldsymbol{\zeta} \times \boldsymbol{q}_I]) &= -\boldsymbol{\zeta} \cdot \int\limits_{\Gamma_c^{(1)}} t_N \boldsymbol{n} \times (\boldsymbol{q}_s^{(1)} - \bar{\boldsymbol{q}}_s^{(2)}) + \\ &\qquad t_{T_\alpha} A^{\alpha\beta} \left[\boldsymbol{a}_\beta \times (\boldsymbol{q}_s^{(1)} - \bar{\boldsymbol{q}}_s^{(2)}) + g^h \boldsymbol{n} \times \boldsymbol{a}_\beta \right] \,\mathrm{d}A \\ &= -\boldsymbol{\zeta} \cdot \int\limits_{\Gamma_c^{(1)}} t_N \boldsymbol{n} \times g^h \boldsymbol{n} + \\ &\qquad t_{T_\alpha} A^{\alpha\beta} \left[g^h \boldsymbol{a}_\beta \times \boldsymbol{n} + g^h \boldsymbol{n} \times \boldsymbol{a}_\beta \right] \,\mathrm{d}A = 0 \end{aligned} \tag{5.151}$$

Note that the simplified variation (5.130) conserves angular momentum only if the normal gap is equal zero.

Finally, we verify the conservation properties of the augmented system in (5.135). The corresponding contact virtual work reads

$$G^{c,h}(\boldsymbol{q}, \delta\boldsymbol{q}, \mathfrak{f}) = \delta\boldsymbol{q} \cdot \nabla_{\boldsymbol{q}} \left(\boldsymbol{\Phi}(\boldsymbol{q}, \mathfrak{f}) \cdot \boldsymbol{\lambda} \right) \tag{5.152}$$

where we have taken $(5.135)_1$ into account. Insertion of $\delta\boldsymbol{q}_I = \boldsymbol{\zeta}$ into the augmented system yields

$$G^{c,h}(\boldsymbol{q}, [\boldsymbol{\zeta}], \mathfrak{f}) = \boldsymbol{\zeta} \cdot \sum_I \nabla_{q_\mathrm{I}} \left(\boldsymbol{\Phi}(\boldsymbol{q}, \mathfrak{f}) \cdot \boldsymbol{\lambda} \right) \tag{5.153}$$

whereas insertion of $\delta\boldsymbol{q}_I = \boldsymbol{\zeta} \times \boldsymbol{q}_I$ yields

$$G^{c,h}(\boldsymbol{q}, [\boldsymbol{\zeta} \times \boldsymbol{q}_I], \mathfrak{f}) = \boldsymbol{\zeta} \cdot \sum_I \boldsymbol{q}_I \times \nabla_{q_\mathrm{I}} \left(\boldsymbol{\Phi}(\boldsymbol{q}, \mathfrak{f}) \cdot \boldsymbol{\lambda} \right) \tag{5.154}$$

Again, we assume that the constraints are frame indifferent with respect to rigid body motions of the form

$$\bar{\boldsymbol{q}}_I^\sharp = \boldsymbol{c} + \boldsymbol{Q}\bar{\boldsymbol{q}}_I \tag{5.155}$$

We can show that for each NTS element the relation

$$\bar{\boldsymbol{\Phi}}(\bar{\boldsymbol{q}}^\sharp, \bar{\mathfrak{f}}) = \bar{\boldsymbol{\Phi}}(\bar{\boldsymbol{q}}, \bar{\mathfrak{f}}) \tag{5.156}$$

is valid. Substituting $\boldsymbol{c} = \epsilon\boldsymbol{\zeta}$, $\boldsymbol{\zeta} \in \mathbb{R}^3$, $\boldsymbol{Q} = \boldsymbol{I}$ and subsequent derivation with respect to ϵ yields

$$\boldsymbol{0} = \left.\frac{\mathrm{d}}{\mathrm{d}\epsilon}\right|_{\epsilon=0} \bar{\boldsymbol{\Phi}}(\bar{\boldsymbol{q}}^\sharp, \bar{\mathfrak{f}}) = \boldsymbol{\zeta} \cdot \sum_I \nabla_{q_\mathrm{I}} \bar{\boldsymbol{\Phi}}(\bar{\boldsymbol{q}}, \bar{\mathfrak{f}}) \tag{5.157}$$

Thus, (5.153) holds for arbitrary $\boldsymbol{\zeta}$ and linear momentum is conserved. Substituting $\boldsymbol{c} = \boldsymbol{0}$ and $\boldsymbol{Q} = \exp(\epsilon\hat{\boldsymbol{\zeta}})$, we end up with

$$\boldsymbol{0} = \left.\frac{\mathrm{d}}{\mathrm{d}\epsilon}\right|_{\epsilon=0} \bar{\boldsymbol{\Phi}}(\bar{\boldsymbol{q}}^\sharp, \bar{\mathfrak{f}}) = \boldsymbol{\zeta} \cdot \sum_I \boldsymbol{q}_I \times \nabla_{q_\mathrm{I}} \bar{\boldsymbol{\Phi}}(\bar{\boldsymbol{q}}, \bar{\mathfrak{f}}) \tag{5.158}$$

Thus, (5.154) holds for arbitrary $\boldsymbol{\zeta}$ and angular momentum is conserved for the semi-discrete system. The same statements are true for the reduced system, since the algebraic reformulation does not change the general characteristics of the system.

Temporal discretization Now, for a typical time step $t_n \to t_{n+1}$ the full discrete version of (5.132) reads

$$\begin{aligned} \boldsymbol{q}_{n+1} - \boldsymbol{q}_n =& \Delta t \boldsymbol{v}_{n+1/2} \\ \boldsymbol{M}(\boldsymbol{v}_{n+1} - \boldsymbol{v}_n) =& - \Delta t \overline{\nabla}_{\boldsymbol{q}} V(\boldsymbol{q}_n, \boldsymbol{q}_{n+1}) - \nabla_{\boldsymbol{q}} \boldsymbol{\Phi}^{\mathrm{n}}(\boldsymbol{q}_{n+1/2}) \cdot \boldsymbol{\lambda} - \boldsymbol{f}^{\mathrm{fric}}(\boldsymbol{q}_n, \boldsymbol{q}_{n+1}) \\ \boldsymbol{0} =& \boldsymbol{\Phi}^{\mathrm{n}}(\boldsymbol{q}_{n+1}) \end{aligned} \tag{5.159}$$

Here, $\overline{\nabla} V(\boldsymbol{q}_n, \boldsymbol{q}_{n+1})$ denotes the discrete gradient of the strain energy function (see Betsch & Steinmann [14]).

The discrete version of the frictional kinematics used in $\boldsymbol{f}^{\mathrm{fric}}(\boldsymbol{q}_n, \boldsymbol{q}_{n+1}) = t_{T_\alpha} \delta \bar{\xi}^{\alpha,h}_{s,n+1/2}$ is related to the definition of the convective coordinates

$$\delta \bar{\xi}^{\alpha,h}_{s,n+1/2} = A^{\alpha\beta}_{n+1/2} \left[\left(\delta \boldsymbol{q}^{(1)}_s - \delta \bar{\boldsymbol{q}}^{(2)}_s \right) \cdot \boldsymbol{a}_{\beta,n+1/2} + g^h_{n+1/2} \boldsymbol{n}_{n+1/2} \cdot \delta \boldsymbol{a}_\beta \right] \tag{5.160}$$

Note that we deal with the adjoint discrete traction t_{T_α} using a local evolution scheme in Appendix C. The time-discrete version of the augmented system in (5.135) reads

$$\begin{aligned} \boldsymbol{q}_{n+1} - \boldsymbol{q}_n =& \Delta t \boldsymbol{v}_{n+1/2} \\ \boldsymbol{M}(\boldsymbol{v}_{n+1} - \boldsymbol{v}_n) =& - \Delta t \overline{\nabla}_{\boldsymbol{q}} V(\boldsymbol{q}_n, \boldsymbol{q}_{n+1}) - \Delta t \nabla_{\boldsymbol{q}} \boldsymbol{\Phi}_{n+1/2} \cdot \boldsymbol{\lambda} \\ \boldsymbol{0} =& \nabla_{\mathfrak{f}} \boldsymbol{\Phi}_{n+1/2} \cdot \boldsymbol{\lambda} + \boldsymbol{f}^{\mathrm{aug}}_{n+1/2} \\ \boldsymbol{0} =& \boldsymbol{\Phi}_{n+1} \end{aligned} \tag{5.161}$$

where $\nabla_{\boldsymbol{q}} \boldsymbol{\Phi}_{n+1/2} = \nabla_{\boldsymbol{q}} \boldsymbol{\Phi}(\boldsymbol{q}_{n+1/2}, \mathfrak{f}_{n+1/2})$, $\nabla_{\mathfrak{f}} \boldsymbol{\Phi}_{n+1/2} = \nabla_{\mathfrak{f}} \boldsymbol{\Phi}(\boldsymbol{q}_{n+1/2}, \mathfrak{f}_{n+1/2})$ and $\boldsymbol{\Phi}_{n+1} = \boldsymbol{\Phi}(\boldsymbol{q}_{n+1}, \mathfrak{f}_{n+1})$. As already mentioned, $\boldsymbol{f}^{\mathrm{aug}}$ consists of the tractions t_{T_α}, see (5.135). Accordingly, $\boldsymbol{f}^{\mathrm{aug}}_{n+1/2}$ has to be evaluated as shown to Appendix C. Following the arguments outlined in the previous section, we create a local projection matrix as follows

$$\bar{\mathfrak{P}}_{n+1/2} = -\nabla_{\boldsymbol{q}_{\mathrm{A}}} \bar{\boldsymbol{\Phi}}^{\mathrm{aug}}_{n+1/2} \left(\nabla_{\mathfrak{f}_{\mathrm{A}}} \bar{\boldsymbol{\Phi}}^{\mathrm{aug}}_{n+1/2} \right)^{-1} \tag{5.162}$$

and obtain for the reduced system

$$\begin{aligned} \boldsymbol{q}_{n+1} - \boldsymbol{q}_n =& \Delta t \boldsymbol{v}_{n+1/2} \\ \boldsymbol{M}(\boldsymbol{v}_{n+1} - \boldsymbol{v}_n) =& - \Delta t \overline{\nabla}_{\boldsymbol{q}} V(\boldsymbol{q}_n, \boldsymbol{q}_{n+1}) - \Delta t \nabla_{\boldsymbol{q}} \boldsymbol{\Phi}^n_{n+1/2} \cdot \boldsymbol{\lambda}^n - \Delta t \mathfrak{P}_{n+1/2} \boldsymbol{f}^{\mathrm{aug}}_{n+1/2} \\ \boldsymbol{0} =& \boldsymbol{\Phi}_{n+1} \end{aligned} \tag{5.163}$$

The second reduction step follows immediately from (5.145) using the discretized projection matrix in (5.162) evaluated at time $n+1$

$$\bar{\mathfrak{P}}_{n+1} = -\nabla_{\boldsymbol{q}_{\mathrm{A}}} \bar{\boldsymbol{\Phi}}^{\mathrm{aug}}_{n+1} \left(\nabla_{\mathfrak{f}_{\mathrm{A}}} \bar{\boldsymbol{\Phi}}^{\mathrm{aug}}_{n+1} \right)^{-1} \tag{5.164}$$

The full discrete system to be solved in each Newton-Raphson iteration now reads

$$\begin{bmatrix} \boldsymbol{K}_{qq} + \boldsymbol{K}_{q\mathfrak{f}} \mathfrak{P}^T_{n+1} & \Delta t \nabla_{\boldsymbol{q}} \boldsymbol{\Phi}^n_{n+1/2} \\ \nabla_{\boldsymbol{q}}{}^T \boldsymbol{\Phi}^n_{n+1} & \boldsymbol{0} \end{bmatrix} \cdot \begin{bmatrix} \Delta \boldsymbol{q} \\ \Delta \boldsymbol{\lambda}^n \end{bmatrix} = \begin{bmatrix} \boldsymbol{R}_{q,n+1/2} - \boldsymbol{K}_{q\mathfrak{f}} \left(\nabla_{\mathfrak{f}}{}^T \bar{\boldsymbol{\Phi}}^{\mathrm{aug}}_{n+1} \right)^{-1} \boldsymbol{\Phi}^{\mathrm{aug}}_{n+1} \\ \boldsymbol{\Phi}^n_{n+1} \end{bmatrix} \tag{5.165}$$

where $\boldsymbol{R}_{q,n+1/2}$ consists of the residual contributions in $(5.163)_2$ and $\boldsymbol{K}_{qq}$, $\boldsymbol{K}_{q\mathfrak{f}}$ denotes the consistent linearization of $\boldsymbol{R}_{q,n+1/2}$ with respect to $\boldsymbol{q}$ and $\mathfrak{f}$, respectively. In a final step, we recover the augmented coordinates by solving

$$\Delta\boldsymbol{\mathfrak{f}}_A = \left(\nabla_{\mathfrak{f}_{\mathrm{A}}}{}^T \bar{\boldsymbol{\Phi}}_{n+1}^{\mathrm{aug}}\right)^{-1} \bar{\boldsymbol{\Phi}}_{n+1}^{\mathrm{aug}} + \bar{\boldsymbol{\mathfrak{P}}}_{n+1}^{T} \Delta\boldsymbol{q}_A \tag{5.166}$$

for each NTS element.

It is obvious that the linearization is extremely simplified compared with traditional schemes. Furthermore, the proposed scheme is more consistent, since it ensures the exact fulfillment of the orthogonality conditions $(5.161)_4$ at each time node within the chosen mid-point type scheme.

Conservation properties. As before we focus on the contact contribution and begin with the verification of the conservation of linear momentum. To this end, we substitute $\delta\boldsymbol{q}_I = \boldsymbol{\zeta}$ into the weak form of the contact contributions

$$\begin{aligned} G^{c,h}(\boldsymbol{q}_{n+1/2}, [\boldsymbol{\zeta}]) = \int\limits_{\Gamma_c^{(1)}} & t_N \boldsymbol{n}_{n+1/2} \cdot (\boldsymbol{\zeta} - \boldsymbol{\zeta}) + \\ & t_{T\alpha} A_{n+1/2}^{\alpha\beta} \left[(\boldsymbol{\zeta} - \boldsymbol{\zeta}) \cdot \boldsymbol{a}_{\beta,n+1/2} + g_{n+1/2}^{h} \boldsymbol{n}_{n+1/2} \cdot \sum_I \hat{N}_{,\beta}^{I} \boldsymbol{\zeta} \right] \, \mathrm{d}A \\ & =0 \end{aligned} \tag{5.167}$$

which confirms that the constraints do not affect linear momentum conservation. Following the arguments in (4.30), we substitute $\delta\boldsymbol{q}_I = \boldsymbol{\zeta} \times \boldsymbol{q}_{I,n+1/2}$ and obtain

$$\begin{aligned} G^{c,h}(\boldsymbol{q}_{n+1/2}, [\boldsymbol{\zeta} \times \boldsymbol{q}_{I,n+1/2}]) = -\,\boldsymbol{\zeta} \cdot \int\limits_{\Gamma_c^{(1)}} & t_N \boldsymbol{n}_{n+1/2} \times g_{n+1/2}^{h} \boldsymbol{n}_{n+1/2} + \\ & t_{T_\alpha} A^{\alpha\beta} g_{n+1/2}^{h} \left[\boldsymbol{a}_{\beta,n+1/2} \times \boldsymbol{n}_{n+1/2} + \boldsymbol{n}_{n+1/2} \times \boldsymbol{a}_{\beta,n+1/2} \right] \, \mathrm{d}A \\ & =0 \end{aligned} \tag{5.168}$$

which confirms that the constraints do not affect angular momentum conservation as well.

At last we verify the conservation properties of the full discrete system in (5.161) and substitute $\delta\boldsymbol{q}_I = \boldsymbol{\zeta}$

$$G^{c,h}(\boldsymbol{q}_{n+1/2}, \boldsymbol{\zeta}, \mathfrak{f}_{n+1/2}) = \boldsymbol{\zeta} \cdot \sum_I \nabla_{q_{\mathrm{I}}} \boldsymbol{\Phi}(\boldsymbol{q}_{n+1/2}, \mathfrak{f}_{n+1/2}) \cdot \boldsymbol{\lambda} \tag{5.169}$$

whereas we obtain

$$G^{c,h}(\boldsymbol{q}_{n+1/2}, [\boldsymbol{\zeta} \times \boldsymbol{q}_{I,n+1/2}], \mathfrak{f}_{n+1/2}) = \boldsymbol{\zeta} \cdot \sum_I \boldsymbol{q}_{I,n+1/2} \times \nabla_{q_{\mathrm{I}}} \boldsymbol{\Phi}(\boldsymbol{q}_{n+1/2}, \mathfrak{f}_{n+1/2}) \cdot \boldsymbol{\lambda} \tag{5.170}$$

if we substitute $\delta \boldsymbol{q} = \boldsymbol{\zeta} \times \boldsymbol{q}_{I,n+1/2}$. Once again, frame-indifference of the vector of constraints $\boldsymbol{\Phi}(\boldsymbol{q}, \mathfrak{f})$ against rigid body motions is crucial for the fulfillment of the conservation laws. Proceeding along the lines of Section 5.3, we can easily verify that

$$\bar{\boldsymbol{\Phi}}(\bar{\boldsymbol{q}}^{\sharp}_{n+1/2}, \bar{\mathfrak{f}}_{n+1/2}) = \bar{\boldsymbol{\Phi}}(\bar{\boldsymbol{q}}_{n+1/2}, \bar{\mathfrak{f}}_{n+1/2}) \tag{5.171}$$

where $\bar{\boldsymbol{q}}^{\sharp}_{I,n+1/2} = \boldsymbol{c} + \boldsymbol{Q}\bar{\boldsymbol{q}}_{I,n+1/2}$. Substituting $\boldsymbol{c} = \epsilon\boldsymbol{\zeta}$, $\boldsymbol{Q} = \boldsymbol{I}$ yields

$$\boldsymbol{0} = \left.\frac{\mathrm{d}}{\mathrm{d}\epsilon}\right|_{\epsilon=0} \bar{\boldsymbol{\Phi}}(\bar{\boldsymbol{q}}^{\sharp}_{n+1/2}, \bar{\mathfrak{f}}_{n+1/2}) = \boldsymbol{\zeta} \cdot \sum_{I} \nabla_{\boldsymbol{q}_{\mathrm{I}}} \bar{\boldsymbol{\Phi}}(\bar{\boldsymbol{q}}_{n+1/2}, \bar{\mathfrak{f}}_{n+1/2}) \tag{5.172}$$

Analogues to the semi-discrete system, linear momentum is algorithmically conserved. Substituting $\boldsymbol{c} = \boldsymbol{0}$ and $\boldsymbol{Q} = \exp(\epsilon\hat{\boldsymbol{\zeta}})$ yields

$$\boldsymbol{0} = \left.\frac{\mathrm{d}}{\mathrm{d}\epsilon}\right|_{\epsilon=0} \bar{\boldsymbol{\Phi}}(\bar{\boldsymbol{q}}^{\sharp}_{n+1/2}, \bar{\mathfrak{f}}_{n+1/2}) = \boldsymbol{\zeta} \cdot \sum_{I} \boldsymbol{q}_{I,n+1/2} \times \nabla_{\boldsymbol{q}_{\mathrm{I}}} \bar{\boldsymbol{\Phi}}(\bar{\boldsymbol{q}}_{n+1/2}, \bar{\mathfrak{f}}_{n+1/2}) \tag{5.173}$$

Thus, angular momentum is algorithmically conserved for the full-discrete system. Note that the last statement is also true for the reduced system, since the algebraic reformulation of the system does not change any properties of the underlying formulation.

5.4 Examples

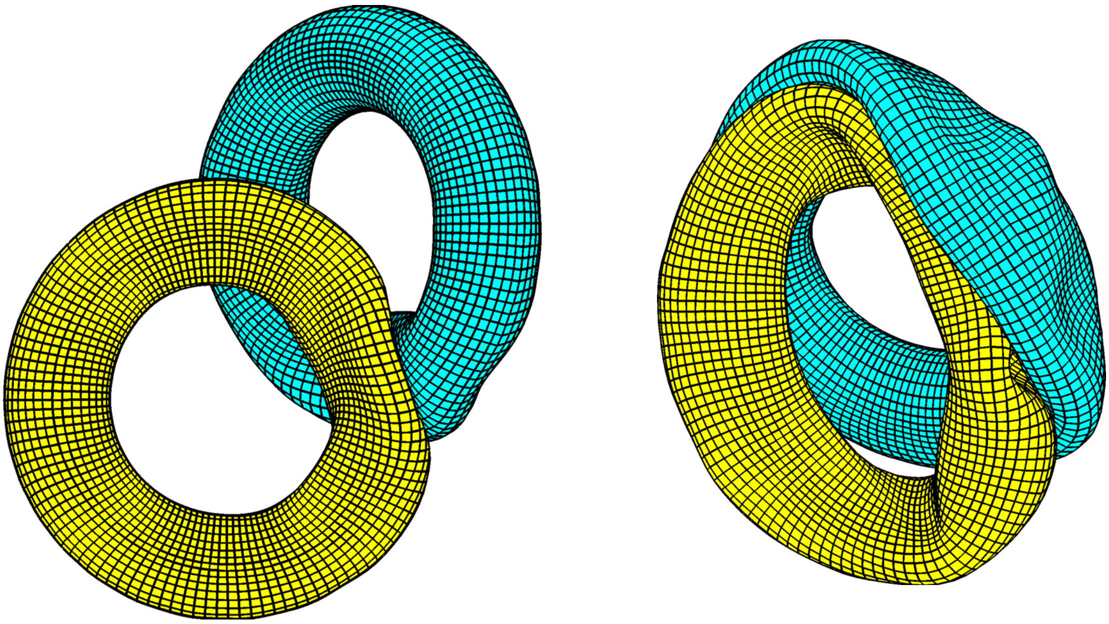

Figure 5.4: Configurations at time $t = 2$ and $t = 5$.

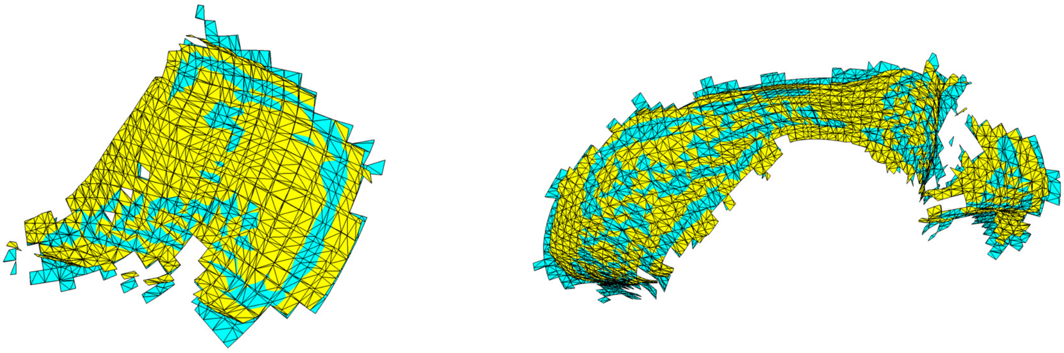

Figure 5.5: Segmentation at time $t = 2$ and $t = 5$.

Two tori impact problem As a first example we consider an impact simulation of two tori using a mortar based approach. Both tori are discretized using 8024 eight-node brick elements with overall 72216 degrees of freedom. The inner and outer radii are 52 and 100 respectively, the wall thickness of each hollow torus is 4.5. A standard Neo-Hookean hyperelastic material with $\mathcal{E} = 2250$ and $\nu = 0.3$ is used. The initial density $\rho = 0.1$ and the homogeneous, initial velocity of the left torus is given by $\boldsymbol{v} = [30, 0, 23]$. A time-step size of $\Delta t = 0.0025$ has been used for the first approach, whereas a time-step size of both simplified approaches has been set to $\Delta t = 0.01$.

Excluding the augmented coordinates $\boldsymbol{f}$ from the calculations as shown in (3.14), a reduction of the average calculation time of a Newton step of about 12% could be achieved in this specific example. Furthermore, we were able to use 4-10 times larger time-step sizes. This stability feature is of major importance especially in large sliding situations.

In Figure 5.4 the configuration at $t = 2$ and $t = 5$ is shown. The associated segmentations are displayed in Fig. 5.5. 2318 segments are automatically constructed at time $t = 2$

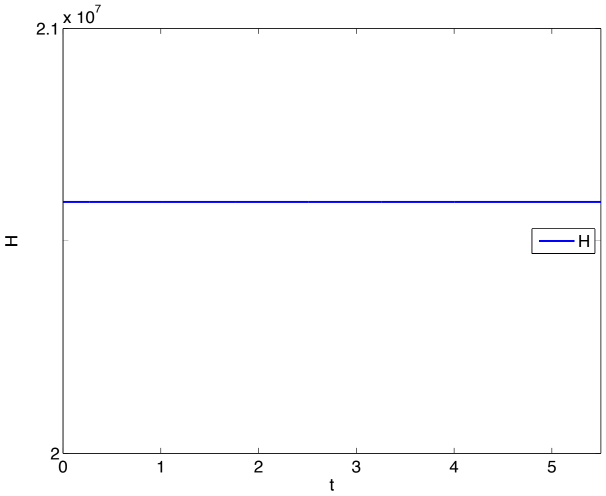

Figure 5.6: Total energy versus time using approach 1.

for overall 331 mortar constraints. For the first approach where the mortar integrals remain not constant throughout each time step, an additional 355 constraints for $\mathbf{\Phi}_{\mathrm{Aug}_1}$, 240 constraints for $\mathbf{\Phi}_{\mathrm{Aug}_2}$ and 703 constraints for $\mathbf{\Phi}_{\mathrm{Aug}_3}$ are necessary. Furthermore, 6954 constraints for the augmentation of the normal vector have to be considered. At $t = 5$, 5896 segments with overall 755 mortar constraints are determined. Correspondingly, we need 923 constraints for $\mathbf{\Phi}_{\mathrm{Aug}_1}$, 529 constraints for $\mathbf{\Phi}_{\mathrm{Aug}_2}$, 1866 constraints for $\mathbf{\Phi}_{\mathrm{Aug}_3}$ and 20862 constraints for the augmentation of the normal vector. Clearly, this is not acceptable. In contrast, if we apply approach 3, we only have to add 755 mortar constraints to the global system. We then need the same amount of constraints as for the NTS method, since each mortar constraint refers to a specific node on the non-mortar side. Although the evaluation of the mortar constraints is more involved, the solver clearly dominates the overall calculation time and thus, we have no drawback in the calculation time due to the use of mortar methods. In Figure 5.6 total energy versus time is displayed using the proposed energy-momentum scheme together with deformable mortar segments. As shown in Figure 5.7, approach 3 does not conserve energy. The increase in total energy is acceptable, since we used relatively large time steps. The last diagram shows the values of change of the first component of angular momentum. Note that the values are below the stopping criterion of the Newton iteration (10^{-5}).

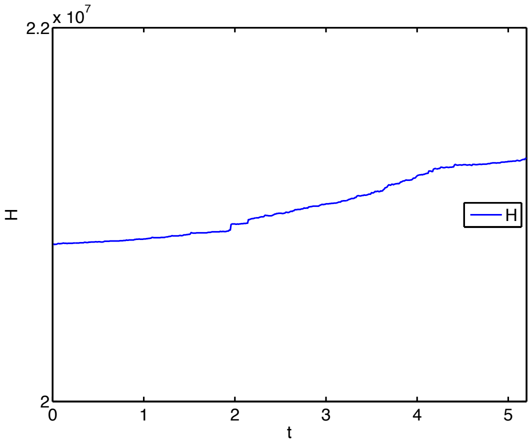

Figure 5.7: Total energy versus time using approach 3.

Torus-cylinder impact example This example deals with a three-dimensional problem similar to the last example in Yang & Laursen [79] using a NTS based approach. The material properties and the initial geometry of the torus are the same as before. The inner diameter of the cylinder is 100, the wall thickness is 7.5 and the initial velocity of the torus is [0, 0, 20]. In Fig. 5.9 a sequence of configurations at $t = 0, 20, 50$ is displayed. The torus consists of 2288 elements, the cylinder of 1900 elements. Furthermore, the time-step size has been set to $\Delta t = 0.01$. Once again, the evolution of the total angular momentum is depicted in the left diagram of Fig, 5.10, whereas the upper and lower diagrams on the

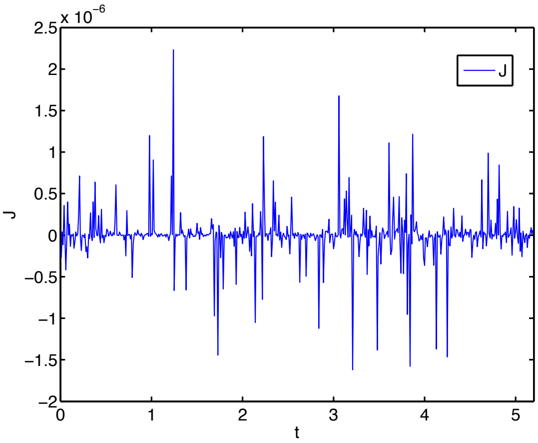

Figure 5.8: Values of change of the first component of angular momentum versus time using approach (5.93).

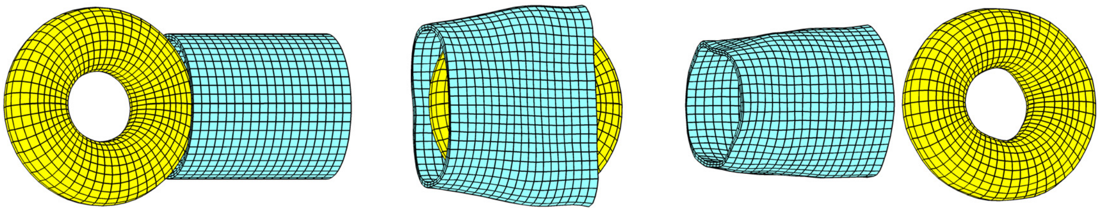

Figure 5.9: Deformed configuration at $t = [0,\ 20,\ 50]$.

right side show the total linear momentum and the total energy, respectively. As expected, all quantities are conserved exactly.

Two tori impact problem In this last example for contact, we consider a frictional impact problem of the two tori problem, introduced previously. All material and geometrical data are identical to the previous ones. A time step size of 0.01 has been used throughout the whole simulation. The deformation at different time steps is shown in Fig. 5.11.

The evolution of the total energy is shown in Fig. 5.12 together with the three components of angular momentum. As expected, total energy decreases due to the frictional behavior. Since we used the proposed mid-point type evaluation of the system, angular momentum is conserved.

Finally, Fig. 5.13 shows the deformation at $t = 5$ for different friction coefficients, using $\mu = 0.1$ and $\mu = 0.3$. The deformation changes significantly, since large sliding effects are directly correlated with the friction coefficient.

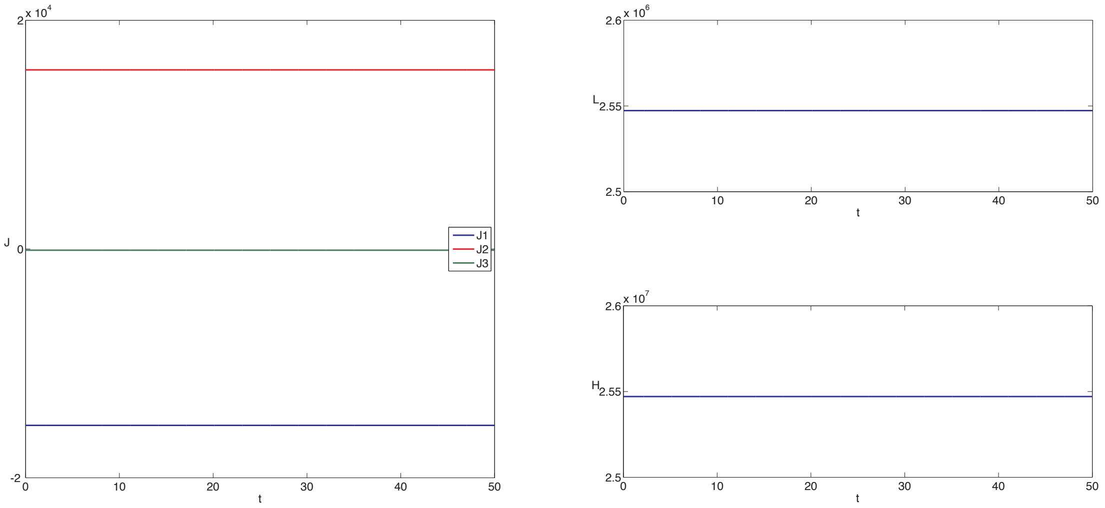

Figure 5.10: Total linear, angular momentum and total energy.

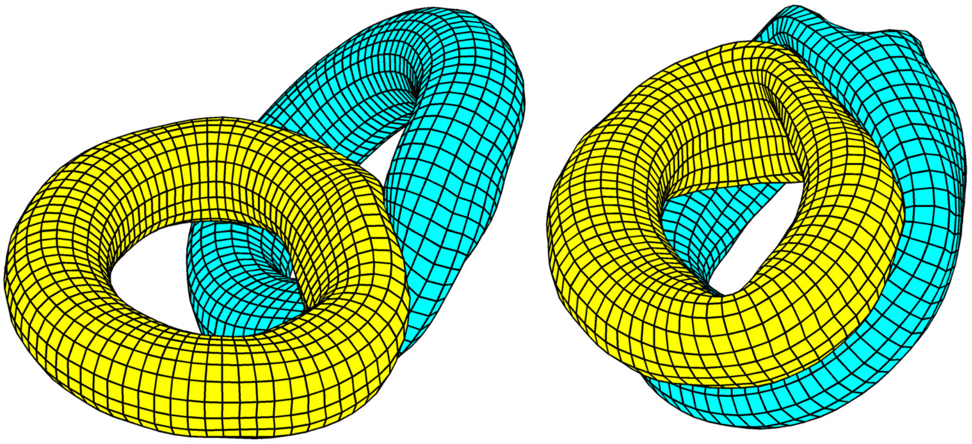

Figure 5.11: Deformation at time 2.5 and 5.

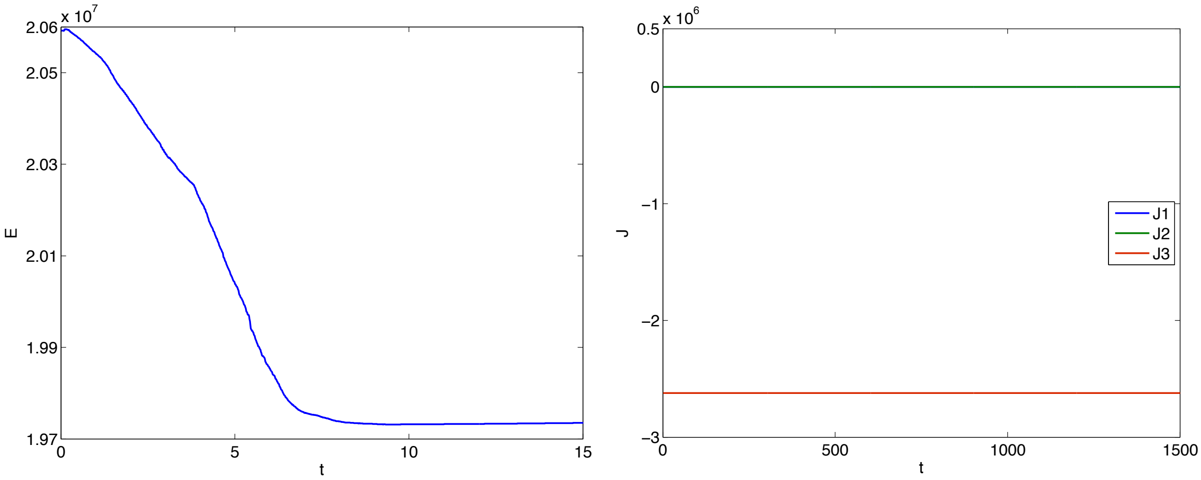

Figure 5.12: Total energy and components of angular momentum plotted over time.

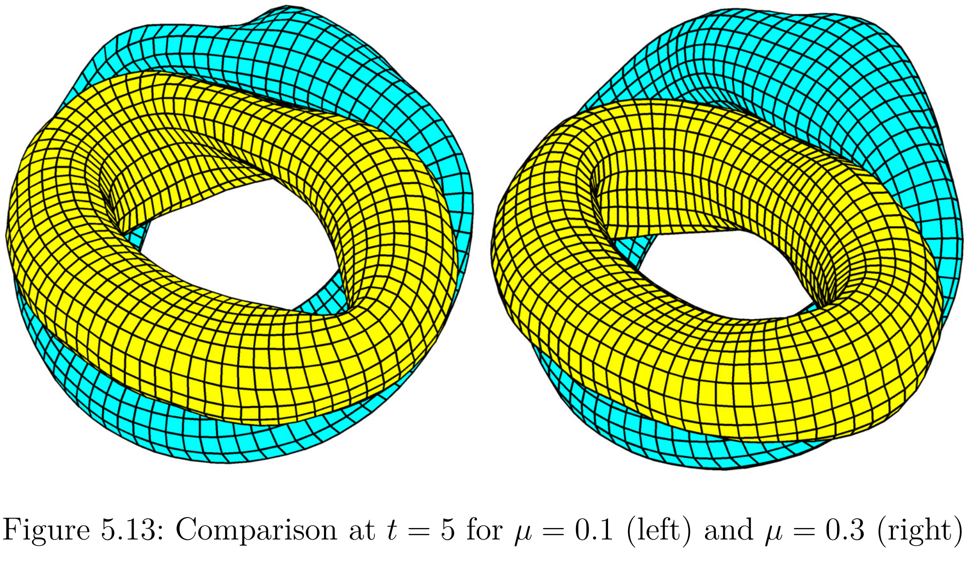

Figure 5.13: Comparison at $t = 5$ for $\mu = 0.1$ (left) and $\mu = 0.3$ (right).

6 Fluid-structure interaction

Continuum immersed strategies are widely used these days for the computational simulation of fluid-structure interaction problems (see Peskin [57, 58, 59]). The principal characteristic of such immersed techniques is the representation of the immersed solid via a momentum forcing source in the Navier-Stokes equations. This is in contrast to well-established formulations using coupled Dirichlet-Neumann schemes to transfer the momentum between the fluid and the solid (see Tezduyar [70]). Recently, mortar based discretization schemes of the interface has been proposed by Kloeppel et al. [46]. Here, we will focus on the Immersed Finite Element Method (IFEM) proposed by Zhang & Liu [83, 74, 73] and on the Immersed Structural Potential Method (ISPM), proposed by Gil et al. [22, 23]. A comparison of both methods can be found in Hesch et al. [38].

6.1 Immersed formulation

Let us consider a deformable solid, fully immersed within the surrounding incompressible viscous fluid. For the calculation of the fluid-structure interaction (FSI), an immersed continuum numerical strategy will be applied, where the deformable solid phase is modelled as embedded into the background fluid phase (see Liu et al. [55]). The resulting FSI forces are formulated in terms of a volumetric force field $\boldsymbol{\mathcal{F}} : \mathcal{B}^s \times [0,\, T] \to \mathbb{R}^d$ which emanates from the interaction of the background fluid system defined on the domain $\mathcal{B}$ with the immersed solid system defined by the domain $\mathcal{B}^s$ at time t. In Gil et al. [22, 23], the authors model the solid as a Helmholtz's free energy functional whose spatial gradient defines the FSI force field. This force vector field $\boldsymbol{\mathcal{F}}$ can be introduced with no difficulty within the balance of linear momentum of the background fluid phase in equation (1.35) as follows[*]

$$\rho^f \dot{\boldsymbol{v}} = \nabla_{\boldsymbol{x}} \cdot \boldsymbol{\sigma}^f + \rho^f \boldsymbol{g} + \boldsymbol{\mathcal{F}} \tag{6.1}$$

The volumetric force field $\boldsymbol{\mathcal{F}}$ of the immersed solid reads

$$\boldsymbol{\mathcal{F}} = \begin{cases} \boldsymbol{0} & \text{in} \quad \mathcal{B} \backslash \mathcal{B}^s \\ (\rho^f - \rho^s)(\dot{\boldsymbol{v}} - \boldsymbol{g}) + \nabla \cdot (\boldsymbol{\sigma}^s - \boldsymbol{\sigma}^f) & \text{in} \quad \mathcal{B}^s \end{cases} \tag{6.2}$$

---

[*] Contributions to the solid system are marked with $(\bullet)^s$, whereas contributions to the fluid system are marked with $(\bullet)^f$.

In addition, the conservation of mass equation (1.33) is modified allowing for the immersed solid to possibly experience non-isochoric deformations within the surrounding incompressible fluid, resulting in

$$\nabla_{\boldsymbol{x}} \cdot \boldsymbol{v} = \mathcal{F}^p \tag{6.3}$$

where the scalar field $\mathcal{F}^p : \mathcal{B}^s \times [0,\, T] \rightarrow \mathbb{R}$ is defined as

$$\mathcal{F}^p = \begin{cases} 0 & \text{in} \quad \mathcal{B} \backslash \mathcal{B}^s \\ \frac{j}{J} & \text{in} \quad \mathcal{B}^s \end{cases} \tag{6.4}$$

Within the context of Green elastic materials [40], we next postulate the existence of a hyperelastic constitutive law for the calculation of the solid stress field by introducing a scalar valued stored strain energy functional $W(\boldsymbol{C})$. In general, additional internal thermodynamic variables can also be used to further characterise the constitutive law of the immersed solid (i.e. including plastic or viscoelastic behaviour). Moreover, in the case of nearly incompressible materials, sophisticated mixed formulations based upon the use of enhanced modes can also be utilised (see Appendix A for further details). The actual stress field of the immersed solid can be obtained via a push forward operation of the purely material derivative of the stored strain energy functional as

$$\boldsymbol{\sigma}^s = \frac{2}{J} \boldsymbol{F} \frac{\partial W(\boldsymbol{C})}{\partial \boldsymbol{C}} \boldsymbol{F}^T \tag{6.5}$$

For numerical convenience, it is customary to employ a Lagrangian mapping for the description of the immersed solid whilst the fluid is modelled by means of an Eulerian mapping. The kinematic information in terms of velocity and spatial position can easily be measured in the Eulerian background fluid and must be suitably linked to the solid phase in a compatible fashion (i.e. non-slip condition). Computations within the solid phase require then the definition of an Euler-Lagrange mapping $\mathcal{I}_{\mathcal{B}^s}$ for any given function ψ of the solid system such that $\psi(\boldsymbol{x}, t) : \mathcal{B}^s \times [0,\, T]$ is mapped to $\mathcal{I}_{\mathcal{B}^s}(\psi(\boldsymbol{X}, t)) : \mathcal{B}_0^s \times [0,\, T]$. In the continuum this transfer mapping is simply defined by the identity

$$\mathcal{I}_{\mathcal{B}^s}(\psi(\boldsymbol{X}, t)) = \psi(\boldsymbol{x}\left(\boldsymbol{X}, t\right), t) = \psi(\boldsymbol{x}, t) \tag{6.6}$$

However, the use of different spatial interpolation strategies for the fluid and solid phases will require an appropriate transfer operator that will be described below. Specifically, for the velocity field

$$\boldsymbol{v}(\boldsymbol{x}, t) = \mathcal{I}_{\mathcal{B}^s}(\boldsymbol{v}(\boldsymbol{X}, t)) \tag{6.7}$$

In order to complete the strong form for the solid phase, appropriate Dirichlet boundary conditions can be defined as follows

$$\boldsymbol{x}(\boldsymbol{X}, t) = \boldsymbol{x}_0, \quad \text{on} \quad \partial \mathcal{B}_D^s \tag{6.8}$$

Since the immersed solid is surrounded by the fluid, additional Neumann boundary conditions are not treated explicitly as the interaction is already accounted for in the FSI force term $\boldsymbol{\mathcal{F}}$.

The variational formulation of the balance of linear momentum follows the same arguments outlined in Section 1.3 and reads

$$\langle \rho^f (\dot{\boldsymbol{v}} - \boldsymbol{g}) - \boldsymbol{\mathcal{F}}, \delta \boldsymbol{v} \rangle_{\mathcal{B}} + \langle \boldsymbol{\sigma}^f, \nabla_{\boldsymbol{x}} (\delta \boldsymbol{v}) \rangle_{\mathcal{B}} - \langle \boldsymbol{h}, \delta \boldsymbol{v} \rangle_{\partial \mathcal{B}^\sigma} = 0 \tag{6.9}$$

and for the conservation of mass

$$\langle \nabla_{\boldsymbol{x}} \cdot \boldsymbol{v} - \mathcal{F}^p, \delta p \rangle_{\mathcal{B}} = 0 \tag{6.10}$$

Equations (6.9-6.10) summarise the weak form for the overall problem (i.e. fluid-solid). It is convenient to split the above formulae into fluid and solid phases. Introducing the Jacobian of the deformation in the solid phase $J^s = \det(\boldsymbol{F}^s)$, taking into account the Euler-Lagrange mapping $\mathcal{I}_{\mathcal{B}^s}$ defined above the weak form expression (6.9) can be rewritten as

$$\begin{aligned}
&\langle \rho^f (\dot{\boldsymbol{v}} - \boldsymbol{g}), \delta \boldsymbol{v} \rangle_{\mathcal{B}} + \langle \boldsymbol{\sigma}^f, \nabla_{\boldsymbol{x}} (\delta \boldsymbol{v}) \rangle_{\mathcal{B}} - \langle \boldsymbol{h}, \delta \boldsymbol{v} \rangle_{\partial \mathcal{B}^\sigma} \\
&-\langle (\rho^f - \rho^s) \left(\frac{\partial}{\partial t} \mathcal{I}_{\mathcal{B}^s}(\boldsymbol{v}(\boldsymbol{X}, t)) - \boldsymbol{g} \right), \mathcal{I}_{\mathcal{B}^s}(\delta \boldsymbol{v}) J^s \rangle_{\mathcal{B}_0^s} \\
&\langle \boldsymbol{\sigma}^s - \boldsymbol{\sigma}^f, \nabla_{\boldsymbol{x}} \mathcal{I}_{\mathcal{B}^s}(\delta \boldsymbol{v}) J^s \rangle_{\mathcal{B}_0^s} = 0
\end{aligned} \tag{6.11}$$

Similarly, the weak form expression (6.10) can be reformulated as

$$\langle \nabla_{\boldsymbol{x}} \cdot \boldsymbol{v}, \delta p \rangle - \langle \dot{J}^s, \mathcal{I}_{\mathcal{B}^s}(\delta p) \rangle_{\mathcal{B}_0^s} = 0 \tag{6.12}$$

The internal virtual work within the solid phase defined in terms of the conjugate pair $\{\boldsymbol{\sigma}^s, \nabla_{\boldsymbol{x}} \mathcal{I}_{\mathcal{B}^s}(\delta \boldsymbol{v})\}$ can be reformulated by means of the Piola transformation in terms of an alternative conjugate pair $\{\boldsymbol{\Sigma}^s, (\boldsymbol{F}^s)^T \nabla_{\boldsymbol{X}} \mathcal{I}_{\mathcal{B}^s}(\delta \boldsymbol{v})\}$ as

$$\langle \boldsymbol{\sigma}^s, \nabla_{\boldsymbol{x}} \mathcal{I}_{\mathcal{B}^s}(\delta \boldsymbol{v}) J^s \rangle_{\mathcal{B}_0^s} = \langle \boldsymbol{\Sigma}^s, (\boldsymbol{F}^s)^T \nabla_{\boldsymbol{X}} \mathcal{I}_{\mathcal{B}^s}(\delta \boldsymbol{v}) \rangle_{\mathcal{B}_0^s} \tag{6.13}$$

where $\boldsymbol{\Sigma}^s = 2 \frac{\partial W(\boldsymbol{C}^s)}{\partial \boldsymbol{C}^s}$ denotes once again the second Piola-Kirchhoff stress tensor and $\boldsymbol{C}^s = (\boldsymbol{F}^s)^T \boldsymbol{F}^s$ is the right Cauchy-Green tensor particularised for the solid phase. The evaluation of the fluid stress $\boldsymbol{\sigma}^f$ within the solid phase follows immediately from the definition (1.34) in conjunction with the incompressibility constraint as[†]

$$\boldsymbol{\sigma}^f = -\mathcal{I}_{\mathcal{B}^s}(p) \boldsymbol{I} + \mu \left(\nabla_{\boldsymbol{X}} \mathcal{I}_{\mathcal{B}^s}(\boldsymbol{v}) + (\nabla_{\boldsymbol{X}} \mathcal{I}_{\mathcal{B}^s}(\boldsymbol{v}))^T \right) (\boldsymbol{F}^s)^{-1} \tag{6.14}$$

It is worthwhile emphasising that the evaluation of the spatial gradients $\nabla_{\boldsymbol{x}} \mathcal{I}_{\mathcal{B}^s}(\boldsymbol{v})$ and $\nabla_{\boldsymbol{x}} \mathcal{I}_{\mathcal{B}^s}(\delta \boldsymbol{v})$, and the subsequent construction of the deformation gradient $\boldsymbol{F}^s$ is one of the most challenging processes in any computational immersed methodology. From the spatial discretization point of view, various approaches have been developed, using either local elementwise shape functions such as in the Immersed Finite Element Method (IFEM) and its variants [83, 74, 55, 73] or kernel shape functions with larger compact support such as in the Immersed Structural Potential Method (ISPM) [22, 23]. This important aspect will be discussed in length in the following sections.

[†] Notice that the stress contribution in $\mathcal{B}_t^s$ due the fluid $\boldsymbol{\sigma}^f$ is several orders of magnitude smaller than the stress contribution due to the immersed solid $\boldsymbol{\sigma}^s$, hence it is usually neglected [83, 55].

6.2 Discrete Euler-Lagrange mapping

IFEM, Lagrangian mesh. A common approach is to numerically model the immersed solid following a finite element approach. Additional shape functions are introduced to describe the immersed solid (cf. Liu et al. [55]) as follows

$$\mathcal{I}_{\mathcal{B}^s}(\boldsymbol{v}^{\mathrm{h}}) = \sum_{C=1}^{n_{\mathrm{node}}} \bar{N}^C \bar{\boldsymbol{v}}_C; \quad \mathcal{I}_{\mathcal{B}^s}(p^{\mathrm{h}}) = \sum_{C=1}^{n_{\mathrm{node}}} \bar{N}^C \bar{p}_C \tag{6.15}$$

Here, $\bar{N}^C(\boldsymbol{X}) : \mathcal{B}_0^{\mathrm{h},s} \to \mathbb{R}$ are the corresponding shape functions and $\bar{\boldsymbol{v}}_C$ and $\bar{p}_C$ denote the nodal values at the current position of the solid, calculated from the background Eulerian fluid grid as follows

$$\bar{\boldsymbol{v}}_C = \sum_{A\in\omega} N^A(\boldsymbol{x}(\boldsymbol{X}_C,t))\boldsymbol{v}_A; \quad \bar{p}_C = \sum_{B\in\bar{\omega}} N^B(\boldsymbol{x}(\boldsymbol{X}_C,t))p_B \tag{6.16}$$

Combining formulae (6.15) and (6.16) results in the definition of the spatial interpolation operator for the transfer of information between the Eulerian and the Lagrangian meshes as follows

$$\mathcal{I}_{\mathcal{B}^s}(N^A(\boldsymbol{X},t)) = \sum_{C=1}^{n_{\mathrm{node}}} N^A(\boldsymbol{x}(\boldsymbol{X}_C,t))\bar{N}_C(\boldsymbol{X}) \tag{6.17}$$

which renders a linear operator. The Euler-Lagrange mapping is shown in Figure 6.1 for a one dimensional system and linear shape functions. The mapping for the single immersed element reads

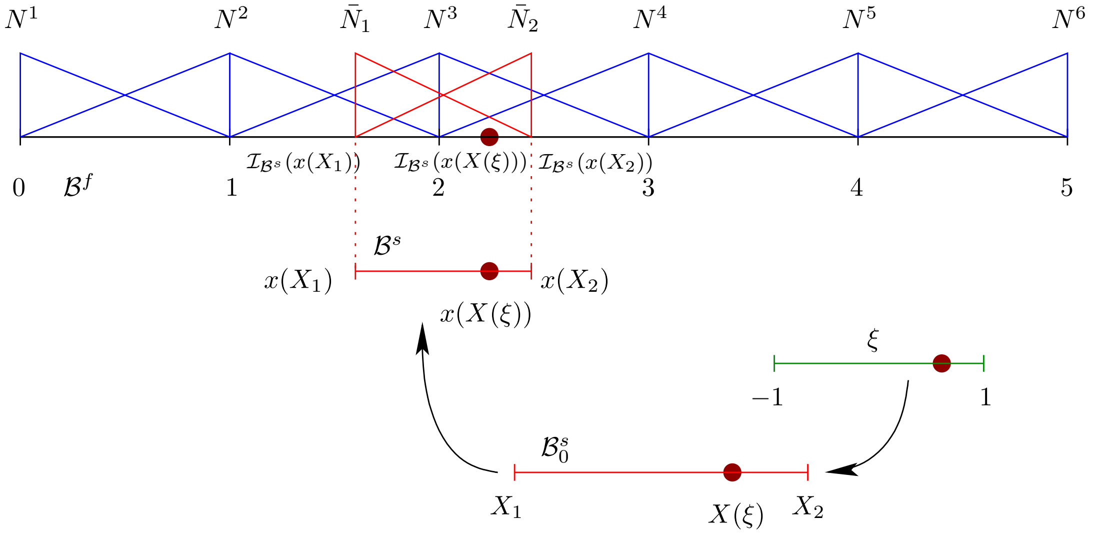

Figure 6.1: One dimensional Euler-Lagrange mapping.

$$\mathcal{I}_{\mathcal{B}^s}(N^A(X(\xi),t)) = N^A(x(X_1,t))\bar{N}_1(X(\xi)) + N^A(x(X_2,t))\bar{N}_2(X(\xi)) \tag{6.18}$$

It is crucial to realise that the finite element mesh generation of the immersed solid cannot be independent of the finite element mesh generation of the surrounding fluid phase. Indeed, a coarse solid mesh, as displayed for instance in Figure 6.2, will not yield optimal

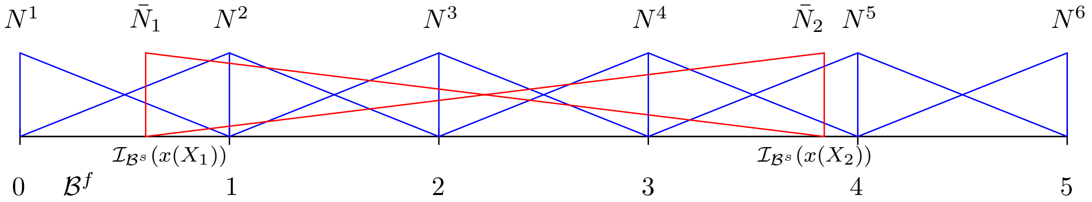

Figure 6.2: Effects of a coarse solid mesh.

results, since the background fluid shape function N^3 is not affected by the presence of the immersed solid. In other words, the numerical integration of the FSI force field $\boldsymbol{\mathcal{F}}$ will not be accurately computed. From the physical point of view, this would mean that the presence of the immersed solid is not properly accounted for by the surrounding fluid, leading to unphysical breaking of the solid phase. On the other hand, an unnecessarily fine solid mesh would result in an exceedingly high condition number of the resulting tangent stiffness matrix of the system (after linearisation) leading to numerical difficulties.

IFEM, NURBS mesh. The Euler-Lagrange mapping can be redefined for the application of a NURBS based finite element fluid description in a straightforward manner. As presented previously, the Lagrangian shape functions are replaced with NURBS shape functions to calculate the nodal values

$$\bar{\boldsymbol{v}}_C = \sum_{A\in\omega} R^A(\boldsymbol{x}(\boldsymbol{X}_C, t))\boldsymbol{v}_A; \quad \bar{p}_C = \sum_{B\in\bar{\omega}} R^B(\boldsymbol{x}(\boldsymbol{X}_C, t))p_B \tag{6.19}$$

leading to the interpolation-spreading operator

$$\mathcal{I}_{\mathcal{B}^s}(R^A(\boldsymbol{X}, t)) = \sum_{C=1}^{n_{\text{node}}} R^A(\boldsymbol{x}(\boldsymbol{X}_C, t))\bar{N}_C(\boldsymbol{X}) \tag{6.20}$$

which is also a linear operator.

ISPM. The last approach described in this section is the Immersed Structural Potential Method introduced in Gil et al. [22]. The solid is represented as a Helmholtz's free energy density functional immersed within the surrounding fluid phase. Moreover, the solid domain is modelled in a Lagrangian manner as a collection of integration points a_p immersed within the fluid, moving from an initial position $\boldsymbol{X}_{a_p}$ to the spatial position $\boldsymbol{x}_{a_p}$ through the deformation defined by the motion of the surrounding continuum (i.e. non-slip condition).

Notice that the integration points' parameters (i.e. spatial location $\boldsymbol{x}_{a_p}$ and associated tributary weight W_{a_p}) can be directly obtained on the solid domain, without the need for an initial tessellation (in the sense of a Finite Element approach). Alternatively, $\boldsymbol{X}_{a_p}$ and W_{a_p} can be obtained directly from the use of optimal high order Gaussian quadrature rules. As shown in [23], the latter approach can ensure accuracy of quadrature of the immersed potential and improve the speed of computation.

Within this approach, global shape functions $\varphi(\boldsymbol{x})$ are established on the Eulerian fluid grid to first interpolate the kinematic information directly to the solid integration points a_p and second, spread the calculated forces back to the balance of linear momentum of the fluid. The construction of the continuous functions $\varphi(\boldsymbol{x})$ starts with the approximation of the Dirac delta distribution through a tensorised discrete approximation

$$\varphi(\boldsymbol{x}) = \prod_{i=1}^{d} \delta_{\Delta x_i}(x_i), \quad d \in [2,\, 3] \tag{6.21}$$

where Δ_{x_i} is related to the size of the background fluid mesh and

$$\delta_{\Delta x_i} = \frac{1}{\Delta x_i} \varphi\left(\frac{x_i}{\Delta x_i}\right) \tag{6.22}$$

is defined in terms of a smoothed representation φ of the one dimensional Dirac delta distribution, to obtain

$$\boldsymbol{v}^{a_p} = \sum_{A} \varphi^A(\boldsymbol{x}^{a_p}) \boldsymbol{v}_A, \quad \varphi^A(\boldsymbol{x}^{a_p}) = \varphi(\boldsymbol{x}^{a_p} - \boldsymbol{x}^A) \tag{6.23}$$

for the interpolation of the velocity field. For details on the construction of sophisticated kernel functions, see Gil et al. [23]. More generally, we can write for the Euler-Lagrange mapping

$$\mathcal{I}_{\mathcal{B}^s}(\varphi^A(\boldsymbol{X}, t)) = \varphi^A(\boldsymbol{x}(\boldsymbol{X}, t)) \tag{6.24}$$

which coincides with the continuum map. A key aspect of this methodology is the direct integration of the deformable solid stresses from solid integration points to fluid nodes, similar to the Material Point Method (MPM) [82], reducing the number of interpolation operations (compare formula (6.24) with formulae (6.17) and (6.20)).

6.3 Calculation of the deformation tensor

The evaluation of the deformation gradient tensor in the IFEM methodology at the corresponding Gauss points requires the time integration of the velocity field at each node C of the immersed solid grid to recover the actual position of the node as

$$\bar{\boldsymbol{x}}_C \equiv \bar{\boldsymbol{x}}_C(\bar{\boldsymbol{v}}_C) = \int_{t_0}^{t} \bar{\boldsymbol{v}}(\tau)\ \mathrm{d}\tau \tag{6.25}$$

Taking equation (6.15) into account, we can express the deformation gradient tensor in a classical Finite Element sense as

$$\boldsymbol{F} = \sum_{C=1}^{n_{\mathrm{node}}} \bar{\boldsymbol{x}}_C \otimes \nabla_{\boldsymbol{X}} \bar{N}^C \tag{6.26}$$

For the ISPM methodology, it is necessary to integrate in time the deformation gradient tensor at any integration point a_p directly using the spatial velocity gradient tensor $\boldsymbol{l}$ defined as

$$\boldsymbol{l} = \sum_A \boldsymbol{v}_A \otimes \nabla_{\boldsymbol{x}} \varphi^A(\boldsymbol{x}) \tag{6.27}$$

and the kinematic relation

$$\dot{\boldsymbol{F}} = \boldsymbol{l}\boldsymbol{F} \tag{6.28}$$

For further details on an explicit representation of useful time integration schemes, refer to Gil et al. [22]. In contrast to the IFEM approach (see equation 6.26), the evaluation of the deformation gradient tensor $\boldsymbol{F}$ in the ISPM manner (equations (6.27)-(6.28)) prevents the occurrence of locking effects in the incompressibility limit. This will be shown at a later stage in this paper by means of a numerical example. Alternatively, an enhanced mode can be added into formula (6.26) in a Hu-Washizu multifield variational sense [6], to overcome the inherent difficulties of the IFEM approach (see Appendix A for further details).

In addition, within a full variational formulation, it is also possible to introduce the weak form of the mapping (6.7) as

$$\langle \left(\frac{\partial \boldsymbol{x}^{\mathrm{h}}(\boldsymbol{X}, t)}{\partial t} - \mathcal{I}_{\mathcal{B}^s}(\boldsymbol{v}^{\mathrm{h}}(\boldsymbol{X}, t)) \right), \delta \boldsymbol{x}^{\mathrm{h}} \rangle_{\mathcal{B}_0^{\mathrm{h},s}} = 0 \tag{6.29}$$

if the solution and test functional spaces

$$\boldsymbol{x}^{\mathrm{h}} = \sum_{C=1}^{n_{\mathrm{node}}} \bar{N}^C \boldsymbol{x}_C, \quad \delta \boldsymbol{x}^{\mathrm{h}} = \sum_{C=1}^{n_{\mathrm{node}}} \bar{N}^C \delta \boldsymbol{x}_C \tag{6.30}$$

of the immersed solid are explicitly defined (cf. Liu et al. [55]). In contrast to the approaches described above where the number of unknowns in the system coincides with those of the fluid phase, the final system of equations is now enlarged by the number of unknowns of the immersed solid.

6.4 Temporal discretization

Immersed solid. The additional immersed solid contributions defined in (6.11) and (6.12) for the solid domain need also to be discretized in time. The contribution to the linear momentum balance equation gives

$$\begin{aligned}
\boldsymbol{\mathcal{F}}^{\mathrm{h}}(\boldsymbol{v}_n,&\boldsymbol{v}_{n+1}, p_{n+1}) = \\
&\langle(\rho_0^f - \rho_0^s)\left(\frac{\mathcal{I}_{\mathcal{B}^s}(\boldsymbol{v}_{n+1}^{\mathrm{h}}) - \mathcal{I}_{\mathcal{B}^s}(\boldsymbol{v}_n^{\mathrm{h}})}{\Delta t} - \boldsymbol{g}_{n+1/2}^{\mathrm{h}}\right), \mathcal{I}_{\mathcal{B}^s}(\delta\tilde{\boldsymbol{v}}^{\mathrm{h}})\rangle_{\mathcal{B}_0^s} \\
&- \langle\tilde{\boldsymbol{\Sigma}}^s, (\boldsymbol{F}^s(\mathcal{I}_{\mathcal{B}^s}(\boldsymbol{v}_{n+1/2}^{\mathrm{h}})))^T \nabla_{\boldsymbol{X}}\, \mathcal{I}_{\mathcal{B}^s}(\delta\tilde{\boldsymbol{v}}^{\mathrm{h}})\rangle_{\mathcal{B}_0^s} \\
&+ \langle\bar{\boldsymbol{\sigma}}^f(\mathcal{I}_{\mathcal{B}^s}(\boldsymbol{v}_{n+1/2}^{\mathrm{h}}), \mathcal{I}_{\mathcal{B}^s}(p_{n+1}^{\mathrm{h}})), \nabla_{\boldsymbol{x}}\, \mathcal{I}_{\mathcal{B}^s}(\delta\tilde{\boldsymbol{v}}^{\mathrm{h}}) J^s(\mathcal{I}_{\mathcal{B}^s}(\boldsymbol{v}_{n+1/2}^{\mathrm{h}}))\rangle_{\mathcal{B}_0^s}
\end{aligned} \tag{6.31}$$

and the additional contribution to the kinematic constraint becomes

$$\mathcal{F}^{p,\mathrm{h}}(\boldsymbol{v}_n, \boldsymbol{v}_{n+1}) = \langle\left(\frac{J^s(\mathcal{I}_{\mathcal{B}^s}(\boldsymbol{v}_{n+1}^{\mathrm{h}})) - J^s(\mathcal{I}_{\mathcal{B}^s}(\boldsymbol{v}_n^{\mathrm{h}}))}{\Delta t}\right), \mathcal{I}_{\mathcal{B}^s}(\delta\tilde{p}^{\mathrm{h}})\rangle_{\mathcal{B}_0^s} \tag{6.32}$$

The evaluation of the second Piola-Kirchhoff stress tensor $\tilde{\boldsymbol{\Sigma}}^s$ in (6.31) is inspired by the development of energy-momentum schemes for solid mechanics

$$\begin{aligned}
&\tilde{\boldsymbol{\Sigma}}^s = 2DW(\boldsymbol{C}_{n+1/2}) + \\
&2\frac{W(\boldsymbol{C}_{n+1}) - W(\boldsymbol{C}_n) - \boldsymbol{\Sigma}^s(\boldsymbol{C}_{n+1/2}) : \Delta\boldsymbol{C}}{\Delta\boldsymbol{C} : \Delta\boldsymbol{C}}\Delta\boldsymbol{C}
\end{aligned} \tag{6.33}$$

which provide enhanced stability for large time steps (see Betsch & Steinmann [13]). Specifically, for a St. Venant-Kirchhoff material the discrete gradient in (6.33) is equal to the evaluation of the strain energy function at the mid-point of the strains, i.e. $\tilde{\boldsymbol{\Sigma}}^s = 2DW(\boldsymbol{C}_{n+1/2})$. Furthermore, this approach also shows enhanced stability for Neo-Hookean materials as presented in [35]. These two constitutive models will be employed in the numerical examples presented at a later stage in this paper.

Euler-Lagrange mapping. The Euler-Lagrange mapping requires an algorithmic search process to identify the local coordinates for the evaluation of the shape functions (i.e. $N^A(\boldsymbol{x}(\boldsymbol{X}_C, t))$. A similar process is also needed in contact mechanics on the actual contact surface and hence, can be applied with very few modifications to the problem at hand. In particular, a local Newton-Raphson iteration process is used to calculate the local values of N^A for each node $\boldsymbol{x}_C$. We cannot incorporate this iterative scheme within the mid-point type discretization without cumbersome modifications. An approach proposed in Hesch & Betsch [36] for contact problems would increase unnecessarily the total number of unknowns, limiting the efficiency of the overall algorithm. Thus, we resort to evaluating the mapping (6.17) itself at time n as follows

$$\mathcal{I}_{\mathcal{B}^s}(N^A(\boldsymbol{X}, t)) = \sum_{C=1}^{n_{\mathrm{node}}} N^A(\boldsymbol{x}(\boldsymbol{X}_C, t_n))\bar{N}_C(\boldsymbol{X}) \tag{6.34}$$

This approach has also been proposed in Hesch & Betsch [36] where it has been shown to be very suitable for contact problems. A similar approach is followed in the case of the IFEM-NURBS mapping (6.20) or the ISPM mapping (6.24).

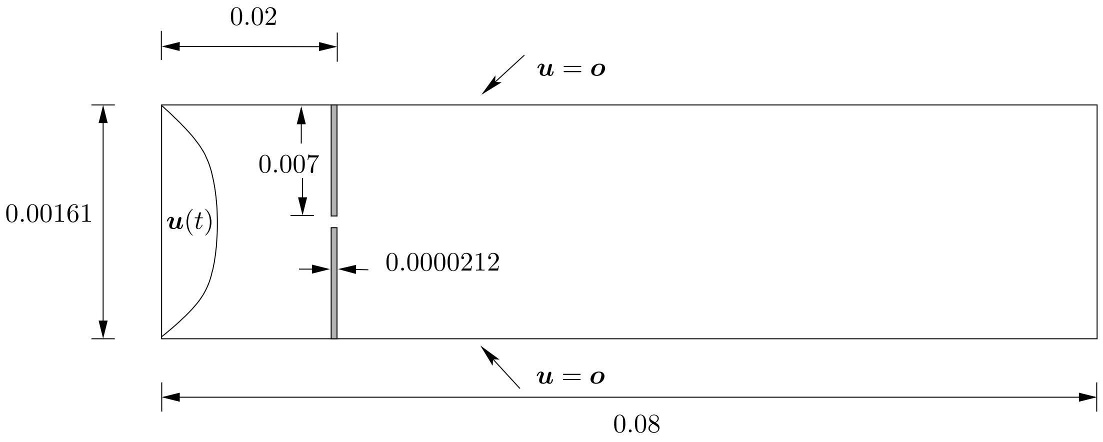

Figure 6.3: Geometry and boundary conditions for an idealised bi-leaflet valve.

6.5 Examples

Idealised bi-leaflet valve. This example is extracted from [22] and is explored in order to study the suitability of an immersed continuum methodology to the analysis of FSI haemodynamical problems. An idealised two-dimensional channel is considered filled with an incompressible Newtonian viscous fluid with viscosity $\mu = 1$ and density $\rho = 1 \cdot 10^5$ mimicking the behaviour of the blood. Two leaflets are inserted into the channel, as seen in Figure 6.3, representing the behaviour of an idealised two-leaflet valve. The top and bottom boundaries of the channel are fixed (i.e. homogeneous Dirichlet boundary conditions), a pulsatile non-reversible inflow is applied at the left hand boundary using the time-varying amplitude function $A(t) = 5 \cdot (\sin(2\pi t) + 1.1)$ and homogeneous Neumann boundary conditions are imposed at the right hand boundary. The leaflets are modelled as Neo-Hookean immersed solids using the Lamé parameters $\lambda^s = 8 \cdot 10^6$ and $\mu^s = 2 \cdot 10^6$ corresponding to a Young's modulus of $E = 5.6 \cdot 10^6$ and a Poisson ratio of $\nu = 0.4$. The leaflets are deliberately shortened to leave a gap between them, in order to simulate the behaviour of a regurgitating mitral valve due to stiffened (stenotic) leaflets (cf. Gil et al. [22]). For the numerical results presented in this section, the IFEM approach will be selected and compared against the results obtained in [22] by using the ISPM approach.

The series of diagrams in Figure 6.4 show the time evolution for the pulsatile flow and deformation of the membranes using a 256x64 Q1Q1 fluid mesh discretisation and 40x4 linear solid elements. The obtained deformation patterns are as expected and in correlation with those reported in [22] with the alternative ISPM methodology. The results demonstrate that the IFEM immersed continuum approach is able to successfully model the inclusion of highly deformable structures into the fluid without the need for expensive moving/remeshing algorithms. The methodology allows for very simple and robust treatment of the structure.

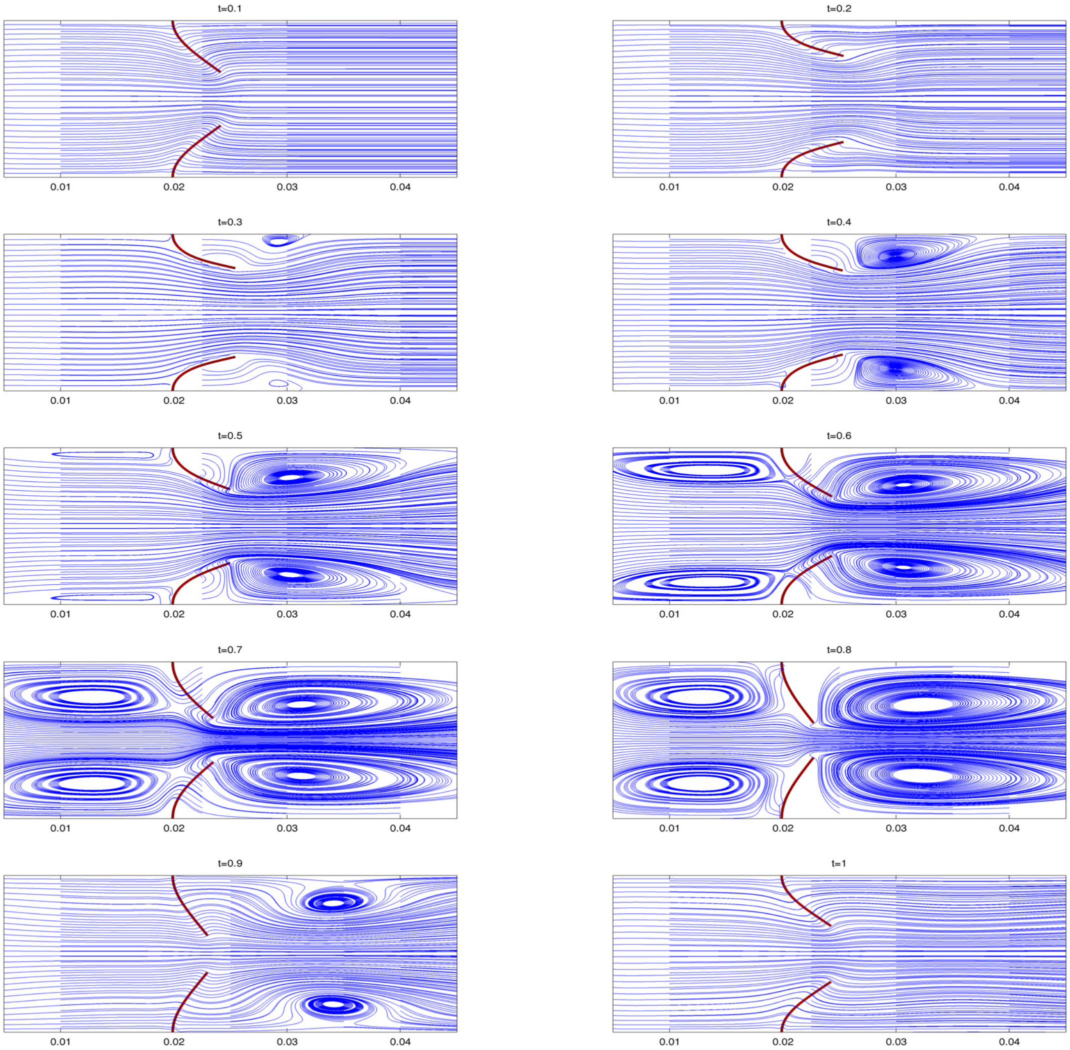

Figure 6.4: Time evolution of the leaflets and streamlines of the fluid.

This example has been analysed for a series of fluid discretisations in order to study the convergence pattern of the algorithm. The movement of the tip of the upper leaflet in the ox and oy directions are shown in Figures 6.5 and 6.6, respectively, for different discretisations. The results based on the Q1Q1 fluid finite element discretisation converge to the results of the Q2Q1 fluid finite element discretisation for a sufficiently fine mesh. Once again, converged results are in perfect agreement with those obtained with the ISPM shown in Gil et al. [22].

Idealised bi-leaflet valve – Locking effects In this subsection, the example described in the previous subsection is analysed again for different solid material parameters. The objective is to investigate possible locking effects in the case of a nearly incompressible behaviour, using a Young's modulus of $E = 5.6 \cdot 10^7$ and a Poisson ratio of $\nu = 0.4990$ for

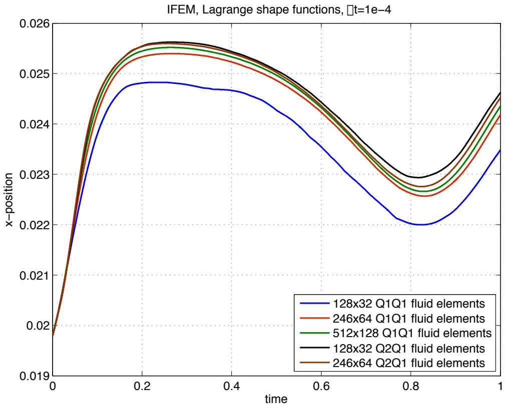

Figure 6.5: X-Position of the upper leaflet.

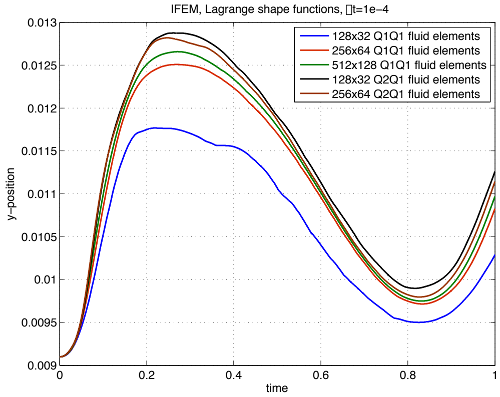

Figure 6.6: Y-Position of the upper leaflet.

both leaflets. The simulation is carried out by using the IFEM approach and the fluid is discretised using 128x32 Q2Q1 Taylor-Hood elements.

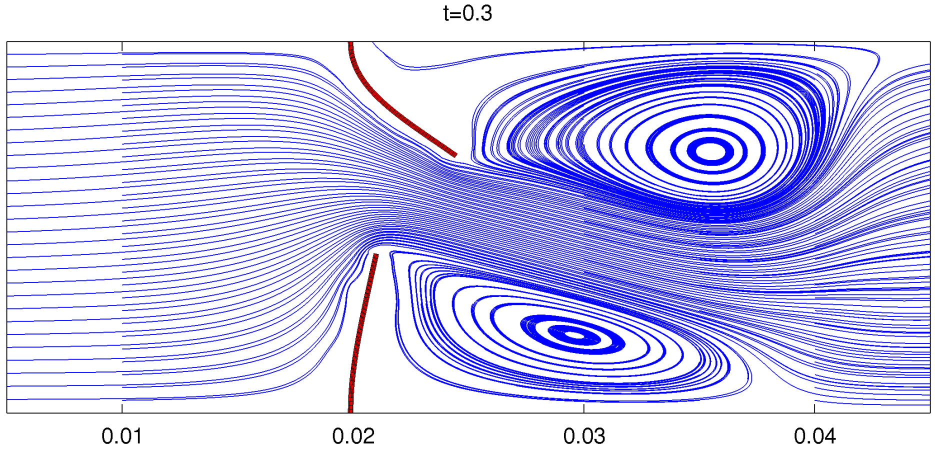

Figure 6.7: Idealised bi-leaflet valve. Locking effects.

The lower membrane is modelled with a standard displacement-based isoparametric quadrilateral linear finite element. It is expected that for this discretisation, the membrane should experience locking effects, classical in displacement-based formulations (see equation 6.26). On the other hand, the upper membrane is modelled by means of an enhanced finite element model, whose detailed formulation is presented in Appendix A). In this case, it is expected that the enhanced model should overcome any locking difficulties.

Figure 6.7 displays the streamlines after $t = 0.3$ and the resulting deformation of the leaflets. Despite the fact that the streamlines should show a symmetrical pattern with respect to the ox axis for this Reynolds number regime, a clear locking effect can be observed in the lower leaflet. On the other hand, the upper leaflet deforms as expected, demonstrating the need to implement enhanced solid finite elements in the range of nearly incompressible scenarios for the IFEM approach. When using the ISPM approach, these locking effects are not observed [22, 23]. This stems from the fact that the deformation gradient tensor $\boldsymbol{F}$ is obtained after time integration of the spatial velocity gradient tensor $\boldsymbol{l}$, which is evaluated from the Euler-Lagrange mapping (see equations 6.27 and 6.28).

7 Phase separation

Similar to immersed techniques, we consider a continuum approach for the different phases by introducing a bipotential operator in the Cahn-Hilliard phase-field model, cf. Cahn & Hilliard [15, 16]. A direct discretization if the interfaces between the various phase is also possible but require the solution of moving boundaries. The numerical treatment of the Cahn-Hilliard equation has been analysed in Anders et al. [2].

7.1 Aging of a Sn-Pb alloy

We assume that for a certain configuration the material tends to the phase with the lowest free energy which is favorable in the sense of thermodynamics. In this way it is possible to construct a single double-well free energy curve. To facilitate the numerical analysis, a smooth function Ψ^{con} is introduced as follows

$$\Psi^{\text{con}} = g_1 c + g_2 (1-c) + g_3 c \ln(c) + g_4 (1-c) \ln(1-c) + g_5 c (1-c) \,. \tag{7.1}$$

The values of the parameters are listed in table 7.1. Here, we simulate the aging of a Sn-Pb alloy using the data in table 7.1. To facilitate the use of dimensionless coordinates, we assume a characteristic length scale $\mathcal{T} = 67.4\text{h}$ for the time period and a characteristic length scale of $\mathfrak{L} = 2\,\mu\text{m}$ for the area of interest. The latter has been chosen to reduce computational cost, thus there are no fundamental reasons to argue against larger systems. The dimensionless system parameters are given as follows

Table 7.1: Coefficients for the free energy function Ψ^{con} at 150°C in GJ/m^3

$g_1 \left[\frac{\text{GJ}}{\text{m}^3}\right]$	$g_2 \left[\frac{\text{GJ}}{\text{m}^3}\right]$	$g_3 \left[\frac{\text{GJ}}{\text{m}^3}\right]$	$g_4 \left[\frac{\text{GJ}}{\text{m}^3}\right]$	$g_5 \left[\frac{\text{GJ}}{\text{m}^3}\right]$
-1.3527	-1.5145	0.3575	0.1585	0.8599

$$M = 6.25, \quad \kappa = 3.125 \cdot 10^{-5}. \tag{7.2}$$

We applied an initial random distribution of inhomogeneities of ±1% to the initial homogeneous composition of 63% Sn and 37% Pb. For the 2D simulation shown in Figs. 7.1 and 7.2 a grid of 128×128 nodes composing overall 15876 elements is used. The initial time step size is set to $2 \cdot 10^{-5}$ and doubled each 500 steps*.

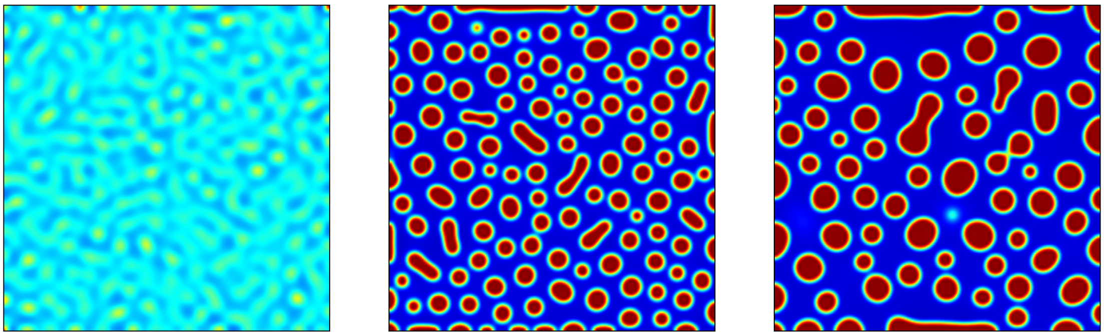

shortly after solidification 30 minutes of aging 2 hours of aging

Figure 7.1: Simulation results for Sn-Pb after 0.05, 0.5 and 2 hours of aging.

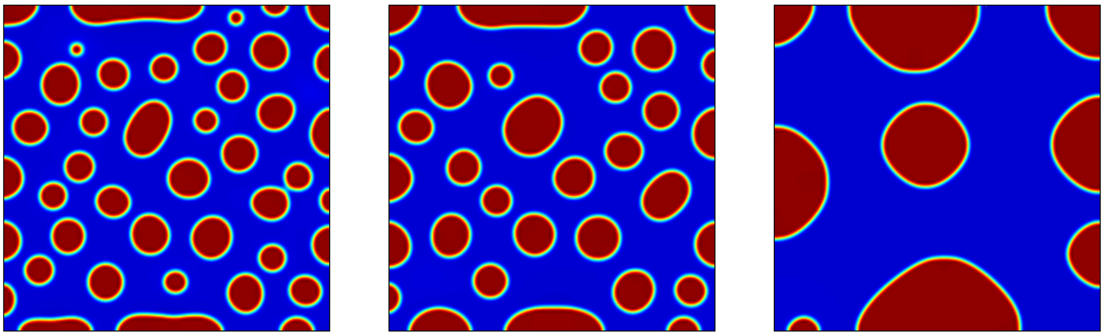

10 hours of aging 50 hours of aging 460 days of aging

Figure 7.2: Simulation results for Sn-Pb after 10, 50 and 11040 hours of aging.

---

*For the problem at hand the used time integration scheme is stable enough. For larger and more complex systems an adaptive time step control as proposed in Gomez et al. [25] should be considered.

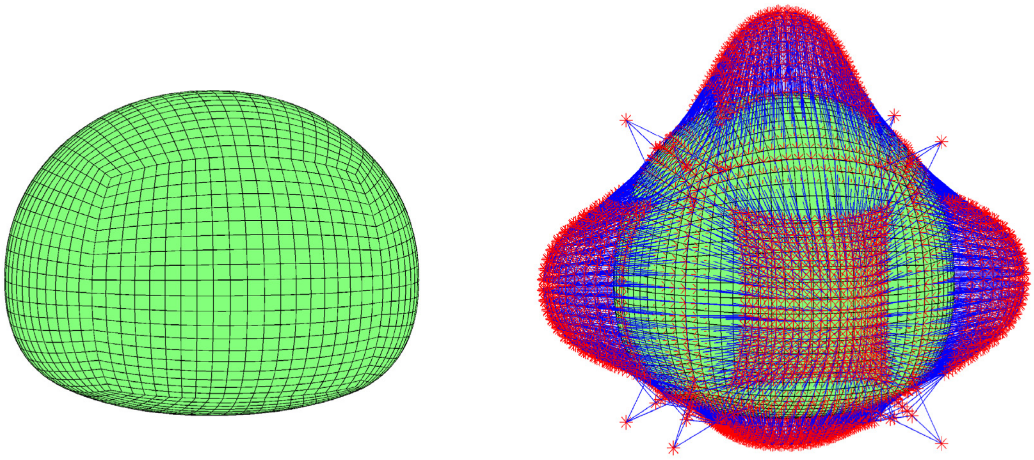

Figure 7.3: figure
Mesh and control nodes of a single bump.

7.2 Aging of a Sn-Pb solder ball

To demonstrate the operational capabilities of the B-spline based approach, we simulate a single bump, consisting of 10648 nodes and 8000 elements (cf. Fig. 7.3 for the mesh and the corresponding B-Spline control nodes[†]). The considered solder bump geometry results from a one-sidedly flattened sphere with rounded-off edges.

Analogously to the two-dimensional case, we reduce the physical size of the bump to 1μm, using the dimensionless system parameters

$$M = 25, \quad \kappa = 1.25 \cdot 10^{-4}. \tag{7.3}$$

Note that especially in the three-dimensional setting the computational cost grows drastically using finer meshes. For this reason, our considerations focus on reproducing the entire process of phase separation and early stages of Ostwald ripening. The initial time step size is set to $1 \cdot 10^{-5}$ and doubled each 500 steps. The evolution of the system is depicted for several time steps in Fig. 7.4. Within the upper row we present isosurfaces of several concentration values $c_i \in \{0.296, 0.37, 0.44\}$ inside the interfacial regions, whereas in the lower row corresponding slices through the body are illustrated. The obtained three-dimensional simulation results nicely corroborate our observations from the two-dimensional studies for the Sn-Pb alloy. After the Sn-Pb solder ball is deposited on the chip pad, the alloy is quenched into the unstable two-phase regime. Due to the thermodynamic instability of the investigated Sn-Pb system a decomposition of phases is induced. After 0.13 hours the solder bump is fully separated into α- and β-phase. Especially three-dimensional computational studies indicate that during phase separation the evolving interfacial regions gradually contract until phases are finally decomposed. This can be seen in the temporally decreasing spacing between the illustrated isosurfaces.

[†] To avoid negative determinants of the Jacobian the eight corner nodes are slightly lifted.

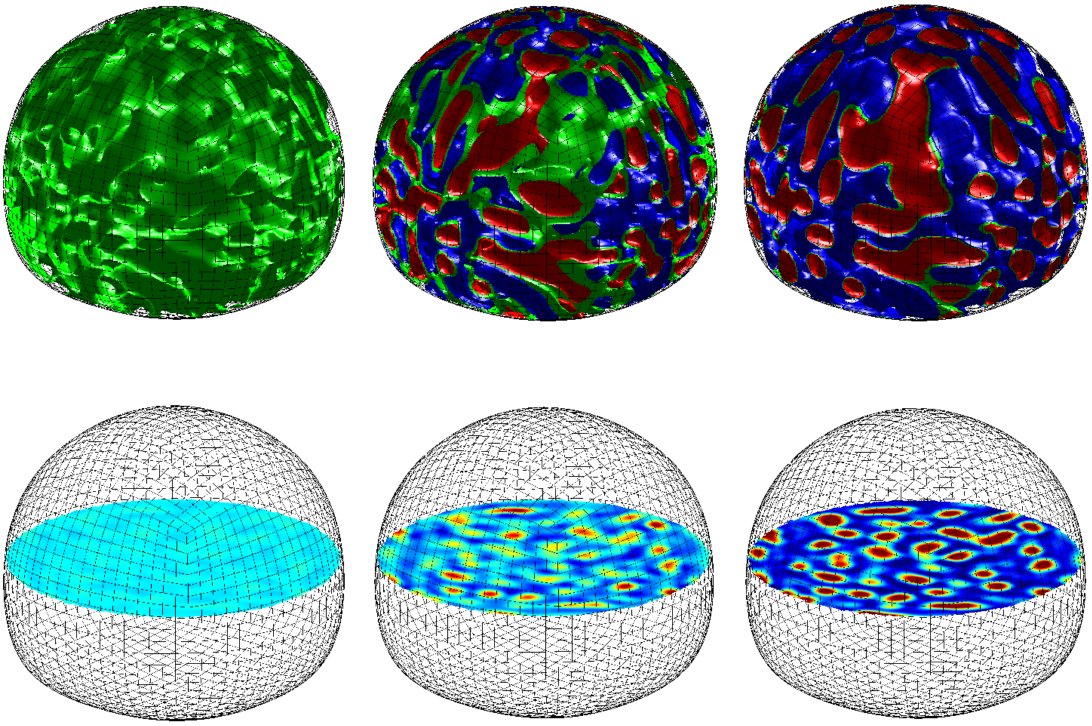

Figure 7.4: figure
Simulation results for a Sn-Pb solder ball after 0.06, 0.13 and 0.2 hours of aging.

Subsequently, Ostwald ripening dominates the further microstructural evolution. Our computational studies show a rearrangement of the evolved particles by the formation of first agglomerates after 0.2 hours of aging. Since we have shown that our model is capable of reproducing phase separating events in a solder ball geometry, we now would like to demonstrate the quality of our approach in terms of consistent scaling behavior and mesh independence. In order to transfer results from computational studies to real-life structures, the employed mathematical analogous model has to be scalable both in time and space. In the context of Cahn-Hilliard phase-field model this means that the numerical results scale with the characteristic length scales $\mathfrak{L}$ and $\mathcal{T}$ which are implicitly contained within the dimensionless system parameters M and κ. To illuminate the scalability of our three-dimensional model we present results for three solder balls of different size still involving the material parameters for eutectic Sn-Pb. Here we regard solder balls in the following scale settings:

1. $\mathfrak{L} = 1\,\mu\text{m}$, $M = 25$, $\kappa = 1.25 \cdot 10^{-4}$.
2. $\mathfrak{L} = 0.5\,\mu\text{m}$, $M = 100$, $\kappa = 5 \cdot 10^{-4}$.
3. $\mathfrak{L} = 0.25\,\mu\text{m}$, $M = 400$, $\kappa = 2 \cdot 10^{-3}$.

The time scale $\mathcal{L}$ is left unchanged for all configurations. Fig. 7.5 depicts the spatial scaling behavior of our numerical model on phase separation events within the abovementioned

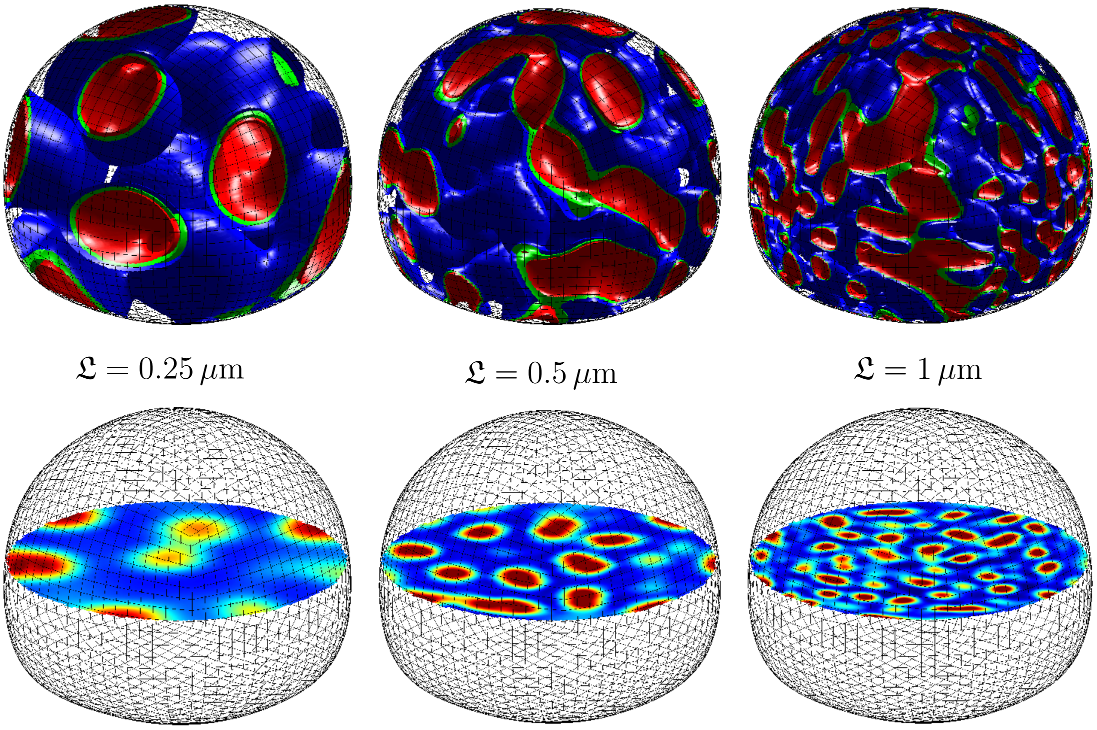

$\mathfrak{L} = 0.25\,\mu$m $\mathfrak{L} = 0.5\,\mu$m $\mathfrak{L} = 1\,\mu$m

Figure 7.5: figure
Comparison of phase separation events in different Sn-Pb solder balls after 0.175 hours of aging.

scale settings. Again the upper row illustrates isosurfaces of interfacial concentration values and in the lower row corresponding slices through the body are presented. Our results correctly indicate that the evolving microstructure scales with the characteristic length of the representative domain. After the same time of thermal aging the $0.25\,\mu$m-bump expectedly exhibits the coarsest microstructure with the biggest agglomerates. It is apparent that the microstructure in the $0.25\,\mu$m- and $0.5\,\mu$m-bump can be regarded as a suitable zoom-in part of the morphological arrangement within the $1\,\mu$m solder ball. This essential property underlines the correct scaling behavior of our model.

We conclude this section with a concise consideration of the mesh independence of our computational approach. To this end we study three solder balls with an equal characteristic length of $1\,\mu$m, which are spatially discretized by different mesh resolutions. Here we aim to demonstrate that within the range of a sufficient spatial resolution of the interfacial regions our model is mesh invariant. Fig. 7.6 presents results from our computational aging experiments starting with a rather coarse discretization by means of 4096 elements in the first column, we provide simulation results on much finer meshes discretized by 8000 elements in the second column and 21953 elements in the third column, respectively. The initial configurations for all simulations have been generated randomly. The simulations evince a deep qualitative agreement between the calculated microstructures on the different meshes. Invariant of the respective spatial resolution, Fig. 7.6 illustrates very similar

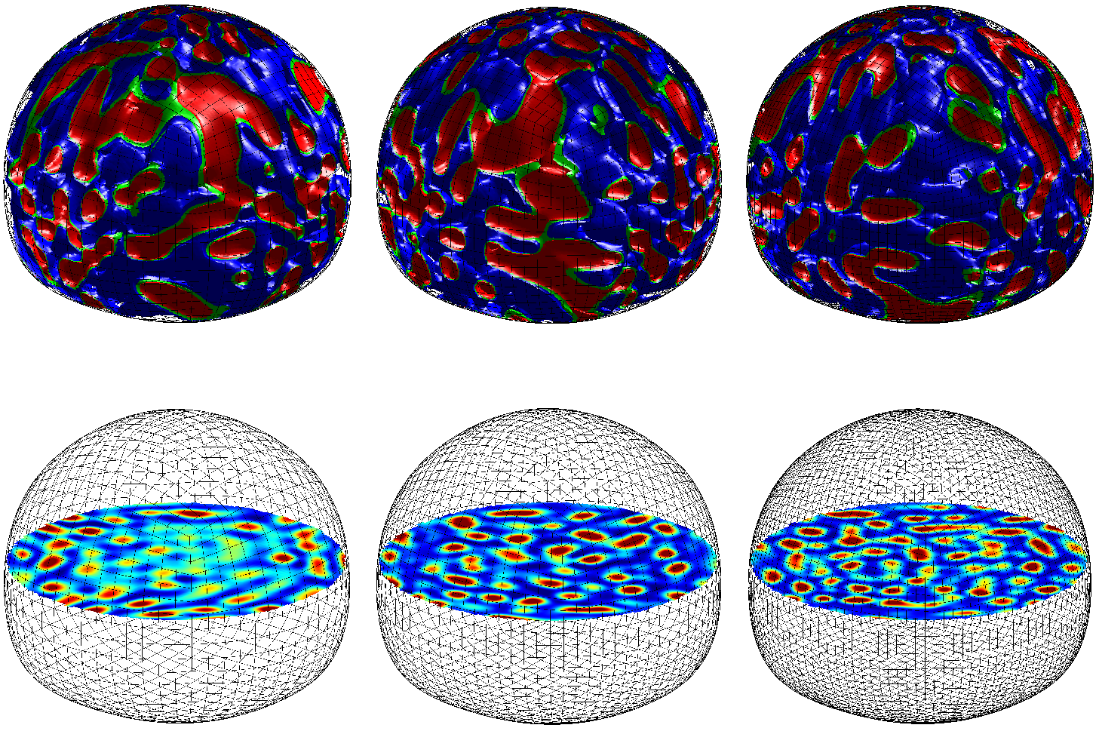

Figure 7.6: Comparison of phase separation events in differently discretized Sn-Pb solder balls after 0.17 hours of aging.

stages of phase separation and incipient Ostwald ripening. Consequently, we can state the mesh invariance of our spatial discretization scheme.

8 Summary and outlook

Within a continuum mechanical framework the most common field problems have been examined. In particular, solid mechanical problems, their extension to thermomechanical problems and fluid mechanical problems have been described in detail in strong and weak form. All three problems involve the solution of the balance of linear momentum, extended by an appropriate energy field equation for the thermal part and extended by a constraint field related to the pressure of an incompressible fluid. In contrast to all of them, the fourth system introduced deals with unsteady convective transport problems, where we have to solve a scalar valued diffusion equation.

For the numerical solution of the given problems, a common finite element framework has been introduced based on Lagrangian as well as NURBS based shape functions. Especially the latter one provides interesting features, which can be used in a wide range of problems and is subject to various research projects. The application to solid and fluid mechanical problems is straight forward, whereas the application to specific transport problems like the Cahn-Hilliard equation rests on the adjustable continuity of NURBS based shape functions.

For the temporal discretization we have applied a common framework to the problems at hand. For the solid and for the thermomechanical problems structure preserving integrators have been adapted to obtain enhanced stability. Although unusual for fluid mechanical system, which do not preserve certain values like total energy due to the specific formulation of the convective term, we have adapted the implicit integrator to the incompressible fluid as well and observed again enhanced stability using time step sizes which are up to a factor of thousand larger then used for explicit schemes. For the transport system, we can show that the application of the implicit integrator conserves algorithmically the total mass. Once again we receive a remarkable stable numerical solution for large time steps.

The main purpose of this work is to derive suitable interface descriptions for the various types of problems. Mortar based discretization schemes in the context of non-conform domain decomposition problems have been introduced for solid mechanical and thermomechanical problems using Lagrangian as well as NURBS based shape functions. The constraints have been rewritten in terms of appropriate invariants, such that we could adopt the constraint forces to the previously introduced structure preserving time integration scheme. Furthermore, inequality constraints in the form of contact problems have been addressed as well, using NTS and Mortar methods for the spatial discretization of the contact interface. For this class of problems we could also demonstrate the enhanced numerical stability provided by structure preserving time integration schemes.

The last two problems addressed in this work are also related to interface problems. The first one addressed here deals with fluid-structure interaction. Instead of a direct discretization of the boundary to transfer the momentum between the different fields, we employ continuum immersed strategies. Therefore, the immersed solid is represented by a force source field within the fluid using a suitable Euler-Lagrange mapping. This approach allows large deformations of the solid without remeshing the fluid. As before, we could demonstrate that the implicit time integration provides enhanced numerical stability allowing large time steps for the fluid-structure interaction as well. The last problem addressed in this work deals with the solution of the Cahn-Hilliard equations using higher order NURBS based shape functions to resolve the interface between the different phase fields. As before, we avoid a direct discretization of the interface using a single continuum formulation of the whole domain.

Many issues are not addressed here and should be considered in future work:

- The adaptation of NURBS based shape functions to beams and shells. The effects of higher order elements providing higher continuity between the elements should be investigated in the context of geometrically exact beams and shells.
- The existing thermomechanical framework should be applied to contact problems to provide an energy consistent integrator for frictional contact. Therefore, both, NTS as well as Mortar methods, should be considered for the spatial discretization of the interface.
- For fluid-structure interaction problems the framework of Mortar based discretization schemes should be adapted to the interface between the fields. In conjunction with the developed augmentation techniques as well as the structure preserving time integration schemes we assume that the numerical solution should be remarkable stable, reducing the computational costs tremendously for this class of problems.
- The extension of immersed techniques to structural elements should also be investigated.
- It is well known that Galerkin based discretization schemes in space introduce spurious artificial oscillations in the solution of transport problems. Various remedies have been proposed using SUPG and SGS methods. Those methods should be adapted to the Cahn-Hilliard equation within the given framework.

Appendix A

Enhanced assumed strain method

Standard displacement-based elements are subject to volumetric locking effects in the incompressible limit. To enhance the performance of the tri-linear displacement elements we incorporate the enhanced assumed strain method developed by Simo et al. [64, 65] into the present framework.

Based on the developments in Simo et al. [65] the following operator is introduced

$$\widetilde{\mathrm{Grad}}_X(\bullet) = \frac{j_0}{j(\boldsymbol{\xi})} \boldsymbol{J}_0^{-T}\, \mathrm{Grad}_\xi(\bullet) \tag{A.1}$$

with

$$\boldsymbol{J}(\boldsymbol{\xi}) = \frac{\partial \boldsymbol{X}^{\mathrm{h}}}{\partial \boldsymbol{\xi}}, \quad \boldsymbol{J}_0 = \boldsymbol{J}(\boldsymbol{\xi})\Big|_{\boldsymbol{\xi}=0}, \quad j(\boldsymbol{\xi}) = \det[\boldsymbol{J}(\boldsymbol{\xi})], \quad j_0 = j(\boldsymbol{0}) \tag{A.2}$$

The enhanced deformation gradient can now be written as

$$\boldsymbol{F}^{\mathrm{h}} = \sum_{A=1}^{n_{\mathrm{node}}} \boldsymbol{q}_A \otimes \widehat{\mathrm{Grad}}_X(N^A) + \sum_{A=1}^{n_{\mathrm{enh}}} \boldsymbol{\alpha}_A \otimes \widetilde{\mathrm{Grad}}_X(M^A) \tag{A.3}$$

where

$$\widehat{\mathrm{Grad}}(N^A) = \mathrm{Grad}_0(N^A) + \sum_{J=1}^{4} \gamma_J^A \widetilde{\mathrm{Grad}}_X(\mathcal{H}^J) \tag{A.4}$$

Here, $\boldsymbol{\gamma}_J$ are gamma-stabilization vectors and $\mathcal{H}^J$ hourglass functions, defined in Belytschko et al. [6]. Additionally we introduce Wilson's incompatible shape functions (see Wilson et al. [75]) for tri-linear brick elements

$$M^1 = \frac{1}{2}[\xi_1^2 - 1], \quad M^2 = \frac{1}{2}[\xi_2^2 - 1], \quad M^3 = \frac{1}{2}[\xi_3^2 - 1] \tag{A.5}$$

Now the discrete enhanced version of (1.7) reads

$$\begin{aligned} \langle \delta\boldsymbol{\varphi}^{\mathrm{h}}, \dot{\boldsymbol{\pi}}^{\mathrm{h}} \rangle_{\mathcal{B}_0^{\mathrm{h}}} + \langle \boldsymbol{F}^{\mathrm{h}} \boldsymbol{\Sigma}^{\mathrm{h}}, \widehat{\mathrm{Grad}}(\delta\boldsymbol{\varphi}^{\mathrm{h}}) \rangle_{\mathcal{B}_0^{\mathrm{h}}} &= \langle \delta\boldsymbol{\varphi}^{\mathrm{h}}, \bar{\boldsymbol{T}} \rangle_{\partial\mathcal{B}_0^{\mathrm{h},\sigma}} + \langle \delta\boldsymbol{\varphi}^{\mathrm{h}}, \bar{\boldsymbol{B}} \rangle_{\mathcal{B}_0^{\mathrm{h}}} \\ \langle \boldsymbol{F}^{\mathrm{h}} \boldsymbol{\Sigma}^{\mathrm{h}}, \widetilde{\mathrm{Grad}}(\delta\boldsymbol{\alpha}^{\mathrm{h}}) \rangle_{\mathcal{B}_0^{\mathrm{h}}} &= \boldsymbol{0} \end{aligned} \tag{A.6}$$

where $\boldsymbol{\alpha}^{\mathrm{h}} = \sum\limits_{A=1}^{n_{\mathrm{enh}}} M^A \boldsymbol{\alpha}_A$. Concerning the discretization in time the additional $\boldsymbol{\alpha}$-modes are evaluated in the mid-point

$$\boldsymbol{\alpha}^{\mathrm{h}}_{n+\frac{1}{2}} = \frac{1}{2}(\boldsymbol{\alpha}^{\mathrm{h}}_n + \boldsymbol{\alpha}^{\mathrm{h}}_{n+1}) \tag{A.7}$$

The enhanced form of the fully discrete system (3.14) can now be written in the form

$$\begin{aligned}
\delta\boldsymbol{q}_A \cdot \left[M^{AB}(\boldsymbol{v}_{B,n+1} - \boldsymbol{v}_{B,n}) + \Delta t \int\limits_{\mathcal{B}_0} \widehat{\mathrm{Grad}}(N^B) \cdot \boldsymbol{\Sigma}^{\mathrm{h}}_{n,n+1} \boldsymbol{F}^{\mathrm{h}}_{n+\frac{1}{2}} \,\mathrm{d}V \right] &= \Delta t \delta\boldsymbol{q}_A \cdot \left[\boldsymbol{F}^{A,\mathrm{ext}}_{n+\frac{1}{2}} \right] \\
\delta\boldsymbol{\alpha} \cdot \left[\int\limits_{\mathcal{B}_0} \widetilde{\mathrm{Grad}}_X(M^A) \cdot \boldsymbol{\Sigma}^{\mathrm{h}}_{n,n+1} \boldsymbol{F}^{\mathrm{h}}_{n+\frac{1}{2}} \,\mathrm{d}V \right] &= \boldsymbol{0} \\
\delta\Theta_A \left[\Gamma^{AB}_{n,n+1} \Theta_{B,n+\frac{1}{2}} - \Delta t \int\limits_{\mathcal{B}_0} K^{AB}_{n,n+1} \,\mathrm{d}V \Theta_{B,n+\frac{1}{2}} \right] &= \Delta t \delta\Theta_A Q^{\mathrm{h},A}_{n,n+1}
\end{aligned} \tag{A.8}$$

Note that the additional equations $(A.8)_2$ can be eliminated using standard condensation procedures. We further remark that the enhancement of the space discretization outlined above does not affect the conservation and consistency properties of the present energy-momentum integrator.

Appendix B

Variational formulation of thermomechanics

In Section 1.2 we have used the fundamental lemma of calculus of variations to transform the strong form of the balance equations into the weak form. For details on variational calculations of multifield problems see Kovetz [49, Chapter 15]. In this appendix we investigate the connection between the balance equations and an extended Hamilton principle postulated as follows

$$\delta \int_{t_0}^{t_1} L \,\mathrm{d}t = 0 \;\Leftrightarrow\; \delta \int_{t_0}^{t_1} H - \boldsymbol{\pi} \cdot \dot{\boldsymbol{\varphi}} \,\mathrm{d}t = 0 \;\Leftrightarrow\; \delta \int_{t_0}^{t_1} \langle [\frac{1}{2} \rho_0^{-1} \boldsymbol{\pi}^2 + e - \boldsymbol{\pi} \cdot \dot{\boldsymbol{\varphi}}] \rangle_{\mathcal{B}_0} + \Pi^{\text{ext}} \,\mathrm{d}t = 0 \quad \text{(B.1)}$$

Here, $\Pi^{\text{ext}} = \Pi^{\text{ext}}_{\text{mech}}(\boldsymbol{\varphi}) + \Pi^{\text{ext}}_{\text{therm}}(\eta)$ denotes all external contributions to the initial boundary value problem. The last equation can be derived using Livin's theorem (cf. Pars [56, Chapter 10]), which is equivalent to the Legendre transformation of the Lagrangian. To resolve the system in terms of the free Helmholtz energy, we have to incorporate a second Legendre transformation. Thus, we receive

$$\int_{t_0}^{t_1} \delta \langle [\frac{1}{2} \rho_0^{-1} \boldsymbol{\pi}^2 + \Psi + \theta\eta - \boldsymbol{\pi} \cdot \dot{\boldsymbol{\varphi}}] \rangle_{\mathcal{B}_0} + \delta \Pi^{\text{ext}} \,\mathrm{d}t = 0 \quad \text{(B.2)}$$

Note, that we can only include the variation in the time integral if we postulate the absence of non-holonomic constraints. Next, we implement a Hu-Washizu type functional into the equation

$$\int_{t_0}^{t_1} \delta \langle [\frac{1}{2} \rho_0^{-1} \boldsymbol{\pi}^2 + \Psi(\boldsymbol{C}, \theta) + \frac{1}{2} \boldsymbol{\Sigma} : [(D\boldsymbol{\varphi})^T D\boldsymbol{\varphi} - \boldsymbol{C}] + \theta\eta - \boldsymbol{\pi} \cdot \dot{\boldsymbol{\varphi}}] \rangle_{\mathcal{B}_0} + \delta \Pi^{\text{ext}} \,\mathrm{d}t = 0 \quad \text{(B.3)}$$

where we introduce $\boldsymbol{C}$ and $\boldsymbol{\Sigma}$ as additional variables to the system. Note, that Σ are Lagrange multipliers. After short calculations we obtain the canonical formulation of

Hamiltons principle after short calculations

$$\begin{aligned}\int_{t_0}^{t_1} \langle \Big\{ [\rho^{-1}\boldsymbol{\pi} - \dot{\boldsymbol{\varphi}}] \cdot \delta\boldsymbol{\pi} + \left[\frac{\partial \Psi}{\partial \boldsymbol{C}} - \frac{1}{2}\boldsymbol{\Sigma}\right] : \delta\boldsymbol{C} + D\boldsymbol{\varphi}\boldsymbol{\Sigma} : D\delta\boldsymbol{\varphi} + \dot{\boldsymbol{\pi}} \cdot \delta\boldsymbol{\varphi} + \\ \frac{1}{2}\delta\boldsymbol{\Sigma} : [(D\boldsymbol{\varphi})^T D\boldsymbol{\varphi} - \boldsymbol{C}] + [\frac{\partial \Psi}{\partial \theta} + \eta]\delta\theta \Big\} \rangle_{\mathcal{B}_0} + \frac{\partial \Pi^{\text{ext}}_{\text{mech}}}{\partial \boldsymbol{\varphi}} \cdot \delta\boldsymbol{\varphi} \, \mathrm{d}t = 0\end{aligned} \tag{B.4}$$

where we have made use of a partial integration and postulate, that the variation $\delta\boldsymbol{\varphi}$ equals zero at t_0 and t_1. Note, that the variation with respect to the entropy equals the variation of the external contributions as follows

$$\int_{t_0}^{t_1} \langle \theta \delta\eta \rangle_{\mathcal{B}_0} + \frac{\partial \Pi^{\text{ext}}_{\text{therm}}}{\partial \eta} \delta\eta \, \mathrm{d}t = 0 \tag{B.5}$$

The first term in (B.4) reflects the first Legendre transformation, since $\boldsymbol{\pi} = \frac{\partial L}{\partial \dot{\boldsymbol{\varphi}}}$. Moreover, the sixth term reflects the second Legendre transformation. For the rest of the variations we end up with a system of differential algebraic equations

$$\begin{aligned}\langle [\dot{\boldsymbol{\pi}} \cdot \delta\boldsymbol{\varphi} + D\boldsymbol{\varphi}\boldsymbol{\Sigma} : D\delta\boldsymbol{\varphi}] \rangle_{\mathcal{B}_0} + \frac{\partial \Pi^{\text{ext}}_{\text{mech}}}{\partial \boldsymbol{\varphi}} \cdot \delta\boldsymbol{\varphi} &= 0 \\ \frac{1}{2}\langle [(D\boldsymbol{\varphi})^T D\boldsymbol{\varphi} - \boldsymbol{C}] : \delta\boldsymbol{\Sigma} \rangle_{\mathcal{B}_0} &= 0 \\ \langle \left[\frac{\partial \Psi}{\partial \boldsymbol{C}} - \frac{1}{2}\boldsymbol{\Sigma}\right] : \delta\boldsymbol{C} \rangle_{\mathcal{B}_0} &= 0\end{aligned} \tag{B.6}$$

Appendix C

Constitutive evolution equations

Many researchers have investigated various constitutive laws used to describe the tangential tractions. We omit a further investigation and focus on a standard dry friction Coulomb law to complete the set of equations used for the numerical examples. Based on this specific formulation, we state that

$$\|\boldsymbol{t}_T\| \leq \mu\, t_N \quad \text{and} \quad \varphi := \|\boldsymbol{t}_T\| - \mu\, t_N \leq 0 \tag{C.1}$$

The tangential displacement in the case of slip follows from $\boldsymbol{u}_T = \eta\, \boldsymbol{t}_T$ where η denotes the consistency parameter, which depends on (C.1) and we can write

$$\eta \begin{cases} = 0, & \text{if} \quad \varphi < 0 \\ \geq 0, & \text{elseif} \quad \|\boldsymbol{t}_T\| = \mu\, t_N \end{cases} \tag{C.2}$$

In analogy to plasticity, we rewrite the last statement as follows

$$\begin{gathered} \varphi \leq 0, \quad \eta \geq 0, \quad \eta\varphi = 0 \\ \boldsymbol{v}_T = \eta \left(\frac{\partial}{\partial \boldsymbol{t}_T} \varphi \right) = \eta\, \frac{\boldsymbol{t}_T}{\|\boldsymbol{t}_T\|} \end{gathered} \tag{C.3}$$

and regularize the equation for the tangential velocity $\boldsymbol{v}_T$ $(C.3)_2$ using a penalty method

$$\boldsymbol{v}_T = \eta\, \frac{\boldsymbol{t}_T}{\|\boldsymbol{t}_T\|} + \frac{1}{\epsilon_T}\, \dot{\boldsymbol{t}}_T \tag{C.4}$$

Note that the components in tangential direction read

$$\frac{\dot{t}_{T_\alpha}}{\epsilon_T} = m_{\alpha\beta}\, \dot{\xi}^\beta - \eta\, \frac{t_{T_\alpha}}{\|\boldsymbol{t}_T\|} \tag{C.5}$$

where we have made use of $\boldsymbol{v}_T = m_{\alpha\beta}\, \dot{\xi}^\beta\, \boldsymbol{a}^\alpha$.

Local time stepping scheme for the frictional evolution equations Here, we apply a one-step integration scheme of the local evolution equations (C.5) following the arguments in Armero & Petöcz [4]. Consequently, the approximation of the tractions can be written as follows

$$t_{T_{\alpha,n+\vartheta}} - t_{T_{\alpha,n}} = \epsilon_T \, m_{\alpha\beta_{n+\vartheta}} \left(\xi^{\beta}_{n+\vartheta} - \xi^{\beta}_{n} \right) - \epsilon_T \, \eta \, \frac{t_{T_{\alpha,n+\vartheta}}}{\|\boldsymbol{t}_{T_{n+\vartheta}}\|} \tag{C.6}$$

where $\vartheta \in [0,1]$ controls the corresponding time stepping scheme and should be chosen consistent with the global time stepping scheme. Taking the inequality conditions (C.3) into account, we obtain

$$\begin{aligned} \varphi_{n+\vartheta} &= \|\boldsymbol{t}_{T_{n+\vartheta}}\| - \mu \, t_N \leq 0, \quad \eta \geq 0, \quad \eta \, \varphi_{n+\vartheta} = 0 \\ t_{T_{\alpha,n+\vartheta}} &= t_{T_{\alpha,n}} + \epsilon_T \left(m_{\alpha\beta_{n+\vartheta}} \left(\xi^{\beta}_{n+\vartheta} - \xi^{\beta}_{n} \right) - \eta \, \vartheta \, \frac{t_{T_{\alpha,n+\vartheta}}}{\|\boldsymbol{t}_{T_{n+\vartheta}}\|} \right) \end{aligned} \tag{C.7}$$

Note that t_N is represented by a Lagrange multiplier, constant within the time step. To implement (C.7) we apply a return mapping scheme and start by considering the stick case, i.e. $\eta = 0$

$$\begin{aligned} t^{tr}_{T_{\alpha,n+\vartheta}} &= t_{T_{\alpha,n}} + \epsilon_T \, m_{\alpha\beta_{n+\vartheta}} \left(\xi^{\beta}_{n+\vartheta} - \xi^{\beta}_{n} \right) \\ \varphi^{tr}_{n+\vartheta} &= \|\boldsymbol{t}^{tr}_{T_{n+\vartheta}}\| - \mu \, t_N \leq 0 \end{aligned} \tag{C.8}$$

which defines our trial state. Depending on the condition $(C.8)_2$, slip occurs and we obtain

$$t^{tr}_{T_{\alpha,n+\vartheta}} = \epsilon_T \, \vartheta \, \eta \, \frac{t_{T_{\alpha,n+\vartheta}}}{\|\boldsymbol{t}_{T_{n+\vartheta}}\|} + t_{T_{\alpha,n+\vartheta}} \tag{C.9}$$

by comparing $(C.7)_2$ and $(C.8)_1$. After short calculations using the relation $\boldsymbol{t}^{tr}_{T_{n+\vartheta}} / \|\boldsymbol{t}^{tr}_{T_{n+\vartheta}}\| = \boldsymbol{t}_{T_{n+\vartheta}} / \|\boldsymbol{t}_{T_{n+\vartheta}}\|$ the consistency parameter in the case of slip is determined by

$$\eta = \frac{\varphi^{tr}_{n+\vartheta}}{\vartheta \, \epsilon_T} > 0 \tag{C.10}$$

Thus, the final contribution in the case of slip reads

$$t_{T_{\alpha,n+\vartheta}} = \mu \, t_{N_{n+\vartheta}} \frac{t_{T_{\alpha,n+\vartheta}}}{\|\boldsymbol{t}^{tr}_{T_{n+\vartheta}}\|} \tag{C.11}$$

To summarize, the return mapping scheme can be written as follows

$$t_{T_{\alpha,n+\vartheta}} = \begin{cases} t^{tr}_{T_{\alpha,n+\vartheta}}, & \text{if}\, \varphi^{tr}_{n+\vartheta} \leq 0 \\ \mu \, t_{N_{n+\vartheta}} \frac{t^{tr}_{T_{\alpha,n+\vartheta}}}{\|\boldsymbol{t}^{tr}_{T_{n+\vartheta}}\|}, & \text{elseif}\, \varphi^{tr}_{n+\vartheta} > 0 \end{cases} \tag{C.12}$$

which completes the used definition for the tractions.

Appendix D

Null space method

The direct discretization of the DAEs governing the motion of constrained mechanical systems necessitates the solution of saddle point systems of the form

$$\begin{bmatrix} \boldsymbol{\mathcal{N}} & \widetilde{\boldsymbol{\mathcal{G}}}^T \\ \boldsymbol{\mathcal{G}} & \mathbf{0} \end{bmatrix} \begin{bmatrix} \Delta \boldsymbol{q} \\ \Delta \widetilde{\boldsymbol{\lambda}} \end{bmatrix} = - \begin{bmatrix} \boldsymbol{R}_q \\ \boldsymbol{R}_\lambda \end{bmatrix} \tag{D.1}$$

where

$$\begin{aligned} &\boldsymbol{\mathcal{N}} = D_1 \boldsymbol{R}_q(\boldsymbol{q}_{n+1}, \boldsymbol{\lambda}_{n+1}), \quad &&\boldsymbol{\mathcal{G}} = D\boldsymbol{\Phi}(\boldsymbol{q}_{n+1}), \quad \widetilde{\boldsymbol{\mathcal{G}}} = D_2 \boldsymbol{R}_q(\boldsymbol{q}_{n+1}, \boldsymbol{\lambda}_{n+1})^T \\ &\boldsymbol{R}_\lambda = \boldsymbol{\Phi}(\boldsymbol{q}_{n+1}), &&\Delta \widetilde{\boldsymbol{\lambda}} = \Delta t \Delta \boldsymbol{\lambda} \end{aligned}$$

Although the above saddle point system could be directly solved, we advocate a reformulation of (D.1) which fits into the framework of the discrete null space method. In this context, the discrete null space method has been developed by Betsch [10] to achieve a size-reduction along with an improved conditioning of the system to be solved. Our approach can be linked to null space methods often used in optimization, cf. Benzi et al. [8, Section 6.].

Let n be the number of redundant coordinates and m be the number of constraints. We start with the introduction of a change of coordinates

$$\Delta \boldsymbol{q} = \boldsymbol{U} \Delta \boldsymbol{u} \tag{D.2}$$

with $\Delta \boldsymbol{u} \in \mathbb{R}^n$ and a nonsingular transformation matrix $\boldsymbol{U} \in \mathbb{R}^{n \times n}$. Next, split $\Delta \boldsymbol{u}$ into independent coordinates $\Delta \boldsymbol{u}_I \in \mathbb{R}^{n-m}$ and dependent coordinates $\Delta \boldsymbol{u}_D \in \mathbb{R}^m$, such that

$$\Delta \boldsymbol{u} = \begin{bmatrix} \Delta \boldsymbol{u}_I \\ \Delta \boldsymbol{u}_D \end{bmatrix} \tag{D.3}$$

and, correspondingly, $\boldsymbol{U} = [\boldsymbol{U}_I, \, \boldsymbol{U}_D]$. In this connection, we require that the $m \times m$ matrix $\widetilde{\boldsymbol{\mathcal{G}}} \boldsymbol{U}_D$ is invertible. Making use of the above coordinate partitioning, (D.2) can be recast in the form

$$\Delta \boldsymbol{q} = \boldsymbol{U}_I \Delta \boldsymbol{u}_I + \boldsymbol{U}_D \Delta \boldsymbol{u}_D \tag{D.4}$$

Premultiplying the first row in (D.1) by $\boldsymbol{U}^T$ yields

$$\boldsymbol{U}_I^T \boldsymbol{\mathcal{N}} \Delta \boldsymbol{q} + \boldsymbol{U}_I^T \widetilde{\boldsymbol{\mathcal{G}}}^T \Delta \widetilde{\boldsymbol{\lambda}} = -\boldsymbol{U}_I^T \boldsymbol{R}_q \tag{D.5}$$

$$\boldsymbol{U}_D^T \boldsymbol{\mathcal{N}} \Delta \boldsymbol{q} + \boldsymbol{U}_D^T \widetilde{\boldsymbol{\mathcal{G}}}^T \Delta \widetilde{\boldsymbol{\lambda}} = -\boldsymbol{U}_D^T \boldsymbol{R}_q \tag{D.6}$$

The second of the above equations gives rise to

$$\Delta \widetilde{\boldsymbol{\lambda}} = -(\widetilde{\boldsymbol{\mathcal{G}}} \boldsymbol{U}_D)^{-T} \boldsymbol{U}_D^T \left[\boldsymbol{R}_q + \boldsymbol{\mathcal{N}} \Delta \boldsymbol{q} \right] \tag{D.7}$$

Substituting the last equation into (D.5) leads to

$$\widetilde{\boldsymbol{P}}^T \boldsymbol{\mathcal{N}} \Delta \boldsymbol{q} = -\widetilde{\boldsymbol{P}}^T \boldsymbol{R}_q \tag{D.8}$$

where the $n \times (n - m)$ matrix

$$\widetilde{\boldsymbol{P}} := \left(\boldsymbol{I}_n - \boldsymbol{U}_D (\widetilde{\boldsymbol{\mathcal{G}}} \boldsymbol{U}_D)^{-1} \widetilde{\boldsymbol{\mathcal{G}}} \right) \boldsymbol{U}_I \tag{D.9}$$

can be identified as a discrete null space matrix (cf. Betsch [10], Section 3.2.1). Note that, by design, $\widetilde{\boldsymbol{P}}$ spans the null space of the discrete constraint Jacobian $\widetilde{\boldsymbol{\mathcal{G}}}$. Consequently, $\widetilde{\boldsymbol{\mathcal{G}}} \widetilde{\boldsymbol{P}} = \boldsymbol{0}$. Now the generalized saddle point system (D.1) can be solved by applying two successive steps. First solve

$$\begin{bmatrix} \widetilde{\boldsymbol{P}}^T \boldsymbol{\mathcal{N}} \\ \boldsymbol{\mathcal{G}} \end{bmatrix} \Delta \boldsymbol{q} = - \begin{bmatrix} \widetilde{\boldsymbol{P}}^T \boldsymbol{R}_q \\ \boldsymbol{R}_\lambda \end{bmatrix} \tag{D.10}$$

for $\Delta \boldsymbol{q} \in \mathbb{R}^n$. Then ($D$.7) can be used to determine $\Delta \boldsymbol{\lambda} \in \mathbb{R}^m$. Table D.1 contains a summary of the solution procedure which is embedded into the active set strategy as outlined in Section 5.1.

Alternative solution of the reduced system We next outline a further reformulation of the system to be solved that retains the symmetry in case the underlying saddle point system (D.1) is symmetric, e.g. for equilibrium problems. The size-reduced system (D.10) may be solved alternatively by making use of the generalized coordinate partitioning (D.4) again. To this end, the second row in (D.10) may be written as

$$\boldsymbol{\mathcal{G}} \boldsymbol{U}_I \Delta \boldsymbol{u}_I + \boldsymbol{\mathcal{G}} \boldsymbol{U}_D \Delta \boldsymbol{u}_D = -\boldsymbol{R}_\lambda \tag{D.11}$$

so that

$$\Delta \boldsymbol{u}_D = -(\boldsymbol{\mathcal{G}} \boldsymbol{U}_D)^{-1} \left[\boldsymbol{R}_\lambda + \boldsymbol{\mathcal{G}} \boldsymbol{U}_I \Delta \boldsymbol{u}_I \right] \tag{D.12}$$

Now the first row in (D.10), in conjunction with (D.4) and (D.12), can be recast in the form

$$\widetilde{\boldsymbol{P}}^T \boldsymbol{\mathcal{N}} \boldsymbol{P} \Delta \boldsymbol{u}_I = -\widetilde{\boldsymbol{P}}^T \left[\boldsymbol{R}_q - \boldsymbol{\mathcal{N}} \boldsymbol{U}_D (\boldsymbol{\mathcal{G}} \boldsymbol{U}_D)^{-1} \boldsymbol{R}_\lambda \right] \tag{D.13}$$

where

$$\boldsymbol{P} := \left(\boldsymbol{I}_n - \boldsymbol{U}_D (\boldsymbol{\mathcal{G}} \boldsymbol{U}_D)^{-1} \boldsymbol{\mathcal{G}} \right) \boldsymbol{U}_I \tag{D.14}$$

Table D.1: Solution procedure for one representative time step

---

1. Subdivide the set of all possible contact constraints $\bar{\omega}^{(1)}$ into the set of active constraints $\mathcal{A}_k$ and the set of inactive constraints $\mathcal{I}_k$, such that $\bar{\omega}^{(1)} = \mathcal{A}_k \cup \mathcal{I}_k$ and $\mathcal{A}_k \cap \mathcal{I}_k = \emptyset$, and set $k = 1$ for initialization.
2. Find $\boldsymbol{q}_{n+1} \in \mathbb{R}^n$ and $\boldsymbol{\lambda}_{A,n+1} = [\lambda_{A,n+1}]$ for $A \in \mathcal{A}_k$ ($\lambda_{A,n+1} = 0$ for $A \in \mathcal{I}_k$), set the iteration index $l = 1$.
    a) Given $\boldsymbol{q}_{n+1}^{(l)}$ and $\boldsymbol{\lambda}_{n+1}^{(l)}$, calculate the residual vector

    $$\boldsymbol{R}^{(l)} = \begin{bmatrix} \boldsymbol{R}_q(\boldsymbol{q}_{n+1}^{(l)}, \boldsymbol{\lambda}_{n+1}^{(l)}) \\ \boldsymbol{R}_\lambda(\boldsymbol{q}_{n+1}^{(l)}) \end{bmatrix}$$

    and check for convergence, i.e. check whether $\|\boldsymbol{R}^{(l)}\| < \epsilon$, where ϵ is a prescribed tolerance.

    b) If convergence has not been attained, calculate the discrete null space matrix

    $$\widetilde{\boldsymbol{P}}^{(l)} = \left(\boldsymbol{I}_n - \boldsymbol{U}_D^{(l)} (\widetilde{\boldsymbol{\mathcal{G}}}^{(l)} \boldsymbol{U}_D^{(l)})^{-1} \widetilde{\boldsymbol{\mathcal{G}}}^{(l)}\right) \boldsymbol{U}_I^{(l)}$$

    and solve the algebraic system of linear equations

    $$\begin{bmatrix} \widetilde{\boldsymbol{P}}^{(l)^T} \boldsymbol{\mathcal{N}}^{(l)} \\ \boldsymbol{\mathcal{G}}^{(l)} \end{bmatrix} \Delta \boldsymbol{q} = - \begin{bmatrix} \widetilde{\boldsymbol{P}}^{(l)^T} \boldsymbol{R}_q^{(l)} \\ \boldsymbol{R}_\lambda^{(l)} \end{bmatrix}$$

    Now, determine $\Delta\boldsymbol{\lambda}$ via

    $$\Delta\boldsymbol{\lambda} = -\frac{1}{\Delta t} \left(\widetilde{\boldsymbol{\mathcal{G}}}^{(l)} \boldsymbol{U}_D^{(l)}\right)^{-T} \boldsymbol{U}_D^{(l)^T} \left[\boldsymbol{R}_q^{(l)} + \boldsymbol{\mathcal{N}}^{(l)} \Delta \boldsymbol{q}\right]$$

    c) Update the unknowns according to

    $$\begin{aligned} \boldsymbol{q}_{n+1}^{(l+1)} &= \boldsymbol{q}_{n+1}^{(l)} + \Delta\boldsymbol{q} \\ \boldsymbol{\lambda}_{n+1}^{(l+1)} &= \boldsymbol{\lambda}_{n+1}^{(l)} + \Delta\boldsymbol{\lambda} \end{aligned}$$

    and repeat the procedure with new iteration counter $l + 1$ until convergence.
3. Update the sets $\mathcal{A}_k$ and $\mathcal{I}_k$ according to

    $$\begin{aligned} \mathcal{A}_{k+1} &= \{A \in \bar{\omega}^{(1)} : \lambda_{A,n+1} + c\Phi_A(\boldsymbol{q}_{n+1}) > 0\} \\ \mathcal{I}_{k+1} &= \{A \in \bar{\omega}^{(1)} : \lambda_{A,n+1} + c\Phi_A(\boldsymbol{q}_{n+1}) \leq 0\} \end{aligned}$$

    (for some $c > 0$), and repeat the procedure with new iteration counter $k + 1$ until the sets remain unchanged.

The solution of $(D.10)$ is given by

$$\Delta\boldsymbol{q} = \boldsymbol{U}_I \Delta\boldsymbol{u}_I + \boldsymbol{U}_D \Delta\boldsymbol{u}_D \tag{D.15}$$

where $\Delta\boldsymbol{u}_I \in \mathbb{R}^{n-m}$ can be obtained from $(D.13)$ and $\Delta\boldsymbol{u}_D \in \mathbb{R}^m$ from $(D.12)$. In essence, the implementation of this approach is contained in [10, Table 3]. It is worth noting that the staggered solution for $\Delta\boldsymbol{u}_I$ and $\Delta\boldsymbol{u}_D$ corresponds to the application of forward substitution to the block lower triangular system

$$\begin{bmatrix} \widetilde{\boldsymbol{P}}^T \boldsymbol{\mathcal{N}} \boldsymbol{P} & \boldsymbol{0} \\ \boldsymbol{\mathcal{G}} \boldsymbol{U}_I & \boldsymbol{\mathcal{G}} \boldsymbol{U}_D \end{bmatrix} \begin{bmatrix} \Delta\boldsymbol{u}_I \\ \Delta\boldsymbol{u}_D \end{bmatrix} = - \begin{bmatrix} \widetilde{\boldsymbol{P}}^T \boldsymbol{R}_q \\ \boldsymbol{R}_\lambda \end{bmatrix} \tag{D.16}$$

Premultiplying equation $(D.16)$ by

$$\begin{bmatrix} \boldsymbol{I}_{n-m} & (\boldsymbol{\mathcal{G}} \boldsymbol{U}_I)^T \\ \boldsymbol{0} & (\boldsymbol{\mathcal{G}} \boldsymbol{U}_D)^T \end{bmatrix} \tag{D.17}$$

yields

$$\left\{\begin{bmatrix}\widetilde{\boldsymbol{P}}^T\boldsymbol{\mathcal{N}}\boldsymbol{P} & \boldsymbol{0}\\ \boldsymbol{0} & \boldsymbol{0}\end{bmatrix} + (\widetilde{\boldsymbol{\mathcal{G}}}\boldsymbol{U})^T\boldsymbol{\mathcal{G}}\boldsymbol{U}\right\}\begin{bmatrix}\Delta\boldsymbol{u}_I\\ \Delta\boldsymbol{u}_D\end{bmatrix} = -\begin{bmatrix}\widetilde{\boldsymbol{P}}^T\boldsymbol{R}_q\\ \boldsymbol{0}\end{bmatrix} - (\widetilde{\boldsymbol{\mathcal{G}}}\boldsymbol{U})^T\boldsymbol{R}_\lambda \tag{D.18}$$

It can be easily verified by a straightforward calculation, that (D.18) can be written in the alternative form

$$\left\{\widetilde{\boldsymbol{\Pi}}^T\boldsymbol{U}^T\boldsymbol{\mathcal{N}}\boldsymbol{U}\boldsymbol{\Pi} + (\widetilde{\boldsymbol{\mathcal{G}}}\boldsymbol{U})^T\boldsymbol{\mathcal{G}}\boldsymbol{U}\right\}\begin{bmatrix}\Delta\boldsymbol{u}_I\\ \Delta\boldsymbol{u}_D\end{bmatrix} = -\widetilde{\boldsymbol{\Pi}}^T\boldsymbol{U}^T\boldsymbol{R}_q - (\widetilde{\boldsymbol{\mathcal{G}}}\boldsymbol{U})^T\boldsymbol{R}_\lambda \tag{D.19}$$

with

$$\widetilde{\boldsymbol{\Pi}} := \boldsymbol{I}_n - \widetilde{\boldsymbol{W}}\widetilde{\boldsymbol{\mathcal{G}}}\boldsymbol{U}, \quad \widetilde{\boldsymbol{W}} = \begin{bmatrix}\boldsymbol{0}_{(n-m)\times m}\\ (\widetilde{\boldsymbol{\mathcal{G}}}\boldsymbol{U}_D)^{-1}\end{bmatrix} \tag{D.20}$$

and

$$\boldsymbol{\Pi} := \boldsymbol{I}_n - \boldsymbol{W}\boldsymbol{\mathcal{G}}\boldsymbol{U}, \quad \boldsymbol{W} = \begin{bmatrix}\boldsymbol{0}_{(n-m)\times m}\\ (\boldsymbol{\mathcal{G}}\boldsymbol{U}_D)^{-1}\end{bmatrix} \tag{D.21}$$

We finally remark that the described procedure for solving the underlying saddle point system (D.1) is closely related to previous works by Krause & Wohlmuth [50, Section 3.] and Ainsworth [1] dealing with the solution of symmetric saddle point systems.

Application to the 2D NTS contact element. The application of the discrete null space method to contact problems rests on the design of a viable discrete null space matrix (D.9). To this end, the matrices $\boldsymbol{U}_I$ and $\boldsymbol{U}_D$ resulting from a suitable coordinate partitioning of the form (D.3) have to be devised.

We first illustrate our approach with the NTS method dealt with in Betsch & Hesch [11, Section 3.5]. Accordingly, consider a NTS contact element with the vector of relevant nodal coordinates

$$\overline{\boldsymbol{q}} = \begin{bmatrix}\boldsymbol{x}_S\\ \boldsymbol{y}_1\\ \boldsymbol{y}_2\end{bmatrix} \tag{D.22}$$

Note that to each slave node $\boldsymbol{x}_S$, there is associated one constraint of impenetrability. We now perform the decomposition

$$\Delta\boldsymbol{x}_S = \boldsymbol{\tau}\Delta u_{S,I} + \boldsymbol{\nu}\Delta u_{S,D} \tag{D.23}$$

where, on the master side, the unit tangent and normal vectors are defined by

$$\begin{aligned}\boldsymbol{\tau} &= (\boldsymbol{y}_2 - \boldsymbol{y}_1)/\|\boldsymbol{y}_2 - \boldsymbol{y}_1\|\\ \boldsymbol{\nu} &= -\boldsymbol{\Lambda}\boldsymbol{\tau}\end{aligned} \tag{D.24}$$

and $\boldsymbol{\Lambda}$ is given as

$$\boldsymbol{\Lambda} = \begin{bmatrix}0 & 1\\ -1 & 0\end{bmatrix} \tag{D.25}$$

According to (D.23), the displacement of the slave node $u_{S,D}$ in normal direction has been chosen as dependent coordinate. Now, for the NTS element under consideration, the partitioning (D.4) can be written as

$$\Delta\overline{\boldsymbol{q}} = \overline{\boldsymbol{U}}_I \Delta\overline{\boldsymbol{u}}_I + \overline{\boldsymbol{U}}_D \Delta\overline{u}_D \tag{D.26}$$

where

$$\Delta\overline{\boldsymbol{u}}_I = \begin{bmatrix} \Delta u_{S,I} \\ \Delta\boldsymbol{y}_1 \\ \Delta\boldsymbol{y}_2 \end{bmatrix}, \quad \Delta\overline{u}_D = \Delta u_{S,D} \tag{D.27}$$

and

$$\overline{\boldsymbol{U}}_I = \begin{bmatrix} \boldsymbol{\tau} & \boldsymbol{0} & \boldsymbol{0} \\ \boldsymbol{0} & \boldsymbol{I}_2 & \boldsymbol{0} \\ \boldsymbol{0} & \boldsymbol{0} & \boldsymbol{I}_2 \end{bmatrix}, \quad \overline{\boldsymbol{U}}_D = \begin{bmatrix} \boldsymbol{\nu} \\ \boldsymbol{0} \\ \boldsymbol{0} \end{bmatrix} \tag{D.28}$$

Since the constraint Jacobian pertaining to the NTS element is given by (cf. equation (71) in Betsch & Hesch [11])

$$\overline{\boldsymbol{\mathcal{G}}} = \begin{bmatrix} \boldsymbol{\nu}^T & -N^1\boldsymbol{\nu}^T & -N^2\boldsymbol{\nu}^T \end{bmatrix} \tag{D.29}$$

we obtain

$$\overline{\boldsymbol{\mathcal{G}}}\,\overline{\boldsymbol{U}}_D = \boldsymbol{\nu}\cdot\boldsymbol{\nu} = 1 \tag{D.30}$$

Accordingly, in the static case, equation (D.9) for the null space matrix (which is identical to (D.14) in the case of equilibrium problems) can be evaluated in a straightforward way, taking into account that, due to property (D.30), $\boldsymbol{\mathcal{G}}\boldsymbol{U}_D$ coincides with the $m \times m$ identity matrix. Thus (D.9) gives the null space matrix

$$\boldsymbol{P} = (\boldsymbol{I}_n - \boldsymbol{U}_D\boldsymbol{\mathcal{G}})\,\boldsymbol{U}_I \tag{D.31}$$

where the $n \times m$ matrix $\boldsymbol{U}_D$ follows from the assembly of the matrices $\overline{\boldsymbol{U}}_D$ pertaining to the respective slave node. The $n \times (n-m)$ matrix $\boldsymbol{U}_I$ can be viewed as modification of the identity matrix resulting from the contributions $\overline{\boldsymbol{U}}_I$ of the slave nodes, given by (D.28). It is worth remarking that recently Muñoz [45] proposed an alternative way to set up a null space matrix for the NTS method based on a global parametrization of the master surface in terms of cubic B-splines. Yet another related approach can be found in Chow et al. [17].

For transient problems, in (D.9), $\widetilde{\boldsymbol{\mathcal{G}}}$ contains the contributions of the discrete constraint gradient associated with each slave node, $\overline{\nabla}_{\mathrm{q}}\,\Phi_S(\overline{\boldsymbol{q}}_n, \overline{\boldsymbol{q}}_{n+1})$ (cf. equation (75) in Betsch & Hesch [11]). In this case we choose

$$\overline{\boldsymbol{U}}_I = \begin{bmatrix} \overline{\boldsymbol{\tau}} & \boldsymbol{0} & \boldsymbol{0} \\ \boldsymbol{0} & \boldsymbol{I}_2 & \boldsymbol{0} \\ \boldsymbol{0} & \boldsymbol{0} & \boldsymbol{I}_2 \end{bmatrix}, \quad \overline{\boldsymbol{U}}_D = \begin{bmatrix} \overline{\boldsymbol{\nu}} \\ \boldsymbol{0} \\ \boldsymbol{0} \end{bmatrix} \tag{D.32}$$

where

$$\overline{\boldsymbol{\nu}} = \varsigma/\|\varsigma\|\,, \quad \overline{\boldsymbol{\tau}} = \boldsymbol{\Lambda}\overline{\boldsymbol{\nu}}\,, \quad \varsigma = \overline{\nabla}_{\mathrm{x_S}}\,\Phi_S(\overline{\boldsymbol{q}}_n, \overline{\boldsymbol{q}}_{n+1}) \tag{D.33}$$

Similar to the static case, property (D.30) holds again. Consequently, analogous to (D.31), the discrete null space matrix assumes the form

$$\widetilde{\boldsymbol{P}} = \left(\boldsymbol{I}_n - \boldsymbol{U}_D \widetilde{\boldsymbol{\mathcal{G}}}\right) \boldsymbol{U}_I \tag{D.34}$$

where, as before, $\boldsymbol{U}_I$ and $\boldsymbol{U}_D$ are associated with the slave node contributions (D.32).

Mortar contact description Guided by our previous developments in the context of the NTS method, we choose the nodes on the non-mortar side to perform a decomposition similar to (D.23). Accordingly, consider the position vector $\boldsymbol{q}_A^{(1)}$ on the non-mortar side (i.e. $A \in \bar{\omega}^{(1)}$) and perform the split

$$\Delta \boldsymbol{q}_A^{(1)} = \boldsymbol{\tau}_A^{(1)} \Delta u_{A,I}^{(1)} + \boldsymbol{\nu}_A^{(1)} \Delta u_{A,D}^{(1)} \tag{D.35}$$

where

$$\boldsymbol{\nu}_A = \boldsymbol{\varsigma}_A / \|\boldsymbol{\varsigma}_A\| \,, \quad \boldsymbol{\tau}_A = \boldsymbol{\Lambda} \boldsymbol{\nu}_A \,, \quad \boldsymbol{\varsigma}_A = \overline{\nabla}_{\boldsymbol{q}_A^{(1)}} \Phi^A(\boldsymbol{q}_n, \boldsymbol{q}_{n+1}) \tag{D.36}$$

Taking into account the structure of the system configuration vector (2.2), the above decomposition gives rise to

$$\begin{bmatrix} \Delta \boldsymbol{q}_1^{(1)} \\ \vdots \\ \Delta \boldsymbol{q}_A^{(1)} \\ \vdots \\ \Delta \boldsymbol{q}^{(2)} \end{bmatrix} = \underbrace{\begin{bmatrix} \boldsymbol{I}_2 & & & & \\ & \ddots & & & \\ & & \boldsymbol{\tau}_A^{(1)} & & \\ & & & \ddots & \\ & & & & \boldsymbol{I}_{2n_{\text{node}}^{(2)}} \end{bmatrix}}_{\boldsymbol{U}_{I,A}} \begin{bmatrix} \Delta \boldsymbol{q}_1^{(1)} \\ \vdots \\ \Delta u_{A,I}^{(1)} \\ \vdots \\ \Delta \boldsymbol{q}^{(2)} \end{bmatrix} + \underbrace{\begin{bmatrix} \boldsymbol{0} \\ \vdots \\ \boldsymbol{\nu}_A^{(1)} \\ \vdots \\ \boldsymbol{0} \end{bmatrix}}_{\boldsymbol{U}_{D,A}} \Delta u_{A,D}^{(1)} \tag{D.37}$$

The assembly of the column matrices $\boldsymbol{U}_{D,A}$ yields the $n \times m$ matrix $\boldsymbol{U}_D$. Note that, by design, the diagonal elements of the $m \times m$ matrix $\widetilde{\boldsymbol{\mathcal{G}}} \boldsymbol{U}_D$ are equal to one. However, in contrast to the NTS method treated above, $\widetilde{\boldsymbol{\mathcal{G}}} \boldsymbol{U}_D$ does not coincide with the identity matrix anymore. Due to the structure of the mortar contact constraints, $\widetilde{\boldsymbol{\mathcal{G}}} \boldsymbol{U}_D$ has at most three non-zero elements per row. With regard to (D.9), the discrete null space matrix is given by

$$\widetilde{\boldsymbol{P}} = \left(\boldsymbol{I}_n - \boldsymbol{U}_D (\widetilde{\boldsymbol{\mathcal{G}}} \boldsymbol{U}_D)^{-1} \widetilde{\boldsymbol{\mathcal{G}}}\right) \boldsymbol{U}_I \tag{D.38}$$

where $\boldsymbol{U}_I$ is a $n \times (n-m)$ matrix which results from the $n \times n$ identity matrix by replacing the 2×2 block identity matrices on the diagonal with column vectors $\boldsymbol{\tau}_A^{(1)}$ (cf. equation (D.37)).

Bibliography

[1] M. Ainsworth. Essential boundary conditions and multi-point constraints in finite element analysis. *Comput. Methods Appl. Mech. Engrg.*, 190:6323–6339, 2001.

[2] D. Anders, C. Hesch, and K. Weinberg. Computational modeling of phase separation and coarsening in solder alloys. *Int. J. Solids Structures*, 49:1557–1572, 2012.

[3] F. Armero and E. Petöcz. Formulation and analysis of conserving algorithms for frictionless dynamic contact/impact problems. *Comput. Methods Appl. Mech. Engrg.*, 158:269–300, 1998.

[4] F. Armero and E. Petöcz. A new dissipative time-stepping algorithm for frictional contact problems: formulation and analysis. *Comput. Methods Appl. Mech. Engrg.*, 179:159–178, 1999.

[5] T. Belytschko, W.K. Liu, and B. Moran. *Nonlinear Finite Elements for Continua and Structures*. John Wiley & Sons, 2000.

[6] T. Belytschko, J.S. Ong, W.K. Liu, and J.M. Kennedy. Hourglass control in linear and nonlinear problems. *Comput. Methods Appl. Mech. Engrg.*, 43:251–276, 1984.

[7] D.J. Benson and J.O. Hallquist. A single surface contact algorithm for the post-buckling analysis of shell structures. *Comput. Methods Appl. Mech. Engrg.*, pages 141–163, 1990.

[8] M. Benzi, G.H. Golub, and J. Liesen. Numerical solution of saddle point problems. *Acta Numerica*, 14:1–137, 2005.

[9] C. Bernardi, Y. Mayday, and A.T. Patera. A new nonconforming approch to domain decomposition: the mortar element method. *Nonlinear partial differential equations and their applications*, pages 13–51, 1994.

[10] P. Betsch. The discrete null space method for the energy consistent integration of constrained mechanical systems Part I: Holonomic constraints. *Comput. Methods Appl. Mech. Engrg.*, 194:5159–5190, 2005.

[11] P. Betsch and C. Hesch. Energy-momentum conserving schemes for frictionless dynamic contact problems. Part I: NTS method. In P. Wriggers and U. Nackenhorst, editors, *IUTAM Symposium on Computational Methods in Contact Mechanics*, volume 3 of *IUTAM Bookseries*, pages 77–96. Springer-Verlag, 2007.

[12] P. Betsch, C. Hesch, N. Sänger, and S. Uhlar. Variational integrators and energy-momentum schemes for flexible multibody dynamics. *Journal of Computational and Nonlinear Dynamics*, 5(3), March 2010.

[13] P. Betsch and P. Steinmann. Conserving properties of a time FE method - Part II: Time-stepping schemes for non-linear elastodynamics. *Int. J. Numer. Methods Eng.*, 50:1931–1955, 2001.

[14] P. Betsch and P. Steinmann. Conservation Properties of a Time FE Method. Part III: Mechanical systems with holonomic constraints. *Int. J. Numer. Methods Eng.*, 53:2271–2304, 2002.

[15] J.W. Cahn and J.E. Hilliard. Free Energy of a Nonuniform System. I. Interfacial Free Energy. *Journal of Chemical Physics*, 28(2):258–267, 1958.

[16] J.W. Cahn and J.E. Hilliard. Free Energy of a Nonuniform System. ITI. Nucleation in a Two-Component Incompressible Fluid. *Journal of Chemical Physics*, 31(2):688–699, 1959.

[17] E. Chow, T.A. Manteuffel, C. Tong, and B.K. Wallin. Algebraic elimination of slide surface constraints in implicit structural analysis. *Int. J. Numer. Methods Eng.*, 57:1129–1144, 2003.

[18] J.A. Cottrell, T.J.R. Hughes, and Y. Bazilevs. *Isogeometric Analysis: Toward Integration of CAD and FEA.* Wiley, New York, 2009.

[19] J. Donea and A. Huerta. *Finite element methods for flow problems.* John Wiley & Sons, 2003.

[20] K.A. Fischer and P. Wriggers. Mortar based frictional contact formulations for higher order interpolations using the moving friction cone. *Comput. Methods Appl. Mech. Engrg.*, 195:5020–5036, 2006.

[21] M. Franke, C. Hesch, and P. Betsch. An augmentation technique for large deformation frictional contact problems. *Int. J. Numer. Methods Eng.*, DOI: 10.1002/nme.4466.

[22] A.J. Gil, A. Arranz Carreño, J. Bonet, and O. Hassan. The immersed structural potential method for haemodynamic applications. *Journal of Computational Physics*, 229:8613–8641, 2010.

[23] A.J. Gil, A. Arranz Carreño, J. Bonet, and O. Hassan. An enhanced Immersed Structural Potential Method for fluid–structure interaction. *Journal of Computational Physics*, 2012. submitted.

[24] M. Gitterle, A. Popp, W. Gee, and W.A. Wall. Finite deformation frictional mortar contact using a semi-smooth newton method with consistent linearization. *Int. J. Numer. Methods Eng.*, 84:543–571, 2010.

[25] H. Gomez, V.M. Calo, Y. Bazilevs, and T.J.R. Hughes. Isogeometric analysis of the Cahn–Hilliard phase-field model. *Comput. Methods Appl. Mech. Engrg.*, 197:4333–4352, 2008.

[26] O. Gonzalez. Time integration and discrete Hamiltonian systems. *J. Nonlinear Sci.*, 6:449–467, 1996.

[27] O. Gonzalez. Mechanical systems subject to holonomic constraints: Differential - algebraic formulations and conservative integration. *Physica D*, 132:165–174, 1999.

[28] O. Gonzalez and A.M. Stuart. *A First Course in Continuum Mechanics*. Cambridge Univ. Press, 1nd edition, 2008.

[29] G. Haikal and K.D. Hjelmstad. A finite element formulation of non-smooth contact based on oriented volumes for quadrilateral and hexahedral elements. *Comput. Methods Appl. Mech. Engrg.*, 196:4690–4711, 2007.

[30] J.O. Hallquist. Nike2d. *Technical Report UCRL-52678, University of California, Lawrence Livermore National Laboratory*, 1979.

[31] P. Hauret and P. LeTallec. Energy-controlling time integration methods for nonlinear elastodynamics and low-velocity impact. *Comput. Methods Appl. Mech. Engrg.*, 195:4890–4916, 2006.

[32] P. Hauret and P. LeTallec. A discontinous stabilized mortar method for general 3D elastic problems. *Comput. Methods Appl. Mech. Engrg.*, 196:4881–4900, 2007.

[33] C. Hesch and P. Betsch. A mortar method for energy-momentum conserving schemes in frictionless dynamic contact problems. *Int. J. Numer. Methods Eng.*, 77:1468–1500, 2009.

[34] C. Hesch and P. Betsch. Transient 3D Domain Decomposition Problems: Frame-indifferent mortar constraints and conserving integration. *Int. J. Numer. Methods Eng.*, 82:329–358, 2010.

[35] C. Hesch and P. Betsch. Energy-momentum consistent algorithms for dynamic thermomechanical problems - Application to mortar domain decomposition problems. *Int. J. Numer. Methods Eng.*, 86:1277–1302, 2011.

[36] C. Hesch and P. Betsch. Transient 3d contact problems – Mortar method: Mixed methods and conserving integration. *Computational Mechanics*, 48:461–475, 2011.

[37] C. Hesch and P. Betsch. Transient 3d contact problems – NTS method: Mixed methods and conserving integration. *Computational Mechanics*, 48:437–449, 2011.

[38] C. Hesch, A.J. Gil, A. Arranz Carreño, and J. Bonet. On immersed techniques for fluid-structure interaction. *Comput. Methods Appl. Mech. Engrg.*, 247-248:51–64, 2012.

[39] C. Hesch and P.Betsch. Isogeometric analysis and domain decomposition methods. *Comput. Methods Appl. Mech. Engrg.*, 213:104–112, 2012.

[40] G.A. Holzapfel. *Nonlinear Solid Mechanics.* John Wiley & Sons, 2001.

[41] G.A. Holzapfel and J.C. Simo. Entropy elasticity of isotropic rubber-like solids at finite strains. *Comput. Methods Appl. Mech. Engrg.*, 132:17–44, 1996.

[42] S. Hüeber and B.I. Wohlmuth. A primal-dual active set strategy for non-linear multibody contact problems. *Comput. Methods Appl. Mech. Engrg.*, 194:3147–3166, 2005.

[43] S. Hüeber and B.I. Wohlmuth. Mortar methods for contact problems. In P. Wriggers and U. Nackenhorst, editors, *Analysis and Simulation of Contact Problems*, volume 27 of *Lecture Notes in Applied and Computational Mechanics*, pages 39–47. Springer-Verlag, 2006.

[44] T.J.R. Hughes. *The Finite Element Method.* Dover Publications, 2000.

[45] J.J. Mũnoz. Modelling unilateral frictionless contact using the null-space method and cubic B-spline interpolation. *Comput. Methods Appl. Mech. Engrg.*, 979-993:197, 2008.

[46] T. Kloeppel, A. Popp, U. Kuettler, and W.A. Wall. Fluid–structure interaction for non-conforming interfaces based on a dual mortar formulation. *Comput. Methods Appl. Mech. Engrg.*, 200:3111–3126, 2011.

[47] A. Konyukhov and K. Schweizerhof. Covariant description for frictional contact problems. *Comput. Methods Appl. Mech. Engrg.*, 35:190–213, 2005.

[48] A. Konyukhov and K. Schweizerhof. Covariant description of contact interfaces considering anisotropy for adhesion and friction: Part 1. Formulation and analysis of the computational model. *Comput. Methods Appl. Mech. Engrg.*, 196:103–117, 2006.

[49] A. Kovetz. *Electromagnetic Theory: With 225 Solved Problems.* Oxford University Press, 2001.

[50] R. Krause and B.I. Wohlmuth. Nonconforming domain decomposition techniques for linear elasticity. *East-West J. Numer. Math.*, 8(3):177–206, 2000.

[51] T.A. Laursen. *Formulation and treatment of frictional contact problems using finite elements.* PhD thesis, Stanford University, 1992.

[52] T.A. Laursen. *Computational Contact and Impact Mechanics.* Springer-Verlag, 2002.

[53] T.A. Laursen and V. Chawla. Design of energy conserving algorithms for frictionless dynamic contact problems. *Int. J. Numer. Methods Eng.*, 40:863–886, 1997.

[54] T.A. Laursen and G.R. Love. Improved implicit integrators for transient impact problems – geometric admissibility within the conserving framework. *Int. J. Numer. Methods Eng.*, 53:245–274, 2002.

[55] W.K. Liu, D.W. Kim, and S. Tang. Mathematical foundations of the immersed finite element method. *Computational Mechanics*, 39:211–222, 2007.

[56] L.A. Pars. *A Treatise on Analytical Dynamics* . Ox Bow Press, 1965.

[57] C.S. Peskin. Flow patterns around heart values: A numerical method. *Journal of Computational Physics*, 10:252–271, 1972.

[58] C.S. Peskin. Numerical analysis of blood flow in the heart. *Journal of Computational Physics*, 25:220–252, 1977.

[59] C.S. Peskin. The immersed boundary method. *Acta Numerica*, 11:479–517, 2002.

[60] L. Piegl and W. Tiller. *The NURBS Book*. Springer, 2nd edition, 2010.

[61] A. Popp, M. Gitterle, W. Gee, and W.A. Wall. A dual mortar approach for 3d finite deformation contact with consistent linearization. *Int. J. Numer. Methods Eng.*, 83:1428–1465, 2010.

[62] M.A. Puso. A 3D mortar method for solid mechanics. *Int. J. Numer. Methods Eng.*, 59:315–336, 2004.

[63] M.A. Puso, T.A. Laursen, and J.M. Solberg. A segment-to-segment mortar contact method for quadratic elements and large deformations. *Comput. Methods Appl. Mech. Engrg.*, 197:555–566, 2008.

[64] J.C. Simo and F. Armero. Geometrically non-linear enhanced strain mixed methods and the method of incompatible modes. *Int. J. Numer. Methods Eng.*, 33:1413–1449, 1992.

[65] J.C. Simo, F. Armero, and R.L. Taylor. Improved versions of assumed enhanced strain tri-linear elements for 3d finite deformation problems. *Comput. Methods Appl. Mech. Engrg.*, 110:359–386, 1993.

[66] J.C. Simo and N. Tarnow. The discrete energy-momentum method. Conserving algorithms for nonlinear elastodynamics. *Z. angew. Math. Phys. (ZAMP)*, 43:757–792, 1992.

[67] J.C. Simo, N. Tarnow, and K.K. Wong. Exact energy-momentum conserving algorithms and symplectic schemes for nonlinear dynamics. *Comput. Methods Appl. Mech. Engrg.*, 100:63–116, 1992.

[68] I. Temizer, P. Wriggers, and T.J.R. Hughes. Contact treatment in isogeometric analysis with NURBS. *Comput. Methods Appl. Mech. Engrg.*, 200:1100–1112, 2011.

[69] T.E. Tezduyar. Stabilized finite element formulations for incompressible flow computations. *Advances in applied mechanics*, 28:1–44, 1992.

[70] T.E. Tezduyar. Finite element methods for flow problems with moving boundaries and interfaces. *Arch. Comput. Methods Engrg.*, 8:83–130, 2001.

[71] T.E. Tezduyar and Y. Osawa. Finite element stabilization parameters computed from element matrices and vectors. *Comput. Methods Appl. Mech. Engrg.*, 190:411–430, 2000.

[72] M. Tur, F.J. Fuenmayor, and P. Wriggers. A mortar-based frictional contact formulation for large deformations using Lagrange multipliers. *Comput. Methods Appl. Mech. Engrg.*, 198:2860–2873, 2009.

[73] H. Wang, J. Chessa, W.K. Liu, and T. Belytschko. The immersed/fictitious element method for fluid-structure interaction: Volumetric consistency, compressibility and thin memebers. *Int. J. Numer. Methods Eng.*, 74:32–55, 2008.

[74] X. Wang and W.K. Liu. Extended immersed boundary method using FEM and RKPM. *Comput. Methods Appl. Mech. Engrg.*, 193:1305–1321, 2004.

[75] E.L. Wilson, R.L. Taylor, W.P. Doherty, and J. Ghaboussi. Incompatible displacement models. *Numerical and Computer Models in Structural Mechanics, Academic Press, New York*, 1973.

[76] B.I. Wohlmuth. Variationally consistent discretization schemes and numerical algorithms for contact problems. *Acta Numerica*, 20:569–734, 2011.

[77] P. Wriggers. *Computational Contact Mechanics.* Springer-Verlag, 2nd edition, 2006.

[78] P. Wriggers, T.V. Van, and E. Stein. Finite element formulations of large deformation impact-contact problems with friction. *Computers and Structures*, 37:319–331, 1990.

[79] B. Yang and T.A. Laursen. A contact searching algorithm including bounding volume trees applied to finite sliding mortar formulation. *Computational Mechanics*, 41:189–205, 2008.

[80] B. Yang and T.A. Laursen. A large deformation mortar formulation of self contact with finite sliding. *Comput. Methods Appl. Mech. Engrg.*, 197:756–772, 2008.

[81] B. Yang, T.A. Laursen, and X. Meng. Two dimensional mortar contact methods for large deformation frictional sliding. *Int. J. Numer. Methods Eng.*, 62:1183–1225, 2005.

[82] Allen R. York II, Deborah Sulsky, and Howard L. Schreyer. Fluid-membrane interaction based on the material point method. *International Journal for Numerical Methods in Engineering*, 48(6):901–924, 2000.

[83] L. Zhang, A. Gerstenberger, X. Wang, and W.K. Liu. Immersed finite element method. *Comput. Methods Appl. Mech. Engrg.*, 193:2051–2067, 2004.

[84] O.C. Zienkiewicz and R.L. Taylor. *The Finite Element Method for solid and structural mechanics.* Butterworth Heinemann, 6th edition, 2005.

[85] O.C. Zienkiewicz, R.L. Taylor, and P. Nithiarasu. *The Finite Element Method for Fluid Dynamics.* Butterworth Heinemann, 6th edition, 2005.

[86] O.C. Zienkiewicz, R.L. Taylor, and J.Z. Zhu. *The Finite Element Method. Its Basis and Fundamentals.* Butterworth Heinemann, 6th edition, 2005.